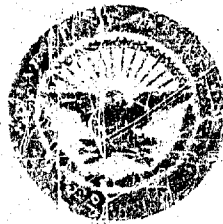


UNCLASSIFIED

AD 267 289

*Reproduced
by the*

ARMED SERVICES TECHNICAL INFORMATION AGENCY
ARLINGTON HALL STATION
ARLINGTON 12, VIRGINIA



This Document
Reproduced From
Best Available Copy

**This Document
Reproduced From
Best Available Copy**

NOTICE: When government or other drawings, specifications or other data are used for any purpose other than in connection with a definitely related government procurement operation, the U. S. Government thereby incurs no responsibility, nor any obligation whatsoever; and the fact that the Government may have formulated, furnished, or in any way supplied the said drawings, specifications, or other data is not to be regarded by implication or otherwise as in any manner licensing the holder or any other person or corporation, or conveying any rights or permission to manufacture, use or sell any patented invention that may in any way be related thereto.

This Document
Reproduced From
Best Available Copy

MASSACHUSETTS INSTITUTE OF TECHNOLOGY
Aeroblastic and Structures Research Laboratory

Survey of Hypervelocity Impact Information

Walter Herrmann and Arfon H. Jones

A. S. P. L. Report No. 99-1

September 1961

DEC 8 1961

The work reported in this document was performed at the
Aeroblastic and Structures Research Laboratory, M. I. T., for
Lincoln Laboratory under Purchase Order C-00591.

Lincoln Laboratory is a center for research operated by
Massachusetts Institute of Technology with joint support
of the U. S. Army, Navy and Air Force under Air Force
Contract AF 19(605)-7400.

FILE COPY

Return to

ASTIA

ATLINGTON HALL STATION

ATLINGTON, VIRGINIA

This Document
Reproduced From
Best Available Copy

Survey of Hypervelocity Impact Information

Walter Herrmann and Arfon H. Jones

A. S. R. L. Report No. 99-1

September 1961

ABSTRACT

In the volume
Available information relating to cratering and penetration in metallic targets has been gathered. Impact of compact particles, microparticles, and rods at normal and oblique incidence on quasi-infinite targets and on thin targets, multiple spaced targets, and shielded targets is considered. Experimental data ^{are} presented in tabular and graphical form for ready references. Available theories and semi-empirical theories, as well as empirical correlation equations are summarized ~~in uniform notation and are~~ ^{and} compared with each other and with the experimental data. For normal impact on quasi-infinite targets ~~two~~ ² empirical correlation expressions are deduced which are more generally applicable than previous expressions. A qualitative description of the cratering process is given, and realistic regions of impact are defined. Recommendations for future experimental and theoretical work are made.

This Document
Reproduced From
Best Available Copy

ACKNOWLEDGEMENTS

The authors are deeply indebted to personnel, too numerous to mention individually, from most of the laboratories listed in Table I, both for making data and additional information available, and for helpful and stimulating discussion. Special thanks are due to J. W. Gehring Jr., of Ballistic Research Laboratory, R. N. Hopko of NASA Langley, R. Nysmith of NASA Ames, R. L. Bjork of the RAND Corporation, G. M. Bryan Jr. of the Carnegie Institute of Technology and R. E. Slattery of Lincoln Laboratory MIT for making original prints of photographs and diagrams available.

Without the help and patience of Miss Helen Petrides, who programmed the least squares fits, and organized the data on punched cards, of Mrs. Marion Andrews of the Lincoln Computation Centre, and of Miss Maxine Weiner, who typed the manuscript, this study could not have been carried out.

This document contains
blank pages that were
not filmed

LIST OF CONTENTS

Section		Page
	Abstract	ii
	Acknowledgements	iii
	List of Contents	iv
	List of Symbols	vi
	List of Tables	viii
	List of Illustrations	ix
I	Introduction	1
II	Experimental Data	3
III	Existing Cratering and Penetration Theories	7
	3.1 Rigid Projectiles	7
	3.2 Hydrodynamic	23
	3.3 Thermal Penetration	31
	3.4 Explosive Analogy	36
IV	Empirical Relationships	39
	4.1 Early Armor Penetration Work	40
	4.2 High Velocity Penetration Work	45
	4.3 Dimensional Analysis	51
	4.4 Comparison of Theories and Empirical Expressions on the Basis of Resistance to Penetration	59
V	Normal Impact on Quasi-Infinite Targets	69
	5.1 Description of Phenomena	69
	5.2 Comparison of Data with Existing Theories	77

LIST OF CONTENTS (Cont'd)

Section	Page
5.3 Empirical Power Law	82
5.4 Empirical Logarithmic Law	101
5.5 Extrapolation of Empirical Penetration Laws	108
5.6 Definition of Regions of Impact	111
5.7 Discussion	114
VI Other Project -e-Target Configurations	119
6.1 Microparticle Penetration	119
6.2 Oblique Impact on Quasi-Infinite Targets	121
6.3 Rod Impact on Quasi-Infinite Targets	124
6.4 Thin Targets	132
VII Conclusions	143
Appendices	
A Zaid's Theory	147
B Opik's Meteorite Impact Theory	155
C Stanyukovitch's Equivalent Explosive Analogy	159
D Shock Relations	163
Bibliography	167
Tables	193
Figures	199
Addendum	
Tabulated Experimental Data	Vol. II

LIST OF SYMBOLS

b	Instantaneous crater radius
B	$= \rho V^2 / H$ Best Number
c	Dilatational bulk sonic velocity
\bar{c}	Longitudinal bar sonic velocity
d	Projectile diameter
D	Crater diameter in the plane of the original surface
e	Internal energy
E	Initial projectile energy
f	Shape factor
F	Force resisting penetration
g	Gravitational constant
G	Elastic modulus
h	Thickness
H	Brinell Hardness Number
k, K	Constants
L	Projectile length
m	Mass
M	$= V/c$ Mach number
p	Penetration, measured from the plane of the original surface
P	Pressure
q	Heat distribution function
Q	Energy to melt or vaporize unit mass of material
R	Projectile radius
S	Shield spacing
t	Time

LIST OF SYMBOLS (Cont'd)

T	Target thickness
u	Displacement
U	Shock velocity
v	Velocity
V	Initial projectile velocity
V_L	Minimum projectile velocity for perforation
V_c	Crater volume
V_p	Projectile volume
W	Resistance
Y	Yield strength
Z	Distance travelled by projectile during penetration
α	Constant
β	$= \rho_p / \rho_t$ Density ratio
γ	Ratio of major to minor axes
η	Efficiency
	Thermal diffusivity
	Deformation rate
ν	Poisson's ratio
ρ	Density
$\sigma_\theta, \sigma_r, \sigma_z$	Normal Stresses
τ	Shear stress
ϕ	Angle of incidence with respect to target normal
$()_p$	Refers to projectile
$()_t$	Refers to target
$()_c$	Refers to crater
$()_s$	Refers to shield
θ, r, z	Cylindrical coordinates

LIST OF TABLES

	Page
Table I Establishments Active in High Velocity Research	193
Table II Experimental Projectile-Semi-Infinite Target Material Combinations for which Data are Available	194
Table III Postulated Empirical Equations	195
Table IV Empirical Fits to the Penetration Law	196
Table V Empirical Fits to the Logarithmic Penetration Law	197

LIST OF ILLUSTRATIONS

Figure		Page
1.1	Projectile-Target Configurations	199
1.2	The Penetration of Aluminum into Aluminum 2024 T-3 Targets	200
1.3	The Penetration of Aluminum Spheres into 24 ST Aluminum Targets	201
1.4	The Penetration of Aluminum Spheres into 1100F Aluminum Targets	202
1.5	The Penetration of Copper into Aluminum 2024 T-3 and T-4 Targets	203
1.6	The Penetration of Copper into Aluminum 2024 T-3 and T-4 Targets	204
1.7	The Penetration of Lead into Aluminum 2024 T-3 Targets	205
1.8	The Penetration of Tungsten Carbide Spheres into Aluminum 2014 Targets	206
1.9	The Penetration of Aluminum Projectiles into 1020 Steel Targets	207
1.10	The Penetration of Aluminum Projectiles into 1030 Steel Targets	208
1.11	The Penetration of 2024 T-4 Aluminum Projectiles into 30 RC Steel Targets	209
1.12	The Penetration of Steel Projectiles in 1020 Steel Targets	210
1.13	The Penetration of Steel Projectiles into 1030 Steel Targets	211
1.14	The Penetration of RC-66 Steel Projectiles into 4140 Steel Targets	212

List of Illustrations (Cont'd)

Figure		Page
1.15	The Penetration of Lead Projectiles into 1020 Steel Targets	213
1.16	The Penetration of Tungsten Carbide Projectiles into 1020 Steel Targets	214
1.17	The Penetration of Steel Projectiles into Copper Targets	215
1.18	Penetration of Copper Projectiles into Copper Targets	216
1.19	The Penetration of Lead Projectiles in Copper Targets	217
1.20	The Penetration of Tungsten Carbide Projectiles into Copper Targets	218
1.21	The Penetration of Aluminum Projectiles into Lead Targets	219
1.22	The Penetration of Steel Projectiles into Lead Targets	220
1.23	The Penetration of Copper Projectiles into Lead Targets	221
1.24	The Penetration of Lead Projectiles into Lead Targets	222
1.25	The Penetration of Tungsten Carbide Projectiles into Lead Targets	223
4.1	Brinell Hardness versus Yield Strength for a Number of Representative Target Materials	224

List of Illustrations (Cont'd)

Figure		Page
4.2	Behaviour of Logarithmic Penetration Laws	225
5.1a	Initial Interface Pressures in one Dimensional Impact	227
5.1b	Initial Interface Velocities in One Dimensional Impact	228
5.2	Craters in Lead Targets formed by 1/8" Spheres at Approximately 700 ft/sec.	229
5.2 Cont'd	Craters in Lead Targets formed by 1/8" Spheres at Approximately 1500 ft/sec.	230
5.2 Cont'd	Craters in Lead Targets formed by 1/8" Spheres at Approximately 2000 ft/sec.	231
5.2 Cont'd	Craters in Lead Targets formed by 1/8" Spheres at Approximately 3000 ft/sec.	232
5.2 Concl.	Craters in Lead Targets formed by 1/8" Spheres at Approximately 5000 ft/sec.	233
5.3	Illustration of Regions of Impact for a Ductile Projectile	234
5.4	Illustration of Regions of Impact for a High Strength Projectile	235

List of Illustrations (Cont'd)

Figure		Page
5.5	Illustration of Cratering in the High Velocity Region. Copper Target Struck by Copper Sphere. The Projectile Material has been Lifted to Illustrate the Plating Effect. (Ref. 30)	236
5.6	High Speed Framing Camera Pictures of Penetration of a Lucite Target by a Steel Projectile (from Ref. 7)	237
5.7	Flash X-radiographs of the Formation of a Crater in a 2-SO Aluminum Target by a 0.18 gm Steel Projectile at 15,000 ft/sec. (Ref. 7)	238
5.8	Flash X-Radiograph of the Spray Issuing from a Crater in the Process of Formation in a Lead Target (Ref. 7)	239
5.9	Numerical Solution of the Penetration of an Iron Projectile into an Iron Target, Neglecting Material Strength (Ref. 128)	240
5.9 Cont'd	Note Changing Scale	241
5.9 Cont'd	Note Changing Scale	242
5.9 Cont'd	Note Changing Scale	243
5.10	Numerical Solution for the Penetration of a Meteorite into Tuff (Ref. 152)	244

List of Illustrations (Cont'd)

Figure		Page
5.10 Cont'd	Note Changing Scale	245
5.10 Cont'd	Note Changing Scale	246
5.10 Cont'd	Note Changing Scale	247
5.10 Cont'd	Note Changing Scale	248
5.10 Cont'd	Note Changing Scale	249
5.10 Concl.	Note Changing Scale	250
5.11	Crystallographic Changes in a 70:30 Brass Target in the Vicinity of the Crater x 500 (Ref. 25)	251
5.12	Penetration in Aluminum Targets	252
5.13	Penetration in Copper Targets	253
5.14	Penetration in Lead Targets	254
5.15	Penetration in Aluminum Targets	255
5.16	Penetration in Copper Targets	256
5.17	Penetration in Lead Targets	257
5.18	Penetration by Various Heat Treated Steel Spheres in 1030 Steel Targets	258
5.19	Penetration by Two Different Hardness Steel Cylinders in 30 RC Steel Targets	259
5.20	Penetration by 302 Stainless Steel and 440 Stainless Steel Spheres in Lead Targets	260

List of Illustrations (Cont'd)

Figure		Page
5.21	Penetration by Copper Spheres in Copper Targets BHN 65 and BHN 36	261
5.22	Penetration by Steel Projectiles in SAE 1020 Steel, 4140 Steel, 30 RC Steel, and AISI 1030 Steel Targets	262
5.23	Penetration by Aluminum Projectiles in 1100F Aluminum and 2024 Aluminum Targets	263
5.24	Penetration Ratio in Aluminum Targets	264
5.25	Penetration Ratio in Copper Targets	265
5.26	Penetration Ratio in Lead Targets	266
5.27	Penetration Dependence on Target Hardness	267
5.28	Penetration Dependence on Target Density	268
5.29	Depth-Diameter Ratios for Craters in Aluminum Targets	269
5.30	Depth-Diameter Ratios for Craters in Copper Targets	270
5.31	Depth-Diameter Ratios for Craters in 1020 Steel Targets	271
5.32	Depth-Diameter Ratios for Craters in Lead Targets	272
5.33	Energy-Volume Ratios for Aluminum Targets	273
5.34	Energy-Volume Ratios for Copper Targets	274
5.35	Energy-Volume Ratios for 1020 Steel Targets	275
5.36	Energy-Volume Ratios for Lead Targets	276

List of Illustrations (Cont'd)

Figure		Page
5.37	Energy-Volume Ratio Dependence on Density Ratio	277
5.38	Energy-Volume Ratio Dependence on Target Hardness	278
5.39	Initial Interface Velocity Dependence on Projectile Density at Constant Projectile Mass and Velocity	279
5.40	Correlation of Logarithmic Penetration Law Parameters with Density Ratio	280
5.41	Correlation of Logarithmic Penetration Law Parameters with Density Ratio	281
5.42	Extrapolation of Empirical Penetration Laws for Aluminum Projectiles and Targets	282
5.43	Extrapolation of Empirical Penetration Laws for Steel Projectiles and Targets	283
6.1	The Penetration of Stainless Steel Spheres (100 μ and 150 μ diameter) into Various Targets	284
6.2	The Penetration of Carbonyl Iron Micro- particles into Lead	285
6.3	Microparticle Cratering by 50 - 200 micron Cast Iron Particles	286
6.4	Craters formed by Lead Spheres in Lead Targets at 7000 ft/sec. at Oblique Angles of Impact	287

List of Illustrations (Cont'd)

Figure		Page
6.4 Concl.	Craters formed by Lead Spheres in Lead Targets at 7000 ft/sec. at Oblique Angles of Impact	288
6.5	Flash X-Radiographs of the Spray formed by Lead Projectile Impacting a Lead Target at about 7000 ft/sec. t is the Approximate Time after Impact (Ref. 153)	289
6.6	Flash X-Radiographs of Crater Formation in Aluminum Targets at 15,000 ft/sec. Radiographs at 50 μ /sec. after Impact	290
6.7	Craters formed in Lead Targets by Steel Projectiles at Oblique Angles of Impact (Ref. 7)	291
6.8	Penetration at Oblique Incidence	292
6.9	Penetration at Oblique Incidence	293
6.10	Microparticle Penetration at Oblique Incidence	294
6.11	Crater Volume at Oblique Incidence	295
6.12	Crater Mouth Dimensions for Oblique Impact	296
6.13	Penetration of Slender Rods Compared to that of Spheres in Aluminum	297
6.14	The Penetration of Aluminum Targets by Aluminum, Copper and Tin Rods	298
6.15	The Penetration of Aluminum Targets by Gold, Lead and Magnesium Rods	299

List of Illustrations (Cont'd)

Figure		Page
6.16	The Penetration of Steel Targets by Steel Rods	300
6.17	The Penetration of Copper Targets by Steel Rods	301
6.18	The Penetration of Copper Targets by Tungsten Carbide Rods	302
6.19	The Penetration of Lead Targets by Tungsten Carbide and Steel Rods	303
6.20	Penetration of Rods of Different Materials into Aluminum Targets at 8300 ft/sec.	304
6.21	Crater formed by a Slender Unyawed Ductile Rod at Low Velocity	305
6.22	Crater formed by a Slender Rod Yawed at 10^0 to Direction of Motion	305
6.23	Rear Surface Damage in Relatively Thick Targets	306
6.24a	Penetration in Finite Thickness Target in Terms of Penetration in a Quasi-Infinite Target	307
6.24b	Diameter of Crater in Finite Thickness Target in Terms of Projectile Diameter	307
6.25	Photographs of Projectile Penetrating a Thin Target	308
6.26	Framing Camera Sequence of Penetration of a Thin Target by a High Velocity Projectile, Showing Resultant Spray (0.22 inch Aluminum Sphere Impacting 1/8 inch Aluminum	309

List of Illustrations (Cont'd)

Figure		Page
6.27	Hole Diameter in a Thin Shield in Terms of Crater Diameter in an Unshielded Target as a Function of Shield Thickness	310
6.28	Total Penetration of a Shielded Target in Terms of Penetration in an Unshielded Target as a Function of Shield Thickness	311
6.29	Total Penetration of a Shielded Target in Terms of Penetration in an Unshielded Target as a Function of Shield Spacing	312
6.30	Spray Half Angle ($\theta = \text{Arc tan } \frac{D_c}{2S}$) as a Function of Shield Thickness (Ref. 102)	313
6.31	Threshold Velocity to just Penetrate all Plates as a Function of Number of Plates	314
6.32	Number of Plates Penetrated as a Function of Velocity	315
6.33	Damage to a Shielded Target 1/8 inch Lead Impacting Lead at 7000 ft/sec.	316

SECTION I

INTRODUCTION

Cratering and penetration of targets by projectiles travelling at velocities at which the projectiles suffer severe deformation or breakup has recently received a great deal of attention, due to the importance of this phenomenon in the protection and lethality of space vehicles and ballistic missiles.

A great deal of experimental data has been published by a number of laboratories, and considerable theoretical work has appeared during the last few years. Limited comparisons of data from one laboratory with that from another, and of experimental data with theory have shown some important discrepancies. Considerable confusion exists because, except in a few instances, the data from one laboratory are not directly comparable with those from another, since identical materials, projectile shapes or velocity ranges were not used. As a result, several more or less contradictory empirical expressions have been produced at different laboratories to fit their own data. Only the lower end of the velocity range of interest in space applications has been explored experimentally in any detail. Extrapolations of the various empirical data fits to higher velocities leads to large discrepancies.

Experimental-theoretical comparisons have been hampered by the fact that on the one hand, target and projectile material properties appearing in the theories have not been measured or reported by many laboratories. On the other hand most of the theories are simplified to the point

where they may be applicable to only very limited ranges of velocity and material properties, and the range of applicability of these theories is not clear.

In an attempt to assess the present status of experimental and theoretical knowledge of impact phenomena, experimental data published prior to 31 March 1961 was gathered and checked as far as possible for consistency, and compared where possible with the available theories. An attempt was also made to correlate the data on the basis of simple empirical expressions.

This report is limited to consideration of impact into metallic targets under conditions such that the projectile suffers severe deformation or breakup in the cratering process. Data on shaped charge jet penetration has been excluded since this has been covered adequately elsewhere.

SECTION II

EXPERIMENTAL DATA

During the data acquisition phase, thirty-nine groups active in high velocity impact or in developing projection techniques were either visited or contacted by telephone. Not every group had performed cratering experiments. Table I lists the laboratories in possession of experimental facilities, together with an indication of the type of work reported. The bibliography lists most of the important publications containing information on cratering generated at these laboratories.

Several different target configurations have been used. Most of the data related to configurations shown in Fig 1.1 They may be classified as:

- (a) Normal impact on quasi-infinite targets
- (b) Oblique impact on quasi-infinite targets
- (c) Rod impact on quasi-infinite targets
- (d) Impact on single thin targets
- (e) Impact on quasi-infinite targets protected by a thin shield
- (f) Impact on multiple spaced thin targets

An attempt has been made to extract the original measured quantities for each experimental firing. In some cases, published reports contained tabulations of measured quantities. In many cases, the data was plotted in non-dimensional form, and the extraction of the measured quantities

required considerable care. In many cases, additional information was requested, and received from the laboratories concerned. In a few cases, some difficulty was experienced in extracting measured quantities due to ambiguities, or excessively small scale data plots, and as a consequence some uncertainty is connected with the corresponding data.

Material properties for both projectile and target materials were quoted in the publications in only a few instances. Some of the data on material properties which were quoted, were handbook values. In only a few instances were material properties measured on the actual test specimens. Where adequate data were missing, additional information was requested from the laboratories concerned. In some instances where no information on material properties was supplied, average handbook values corresponding to the material specification were used. In a few instances no detailed material specifications were supplied, or the material specifications were insufficient to allow reasonably reliable handbook values to be chosen.

The data are tabulated in the Addendum.

By far the largest proportion of firings have been made into targets of quasi-infinite thickness at normal incidence, over 1700 data points having been reported for this configuration. The target material-projectile material combinations which have been used for this configuration are shown in matrix form in Table II. Inserted are the velocity ranges in feet per second used at the various laboratories. Data for those material combinations for which sufficient data points exist are plotted in Figs. 1.2 to 1.25. Cratering in quasi-infinite targets by compact projectiles at normal incidence is discussed in Section V.

Only relatively few firings have been conducted using other projectile-target configurations. Presentation of data and discussion relating to these cases is deferred to later sections.

SECTION III

EXISTING CRATERING AND PENETRATION THEORIES

Several theoretical analyses of high velocity cratering and penetration have been made. These may be conveniently divided into four groups in accordance with the simplifying assumptions involved:

- (a) Rigid Projectile, i.e. the projectile is undeformed during penetration.
- (b) Hydrodynamic, i.e. the projectile has zero shear strength. Strength of the target may be neglected, or accounted for by a correction factor.
- (c) Thermal Penetration, i. e. the material is removed from the target by melting or vaporization.
- (d) Explosive Analogy, i.e. the crater is considered to be identical to that formed by an equivalent mass of high explosive detonated in contact with the surface of the target.

3.1 Rigid Projectile

Several theories in this category refer to penetration of thin targets by armor-piercing projectiles, and as such are strictly not applicable here. They are, however, included for completeness. These include Bethe's theory of penetration of relatively thick target plates^{106*}, later extended to apply to

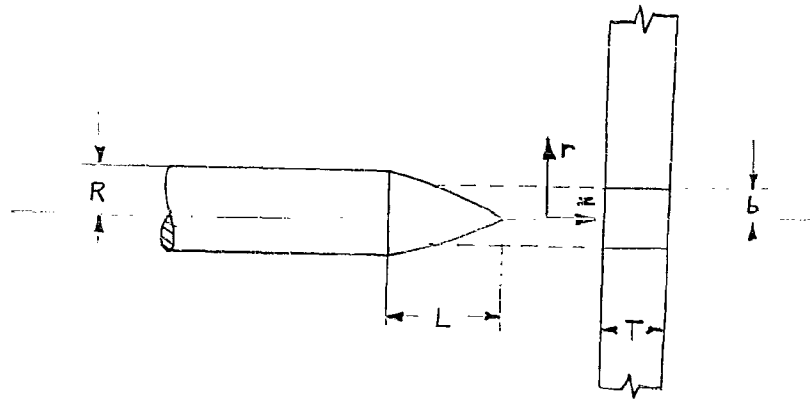
*The numbers appearing in superscript pertain to the references at the end of the report.

relatively thin targets where the target thickens appreciably near the hole,^{106,107}. Thomson's theory of penetration of very thin targets which bend out of their plane during penetration,¹⁰⁸ and Zaid and Paul's theory^{110,111,112,113} for very thin plates which petal.

Three other theories in this category were proposed for the penetration of space vehicles by meteoroids, each assuming that the projectile remains rigid. Grimminger¹¹⁷ assumed that the projectile was slowed by drag during a "fluid" phase of the penetration, and estimated the remaining penetration at low velocity with the aid of an empirical armor-penetration law. Bohn and Fuchs¹¹⁸ assumed a similar "fluid" drag force, with an additional static force proportional to the Brinell Hardness of the target. Zaid^{119,120} considered a rigid projectile which is separated from the rigid target by a zone of incompressible fluid composed of both projectile and target material, which flows radially outwards, eroding the target to form a crater.

3.1.1 Thick Plate Targets, Bethe¹⁰⁶

Bethe approached the problem of target perforation by finding the work required to expand a hole to the radius of the projectile in an infinite plate of thickness T . For the thick plate, plane strain is assumed. A first approximation to the dynamic problem is obtained by using the static solution, making a subsequent correction for dynamic behavior.



The two-dimensional static stress distribution in an infinite plate is

$$\sigma_r = -\frac{Y}{2} \left(\frac{r_1}{r} \right)^2 \quad \sigma_\theta = \frac{Y}{2} \left(\frac{r_1}{r} \right)^2 \quad r \geq r_1 \quad (3.1)$$

$$\sigma_r = -Y \left(\log \frac{r_1}{r} + \frac{1}{2} \right) \quad \sigma_\theta = Y \left(-\log \frac{r_1}{r} + \frac{1}{2} \right) \quad r \leq r_1$$

where

$$r_1 = b \sqrt{\frac{G}{(5/2 - 2\nu) Y}}$$

is the elastic-plastic boundary, for hole radius b , which satisfies the Tresca yield criterion

$$\sigma_\theta - \sigma_r = Y \quad (3.2)$$

σ_r , σ_θ are the radial and circumferential stress respectively at radius r , ν the Poisson's ratio for the target material and Y the yield strength of the target material. In the elastic zone, $r \geq r_1$, the radial displacement u is given by

$$u = \frac{1 + \nu}{5 - 4\nu} \frac{b^2}{r} \quad r > r_1 \quad (3.3)$$

The dynamic equation in the elastic region

$$\rho \frac{\partial^2 u}{\partial t^2} = \frac{\partial \sigma_r}{\partial r} + \frac{\sigma_r - \sigma_\theta}{r} \quad (3.4)$$

is now solved using the static solution as a first approximation, the radius of the hole during perforation being defined by the ogival shape of the projectile,

$$\begin{aligned} b &= 0 & t < 0 \\ b &= R \sin \frac{\pi}{2} \frac{Vt}{L} & 0 < t < \frac{L}{V} \\ b &= R & \frac{L}{V} < t \end{aligned} \quad (3.5)$$

where R is the projectile radius, L the length of ogive, and V the projectile velocity assumed constant during perforation. A second approximation to the solution of this equation is now made using the dynamic boundary conditions, in place of the static boundary conditions initially considered. This effect will be of the relative order $\frac{\pi V R}{2 c_r l}$

where

$$c_r = \sqrt{\frac{G}{(1 - \nu^2) \rho_t}}$$

In order to complete the solution of the problem, it is necessary to solve the plastic equation,

$$\rho \frac{\partial^2 u}{\partial t^2} = \frac{\partial \sigma_r}{\partial r} - \frac{\gamma}{r} \quad (3.6)$$

where the yield stress Y is considered constant, in which the earlier static and dynamic elastic solutions are drawn upon to specify the boundary conditions. In this manner, neglecting second order terms, the radial stress at the hole during the ogival penetration is obtained. The total resistance to penetration calculated for this solution is

$$\begin{aligned}
 W &= -T \int_0^R 2\pi b \cdot \sigma_r(b) \cdot db \\
 &= \pi R^2 T \left[\frac{Y}{2} \left(\log \frac{G}{(5-4\nu)Y} + 1 \right) + 3.8912 \frac{(1+\nu)^2}{(5-4\nu)^2} \rho_t \left(\frac{\pi VR}{2L} \right)^2 \right] \quad (3.7)
 \end{aligned}$$

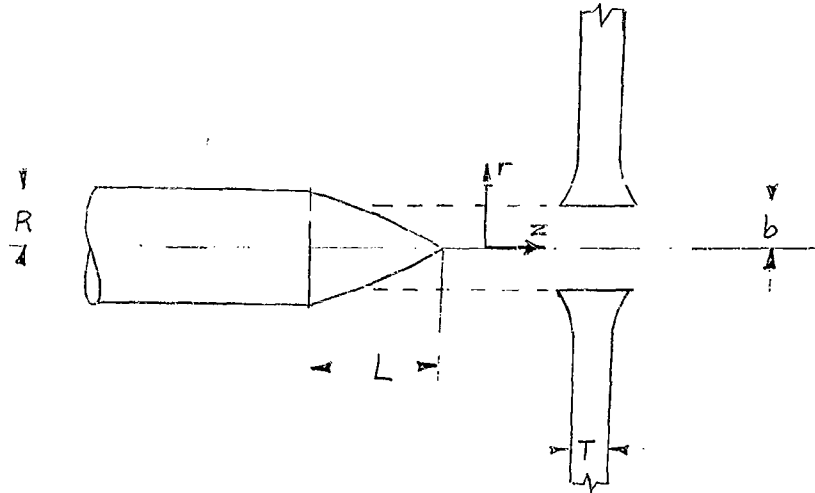
Bethe shows that for Orowan's dynamic yield condition,

$$Y(r) = Y_0 \left(1 - \beta \log \frac{\lambda}{\lambda_0} \right)$$

where λ is the rate of straining, the total resistance should be calculated with a yield corresponding to a rate of deformation

$$\lambda = \frac{\pi}{2} \sqrt{\frac{(5/2 - 2\nu) Y_0}{G}} \frac{V}{L} \quad (3.8)$$

3.1.2 Thin Plate Targets, Bethe¹⁰⁶



During the perforation of a thin plate, the target is found to thicken appreciably near the hole. However, since the plate is thin, plane stress is still assumed. Because of this assumption two yield criteria are necessary to define the plastic zone,

$$\begin{aligned}\sigma_{\theta} - \sigma_r &= Y \quad \text{if } \sigma_{\theta} \text{ is tensile,} \\ -\sigma_r &= Y \quad \text{if } \sigma_{\theta} \text{ is compressive}\end{aligned}$$

σ_r always being compressive. The analysis of the resulting equations is far more complicated than for the thick-plate target. Bethe assumed that the dynamic correction to the initial static solution would be the same as for a thick plate target.

G. I. Taylor¹⁰⁷ has pointed out that the original thin-plate solution formulated by Bethe did not use the correct stress-strain relations in the plastic region. He resolved the equations numerically using the corrected relations and found that the work necessary to expand the hole statically in the incompressible target material was

$$W = 1.33 \pi R^2 T Y$$

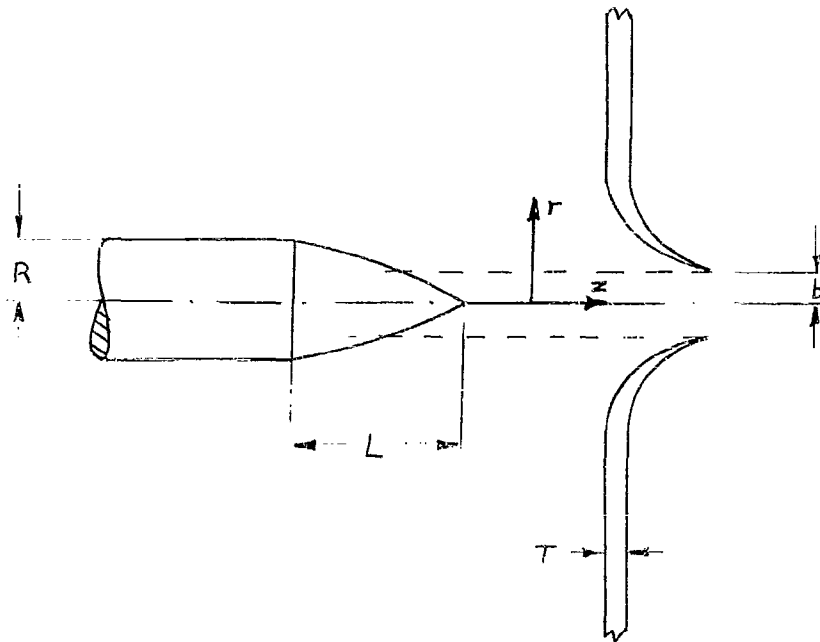
The total resistance to penetration is the sum of this and Bethe's dynamic correction for an ogival projectile, that is

$$W = \pi R^2 T \left\{ 1.33 Y + 0.9728 \rho_t \left(\frac{\pi}{2} \frac{VR}{L} \right)^2 \right\} \quad (3.9)$$

Here the yield stress is taken to be approximately the same as that for a thick plate, i.e. corresponding to a rate of deformation

$$\lambda = \frac{\pi}{2} \sqrt{\frac{(5/2 - 2\nu) Y_0}{G}} \frac{V}{L} \quad (3.10)$$

3.1.3 Very Thin Targets, Thomson¹⁰⁷



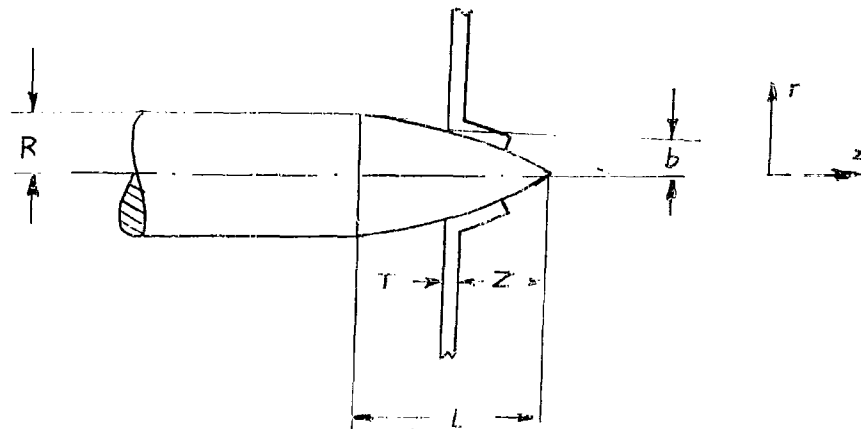
Statically it has been found that a hole can be enlarged symmetrically without bending the plate until its diameter is between 7 and 10 times the thickness of the plate. At about this stage the plate always bends out of its plane, and the material of the tube shaped crater will then expand under the influence of a tangential tension equal to the yield stress Y , the stress perpendicular to the plane of the plate being zero. Thomson and others consider this mode of armor penetration, assuming that the displacement configuration is the same as that under static conditions, but taking into account the heating effect. However, Thomson concluded that the energy dissipation by heating is very small compared with the energy dissipated by plastic

deformation. This has been substantiated by some experimental work carried out by Krafft⁴⁹ at the Naval Research Laboratories.

For these conditions the work done by an ogival projectile in perforation is found to be

$$W = \pi R^2 T \left\{ \frac{Y}{2} + \frac{\rho_t}{4} \left(\frac{\pi}{2} \frac{RV}{L} \right)^2 \right\} \quad (3.11)$$

3.1.4 Very Thin Targets, Zaid and Paul¹¹¹



Zaid and Paul's theory considers the target to be of incompressible material of zero strength. In the theory it is assumed that the non-intersected part of the target remains essentially undeformed, as it is considered that the plastic waves will not have had sufficient time to radiate any appreciable distance. The intersected portion of the target is assumed to take on the shape of the

projectile's surface. Furthermore, since there can be no tensile force between the projectile and the petals formed, contact is maintained only as long as the petal momentum is increasing monotonically, that is, the petals separate from the projectile, when

$$\frac{\partial}{\partial z} (\text{petal momentum}) = 0$$

$$\frac{\partial^2}{\partial z^2} (\text{petal momentum}) < 0$$

In normal impact the motion is axially symmetric and the velocity of a particle in the plate will be

$$\dot{z} = \frac{\partial z}{\partial Z} \frac{\partial Z}{\partial t} = V \frac{\partial z}{\partial Z}$$

where z is the coordinate of the plate out of its plane, and Z the distance travelled by the projectile at constant velocity from its initial position of perforation. The axial momentum transferred to the plate is then

$$\begin{aligned} & \int_0^b 2\pi \rho_t T r \dot{z} dr \\ &= \int_0^b 2\pi \rho_t T V \frac{\partial z}{\partial Z} r dr \end{aligned} \quad (3.12)$$

where b is the radius of the deformed portion of the target. For a truncated projectile¹¹² a further term $Km_s V$ is added to the above expression to allow for the detached mass of the

plate which has the same radius r_m as the projectile méplat (flat nose of the truncated projectile). K is an empirical constant with values between 1 and 2. The velocity lost by the projectile will then be given by

$$m_p \Delta V(z) = K m_s V + \int_{r_m}^b 2 \pi \rho_t T V \frac{dz}{dZ} r dr \quad (3.13)$$

for $\Delta V \ll V$

The oblique impact of a truncated conical projectile was considered in a similar manner¹¹³. Perforation was considered in four stages:

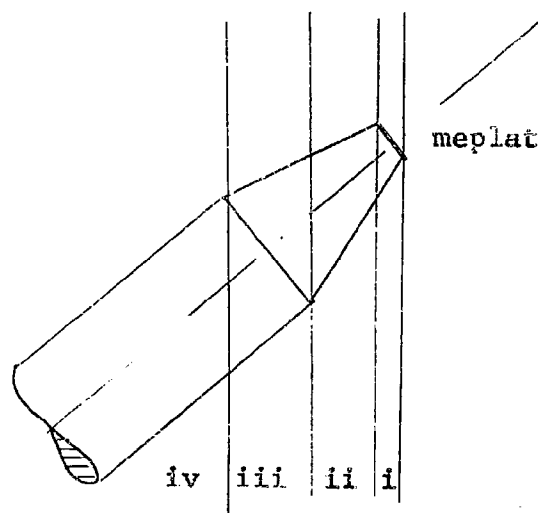
- (i) start of the slug formation, petal element begins to form,
- (ii) slug has been completely formed; petals conform to the conical profile
- (iii) petal formation continues, petal separation and
- (iv) petal formation has ended, petal separation well underway.

The accompanying diagram illustrates those phases.

The decrease in projectile velocity may be computed from the relation

$$\Delta V = \frac{\text{Momentum transferred to target}}{m_p}$$

where $\Delta V \ll V$



3.1.5 Grimmer's Theory¹¹⁷

Grimmer considered that penetration occurred in two phases. During the first, the rigid projectile moves through the target material, which behaves like a compressible perfect fluid, exerting a drag force on the projectile. For very high initial projectile Mach numbers (ratio of velocity to the velocity of plastic deformation waves) the drag coefficient was assumed to be unity. For

a spherical projectile the resultant equation of motion is

$$\frac{\pi}{12} d^3 \rho_p \frac{d(V^2)}{dp} = - \frac{1}{2} \frac{\pi d^2}{4} \rho_t V^2 \quad (3.14)$$

Assuming that this process continues until the projectile is slowed to a Mach number of 5, the penetration is

$$\frac{p}{d} = \frac{4}{3} \frac{\rho_p}{\rho_t} \log_e \frac{V}{5c} \quad (3.15)$$

where c is the velocity of plastic deformation waves.

Subsequent penetration below a Mach number of 5 was assumed to be given by the empirical armor penetration formula

$$\frac{p}{d} = \frac{\rho_p}{3K} V^2 \quad (3.16)$$

where K is empirically defined as

$$K = 5.03 \frac{\text{Ultimate tensile strength of Target Material}}{\text{Ultimate tensile strength of Copper}}$$

with units ft. lb./ft.^3 .

The total penetration therefore is

$$\frac{p}{d} = \frac{4}{3} \frac{\rho_p}{\rho_t} \log_e \frac{V}{5c} + \frac{25c^2}{3} \frac{\rho_p}{K} \quad (3.17)$$

where the speed c of plastic waves was taken as 1000 ft./sec.

Grimminger considered that the assumption that

target melting could be neglected was reasonable, since he considered the transfer of momentum to be a more rapid process than the transfer of heat, and, therefore, the penetration would be completed before the full effects of heating would be felt.

3.1.6 Bohn and Fuchs' Theory¹¹⁸

Bohn and Fuchs assumed the resistance to projectile penetration was made up of two parts, a static part

$$\pi R^2 H$$

and a dynamic part

$$\frac{\pi f \rho_t}{2} R^2 V^2$$

where H is the Brinell Hardness number for the target, R the radius of the projectile and f a shape factor associated with the projectile. This shape factor was taken to be a function of the angle at which a section of the surface of the projectile is inclined towards the direction of flight, defined by

$$f = \frac{\int \sin \phi \, dA}{\pi R^2} \quad (3.18)$$

where dA is the element of the projectile area perpendicular to the direction of flight, and ϕ the inclination of that element to that direction. The following values are given,

for micrometeorites	$f = 1$
spheres	$f = 2/3$
pointed projectiles	$f = 1/3$

The total resistance encountered by the projectile was then assumed to be

$$W = m_p V \frac{dV}{dP} = \pi R^2 \left\{ H^{1/2} + \left(\frac{f \rho_t}{2} \right)^{1/2} V \right\}^2 \quad (3.19)$$

This may be integrated to find the expression for the penetration

$$P = \frac{2}{f} \frac{m_p}{\pi \rho_t R^2} \left\{ \log_e \left[1 + \sqrt{\frac{f \rho_t}{2H}} V \right] - \frac{\sqrt{\frac{f \rho_t}{2H}} V}{1 + \sqrt{\frac{f \rho_t}{2H}} V} \right\} \quad (3.20)$$

For a spherical projectile

$$m_p = \frac{\pi}{6} \rho_p d^3$$

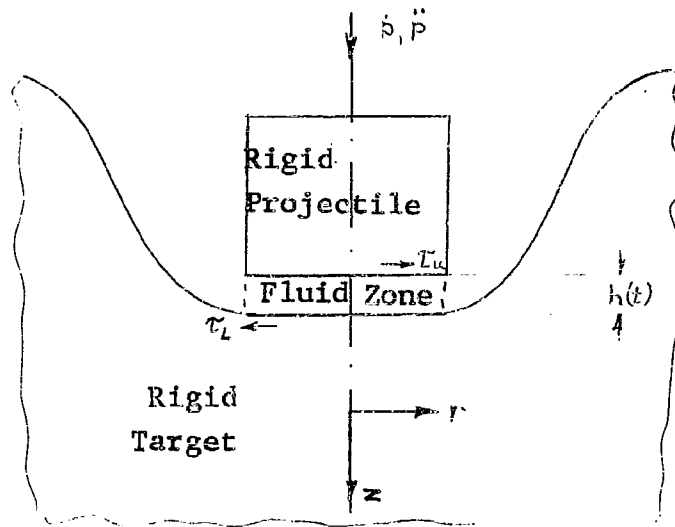
so that

$$\frac{P}{d} = \frac{4}{3f} \frac{\rho_p}{\rho_t} \left\{ \log_e \left[1 + \sqrt{\frac{f}{2} \frac{\rho_t}{H}} V \right] - \frac{\sqrt{\frac{f}{2} \frac{\rho_t}{H}} V}{1 + \sqrt{\frac{f}{2} \frac{\rho_t}{H}} V} \right\} \quad (3.20a)$$

3.1.7 Zaid's Theory^{119,120}

The most recent theory to estimate penetration at very high velocity has been postulated by Zaid. He assumed that the shock waves in the projectile and target could not move at high enough velocity to move away from the projectile-target interface, and therefore the projectile and target could be regarded as rigid, being

separated by a thin layer of material encompassed by the shock



zone which was assumed to be fluid. The fluid is assumed to move radially as the projectile advances eroding the target to form the crater. Inertial expansion of the crater is neglected.

The further assumptions necessary to obtain an

equation of motion were (a) the thickness of the fluid zone is a constant independent of radial position, (b) at radial distances greater than the projectile radius, the dispelled particles do not interact with the material in the fluid zone, so that the fluid pressure at the outer radius of the cylindrical fluid zone is essentially zero, (c) the fluid-zone thickness is small compared with the penetrated distance, and to the radius of the projectile, which is assumed to be cylindrical.

From these assumptions, the following equation of motion is obtained

$$m_p \ddot{p} + \frac{2\pi}{k h} \left\{ \int_0^R \int_0^R \tau_{u} dr r dr + \frac{\rho_t R^3}{16} \left(\ddot{p} + \frac{3}{2} \frac{\dot{p}^2}{p} \right) \right\} = 0 \quad (3.21)$$

where p is the penetration of the projectile, $(\dot{})$ represents differentiation with respect to time, h is the fluid zone thickness, τ_u the shear at the projectile-fluid zone interface, and K an averaging factor which is the product of two averaging factors, i.e. the averaging factor for the pressure gradient dP/dr over the height h of the fluid zone, and the ratio of pressure in the fluid to that at the projectile-fluid zone interface. Solution of the equation depends on assuming relations for the interface shear and the zone growth. The penetration depends strongly on the assumptions made, and satisfactory solutions have so far not been given. Further details are given in Appendix A.

3.2 Hydrodynamic

Birkhoff et al.¹²² suggested that since pressures generated in high-velocity impact are so much greater than the shear strengths of the projectile and target, the shear strengths might be neglected and the projectile and target treated as inviscid fluids. Under this assumption, the resistance to penetration arises entirely from the inertial forces required to accelerate the target material. Theories based on this assumption, therefore, have been termed hydrodynamic theories.

The most detailed solution is that of Bjork¹²⁸ who integrated the two-dimensional equations of motion of a compressible inviscid fluid, together with an entropic equation of state of the solid material, using numerical methods. Analytical solutions of the nonlinear equations could not be obtained.

Solutions may be obtained more simply if the additional assumption is made that the material is incompressible. Opik¹²¹ used a simplified theory of this type, including a correction term for target strength.

Further simplifications arise if only the longitudinal portion of the motion is considered, and the projectile is regarded as a segment of a fluid jet impinging on a fluid target, e.g. Birkhoff et al¹²² and Pack et al¹²³. For these theories, motion continues only as long as the jet continues to impinge on the target, and inertial expansion of the target after dissipation of the jet is neglected. One would expect, therefore, that these theories would give only approximate agreement for very high velocity projectiles of relatively great length compared with diameter, e.g. shaped charge jets or slender rods. Theories of this type have been used nevertheless to estimate penetration by short projectiles.

3.2.1 Bjork's Theory¹²⁸

In this approach to cratering of a target by a high-velocity projectile, the behavior of the material is described by an entropic equation of state that relates the internal energy, pressure, and specific volume, but neglects the shear strength of the material. The problem solved by Bjork was for a cylindrical projectile impacting normally on a semi-infinite target. The equations of motion are

$$\rho \frac{\partial \vec{v}}{\partial t} + \rho \vec{v} \cdot \text{grad } \vec{v} + \text{grad } P = 0$$

(2.22)

$$\frac{\partial \rho}{\partial t} + \vec{v} \cdot \text{grad } \rho + \rho \text{ div } \vec{v} = 0$$

$$\rho \frac{\partial e}{\partial t} + \rho \vec{V} \cdot \text{grad } e + P \text{div } \vec{V} = 0 \quad (3.22)$$

$$P = f(\rho, e)$$

where \vec{V} is the fluid velocity vector, P the pressure, e the internal energy, ρ the density of both the target and projectile, and t the time measured from the time of initial contact. The equations specify an initial value problem for which the initial conditions are $t = 0$, $P = 0$, $e = 0$ everywhere, the initial velocity in the target everywhere zero, and the initial velocity V of the projectile normal to the target surface.

Equations of state of solids under hydrodynamic conditions are available from work at Los Alamos and elsewhere¹³⁷⁻¹⁵¹ for pressures up to several megabars, and from the Fermi-Thomas-Dirac theory for much higher pressures. A numerical solution was obtained by means of a high speed digital computer. The machine representation is fairly rough, since a total space mesh of 25 by 25 cells was used. However, the main features of penetration are displayed quite clearly.

Bjork's theoretical results are fitted approximately by

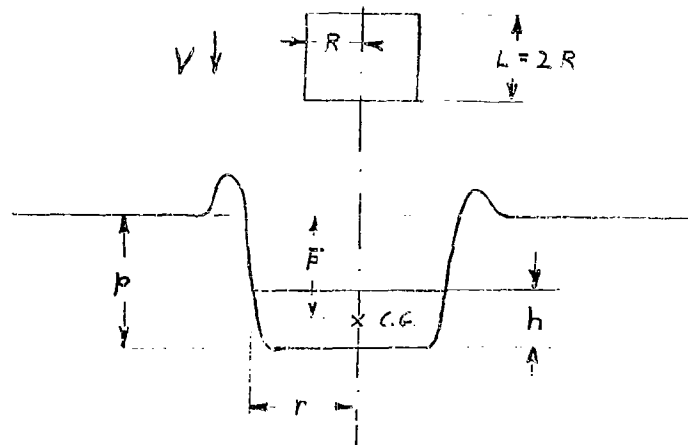
$$\frac{P}{d} = k V^{1/3} \quad (3.23)$$

$$\text{where} \quad d = (4 R^2 L)^{1/3} \quad (3.24)$$

is considered as the representative dimension of the projectile.

3.2.2 Öpik's Theory^{121, 124}

The first theory put forward on cratering by meteoroids was given by Öpik in 1936. In this theory, an allowance is made for the yield strength of the target material.



A cylindrical projectile ($L/d = 1$) of radius R , density ρ_p , mass m_p , and velocity V impacts a semi-infinite target of density ρ_t . The projectile is considered to be incompressible, and its shape to be defined after time t by p , the penetration below the original surface, and r the radius of the crater occupied by the projectile, where

$$2 \pi R^3 \rho_p = 2 \pi r^2 (p - \bar{p}) \rho_p \quad (3.25)$$

Here \bar{p} is the depth of the center of gravity of the deformed projectile below the original surface. The momentum equation then gives

$$m \ddot{\bar{p}} = - \pi r^2 / r \quad (3.26)$$

where P is the pressure at the base of the crater which resists penetration. Applying Bernoulli's theorem

$$P = \frac{1}{2} \rho_t \dot{y}^2 + k \quad (3.27)$$

where k is the strength factor of the target, i.e. it is the minimum pressure for penetration to occur. Similarly for the radial expansion,

$$P' = \frac{1}{2} \rho_t \dot{r}^2 + k \quad (3.28)$$

Öpik relates P and P' by applying Bernoulli's equation in the frame of reference moving with velocity \dot{p} ,

$$P = P' + \frac{1}{2} \rho_p \dot{r}^2 \quad (3.29)$$

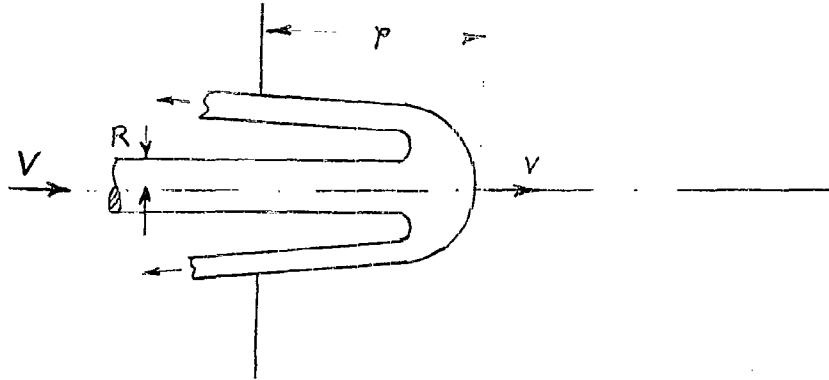
Since the flow in this frame of reference is not steady, this procedure can at best be only a crude approximation.

The differential equation resulting from the elimination of the pressure terms from equations 3.25 to 3.29 is solved subject to the initial conditions, $t = 0$, $r = R$, $p = 0$, $\dot{p} = V$. Details of the integration are given in Appendix B.

3.2.3 Shaped Charge Jet Penetration

Several investigators (Birkhoff et al¹²², Cook¹²⁵, Pack et al¹²³) have proposed similar incompressible theories to explain the penetration produced by a shaped-charge jet. However, cylindrical or spherical projectiles have sometimes also been considered as short jets. In this theory both the jet and target material are regarded

as incompressible fluids. The flow, when viewed from a frame of reference moving with the velocity of the jet-target interface v , is considered to be steady. Applying Bernoulli's



equation along the axis of symmetry, the stagnation pressure is given by

$$P = \frac{1}{2} \rho_t v^2 = \frac{1}{2} \rho_p (V - v)^2 \quad (3.30)$$

Originally, the strength of the material was neglected in comparison with the high pressures produced by the impacting jet. Rostoker¹²⁴ included the target strength in this equation by including a factor k ,

$$\frac{1}{2} \rho_t v^2 + k = \frac{1}{2} \rho_p (V - v)^2 \quad (3.31)$$

where k is the target's dynamic strength. Richelberger¹²⁴ writes this in the form

$$k = \frac{1}{2} \rho_p v_0^2 \quad (3.32)$$

where v_0 is the minimum velocity of the jet that will just cause a crater to form in the target.

For a jet moving at constant velocity V and of density ρ_p , and finite length L , most of the penetration is considered to take place during the steady part of the motion, so that penetration p is approximately

$$p = \int_0^{t_1} v. dt \quad (3.33)$$

where t_1 is the total time elapsed from the time that the jet first struck the target,

$$t_1 = \frac{p + L}{V}$$

Hence

$$\frac{p}{L} = \sqrt{\frac{\rho_p}{\rho_t}} \left\{ \frac{1 - \sqrt{\frac{\rho_p}{\rho_t} \left[1 - \left(\frac{v_0}{V}\right)^2 \left(1 - \frac{\rho_p}{\rho_t}\right) \right]}}{\sqrt{1 - \left(\frac{v_0}{V}\right)^2 \left(1 - \frac{\rho_p}{\rho_t}\right)} - \sqrt{\frac{\rho_p}{\rho_t}}} \right\} \quad (3.34)$$

For a jet of high velocity, such that $V \gg v_0$

$$\frac{p}{L} \approx \sqrt{\frac{\rho_p}{\rho_t}} \quad (3.35)$$

which would have been obtained directly from equation 3.30, which disregards the strength of the target.

Pack et al.¹²³ made a correction for the effect of strength by considering the penetration as a series of

powers of the nondimensional parameter $Y/\rho_p V^2$, the first approximation being

$$\frac{r}{L} = \sqrt{\frac{\rho_p}{\rho_t}} \left(1 - \frac{\alpha_1 Y}{\rho_p V^2} \right) \quad (3.36)$$

where Y is the dynamic yield stress of the target, and α_1 is an empirical function of the densities of the jet and of the target. For armor, the correction term $\alpha_1 Y/\rho_p V^2$ was found to be as high as 0.3.

As has been pointed out earlier, this theory does not consider the inertial expansion of the crater after the jet ceases to impinge on the target. In their experiments with shaped charge jets, Pack et al¹²³ found that the shape at the bottom of the crater was roughly hemispherical with radius equal to that of the hole made by the jet. They reasoned that if the previous pressure which suddenly ceased to apply after the jet had been used up, was uniformly distributed over the bottom of the hole, the latter expanding freely adopted a hemispherical shape. Pack et al therefore modified the expression for the penetration to

$$\frac{r}{L} = \sqrt{\frac{\rho_p}{\rho_t}} \left(1 - \frac{\alpha_1 Y}{\rho_p V^2} \right) + \frac{r}{L} \quad (3.37)$$

where r is the radius of the hole made by the jet.

Cook¹²⁵ has extended the theory to estimate the radius of the hole made by the jet. He assumed that the impulse imparted to the target is used up in the lateral expansion of the hole, i.e.

$$\frac{\pi}{2} \rho_p (V - v)^2 R^2 \Delta t = \left(\frac{1}{2} \rho_t \dot{r}^2 + k \right) \pi r^2 \Delta t \quad (3.38)$$

where R is the radius of the jet, and r that of the crater. The final cross-sectional area will be given when $\dot{r} = 0$, i.e.

$$r = R (V - v) \sqrt{\frac{\rho_p}{2k}}$$

Eliminating v by means of Eq. (3.30), the radius of the hole is

$$r = \frac{\sqrt{\rho_t \rho_p}}{\sqrt{\rho_t} + \sqrt{\rho_p}} \cdot \frac{R}{\sqrt{2k}} \quad (3.39)$$

3.3 Thermal Penetration

In the thermal penetration theories that have been formulated, penetration is assumed to take place by melting or vaporization of the target by the projectile as its energy is dissipated.

3.3.1 Whipple's Theory¹²⁹

Whipple assumes that the crater formed by melting is a right-circular cone for which the total apex angle is 60° . Assuming that all of the initial kinetic energy is converted into heat, the depth of penetration is simply

$$p = \left(\frac{\gamma m_p}{2 \pi \rho_t} \right)^{1/3} \left(\frac{V^2}{Q_t} \right)^{1/3} \quad (3.40)$$

where Q_t is the heat required to remove a unit mass of

the target material, here taken to be the latent heat to fusion. For an equivalent spherical projectile $m_p = \frac{\pi}{6} \rho_p d_e^3$ so that

$$\frac{P}{d_e} = \left(\frac{3}{4} \frac{\rho_p}{\rho_t} \frac{V^2}{Q_t} \right)^{1/3} \quad (3.40a)$$

3.3.2 Langton's Theory¹³⁰

Langton's theory is similar to that given by Whipple since in this case also, the energy of the projectile is assumed to be converted into heat. Four possible cases are considered,

- (a) The projectile velocity is such that neither the projectile nor target melt
- (b) The projectile is melted but the target is not
- (c) The target is melted but the projectile is not
- (d) Both projectile and target melt

Penetration would only occur for cases (c) and (d). A hemispherical crater is assumed to be formed. Case (d) results in the equation

$$\frac{1}{2} m_p V^2 = \frac{2\pi}{3} \frac{P^3}{\rho_t Q_t} + m_p Q_p \quad (3.41)$$

where Q_t and Q_p are the heat per unit mass of target and projectile material respectively, necessary to raise the temperature of the material to the melting point, and to supply the latent heat of fusion. Thus, the penetration is

given by

$$p = \left(\frac{3}{2\pi} \frac{m_p}{\rho_t} \right)^{1/3} \left(\frac{V^2}{2Q_t} - \frac{Q_p}{Q_t} \right)^{1/3} \quad (3.42)$$

For an equivalent spherical projectile this becomes

$$\frac{p}{d_e} = \left(\frac{1}{8} \frac{\rho_p}{\rho_t} \right)^{1/3} \left(\frac{V^2}{Q_t} - 2 \frac{Q_p}{Q_t} \right)^{1/3} \quad (3.42a)$$

3.3.3 Grow's Theory¹³¹

A similar theory has been developed by Grow for the energy lost by a projectile in perforating a thin target. The projectile was assumed not to melt or deform, but a hole equal in diameter to the projectile was assumed to be formed in the target by melting. Denoting the exit velocity by V_e , the resulting expression is

$$\frac{1}{2} m_p (V^2 - V_e^2) = \pi R^2 \rho_t T Q_t + Q_p m_p \quad (3.43)$$

where T is the target thickness and R the projectile radius. Here Q_t is taken to be the energy per unit mass required to raise the temperature of the target to the melting point and supply the latent heat of fusion, but Q_p is taken to be the energy per unit mass necessary to raise the projectile material to target temperature, the projectile not being assumed to melt. Grow further assumed that the last term could be approximate by kV , varying from zero for the velocity at which negligible deformation occurred, to a maximum Q_p for the velocity at which the

projectile shatters.

The theory may be readily extended to cratering in thick targets where no perforation occurs and the exit velocity is zero. The penetration will then equal T , i.e.

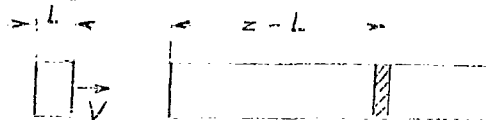
$$P = \pi \frac{m_p}{\rho_t R^2} \left(\frac{V^2}{2 Q_t} - \frac{Q_p}{Q_t} \right) \quad (3.44)$$

For an equivalent spherical projectile, this becomes

$$\frac{P}{d} = \frac{1}{3} \frac{\rho_p}{\rho_t} \left(\frac{V^2}{Q_t} - 2 \frac{Q_p}{Q_t} \right) \quad (3.44a)$$

3.3.4 Lavrent'yev's Theory¹³²

Lavrent'yev considers two cases of thermal penetration, a rod target and a hemispherical plate target, both being of incompressible material. The analysis is idealized by considering the media to be made up of a set of infinitesimally-thin layers which impact inelastically, and for which the energy dissipation distribution is evaluated. If the density of this distribution is greater than the amount required to vaporize the material, a crater will be formed.



The first case considers a plate, depth L , of initial velocity V , impacting upon a rod of the same material and cross-section. If a total length z of material

is set in motion at time t , the conservation of momentum gives

$$z dv + v dz = 0 \quad (3.45)$$

which on integration for the initial condition $z = L$, $v = V$, yields

$$v = \frac{L}{z} V$$

The kinetic energy is given by

$$E = \frac{1}{2} z v^2$$

or differentiating

$$dE = \frac{1}{2} v^2 dz + z v dv$$

which by Eq. (3.45) becomes

$$dE = -\frac{1}{2} v^2 dz = -\frac{1}{2} V^2 \left(\frac{L}{z}\right)^2 dz$$

Assuming that all the kinetic energy is converted into heat, its distribution along the rod will be

$$-\frac{dE}{dz} = \frac{1}{2} V^2 \left(\frac{L}{z}\right)^2$$

If the heat density necessary to vapourise the material is Q , then a length

$$z = \left(\frac{1}{2} L^2 \frac{V^2}{Q} \right)^{1/2} \quad (3.46)$$

will be vapourised, this length including the length of the projectile. A similar analysis was given assuming spherical symmetry for a hemispherical plate projectile.

3.4 Explosive Analogy

Several investigators, Baldwin, Rinehart⁹³ and Stanyukovitch^{133,134} have proposed that crater formation due to high velocity impact is similar to crater formation by high explosives. Allison¹¹⁵ has given a review of this subject, illustrating the similarity of craters formed in lead targets by a projectile with a kinetic energy of 9.3×10^3 Joules, and by a tetryl charge with an explosive energy of 63×10^3 Joules.

3.4.1 Stanyukovitch's Theory^{133,134}

Stanyukovitch considers the phenomenon of cratering to be similar for both the high velocity impact and an explosion. The pressure on the front of the shock wave caused by either the explosion or impact, drops sharply with increasing distance from the point of initiation, and the mechanism of cratering changes from vaporization, to melting and pulverization of the material. This ceases when the energy density at the shock front becomes less than a certain value. However, the evaporated and finely fragmented material expands, and has an effect similar to an explosion.

The equivalent mass of explosive is determined by the relation

$$m_e = \frac{\gamma m_p V^2}{2 Q} \quad (3.47)$$

where m_c is the mass of the equivalent explosive material, η the explosive efficiency, and Q the energy/unit mass of explosive.

The approach used by Stanyukovitch for estimating the radius of the crater is empirical. See Appendix C for a more detailed account of his analysis.

SECTION IV

EMPIRICAL RELATIONS

Due to the lack of adequate theories, many attempts have been made to correlate experimental cratering data with the aid of empirical expressions. Many of these correlations have been based on simple functions of independent quantities, such as

$$P = k m_p^i V^j$$

where m_p , and V are the independent variables projectile mass and velocity, respectively.

Other correlations have been attempted using nondimensional parameters, so that the constants to be fitted empirically are non-dimensional

More refined correlation schemes have been evolved by assuming some type of resistance law based on the physical phenomena considered to be dominant. The resultant equations contain non-dimensional constants which are then fitted to the data.

In order to gain perspective, the low velocity armor penetration work is included first in the following discussion. After presenting the high velocity correlation equations, a general discussion of dimensional analysis of the cratering problem is given, and the important parameters based on elementary static material properties are discussed.

4.1 Early Armor Penetration Work

The study of ballistic penetration is generally considered to have begun with the work of the English ballisticians Robins¹⁰⁹ (1742) whose ideas were elaborated a few years later by Euler¹⁰⁹, both in theory and experiment.

In armor penetration, the object has been to estimate the limiting velocity, i.e. the minimum velocity of a projectile necessary to perforate the target completely. This was done by assuming a law of penetration based on the physical phenomena assumed to predominate, solving the ensuing equation, and fitting the resulting expression to experimental data with suitable constants. Most of the laws postulated are variations of the form

$$V_L = k m_p^{-1/2} T^b R^c \quad (4.1)$$

where V_L is the limiting perforation velocity,

T the thickness of the target

m_p the weight of the projectile

R the radius of the projectile

and k a constant.

In the theory postulated by Robins¹⁰⁵ the resistance to penetration was taken to be constant, hence

$$\frac{1}{2} m_p V_L^2 = \pi k T R^2$$

leading to

$$V_L = \left[\frac{2 \pi k T R^2}{m_p} \right]^{1/2} \quad (4.2)$$

Euler evaluated k from experiments on elm wood and earth.

Workers at the Naval Research Laboratory¹⁰⁵ modified this equation in order to allow for free surface effects. The idea involved is that the material near the free surface is more easily pushed aside than material near the plate center line. This is taken into account by subtracting from the plate thickness an amount proportional to R . Thus,

$$V_L = \left[\frac{2 \pi k R^2 (T - \gamma R)}{m_p} \right]^{1/2} \quad (4.3)$$

Poncelot (1829)^{105, 109} published a theory which combined the Euler-Robins type resisting force with a force proportional to the square of the velocity. This was proposed for application to materials weak enough so that their inertial resistance to motion is significant. The constant force k is interpreted as the pressure necessary to break the cohesion of the target. Thus, the resistance is expressed by

$$W = \pi R^2 \left(k + \frac{\alpha}{2} \rho_t V^2 \right)$$

which leads to the differential equation

$$m_p V \frac{dV}{dp} = - \pi \left(k + \frac{\alpha}{2} \rho_t V^2 \right) R^2$$

where p is the distance penetrated into the target. The integration of this equation yields

$$\frac{1}{2} \rho_t V_L^2 = \frac{K}{\alpha} \left[\exp \left(\alpha \frac{\pi \rho_t R^2 T}{m_p} \right) - 1 \right] \quad (4.4)$$

α is empirically found to be not far from 1/2.

In 1945 Roberson and Irwin¹⁰⁵ worked out a similar expression in which account was taken of the target cohesive resistance, the inertial resistance, and the free-surface effects. They presented an equation in the form

$$\frac{V_L^2}{2} = K_1 \left\{ \frac{1}{\alpha} \left[\exp \left(\alpha \frac{\pi \rho_t R^2 T}{m_p} \right) - 1 \right] - \left[c_1 + c_2 \exp \left(\alpha \frac{\pi \rho_t R^2 T}{m_p} \right) \right] \right\} \quad (4.5)$$

They also took into account the increase of projectile cross-sectional area due to projectile deformation in the high-velocity range. The value of the area was obtained by measuring the diameter of the projectile after deformation. They found that the radius of the projectile could be expressed empirically as

$$R = R_c \left\{ 1 + K \frac{V - 2500}{2500} \right\}^{1/2} \quad (4.6)$$

for impact velocities greater than 2,500 ft/sec.

Early experimental work¹⁰⁴ showed that the force required to perforate a plate varied approximately as the plate thickness if the diameter is constant, and as the diameter if the thickness of the plate is constant. Making these assumptions, the force is proportional to TR , consequently, the work done to perforate the plate is proportional

to T^2R . Hence

$$V_L = k \frac{T R^{1/2}}{m_p^{1/2}} \quad (4.7)$$

Even over a restricted velocity range it was found that there is a variation in the proportionality constant. For cast-iron shot on wrought iron plate, Fairbairn¹⁰⁴ (1861) derived

$$V_L = 1840 \frac{T R^{1/2}}{m_p^{1/2}} \quad (4.8)$$

where T and R are in inches, m_p in pounds and V_L in ft/sec.

On the assumption that in high velocity penetration the force required is proportional to TR/V , Tresidder¹⁰⁴ obtained for the perforation of wrought iron

$$V_L = k \frac{T^{2/3} R^{1/3}}{m_p^{1/3}} \quad (4.9)$$

where $\log k = 3.0473$, for T and R inches, m_p in pounds, and V_L in ft/sec. The Krupps¹⁰⁴ expression for wrought iron is

$$V_L = k \frac{T^{2/3} R^{5/6}}{m_p^{1/2}} \quad (4.10)$$

where $\log k = 3.1397$, while De Marre¹⁰⁴ postulated

$$V_L = k \frac{T^{0.65} R^{0.75}}{m_p^{0.5}} \quad (4.11)$$

where $\log k = 3.1874$, for the same material.

A later expression adopted by Krupps¹⁰⁴ for hard faced plates is

$$V_L = k \frac{T R^{1/2}}{m_p^{1/2}} \quad (4.12)$$

where $\log k = 3.3271$. And for ordinary steel De Marre¹⁰⁴ modified his wrought iron expression to

$$V_L = k \frac{T^{0.7} R^{0.75}}{m_p^{0.5}} \quad (4.13)$$

where $\log k = 3.23522$. In order to correlate the resistance of various targets of the same thickness, the "De Marre coefficient" was adopted. This is the ratio between the velocity calculated from the limiting velocity expression for ordinary steel.

About 1930, Robert Kent¹⁰⁵ put into use a slightly modified version of the De Marre expression. This relation is

$$V_L = k \frac{T^{3/4} R^{3/2}}{m_p^{3/4}} \quad (4.14)$$

and has been used extensively for armor perforation and penetration work. At about the same time, L.T.E. Thompson¹⁰⁵ at Dahlgren introduced the expression

$$V_L = k \left(\frac{T R^2}{m_p} \right)^{1/2} \quad (4.15)$$

where ϕ is the angle of obliquity of the projectile's path to the plate normal. This expression has been used extensively by the Naval authorities for the design of ship armor plating.

The above expressions are all applicable to plate penetration where the projectile is essentially intact after penetration, but are of no use at higher velocities where the projectile disintegrates.

4.2 High Velocity Penetration Work

In order to correlate the experimental data on penetration depths and volumes of craters formed in high-velocity impact, numerous empirical expressions have been proposed. Some of the most widely used expressions are listed in Table III, together with conditions for which the constants were evaluated.

One of the earliest and most frequently used assumptions was put forward by Rinehart and Pearson⁹³. They assumed that the crater volume was proportional to the projectile kinetic energy. If, in addition, it is assumed that the crater shape does not change with velocity, then taking the crater volume proportional to the projectile kinetic energy leads to an expression of the form

$$\frac{p}{d} = k \rho_p^{1/3} V^{2/3} \quad (4.16)$$

where p is the depth of penetration, d the diameter of the projectile, m_p the projectile mass, and V the projectile velocity.

On the other hand Pugh and Eichelberger¹⁴ found that the crater depth was proportional to the projectile momentum, leading to an expression of the form

$$\frac{P}{d} = k \rho_p^{1/2} V^{1/3} \quad (4.17)$$

Several other equations have been put forward. The De Marre formula for plates has been adapted for use with semi-infinite targets at low velocities of impact. If the plate thickness is regarded to be the penetration depth corresponding to the limiting velocity, the following expression results

$$\frac{P}{d} = k \rho_p^{0.7} V^{1.1} \quad (4.18)$$

Partridge et al⁶⁶ proposed that the crater volume for lead to lead impact could be represented by the equation

$$V_c = V_p \left\{ 1 - \exp(-k E) \right\} \quad (4.19)$$

where V_c is the crater volume, V_p the volume of the projectile, and E the projectile kinetic energy.

All the equations as they have been written above require a different empirical constant for different projectile-target material combinations. The next step, therefore, was to relate the constants to material properties in order to obtain a more general correlation. Huth⁶⁸ in examining impact data for projectiles and targets of similar material proposed a possible dimensionless relationship of the form

$$\frac{P}{d} = k \left(\frac{V}{c_t} \right)^a \left(\frac{V}{Q_t} \right)^b \left(\frac{V d}{K} \right)^c$$

where c_t was the sonic velocity in the target, Q_t the energy necessary to melt or vaporize a unit mass of the target material, and K the thermal diffusivity. He found that his data correlated best on the basis of V/\bar{c}_t where \bar{c}_t is the longitudinal bar velocity of sound. The velocity range in which the tests were carried out was $0.1 < (V/\bar{c}_t) < 1.0$. In this range the terms V^2/Q_t and Vd/K were found to be insignificant. He also concluded that the crater volume was not precisely proportional to either the energy or the momentum of the projectile.

On the other hand van Valkenburg et al⁶⁷ found that the volume-energy relation could be correlated for nonalloy metals using ρ_t and \bar{c}_t , that is

$$\frac{V_c}{E} = k_1 \frac{1}{\bar{c}_t f_t} \quad (4.20)$$

The equation reduces, on assuming

$$\frac{P}{D} = k_2 \frac{V}{\bar{c}_t}$$

where D is the diameter of the mouth of crater, which in this case is taken to be a section of a sphere, to

$$P = \left(\frac{3 k_1 k_2}{2\pi} \right)^{1/3} V^{1/3} \left(\frac{\rho_t}{f_t} \right)^{1/3} \left(\frac{V}{\bar{c}_t} \right) \frac{1}{3 - k_2 \left(\frac{V}{\bar{c}_t} \right)} \quad (4.21)$$

for $V \leq \bar{c}_t$

Van Valkenburg et al measured the crater dimensions to the top of the projectile material remaining in the crater.

The parameter (V/c) has subsequently been used quite extensively, various experimenters finding different exponents to fit their own data. Charters et al²⁸ added a term consisting of the ratio of projectile to target density to account for a variety of projectile materials finding that data in lead and copper targets were best fitted by

$$\frac{p}{d} = 2.28 \left(\frac{\rho_p}{\rho_t} \right)^{2/3} \left(\frac{V}{c_t} \right)^{2/3} \quad (4.22)$$

Several other groups used this expression or expressions based on these parameters, e.g. at Poulter Laboratories and CARDE.

Partridge et al⁷¹ and Collins et al³⁵ on the other hand noted that their data seemed to be best fitted by the first power of velocity. The Langley investigators theorized that penetration might be proportional to the momentum per unit presented area of the projectile,

$$p = k_1 (\rho_p V L - k_2) \quad (4.23)$$

where k_2 is the momentum per unit area below which no permanent deformation of the target was observed. They further found that the proportionality constant was a function of the projectile density and modulus of elasticity of the target, finding that their data could be fitted by the expression

$$p = \frac{3096 (\rho_p V L - k)}{\rho_p^{0.278} (G_t + 2.8 \times 10^6)^{0.78}} \quad (4.24)$$

Apart from Collins and Kinard's expression, none of those mentioned so far have included a term which allows for either the target or projectile strength.

Pugh and Eichelberger¹⁴ first introduced the effect of target strength through the use of the Brinell Hardness number. They found that the constant in the expression

$$p = k m_p^{1/3} V^{1/3}$$

could be reduced for various target materials by the Brinell Hardness number and the density, and found that experimental data for several materials could be correlated by

$$p = 2.54 \frac{m_p^{1/3} V^{1/3}}{\rho_t^{1/6} H^{1/4}} \quad (4.25)$$

Experimenters at the Ballistic Research Laboratory⁶ subsequently noted that the energy per unit volume tended to become constant as the velocity increased, and found that this constant could be correlated roughly with Brinell Hardness number. Assuming a constant crater shape, this leads to an expression of the form

$$p = k \frac{m_p^{1/3} V^{2/3}}{H_t^{1/3}} \quad (4.26)$$

A similar expression is also in use at the Naval Research Laboratory.⁵²

Engel⁴⁰ introduced the yield strength as a correction term to the equation which assumes penetration

proportional to the projectile velocity. The equation was of the form

$$p = k_1 V - k_2 \quad (4.27)$$

the yield being included in the last term. K_1 was developed by considering the movement of a cylindrical core of material through the target plate under the area of contact involved during the collision. This cylinder is restrained laterally, but is assumed to be free to move in the direction of the impact for the time taken by a stress wave to make a round trip through the projectile, i.e. $2d/c_p$. For an elastic collision, this cylindrical core within the target will traverse a depth

$$2d \frac{c_p \rho_p}{c_t \rho_t + c_p \rho_p} \frac{V}{c_p}$$

$c_p \rho_p$ and $c_t \rho_t$ being the acoustic impedances of the projectile and target materials, respectively. Experimental data for a number of target materials impacted by mercury and water drops indicated the need for a correction factor of 3.6. Thus, the equation is

$$\frac{p}{d} = 7.2 \frac{c_p \rho_p}{c_t \rho_t + c_p \rho_p} \frac{V}{c_p} - \frac{k_2}{d} \quad (4.28)$$

The intercept of this equation with the velocity axis represents the impact speed below which no indentation would occur. This speed appeared to be a function of the target strength. Engel found that it could be accounted for

by the dimensionless product

$$k_2 \left(\frac{Y_t}{\rho_p c_p^2} \right) \left(\frac{\rho_p}{\rho_t} \right)^{1/2} \left(\frac{c_p \rho_p}{c_t \rho_t} \right) \left(\frac{c_p}{\rho_p} \right) = k_2 \frac{Y_t \rho_p^{1/2}}{c_t^2 \rho_t^{3/2}}$$

yielding the final equation

$$\frac{p}{d} = \frac{7.2 c_p \rho_p}{c_t \rho_t + c_p \rho_p} \left(\frac{V}{c_p} \right) - 136.8 \frac{Y_t \rho_p^{1/2}}{c_t^2 \rho_t^{3/2}} \quad (4.29)$$

where $k_2 = 136.8$ and Y_t is the dynamic yield strength of the target. Note that the targets used for the evaluation of k_1 and k_2 had thicknesses of between 1.5 times and 5 times the diameter of the impinging projectile, the back of the target being unsupported.

4.3 Dimensional Analysis

In carrying out a dimensional analysis of the high-velocity cratering problem, the main difficulty lies in distinguishing the main features of the phenomena, and defining appropriate physical quantities describing the behavior of the materials involved.

The geometric quantities of importance are:

- d relevant dimension of the projectile
- p relevant dimension of the crater
- V projectile velocity relative to the target
- ϕ angle of incidence of projectile on the target surface
- T target thickness, or other relevant target dimension.

Where projectiles of different shapes are involved, the relevant projectile dimension is not obvious. Several investigators have used different systems. Shaped charge jet penetration has been correlated on the basis of the length of the jet. Summers and Charters²⁷ similarly used the length of the projectile in the direction of initial projectile motion. Others have in effect used the cube root of the mass, to define an equivalent diameter

$$d_e = \frac{m_p^{1/3}}{\rho_p^{1/3}} \quad (4.30)$$

Where spheres and cylinders only are compared, the diameter of an equivalent sphere of mass equal to that of the cylinder has sometimes been used i.e.

$$d_e = \left(\frac{3}{2} d^2 L \right)^{1/3} \quad (4.31)$$

Where d is the cylinder diameter and L its length. Bjork¹²⁸ used arbitrarily

$$d_e = (d^2 L)^{1/3} \quad (4.32)$$

to compare his theory for cylindrical projectiles with experiments conducted with spherical projectiles.

As long as the crater shape remains identical as other parameters are varied, the crater size may be represented by a single parameter. Throughout the range explored experimentally, however, the crater shape varies from a cylindrical cavity of the same diameter as the projectile at very low velocities, to an almost hemispherical crater at the

highest velocities examined. Of prime importance in practice is the penetration, or depth of crater, and this parameter has been used most in empirical correlations of cratering in thick targets. Other parameters of interest are the crater volume, and diameter of the crater in the plane of the original surface.

Quantities describing the relevant material properties are not so straightforward. Cratering involves shock compression of the materials to very high pressures, possibly accompanied by melting or vaporization. Subsequent motion involves both extremely high stresses and strain rates. The final phase of the motion has been shown to involve elastic springback of the crater.⁷

Parameters describing the behavior of solids under very high stresses and strain rates have not been adequately formulated. Equations of state of solids under extremely high pressures have received considerable attention recently. From the work of the group at Los Alamos¹³⁷⁻¹⁵¹ and elsewhere, it appears that the shock Hugoniot may be described adequately by only two parameters in addition to the density at zero pressure. For a number of metals, one parameter coincides with the adiabatic sound speed. The physical interpretation of the other parameter is not clear, but it appears to be related to the change of compressibility with pressure.

The parameters necessary to define the strength of the material are also not clear. The conventional engineering stress-strain properties are not related in a simple way to the stress-strain properties of the material under complex combined stresses at high strain rates. Nevertheless, drawing on properties which are defined under static conditions, one has the relevant elastic modulus G and yield stress Y .

In addition there would be quantities describing the strain hardening and strain rate behavior.

One quantity which has been widely measured, but which is difficult to relate to other physical properties, is the indentation hardness. Its ease of measurement together with the fact that the process of pushing a ball or pyramid into a solid surface is suggestive of the cratering process has nevertheless led to its use in empirical expressions. The Brinell Hardness number H is strictly defined as the load used divided by the surface area of the indentation produced by a spherical stylus, and thus has dimensions of a stress, with units kilograms per square millimeter.

Not all of these elementary material properties are independent. For example, the sound speed is related to the density and relevant elastic modulus:

$$c^2 = \frac{G}{\rho}$$

There appears to be a relation between Brinell Hardness and yield stress. In Fig 4.1 Brinell Hardness has been plotted versus yield stress for a number of representative target materials, and it is seen that Brinell Hardness is roughly proportional to yield stress, at least within the scatter usually associated with empirical correlations.

Using the independent elementary material properties ρ , c , and H together with the geometric quantities allows the following dimensionless parameters to be formed.

$$\left(\frac{P}{d}\right) \quad \text{Penetration ratio}$$

$$\beta = \left(\frac{\rho_p}{\rho_t}\right) \quad \text{Density ratio}$$

$$M = \left(\frac{V}{c} \right)$$

Mach number

$$B = \left(\frac{\rho V^2}{H} \right)$$

Best number

The last parameter appears frequently in one or another of its equivalent forms in both the empirical and theoretical cratering equations, and it appears appropriate to give it a name. Following a suggestion of Dr. John S. Rinehart, it is proposed here to call this the Best number, after the French ballistician Best. Between 1835 and 1845 the French carried out a series of experiments to measure the velocity of fragments by putting hollow cannon balls loaded with powder into a well and detonating them. At the bottom of the well was a 1 1/2 foot layer of damp clay. They measured the volume of the holes made in the clay by the fragments. In order to calibrate the clay, they fired a pistol into the clay alongside the fragment hole. Knowing the velocity of the pistol ball, and its mass, and the volume of the hole produced together with the fragment mass and its hole volume, the fragment velocity could be calculated by assuming that the cratering efficiency remained constant.

The cratering efficiency is defined as the crater volume divided by the kinetic energy of the projectile. It has been noted in some experiments that the cratering efficiency is proportional to target hardness. Under this assumption

$$\frac{V_c}{E} = k H$$

or rearranging, by noting that the crater volume is proportional to the cube of a linear dimension of the crater if the crater shape remains constant,

$$\frac{\rho_p^3}{d^3 V^2} = k H$$

$$\frac{\rho}{d} = k \left(\frac{\rho_p V^2}{H} \right)^{1/3}$$

Thus, it appears particularly apt to apply the name Best number to the parameter $\left(\frac{\rho V^2}{H} \right)$.

If melting or vaporization are considered important, then the relevant quantity will be the energy to melt or vaporize unit mass of material. This will be related to specific and latent heat. Although melting or vaporization are a result of shock heating, and may be considered to occur at some time during the high-pressure phase of the motion, the material is finally ejected at ambient (zero) pressure, and thus the energy carried away by melted or vaporized material may be described by zero pressure data on specific and latent heats.

If the energy necessary to sublimate or melt unit mass of material is denoted by Q , an additional non-dimensional parameter may be formed, i.e.

$$\left(\frac{V^2}{Q} \right) \quad \text{Thermal parameter}$$

It is not possible at this time to form other dimensionless parameters based on compressibility, strain

hardening, or strain rate effects, since suitable material properties have not been adequately defined.

Examining the various empirical and theoretical equations, it may be seen that the equations which are dimensionally correct can be reduced to relations between the dimensionless parameters presented above.

It is evident that the density ratio (ρ_p/ρ_t) and Mach number (V/c_t) have been used in numerous empirical expressions.

By noting that

$$m_p = k \rho_p d^3$$

the expressions used at BRL and NRL Eq. (4.26) may be reduced to

$$\frac{p}{d} = k \left(\frac{\rho_p}{\rho_t} \right)^{1/3} \left(\frac{\rho_t V^2}{H_t} \right)^{1/3} \quad (4.33)$$

thus involving the Best number, while Pugh and Eichelberger's¹⁴ expression, Eq. (4.25), is very nearly equivalent to

$$\frac{p}{d} = k \left(\frac{\rho_p}{\rho_t} \right)^{1/3} \left(\frac{\rho_t V^2}{H} \right)^{1/6} \quad (4.34)$$

except for the exponent in Brinell Hardness.

The expression used by Engel⁴⁰, Eq. (4.29), involves a variation of the Best number. It may be written

$$\frac{p}{d} = k_1 \frac{1}{\frac{c_t \rho_t}{c_p \rho_p} + 1} \left(\frac{V}{c_t} \right) - k_2 \left(\frac{\rho_p}{\rho_t} \right)^{1/2} \left(\frac{Y_t}{\rho_t c_t^2} \right) \quad (4.35)$$

In Collins and Kinard's³⁵ expression, Eq. (4.24)

$$p = k_1 \frac{(\rho_p V L - k_2)}{\rho_p^{0.278} (G_t + k_3)^{0.78}} \quad (4.36)$$

the constants are evidently not dimensionless. Terms of the form

$$\frac{p}{d} = k \frac{\rho_p^{0.72} V}{G_t^{0.78}}$$

are involved.

By rewriting Bohn and Fuchs'¹¹⁸ theoretical expression, Eq. (3.21), slightly, it may be seen that they also use the Best number,

$$\frac{p}{d} = k_1 \left(\frac{\rho_p}{\rho_t} \right) \left\{ \log_e \left(1 + k_2 \sqrt{\frac{\rho_t V^2}{H}} \right) - \frac{k_2 \sqrt{\frac{\rho_t V^2}{H_t}}}{1 + k_2 \sqrt{\frac{\rho_t V^2}{H_t}}} \right\} \quad (4.37)$$

It will be remembered that shaped charge jet penetration results, Eq. (3.36) were extensively correlated with the use of the Best number, i.e.,

$$\frac{p}{L} = \left(\frac{\rho_p}{\rho_c} \right)^{1/2} \left\{ 1 - \frac{\alpha}{\left(\frac{\rho_p}{\rho_c} \right) \left(\frac{\rho_t V^2}{H_t} \right)} \right\} \quad (4.38)$$

While no empirical fits have been previously attempted using thermal quantities, the thermal penetration theories (Section 3.3) all involve only the parameters

$$\left(\frac{f_p}{f_t}\right), \quad \left(\frac{V^2}{Q_t}\right), \quad \left(\frac{Q_p}{Q_t}\right)$$

4.4 Comparison of Theories and Empirical Expressions on the Basis of Resistance to Penetration

Some of the penetration theories and empirical expressions were devised by either deducing or assuming the dependence of the force resisting penetration on the physical parameters, and solving the resultant equation of motion

$$\frac{\pi}{6} f_p d^3 v dv = - F dp \quad (4.38)$$

where F is the resistance force.

It is very interesting to compare these theories and empirical expressions on the basis of the resistance to penetration which they implicitly assume. For those empirical expressions which were not derived by assuming the form of the expression for the resistance, F may be obtained simply by differentiating the expression for penetration.

4.4.1 Resistance Independent of Velocity

If the resistance is assumed to be independent of velocity, and simply dependent on the presented area of the

projectile,

$$F = k d^2 \qquad \frac{P}{d} = K \rho_p V^2 \qquad (4.39)$$

which is equivalent to the Euler-Robins penetration law, Eq. (4.2). Adding a constant to allow for free surface effects yields the NRL expression, Eq. (4.3).

$$\frac{P}{d} = K_1 \rho_p V^2 + K_2 \qquad (4.40)$$

If free surface effects are taken into account by assuming that the resistance depends on the depth of penetration,

$$F = k p \cdot d \qquad \frac{P}{d} = K \rho_p^{1/2} V \qquad (4.41)$$

which is equivalent to the expression introduced by Fairbairn, Eq. (4.3). Assuming a stronger dependence of resistance on depth of penetration

$$F = k \cdot p^2 \qquad \frac{P}{d} = K \rho_p^{1/3} V^{2/3} \qquad (4.42)$$

which is the expression proposed by Rinehart, Eq. (4.16), and which is in use at the Naval Research Laboratory and the Ballistics Research Laboratory, Eq. (4.26). A slight variation yields

$$F = K \frac{p^2}{\rho_p} \qquad \frac{P}{d} = K \rho_p^{1/3} V^{2/3} \qquad (4.43)$$

which may be recognized as the expression introduced by Charters, Eq. (4.22)

4.4.2 Resistance Dependent on Velocity

If the resistance is assumed to be directly proportional to velocity,

$$F = k d^2 v \qquad \frac{P}{d} = K \rho_r V \qquad (4.44)$$

An expression of this type, with the addition of a constant to allow for a minimum velocity to produce finite penetration has been used by Kinard and Collins, Eq. (4.24), and by Engel, Eq. (4.28). By allowing for an increase of resistance with penetration depth

$$F = k p^2 v \qquad \frac{P}{d} = K \rho_r^{1/3} V^{1/3} \qquad (4.45)$$

which is the expression proposed by Pugh and Eichelberger, Eq. (4.17).

Expressions in effect assuming an inverse dependence on velocity are the Tresidder equation, Eq. (4.9).

$$F = k \frac{p \cdot d}{v} \qquad \frac{P}{d} = K \rho_r^{1/2} V^{3/2} \qquad (4.46)$$

and the DeMarre expression, Eq. (4.13).

$$F = k \frac{p^2}{\rho_r v^2} \qquad \frac{P}{d} = K \rho_r^{2/3} V^{4/3} \qquad (4.47)$$

It may be noted that all the expressions in this subsection may also be derived by assuming resistance independent of velocity, but dependent on some power of the penetration depth. Thus Kinard and Collins' and Engel's

expressions also imply

$$F = k \frac{p \, d}{f_p} \qquad \frac{p}{d} = K f_p V \qquad (4.48)$$

Pugh and Eichelberger's expression implies

$$F = k \frac{p^5}{d^3 f_p} \qquad \frac{p}{d} = K f_p^{1/3} V^{1/3} \qquad (4.49)$$

Tresidder's equation yields

$$F = k (f_p d^5 p)^{1/3} \qquad \frac{p}{d} = K f_p^{1/2} V^{3/2} \qquad (4.50)$$

and the DeMarre expression yields

$$F = k (d^3 p)^{1/2} \qquad \frac{p}{d} = K f_p^{2/3} V^{4/3} \qquad (4.51)$$

4.4.3 Resistance Dependent on Inertia

If the resistance is assumed to be proportional to the inertia forces exerted by the target, the resistance force may be written

$$F = k d^2 f_t V^2 \qquad (4.52)$$

In this case integration of the equation of motion

$$f_p d^3 v \, dv = - k d^2 f_t V^2 \, dp \qquad (4.53)$$

leads to the expression

$$\frac{P}{d} = k_1 \frac{\rho_p}{\rho_t} \log_e V + k_2 \quad (4.54)$$

which is the form of expression used by Grimmer, Eq. (3.17). If the resistance is assumed to be proportional to an inertia term, and a term independent of velocity to allow for material strength, the resistance becomes

$$F = k_1 d^2 (k_2 + \rho_t v^2) \quad (4.55)$$

This is exactly the type of resistance term found in the armor penetration theories of Bethe, and Thomson, (Section 3.1), who derived their results by solving the dynamic elastic-plastic equations of motion of the target. Their resistance expressions are of the form

$$F = k_1 d^2 (k_2 Y + \rho_t v^2) \quad (4.56)$$

See Eq. (3.7), Eq. (3.9) and Eq. (3.11). Substituting the more convenient Brinell hardness for the yield strength, since these have been shown to be roughly proportional, the equation of motion becomes

$$\int_p d^3 v dv = -k_1 d^2 (k_2 H + \rho_t v^2) dp \quad (4.57)$$

When integrated this yields the equation

$$\frac{P}{d} = \frac{1}{2 k_1} \left(\frac{\rho_p}{\rho_t} \right) \log_e \left\{ 1 + \frac{1}{k_2} \left(\frac{\rho_t v^2}{H_t} \right) \right\} \quad (4.58)$$

Bohn and Fuchs (Section 3.1.6) assumed a resistance force of the form

$$F = k_1 d^2 \left(\sqrt{k_2 H_t} + \sqrt{\rho_t} V \right)^2 \quad (4.59)$$

Integration of the equation of motion then led to Eq. (3.20)

$$\frac{p}{d} = \frac{1}{k_1} \left(\frac{\rho_e}{\rho_t} \right) \left\{ \log \left(1 + \sqrt{\frac{\rho_t V^2}{k_2 H_t}} \right) - \frac{\sqrt{\frac{\rho_t V^2}{k_2 H_t}}}{1 + \sqrt{\frac{\rho_t V^2}{k_2 H_t}}} \right\} \quad (4.60)$$

4.4.4 Discussion

It may be seen from the above, that the penetration laws in use may be divided into two general categories. In the first, the assumption is made that the resistance varies with some power of the distance from the surface. This assumption then leads to a penetration law of the general form

$$\frac{p}{d} = k \rho_r^m V^n \quad (4.61)$$

If the resistance is assumed to increase more rapidly with increasing distance from the surface (higher power of p), the resultant velocity exponent n decreases.

In the second category, the resistance is assumed to be due to the inertia of the target, and therefore proportional to v^2 . The resultant dependence of penetration on

velocity is logarithmic. When a resistance term independent of velocity is included, the resultant equation has some very interesting properties, see Eq. (4.58). At low velocities, the contribution of the strength term is dominant, i.e. in the neighborhood

$$\left(\frac{\rho_t V^2}{H_t} \right) = O(k_1)$$

However, as the velocity increases, the strength term becomes increasingly less important, so that at

$$\left(\frac{\rho_t V^2}{H_t} \right) \gg k_2$$

Eq. (4.63) becomes very nearly

$$\frac{p}{d} = \frac{1}{2 k_1} \left(\frac{\rho_p}{\rho_t} \right) \left\{ \log_e \left(\frac{\rho_t V^2}{H_t} \right) - \log_e k_2 \right\} \quad (4.62)$$

It is clear that the strength term now enters as a constant correction, much in the way that it was included in Grimmer's theory. Not until

$$\log_e \left(\frac{\rho_t V^2}{H_t} \right) \gg \log_e k_2$$

will the effect of strength become negligible.

It may also be noted that the logarithmic function exhibits a decreasing slope with increasing velocity. In order to compare the logarithmic form with the previous

simple power law, Eq. (4.58) has been plotted on log-log paper in Fig.4.2 denoting $\sqrt{\rho_t/k_2 H_t} = \alpha$. In this way the slope of the curve will correspond to the exponent n in the expression $p = kV^n$.

It is seen that the slope decreases from about 2 at $\alpha V = 0.3$ to $1/6$ at $\alpha V = 100$. The slope is approximately $2/3$ in the range $3 < \alpha V < 6$. Eq. (4.54) and Eq. (4.60) are also plotted in Fig.4.2, the curves having been adjusted to coincide at $\alpha V = 4$, i.e. in the velocity range where the curves are approximated by $p = kV^{2/3}$. Grimminger's form Eq. (4.54) agrees well with the previous curve at higher velocities, but departs drastically at lower velocities. However Bohn and Fuchs' expression Eq. (4.60) agrees very well at lower velocities, but departs at higher velocities, the slope decreasing more slowly, and approximating $1/3$ in the range $20 < \alpha V < 200$.

It is possible to deduce approximate velocity ranges over which the curves of Fig.4.2 may be approximated by $p = kV^n$ for different values of n , for a typical target material. For aluminum targets for example, it is observed that penetration follows the law $p = kV^{2/3}$ above about 10,000 ft/sec. The curves of Fig.4.2 first show agreement with this law at about $\alpha V = 3$. Thus α may be approximately evaluated, and corresponding velocity ranges found.

These are shown in the table.

Approximate Velocity Ranges in ft/sec.
in which Penetration May be Approximate by $p = kV^n$

Velocity Exponent n	Eq. (4.54)	Eq. (4.58)	Eq. (4.60)
V^2	4,000 - 6,000	1200	1200
$V^{4/3}$	6,000 - 10,000	2,000 - 6,000	2,000 - 6,000
V	7,500 - 12,000	5,000 - 10,000	5,000 - 10,000
$V^{2/3}$	10,000 - 20,000	10,000 - 20,000	10,000 - 35,000
$V^{1/3}$	30,000 - 200,000	30,000 - 200,000	60,000 - 300,000
$V^{1/6}$	600,000	600,000	10^6

SECTION V

NORMAL IMPACT ON QUASI-INFINITE TARGETS

This section will be devoted to a discussion of the applicability of the theories presented in Section III and the empirical relationships presented in Section IV to cratering in quasi-infinite targets by projectiles striking the target at normal incidence. The cratering process is an extremely complex one, involving many different types of material behavior. It is therefore necessary to first give a description of the cratering process. The applicable theories are then compared to the appropriate experimental data and the fits of empirical expressions discussed in Section IV to the data are then examined.

5.1 Description of Phenomena

Several excellent studies of cratering by high velocity projectiles have recently been carried out in which high speed photography, X-radiography and other techniques were used to make active observations of phenomena accompanying the penetration process. When taken together with post mortem observations of the crater and adjacent material, and interpreted in the light of present knowledge of the behaviour of solids under high pressures, a fairly detailed qualitative understanding of the physical phenomena involved in cratering can be gained. Several descriptions of these phenomena have recently been given.^{7,81,128}

At the instant of first contact of the projectile with the target, local conditions at the projectile-target interface may be estimated by one-dimensional shock theory. Such theories both for very high pressures, and for low stresses, have recently received a great deal of attention.^{137 to 151} The Hugoniot relations for the shock proceeding into the target and the shock receding back into the projectile determine the initial shock velocities and interface velocity and pressure. (See Appendix D.) Interface pressures and velocities calculated on this basis, and for the acoustic approximation, i.e. neglecting the change of compressibility with pressure of the materials, are plotted as a function of projectile velocity in Fig. 5.1a and b for several common materials. It may be noted that the acoustic approximation leads to very large errors at even modest velocities.

The shock receding into the oncoming projectile will actually be carried below the original target surface when the initial projectile velocity exceeds the velocity of the shock wave generated in the projectile. The critical velocity, above which the shock in the projectile is carried below the original target surface, is a function of the densities and compressibilities of the projectile and target materials, see Appendix D. Critical velocities for several common material combinations are shown below.

Minimum Projectile Velocities for the Shock to
Move Below the Original Target Surface

Target Projectile	Al	Cu	Pb
Al	43	73	79
Cu	22	37	38
Pb	12	20	21

velocities in thousands of feet per second

The initially one-dimensional motion is of course localised around the nose of the projectile, and is almost immediately altered by the geometry of the subsequent motion. Nevertheless the above considerations are useful for estimating maximum pressures, temperatures and shock velocities resulting from the impact.

At low impact velocities of a few thousand feet per second, initial interface pressures are of the order of the dynamic yield strengths of typical materials, as may be seen from Fig. 5.1a. It is therefore clear that the motion will be strongly influenced by material strength.

In cases where the projectile strength is much greater than the target strength, as in the impact of a hard copper projectile on a soft lead target, the projectile may suffer only minor deformation at low impact velocities, and an almost cylindrical crater of diameter equal to that of the projectile is formed by a process of dynamic plastic deformation of the target material. As the initial projectile velocity increases, the projectile suffers increasing plastic deformation. The inertia effects also lead to increased radial motion of the target material, so that the resultant crater is of increasingly greater diameter than the original projectile diameter, until a velocity is reached where the inertia effects predominate, and an almost hemispherical crater is formed.

When the projectile is brittle, a departure from the above behaviour is observed. The shock wave receding into the projectile on reflection at the free surfaces of the projectile may lead to stress concentrations which are sufficient to cause brittle fracture at velocities where

very little plastic deformation of the projectile occurs. Tungsten carbide and hardened steel projectiles exhibit this type of behaviour. Just above the velocity necessary to cause projectile fracture, the projectile is observed to break into several large fragments. The presented area of the fragments is considerably greater than that of the unbroken projectile, and a reduction of penetration may result, although the crater volume continues to increase. At increased velocities, the projectile suffers increasing fragmentation, and the penetration again increases. Finally, when inertia effects predominate, a nearly hemispherical crater again results.

These effects are illustrated in Fig. 5.2 which shows craters formed by lead, copper and hardened steel spheres in soft lead targets at several identical initial projectile velocities. Figure 5.3 shows the penetration as a function of velocity for typical ductile projectile behaviour, while Fig. 5.4 shows the penetration as a function of velocity for typical brittle projectile behaviour.

Three regions of impact are commonly defined:-

- a) Low velocity region in which the projectile suffers only minor deformation, and which has also been termed the armor penetration region or undeformed projectile region.
- b) transition region,
- c) high velocity region where nearly hemispherical craters are formed, and which has also been termed the hypervelocity region, or the "fluid impact" region, from the fact that inertia effects predominate.

It is interesting to note that the penetration appears to be nearly proportional to the $4/3$ power of velocity in the low velocity region, while the penetration

is approximately proportional to the $2/3$ power of velocity in the high velocity region. In the case of ductile projectiles, the high and low velocity regions are connected by a smooth curve in the transition region. Brittle projectiles show an extended low velocity region with the drop in penetration, discussed previously, in the transition region.

At high impact velocities, the initial pressures are very much greater than the dynamic yield strengths of the materials, as may be seen from Fig. 5.1a, and the strength of the materials may well be neglected at early stages of the cratering process. The projectile and target materials are in fact observed to flow very much like fluids in this region. For example, hemispherical craters are often observed to be plated with a thin layer of projectile material, Fig. 5.5. At still higher velocities all the projectile material apparently flows out of the crater.

As the projectile approaches the target, the projectile and target surfaces will generally meet at a small angle. High velocity collision of surfaces at small angles leads to the phenomenon of jetting¹⁴⁴, material being expelled along the bisector of the angle between the surfaces at considerably higher velocities than the closing velocity of the surfaces. The expelled particles may move with sufficient velocity so that ablation occurs and the ablated material burns if air is present. The resultant luminosity is referred to as the impact flash. The phenomenon has been studied in some detail by Grow et al.^{80,83,84,85} Cook^{77,81} has photographically observed areas interpreted to be clouds of metal vapour emanating from the impact area, which very likely are due to the same mechanism.

As the projectile continues to move into the target, the shock wave in the target precedes the projectile-target interface. Rarefactions from the free surface of the target and projectile modify the shock system, and the shock rapidly becomes nearly hemispherical. High speed framing camera sequences of penetration in transparent plastics (Fig. 5.6) and flash X-radiographs sequences of penetration in metallic targets (Fig. 5.7) clearly show this behaviour. At the target surface adjacent to the projectile, the high pressure target material is unsupported and is forced out of the crater to form a spray. Several fine X-radiographs and high speed framing camera sequences of the spray have been made. (Fig. 5.8). It is clear that a large proportion of the material originally in the crater is expelled in the spray, which moves at relatively low velocities.

Numerical solution of the differential equations of motion of an inviscid fluid, with appropriate equation of state, show shock and rarefaction systems closely resembling those observed experimentally, and considerably clarify the understanding of the cratering process. Results obtained by Bjork^{128,152} in the form of pressure contours and velocity vectors for the impact of a cylindrical projectile on a semi-infinite target are shown in Fig. 5.9 and 5.10. (It should be noted that the numerical method uses an artificial viscosity term to render the solution continuous, and shocks are therefore smeared over a finite distance instead of appearing as discontinuities. The shocks are smeared over a fairly large distance in Bjork's solution since a rather coarse finite-difference space mesh was used for reasons of computer time economy.)

Figure 5.9 shows results for the impact of an iron projectile on an iron target at 18,000 ft/sec. The shock in the projectile is seen to rise above the original surface of the target. Figure 5.10 shows results for the impact of an iron projectile on rock (tuff) at 100,000 ft/sec. The shock in the projectile is carried below the original surface of the target, and the resultant differences in the flow pattern can be seen when compared to Fig. 5.9.

If the shock in the projectile is carried below the original surface of the target, the projectile material which has not yet been reached by the shock is carried well below the target surface, and one may expect much greater penetration. On the other hand, if the shock in the projectile recedes above the target surface, the sides of the shock zone in the projectile are unsupported, and increased lateral flow may be expected, with consequent shallower craters. In an extreme case, such as the impact of nylon on aluminum, the stresses in the unsupported shocked zone in the projectile may be sufficiently high to cause the projectile to flow out over the surface of the target, and craters considerably shallower than hemispheres have been observed under such conditions.

While the initial phase of the motion resulting from high velocity impact may be adequately described by hydrodynamic principles, the stresses rapidly decay due to geometrical divergence and dissipation to the point where material strength becomes important. The material being ejected from the crater will now remain attached to form a raised lip. If the target material is brittle, portions of this lip may fracture and be removed. The final phase of the motion will involve a certain amount of elastic springback.

Gehring⁷, using flash X-radiography has estimated that the elastic recovery in crater volume may be as high as 30% in an aluminum target struck by a steel projectile at 16,400 ft/sec.

Material which has been subjected to very intense shock compression, followed by an adiabatic expansion is returned to zero pressure at higher temperature than ambient, due to the entropy increase in the shock process. Under conditions of high velocity impact, this temperature may be above the melting point. For impacts below 20,000 ft/sec, theoretical estimates indicate that a small zone of target material near the initial point of impact may be melted in normal metallic materials. In low melting point materials such as lead, melting may be much more extensive. Since the melted material has no strength on return to zero pressure, it will be ejected from the forming crater somewhat more readily than if it had not been melted. This mechanism may therefore contribute to the cratering process at high impact velocities. The question whether the material melts during the high pressure phase of the motion is academic, since the main effect will be an absorption of latent heat, which is negligible. Theoretical estimates for minimum shock pressures necessary to cause subsequent melting on return to zero pressure for typical materials are 24 kilobars for lead, 225 kilobars for tin, 325 kilobars for cadmium, and 1.4 megabars for copper.

The material immediately adjacent to the crater sometimes shows signs of recrystallisation at the highest experimental impact velocities, confirming that local melting has occurred. More remote material usually shows

evidences of severe plastic deformation in severely deformed crystal structure or shock twinning, and in increased indentation hardness, these effects being reduced at greater distances from the crater. Examples are shown in Fig. 5.11.

5.2 Comparison of the Data with Theory

The penetration data for quasi-infinite targets for which sufficient data points exist have been presented in Fig. 1.2 through 1.25. (See Section II.) The plots represent data for impact of a variety of projectile materials on aluminum, steel, copper and lead targets. The penetration has been normalised with respect to projectile diameter in these plots. For cylindrical projectiles, the diameter of an equivalent sphere of equal mass was used, i.e. $d_e = (3/2 d^2 L)^{1/3}$. Drawn on these figures are curves representing theoretical predictions of penetration according to the applicable theories presented in Section III. Although some of these theories were intended to apply to a much higher velocity range, they have nevertheless been computed in the experimental velocity range, and included in the plots. Each of the theories will be briefly discussed.

5.2.1 Rigid Projectile

The applicable theories in this class are Grimmer's theory (Section 3.1.5) and Bohn and Fuchs' theory (Section 3.1.6). Zaid's theory (Section 3.1.7) was not included since reliable solutions could not be obtained.

Grimmer's theory contains two somewhat arbitrary constants; the transition velocity at which the penetration

mechanism changes from a fluid drag mechanism to one of armor penetration, and the constant in the armor penetration relation. For the present comparison, the values for these two constants given by Grimmer were taken. The transition velocity was taken as five times the plastic wave velocity, the latter being given as 1000 ft/sec for all materials, while the armor penetration constant is defined in Section 3.1.5. Using these values, it may be seen that Grimmer's theory generally underestimates the penetration below 5000 ft/sec, and overestimates the penetration above this velocity. The discrepancy is exceptionally large in the case of lead targets, while agreement is best for copper targets.

A change in the constants would have the effect of altering the level of the portion of the curve above the transition velocity. The most obvious improvement would be to make the transition velocity a multiple of the elastic wave velocity. Taken relative to the results in copper, this would lower the predicted penetration in lead considerably but slightly raise the predicted penetration in aluminum and steel, thus representing an improvement in agreement in the case of lead, but a deterioration in the case of aluminum and steel.

Bohn and Fuchs' theory contains a shape factor, which was assumed to lie between $1/3$ and 1 . For the value of $2/3$ given for spherical projectiles, it may be seen that the theoretical predictions are in rather surprisingly good agreement with the data at low velocities. It may be seen from Fig. 1.2 to 1.25 that for most materials the agreement is very good for low velocities, the theory overestimating penetration at higher velocities. For tungsten carbide

projectiles at low velocities, the theory underestimates penetration. After projectile break-up however, the theory again overestimates penetration.

An increase in shape factor f , would reduce the predicted penetration. At higher velocities the penetration is roughly proportion to $1/f$, thus a value of f of about $4/5$ instead of $2/3$ would lead to considerably improved agreement over the whole velocity range, except for the tungsten carbide projectiles.

5.2.2 Hydrodynamic Theories

Bjork's theory (Section 3.2.1), Opik's theory (Section 3.2.2) and shaped charge jet theory (Section 3.2.3) are considered.

Numerical solution of the equations of fluid dynamics have been given by Bjork for only two metallic target materials at the time of this study, i.e. aluminum impacting aluminum, and iron impacting iron. The theory contains no adjustable constants, all material properties appearing in the theory having been evaluated in independent measurements. Due to the nature of the assumption that material strength is negligible, the theory is only expected to be applicable at very high velocities.

The theoretical curve given by Bjork for aluminum impacting aluminum has been drawn on Fig. 1.2 through 1.4 for 2024-T3, 24ST and 1100F targets respectively and for iron impacting iron on Fig. 1.12 through 1.14 representing 1020, 1030, and 4140 targets respectively. Bjork arbitrarily defined the equivalent diameter of his cylindrical projectile as $d_e = (d^2 L)^{1/3}$. Definition of the equivalent diameter

on the basis of equivalent mass Eq. (5.2) leads to a reduction in predicted penetration of 16 per cent, and leads to the lower curves shown in Fig. 1.2 through 1.4 and 1.12 through 1.14.

It may be seen that the highest velocity experimental points for the 1100F aluminum and 1030 steel targets are clustered on Bjork's original curve, while experimental points for the other alloys lie well below the theoretical curve. However the experimental points show a steeper gradient than $v^{1/3}$ slope predicted by the theory, so that the experimental points disagree with theoretical predictions at lower velocities. No conclusions regarding possible agreement at higher velocities may be drawn on the basis of the present evidence.

Opik's theory (Section 3.2.2) contains an adjustable constant $K = 1/2 \rho_p v_0^2$ where v_0 represents the velocity below which no penetration will occur. In calculating the theoretical curves, v_0 was found by extrapolating the data to zero penetration. It is clear from the curves, (Fig. 1.2, 1.14, 1.15, 1.18, 1.22, 1.24) that the agreement between Opik's theory and experiment is rather poor; in particular, Opik's theory predicts that the rate of increase of penetration with increasing velocity becomes very low at velocities above 10,000 ft/sec. A change in the value of v_0 alters the predicted penetration but does not appreciably alter the slope of the curve at higher velocities, as may be seen from Fig. 1.18 where theoretical curves for $v_0 = 200$ ft/sec and 500 ft/sec are shown.

First order shaped charge jet theory predicts that

penetration will be independent of velocity (Section 3.2.3)

$$\frac{P}{L} = \sqrt{\frac{\rho_r}{\rho_t}}$$

which may be expected to apply only at very high velocities. Including a correction for target strength reduces the predicted penetration at low velocities, the theoretical curve becoming asymptotic to the maximum value predicted by first order theory. Horizontal lines representing first order theory have been drawn on each of Fig. 1.2 through 1.25. It may be seen that there is a consistent trend for the penetration to be considerably greater than the predicted value at higher velocities. Inclusion of the correction for target strength will lead to lower predicted penetrations. No attempt has been made to calculate these curves.

The lack of agreement is not surprising, since the major contribution to the penetration at higher velocities may be expected to be due to the inertial expansion of the crater. The correction for inertial expansion was not included since its value depends strongly on the velocity v_0 for which no penetration occurs, and which must be found empirically. This could not be done accurately with the present data.

5.2.3 Thermal Penetration

The applicable thermal penetration theories are those of Whipple, (Section 3.3.1) Langton (Section 3.3.2) and Grow (Section 3.3.3). Curves representing the three theories are drawn on Fig. 1.2 through 1.25 for comparison with the data.

Whipple's and Langton's theories differ mainly in the proportionality constant between the penetration and the $2/3$ power of the velocity, due to the different shape assumed for the crater. Langton in addition includes a term to account for the melting of the projectile, which becomes relatively less important as the velocity increases. Whipple's theory overestimates penetration in almost all cases except for penetration of tungsten carbide projectiles in the low velocity region. On the other hand, Langton's theory considerably underestimates the penetration in all cases. As may be expected from the dependence of penetration on the first power in velocity, Grow's theory grossly overestimates penetration at all but the lower velocities in all cases for which it was computed.

None of the thermal penetration equations take into account the strength of the target, since they were intended to apply only to extremely high impact velocities, and they can therefore not be made to fit data in targets of the same material but different hardness within the experimental velocity range.

5.3 Empirical Power Law

In this section it is assumed that a penetration law of the form

$$p = k V^n$$

is valid. Sufficient experimental data exists so that the dependence of penetration on each experimental parameter may be investigated separately, and a non-dimensional penetration law is devised. Crater diameters and volumes are then considered.

5.3.1 Consistency of the Data

Several projectile material-target material combinations have been used at different laboratories in the same velocity range, thus allowing a direct comparison of the data from one laboratory with that from another. Except for some early work, the experimental data agree within the experimental scatter, as may be seen in Fig. 1.2 through 1.25. Apparent disagreements, as in the case of aluminum projectiles impacting aluminum targets (Fig. 1.2, 1.3, 1.4) may be traced to differences in strength properties of the targets used at the various laboratories. In subsequent statistical analyses, all of the data was weighted equally.

5.3.2 Dependence on Projectile Dimension

For large number of projectile material-target material combinations, firings have been made with a variety of projectile sizes, and with both spherical and cylindrical projectiles. In plotting Fig. 1.2 through 1.25, the penetration has been normalised to the projectile diameter. In the case of cylindrical projectiles, the diameter of an equivalent sphere of mass equal to that of the cylinder was used, i.e.

$$d_e = \left(\frac{3}{2} d^2 L \right)^{1/3} = \left(\frac{6}{\pi} \frac{m_p}{\rho_p} \right)^{1/3}$$

However, it should be pointed out that nearly all of the projectiles considered had length to diameter ratios (L/d) near unity, and the equivalent sphere diameter did not differ greatly from the cylinder diameter. Almost equally

good correlation could be obtained by using the cylinder diameter or length directly. For L/d far from unity, this scaling is not likely to hold. (See Section 6.3) Insufficient data exists at present to define the limits of L/d over which the correlation on the basis of equivalent sphere diameter can be expected to hold.

Except for a consistent tendency in the data reported by Kinard and Collins³⁵ for the penetration to be slightly greater for 1/2 inch diameter projectiles than 0.22 inch diameter projectiles no size effect could be detected. Nearly all of the data was in the range of projectile diameter of 1/16 to 1/2 inch.

5.3.3 Dependence on Projectile Velocity

If it is assumed that the penetration depends on the velocity through a relation of the form $p = kV^n$, this type of dependence can be most conveniently investigated by means of log-log plots of penetration versus velocity. Typical curves of this type for ductile projectiles impacting aluminum, copper and lead targets are shown in Fig. 5.12, 5.13 and 5.14 and for brittle projectiles in Fig. 5.15, 5.16 and 5.17. Although there is considerable scatter, the curves all show a tendency to vary from a velocity exponent of 4/3 at low velocities to about 2/3 at high velocities, (except for lead, Fig. 5.14 which does not extend to low enough velocities to show a 4/3 power dependence). For the high strength projectiles, the 4/3 slope is maintained to velocities at which the projectile shatters, this effect being most pronounced in the softest material, lead.

5.3.4 Dependence on Projectile Properties

Relatively little information is available on the effect of projectile strength on cratering. Maiden et al¹² shot series of steel projectiles which had received different heat treatments into 1030 steel targets in a velocity range from 4,000 to 13,000 ft/sec. Results (Fig. 5.18) indicate that no significant differences in penetration are observed for projectile Brinell Hardness Numbers of 210, 290 and 580. It is clear that these data lie in the high velocity region, since they conform to the $2/3$ velocity exponent. On the other hand Abbot⁸⁹ found significant differences in penetration in steel targets by two types of steel projectiles, having Brinell Hardness Numbers of 140 and 705 respectively, up to 7,000 ft/sec, i.e. well into the high velocity range, although the differences were small above 5,000 ft/sec. (Fig. 5.19.) Grow et al⁸⁶ shot two types of steel projectiles into lead targets, (Fig. 5.20.) up to a velocity of about 5,000 ft/sec. Significant differences in penetration were observed up to a velocity of about 4,000 ft/sec, which from Fig. 5.17 is seen to correspond to the upper limit of the transition region.

It may be surmised that the projectile strength does not affect penetration above the transition region, particularly for ductile projectiles. It is clear that the same will be true of the undeformed projectile region for high strength projectiles, where no deformation of the projectile occurs.

If this is true, then the only factor to account

for differences in penetration in a given target material by different projectile materials is the projectile density. By analysing proportionality constants k in $p = kv^{2/3}$ obtained from plots of the type of Fig. 5.12 through 5.17, k is found to be very nearly proportional to the $2/3$ power of the projectile density and independent of projectile strength in the high velocity region, for a given target material.

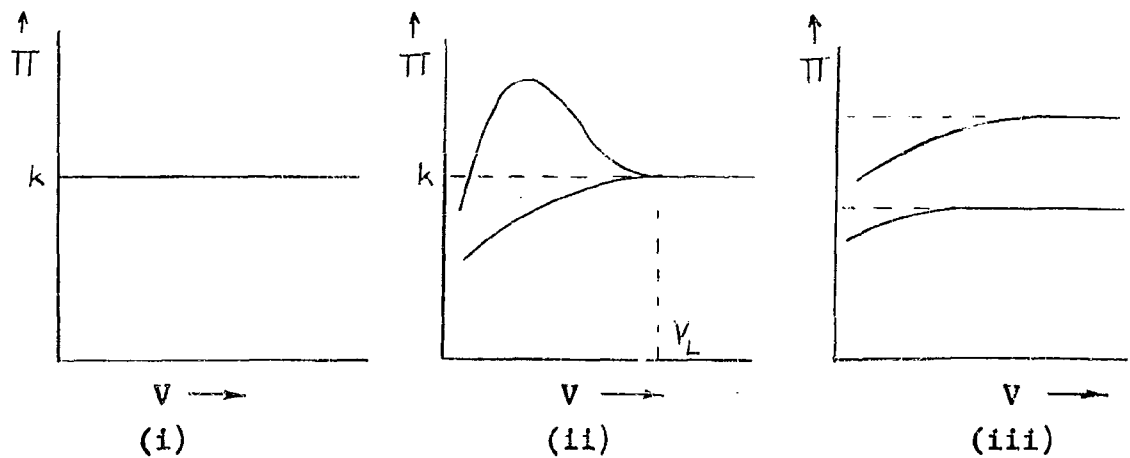
5.3.5 Dependence on Target Properties

While penetration may be expected to depend on target density, there is strong evidence to suggest that penetration also depends on target strength over the entire velocity range covered by the present data. Summers³⁰ has reported firings of copper projectiles into two sets of copper targets heat treated to Brinell Hardness of 65 and 35 respectively. (Fig. 5.21) Significant differences in penetration were observed over the whole velocity range which was explored, extending from a few hundred ft/sec. to 10,000 ft/sec. Figure 5.22 shows penetration results for steel projectiles impacting four different types of steel target ranging in Brinell Hardness from 111 to 302. Differences in penetration are again evident up to at least 8,000 ft/sec, the highest velocity at which a comparison can be made.

A comparison of cratering into hard (2024T-3) aluminum and soft (1100F) aluminum targets by aluminum projectiles can also be made. (Fig. 5.23) Penetration in the 2024T-3 aluminum targets, having a Brinell Hardness of about 120 is observed to be about 60% of that in the softer 1100F alloy up to the highest experimental velocity of 16,000 ft/sec.

The hardness of the 1100F material was unfortunately not measured, but, according to handbook values, lies in the range 23 to 44.

It is therefore clear that target strength will have to be taken into account over the whole of the experimental velocity range. It has already been shown that penetration is proportional to the $2/3$ power of projectile density and velocity. The following procedure was adopted to verify this dependence on projectile density and velocity, to obtain reliable values of the proportionality constant for each target material, and to determine the lower limit of velocity in which the $2/3$ power law is valid for each projectile material--target material combination.



Large scale plots of $P/d = \rho_p V^2$ versus velocity were prepared for each target material. If the penetration did in fact follow the law

$$\frac{P}{d} = k (\rho_p V)^{2/3}$$

the resultant plot should be a horizontal straight line as shown in sketch (i) above. If the penetration were proportional to some other exponent of velocity, the resultant plot would be a curve as shown in sketch (ii) above. At high velocities, the curve should reach the 2/3 power law, and thus become a horizontal straight line. The velocity above which the curve becomes horizontal, then corresponds to the lower limit of the high velocity region. It is to be expected that different projectile materials will produce different curves at low velocities as shown. If on the other hand the penetration were proportional to some other exponent in projectile density, the resultant curves for different projectile materials should tend to horizontal lines which are separated, as shown in sketch (iii) above. Curves for 3 types of aluminum, 4 grades of copper, 4 types of steel, lead, magnesium, silver, zinc, cadmium and tin targets impacted by a variety of projectile materials were prepared. Examples for 2024T-3 aluminum, copper of BHN 65, and for lead targets are shown in Fig. 5.24, 5.25 and 5.26. By far the greatest variety of projectile materials were used with these three target materials. It may be seen that there are relatively very few experimental points in the horizontal region of the curves, but that the curves for the various projectile materials do converge on the horizontal

portion within the experimental scatter. Only very rough values of the limiting velocity could be obtained. However, the value of $p/d (\rho_p V)^{2/3} = k_1$ corresponding to the horizontal portions of the curves could be obtained fairly accurately for several of the target materials. Least squares fits of the values of k_1 , together with standard mean deviations, were obtained using experimental points in the horizontal portions of the curves. These are listed in Table IV.

The effect of target strength could be estimated separately, since k_1 could be evaluated for several types of aluminum, copper, and steel targets, which varied in Brinell Hardness, but had closely similar densities and sonic velocities. Values of k_1 found from least squares fit of the data were plotted versus the Brinell Hardness Number H_t on log-log paper. (Fig. 5.27) The flags represent one standard mean deviation in k_1 and the uncertainty ranges in Hardness. Straight lines of slope $-1/3$ could be fitted through the points representing the different types of each material. Thus the target strength can be approximately accounted for by including a term $H_t^{-1/3}$ i.e.

$$\frac{P}{d} = k_2 \frac{\rho_p^{2/3} V^{2/3}}{H_t^{1/3}}$$

the values of k_2 being found from the previous values of k_1 by

$$k_2 = H_t^{1/3} k_1$$

The effect of density may now be investigated by plotting resultant values of k_2 versus target density on log-log paper (Fig. 5.28) The uncertainty flags shown

are a combination of the mean deviations in k_1 and the uncertainties in H_t . A straight line of slope $-1/3$ has been approximately fitted to the points, again using a least squares fit, leading to a non-dimensional penetration law

$$\frac{P}{d} = (0.36 \pm 0.07) \left(\frac{f_r}{f_t} \right)^{2/3} \left(\frac{f_t V^2}{H_t} \right)^{1/3} \quad (5.1)$$

While most materials fell within the limits given above, penetration for some "anomalous" material combinations may depart from the above expression by as much as 35 per cent.

It might be noted that a slightly higher exponent in ρ_t might be expected to fit slightly better. However it was decided to retain the advantages of a non-dimensional fit. Small changes ($\pm 10\%$) in exponents of the non-dimensional parameters in Eq. (5.1) did not significantly alter the mean deviation.

It should be noted that the empirical expression Eq. (5.1) is necessarily a crude approximation, since it disregards the many complex phenomena actually occurring.

5.3.6 Limits of Validity of the Empirical Power Law

The empirical law deduced in the previous section is clearly limited to a restricted velocity range for each combination of projectile and target materials. Nothing can be said at this time about the upper velocity limit, on the basis of the experimental data. The penetration appears to be proportional to the $2/3$ power in velocity up to the highest velocity data points included here, within the experimental scatter. This point will be discussed later. However, the lower limit of validity of the empirical law may be examined

in some detail.

A number of interesting trends appear from Fig. 5.24, 5.25 and 5.26., in which the ratio $p/d / (\rho_p V)^{2/3}$ is plotted vs. velocity for aluminum, copper and lead targets. Curves have been roughly faired through some of the points for the sake of clarity. It is seen that the penetration is generally less for the low density projectiles, and greater for the high density projectiles at low velocities than predicted by the empirical penetration law Eq. (5.1), the differences diminishing as the velocity increases, until the various curves combine. While the high velocity data is limited almost exclusively to aluminum projectiles, the data representing other projectiles do appear to become asymptotic to the horizontal lines faired through the high velocity points for aluminum projectiles.

On the basis of the qualitative model of cratering presented in Section 5.1, it is possible to suggest the reasons for this behaviour. Reference to Fig. 5.1 shows that the initial maximum pressure generated at the interface is less for the lower density projectiles, and greater for the higher density projectiles.

One might therefore suppose that the strength of the target material may have a relatively greater effect in the case of the lower density projectiles, and therefore restrict the flow and result in smaller craters in a given target material than predicted on the basis of the empirical law Eq. (5.1). Clearly at some low velocity, the initial interface pressure will be so low that no target deformation will occur. This velocity will then be higher for the lower density projectiles. The opposite will be true of higher

density projectiles. One might suppose that the target deformation is related to the quantity $(P^* - Y_t)$ i.e. the initial interface stress in excess of the dynamic yield of the material.

At the same time, there will be a similar effect on the projectile. The degree of deformation of the projectile may also be roughly related to the quantity $(P^* - Y_p)$. Thus, although the initial interface pressure is low for nylon projectiles, nylon also has very low strength, and a nylon projectile may be expected to suffer severe deformation with consequent increase in presented area and decrease in penetration at even moderate velocities. On the other hand tungsten and uranium projectiles, while leading to much higher interface pressures at the same velocities have rather high strength. Thus deformation of the projectile will be inhibited and penetration enhanced, leading to "brittle projectile" type of behaviour. (Section 5.1).

On the basis of this qualitative model, one might expect that the empirical penetration law, Eq. (5.1), will be valid when $P^* \gg Y_p, Y_t$. While the limiting velocities can be estimated only very approximately from curves such as Fig. 5.24 through 5.25, it would appear that a reasonable criterion is given by $P^* > 100 Y_t$ where Y_t is the static yield stress, for material combinations not exhibiting "brittle projectile" behaviour. Noting that the Brinell Hardness is roughly equal to 3.58 from Fig. 4.1, the criterion reduces to

$$P^* > 30 H_t \quad (5.2)$$

For high strength projectiles, the velocity at which breakup is complete may be higher than the velocity

indicated in Eq. (5.2). This is particularly true in lead and other low strength targets. Unfortunately the hardness of projectiles used in experiments has been reported in only very rare instances, so that almost no information exists to guide formulation of a criterion similar to Eq. (5.2). Only one piece of information is available, i.e. stainless steel projectiles shot into lead targets at Utah University (Fig. 5.20). In this one case it also appears satisfactory to use the criterion

$$P^* > 30 H_p \quad (5.3)$$

While it seems logical to extend Eq. (5.3) to other materials, there is presently no other evidence to support such an assumption. If however, the assumption is made, the criterion becomes

$$\frac{P^*}{H_t} > 30 \quad \text{and} \quad \frac{P^*}{H_p} > 30 \quad (5.4)$$

where P^* and H are in identical units.

An attempt has been made to apply empirical corrections to the low velocity data in order to account for the strength effects by the use of correction terms of the type $\frac{P^*}{P^* - kH_t}$, where k is a constant to allow for strain rate effects. This is very difficult because the target and projectile strength effects apply simultaneously, and generally tend to act in the same direction. Furthermore, the uncertainty in the data, (generally $\pm .05$ in p/d or greater) is such that at low velocities, and hence low penetrations, the percentage error is large. It is therefore impossible to

evaluate the effects of target and projectile strength separately with the present data.

5.3.7 Crater Diameters

Diameters of craters in the plane of the original target surface have not been reported in all cases. Figure 5.29 through 5.32 show typical trends in the data for aluminum, copper, steel and lead targets. Shown are the ratios of penetration depth to crater diameter as a function of velocity. This ratio is in effect a shape factor, which should equal 0.5 for hemispherical craters, higher values indicating craters deeper than hemispherical.

It may be seen that projectiles such as copper and lead show a tendency for the ratio p/D_c to increase with velocity, and become asymptotic to the value 0.5. Reference to Fig. 5.12, 5.13, 5.14 indicates that the penetration becomes a function of $v^{2/3}$ at about the same velocity where the ratio p/D_c reaches 0.5. These therefore represent examples of ductile projectile behaviour, described by many authors.

Of interest is the behaviour of aluminum, magnesium and nylon projectiles. In each case, the ratios p/D_c appear to become asymptotic to a value of 0.4, and possibly less in the case of nylon, in the velocity region where the penetration is proportional to $v^{2/3}$.

It may also be seen that projectiles such as hardened steel and tungsten carbide show a tendency for p/D_c to increase with velocity to a maximum much greater than 0.5, and then to decrease and in some cases show a tendency to become asymptotic to 0.5. The velocities at the maxima of

the p/D_c curves may be correlated with the velocities at the maxima of the p/d curves Fig. 5.15, 5.16 and 5.17. These therefore represent examples of brittle projectile behaviour. However, in several cases, the ratio p/D_c has approached a value considerably greater than 0.5 in the velocity region corresponding to a penetration dependence on $v^{2/3}$.

This type of behaviour is exactly what one might expect on the basis of the qualitative model discussed in the previous section. (Sect. 5.3.6) The question as to the velocities at which the craters become hemispherical, or whether the craters will become hemispherical at all, for the very light and very heavy projectiles cannot be answered by the present data. However it is clear that the craters are not necessarily hemispherical in the high velocity region covered by the empirical penetration law Eq. (5.1).

5.3.8 Crater Volumes

Several experimenters report measured crater volumes. The volumes have generally been measured by machining the crater lip flush with the original target surface and filling the crater with a liquid, wax, or powder, the volume of which is subsequently measured.

Of considerable interest is the ratio E/V_c where E is the initial kinetic energy of the projectile and V_c the crater volume. The reciprocal quantity V_c/E has sometimes been termed the cratering efficiency, despite the fact that the quantity is dimensional. Typical plots of E/V_c vs. projectile velocity are presented in Fig. 5.33 through 5.36. For several material combinations a trend has been

noted by many authors for E/V_c to become constant as the velocity increases. Several empirical penetration laws are based on this assumption. For many material combinations, data exists only at low velocities, however several material combinations in Fig. 5.33 through 5.36 do show this trend at higher velocities. It may be noted that the E/V_c curves become horizontal at roughly the same velocities that the penetration becomes proportional to $v^{2/3}$ (Fig. 5.24 through 5.26.)

Asymptotes of E/V_c curves were estimated from plots of the type of Fig. 5.33 through 5.36. There were generally insufficient points in the horizontal portions of the curves to warrant statistical fits.

A tendency for the asymptotic values of E/V_c to depend on the density ratio ρ_p/ρ_t was noted by Summers³⁰. Such a trend is also obvious from Fig. 5.33 through 5.36. Values of E/V_c were obtainable for several different projectile materials impacting lead, copper, steel and aluminum targets. Consequently, asymptotic values of E/V_c were plotted versus density ratio ρ_t/ρ_p on log-log paper (Fig. 5.37). The points for each target material may be approximately fitted by straight lines of slope 2/3, indicating a dependence of E/V_c on $(\rho_t/\rho_p)^{2/3}$.

In order to investigate the dependence on target properties, values of

$$\frac{E}{V_c} \left(\frac{f_p}{f_t} \right)^{2/3}$$

were plotted vs. Brinell Hardness. (Fig. 5.38) A straight line may be approximately fitted to the data leading to a

final correlation

$$\frac{E}{V_c} = (3.1 \pm 0.6) \left(\frac{\rho_t}{\rho_p} \right)^{2/3} H_t \quad (5.5)$$

where the constant is dimensionless, and independent of projectile and target material properties.

It is interesting to note that if the craters are assumed to be hemispherical in the high velocity region, a law of the form of Eq. (5.5) may be derived directly from Eq. (5.1) by noting that

$$E = \frac{1}{2} \frac{\pi}{6} d^3 \rho_p V^2$$

$$V_c = \frac{1}{2} \frac{4\pi}{3} \rho^3$$

resulting in an expression

$$\frac{E}{V_c} \cong 2.9 \left(\frac{\rho_t}{\rho_p} \right) H_t \quad (5.6)$$

This differs slightly from Eq. (5.5) in both the constant and exponent in density ratio. However, in the previous section (Sect. 5.3.7) it was shown that craters formed by low density projectiles were shallower than hemispheres, while craters formed by high density projectiles were deeper than hemispheres. Thus Eq. (5.6) will predict smaller craters than actually formed for aluminum projectiles, and will overestimate craters actually formed by tungsten and tungsten carbide projectiles. The change in exponent of the density ratio just compensates for this effect, as may be seen from Fig. 5.37.

5.3.9 Comparison with Previous Empirical Expressions

In this section it is intended to compare the empirical expression Eq. (5.1) with empirical expressions obtained previously by other authors and listed in Table III. Many of these expressions were devised on the basis of portions of the experimental data used to derive Eq. (5.1), and should therefore be comparable over the limited ranges in experimental parameters considered in their derivation.

Several empirical expressions (Table III) are based on a dependence of penetration on velocity to a power greater than $2/3$. It is clear from previous discussion that these expressions were derived from data in a lower velocity range than that covered by Eq. (5.1). In Section 5.3.6 the complications arising from projectile and target material strength have been discussed. In general, both very low and high density projectile data have been ignored in the derivation of these expressions, thus allowing a reasonable correlation on the basis of elementary material properties.

A number of empirical expressions are based on the form proposed by Charters and Locke²⁸

$$\frac{P}{d} = k \left(\frac{f_r}{f_t} \right)^{2/3} \left(\frac{V}{\bar{c}_t} \right)^{2/3} \quad (5.7)$$

Attempts were made to reduce the data on this basis. However, since the sonic velocity \bar{c}_t does not vary appreciably with hardness in a given target material, expressions of this type are inadequate to correlate data from firings into targets of different hardness, but identical material. The assumption made in the derivation of Charters and Locke's

expression; viz. that the effect of hardness is negligible in the high velocity range, is contradicted by the data up to the highest velocities considered here, and significantly in the region where the penetration is proportional to $v^{2/3}$. Speculation as to the role of strength at much higher velocities will be deferred to a later section. Equation (5.1) fits the data in half-hard copper and lead targets about as well as Eq. (5.7), used by Summers³⁰ to correlate penetration in these materials. It is interesting to note that $P - v$ Hugoniot (Appendix D) are almost identical for copper, iron and lead, so that behaviour associated with low and high density projectiles is absent when these materials only are involved. Furthermore, it might be pointed out that data for annealed copper, and copper of greater Brinell Hardness cannot be correlated by Eq. (5.7), so that the choice of half-hard copper as the basis of Eq. (5.7) must be considered fortuitous.

Expressions derived on the assumption that cratering efficiency is a constant proportional to target hardness and that the craters are hemispheres in the high velocity region, are equivalent to the form Eq. (4.33)

$$\frac{P}{d} = k \left(\frac{\rho_p}{\rho_t} \right)^{1/3} \left(\frac{\rho_t V^2}{H_t} \right)^{1/3} \quad (5.8)$$

This expression differs from Eq. (5.1) only in the exponent in density ratio and in the value of the constant. Attempts to fit the high velocity data used in the derivation of Eq. (5.1) to Eq. (5.8) by the method of least squares led to a considerably increased mean deviation.

It is interesting here to compare the expression

for E/V_c derived by Feldman⁴

$$\frac{L}{V_c} = 2.65 H_t \quad (5.9)$$

with the expression derived in Section 5.3.8

$$\frac{E}{V_c} = 3.1 \left(\frac{f_t}{\rho_p} \right)^{2/3} H_t \quad (5.5)$$

These also differ in the value of the constant and exponent in density ratio. Attempts to fit the data used in the derivation of Eq. (5.5) by Eq. (5.9) again led to a considerably increased mean deviation. Equation (5.8) was derived from Eq. (5.9) by assuming that the crater is hemispherical. This assumption has been shown to be unjustifiable in the velocity range covered by the experimental data in Section 5.3.7 and 5.3.8. Thus it is not surprising that Eq. (5.8) and (5.1) do not correspond.

Bjork^{*} has recently suggested that the penetration in a given target material by projectiles of identical mass and velocity, but different materials, is proportional to the initial interface velocity induced by the impact. For projectiles of identical mass and velocity in a given target, Eq. (5.1) reduces to $p = k \rho_p^{1/3}$. In Fig. 5.39 values of the interface velocity V^* have been plotted against $\rho_p^{1/3}$ for several common target materials at a projectile velocity of 5 km/sec. The interface velocity is very nearly proportional to $\rho_p^{1/3}$. Since the V^* vs. V curves, Fig. 5.1, are very nearly straight lines, a similar degree of scatter may be expected at other velocities. (See Appendix D) Thus, Bjork's suggestion is essentially equivalent to Eq. (5.1)

^{*}To be published

within the experimental accuracy. Experimental scatter does not permit a choice between V^* and $\rho_p^{1/3}$ for correlation purposes, and the density dependence has been retained for the sake of simplicity.

5.4 Empirical Logarithmic Law

In this section, the fit of the experimental data to a penetration law of the form

$$\frac{P}{d} = k_1 \log_e \left(1 + \frac{\rho_t V^2}{k_2 H_t} \right) \quad (5.10)$$

is examined. Based on the discussion of Section 4.4, it may be seen that this expression (Eq. 4.58) and that of Bohn and Fuchs (Eq. 4.60) may be made to almost coincide over the experimental velocity range by suitable choice of constants, in which case serious disagreement between the two expressions would only arise at very high velocities. It is therefore to be expected that it will not be possible to choose between these two expressions on the basis of the present experimental data alone. Equation (5.10) was therefore chosen as the basis of correlation for its relative simplicity.

5.4.1 Data Fits

Individual least squares fits were obtained to the experimental data for each projectile-target material combination, fitting k_1 and k_2 in Eq. (5.10) by using a standard iteration method on a high speed digital computer. Material combinations exhibiting brittle projectile behaviour were excluded, since in these cases the penetration is not a monotonically increasing function of

velocity, and therefore could not be fitted by an expression of the type Eq. (5.10). Results together with standard mean deviations are presented in Table V.

It may be seen that the individual fits are very good, mean deviations in many cases being no larger than the scatter in the data. However the constants k_1 and k_2 vary for the different projectile target material combinations. Attempts were made to obtain correlations of k_1 and k_2 with elementary material properties. No correlating could be found with H_t or c_t , and the best correlations obtained are shown in Fig. 5.40 and 5.41 respectively on the basis of the density ratio, leading to an approximate expression of the form

$$\frac{P}{d} = (0.6 \pm 0.2) \left(\frac{\rho_p}{\rho_t} \right)^{2/3} \log_e \left\{ 1 + \frac{1}{(4 \pm 2)} \left(\frac{\rho_p}{\rho_t} \right)^{2/3} \left(\frac{\rho_t V^2}{H_t} \right) \right\} \quad (5.11)$$

It is evident that the correlation is rather poor. This is hardly surprising. The effects of projectile and target strength in the transition region, discussed in Sections 5.3.6 and 5.3.7, strongly influence k_1 and k_2 , since the fits were made using data from the entire experimental velocity range. It could therefore hardly be expected that a simple correlation with powers of elementary material properties would be obtained. Before embarking upon an attempt to correlate k_1 and k_2 with more complex functions of material properties, it would be desirable to predict reasonable forms of such functions on theoretical grounds.

When material combinations exhibiting extreme target and projectile strength effects, such as magnesium and

aluminum with copper, steel and lead, are omitted, a somewhat improved correlation for k_1 is obtained;

$$k_1 \approx (0.6 \pm 0.1) \left(\frac{\rho_p}{\rho_t} \right)^{1/2} \quad (5.12)$$

However, the correlation for k_2 is not improved.

5.4.2 Theoretical Considerations

In deriving Eq. (5.10), Section 4.4.3, the instantaneous interface pressure was taken to be $1/2 \rho_t v^2$, assuming the target to be an incompressible fluid, and the projectile to be rigid and incompressible. It might be expected that a better approximation might be obtained by assuming that the interface pressure P is related to the interface velocity v by the shock relation (Appendix D)

$$P = \rho_t v (c_t + S_t v) \quad (5.13)$$

This assumes that the conditions between the shock and interface are uniform, which would appear to be a reasonable approximation, except in the later stages of the motion, from pressure contours obtained by Bjork, Fig. 5.9 and 5.10.

Thus, assuming the retardation force on the projectile to be of the form

$$F = k_1 (P + k_2 H_t) \frac{\pi}{4} d^2 \quad (5.14)$$

integration of the equation of motion

$$-F dx = m_p v dv \quad (5.15)$$

between the limits $x = 0$, $P = P^*$, $v = V^*$; $x = p$, $P = 0$, $v = 0$ leads to

$$\frac{P}{d} \cong \frac{1}{6 k_1 S_t} \left(\frac{\rho_p}{\rho_t} \right) \log_e \left\{ 1 + \frac{P^*}{k_1 H_t} \right\} - R \quad (5.16)$$

where R depends on V^* but may be shown to become a relatively small constant at high velocities.

It is interesting to compare Eq. (5.16) with Eq. (5.11). Using the approximate expression for interface velocity, obtained in Appendix D

$$V^* \cong \frac{1}{2} \left(\frac{\rho_p}{\rho_t} \right)^{1/3} V \quad (5.17)$$

the interface pressure may be expressed as

$$P^* \cong \frac{1}{2} \left(\frac{\rho_p}{\rho_t} \right)^{1/3} \rho_t c_t V + \frac{1}{4} S_t \left(\frac{\rho_p}{\rho_t} \right)^{2/3} \rho_t V^2 \quad (5.18)$$

When $V \gg c_t$, the first term of Eq. (5.18) becomes small compared with the second, leading to an approximation for the interface pressure

$$P^* \cong \frac{1}{4} S_t \left(\frac{\rho_p}{\rho_t} \right)^{2/3} \rho_t V^2 \quad (5.19)$$

Values of S_t are all fairly close to 1.5 for the materials considered here. Thus the logarithmic term in Eq. (5.11) is a representation of that in Eq. (5.16) at extremely high velocities. At velocities comparable to the speed of sound c_t , Eq. (5.19) is a very poor approximation, in fact the first term in Eq. (5.18) becomes dominant for $V < c_t$.

Thus some of the large scatter in k_2 may be ascribed to the incorrect use of Eq. (5.19) at low velocities.

In the derivation, an implicit assumption in Eq. (5.17) is that the projectile is decelerated as a rigid body. Thus, although the interface pressure is found correctly by taking the compressibility of the materials into account, the transit times of shock and rarefaction waves across the projectile are neglected. This is probably not a bad assumption, since the waves have time to reverberate through the projectile many times during the flow period. In fact, detailed shock effects in the projectile are also smeared in Bjork's calculations.

However, the assumption implicit in the above derivation, that the projectile remains undeformed, is obviously incorrect at high velocities. X-radiographs, and Bjork's analysis show that the projectile flows so that the motion is more nearly spherically symmetric than linear.

If the projectile is assumed to expand radially as an incompressible fluid, the interface force may be represented by

$$F = k_1 (P + k_2 H_t) 2\pi x^2 \quad (5.20)$$

which, upon integration of the equation of motion Eq. (5.15) leads to the penetration law

$$\left(\frac{P}{\rho_t}\right)^3 = \frac{1}{8 k_1 S_t} \left(\frac{\rho_p}{\rho_t}\right) \log_e \left\{ 1 + \frac{\rho^*}{k_2 H_t} \right\} - R \quad (5.21)$$

where R again becomes a small constant at high velocities.

Thus, it may be expected that the penetration law will change gradually from a form approximating Eq. (5.18) at very low velocities (where R may be expected to vary with V) to a form approximating Eq. (5.21) at very high velocities.

It may be argued that since high velocity effects are of prime concern, Eq. (5.21) should be used to fit the data in the high velocity region only, disregarding the low velocity data. However, present experimental data in the high velocity region covers at most velocities varying by a factor of two. This is insufficient variation to warrant a two parameter logarithmic fit, and it has already been shown that the one parameter fit Eq. (5.1) is adequate over this velocity range.

Thus, the individual fits to Eq. (5.10) must be regarded as convenient two parameter fits over the whole experimental velocity range, without attaching too much physical significance to the form of Eq. (5.10). The fact that there is some correlation of k_1 and k_2 with density ratio must be ascribed to the fact that there is also some correlation between dynamic compressibilities and strength effects with density ratio. The correlation is bound to be rather poor, since it may be observed that some light materials such as aluminum may have high strength, while some heavy materials such as lead have very low strength. As may be expected, aluminum projectiles striking lead targets therefore show very poor correlation with other material combinations, particularly in k_1 , Fig. 5.40. Similar remarks may be made for other "anomalous" material combinations.

It would appear to be impossible to find a penetration law which would adequately cover both a wide range of materials and velocities without taking the correct geometrical, compressibility and strength effects into account. This, of course, requires a full theoretical treatment of the problem. It would therefore be appropriate at this time to carry out further theoretical work before attempting further empirical correlations.

5.4.3 Comparison with Empirical Power Law

When the material combinations exhibiting extreme projectile and target strength effects are omitted, and the value of k_1 from Eq. (5.12) is used, Eq. (5.11) becomes

$$\frac{P}{d} = (0.6 \pm 0.1) \left(\frac{\rho_p}{\rho_t} \right)^{1/2} \log_e \left\{ 1 + \frac{1}{4 \pm 2} \left(\frac{\rho_p}{\rho_t} \right)^{2/3} \left(\frac{\rho_t V^2}{H_t} \right) \right\} \quad (5.22)$$

It has been shown that the function $y = k \log_e (1+x^2)$ may be approximated by the function $y = kx^{2/3}$ over the range $2.7 < x < 5$. (Fig. 4.2) Thus Eq. (5.22) above may be approximated in the high velocity region by

$$\frac{P}{d} = (0.6 \pm 0.1) \left(\frac{\rho_p}{\rho_t} \right)^{1/2} \left\{ \frac{1}{4 \pm 2} \left(\frac{\rho_p}{\rho_t} \right)^{2/3} \left(\frac{\rho_t V^2}{H_t} \right) \right\}^{1/3}$$

or

$$\frac{P}{d} = (0.4 \pm 0.2) \left(\frac{\rho_p}{\rho_t} \right)^{0.72} \left(\frac{\rho_t V^2}{H_t} \right)^{1/3} \quad (5.23)$$

which may be compared with Eq. (5.1). Comparisons for individual material combinations over appropriate velocity ranges, using correct values of k_1 and k_2 in Eq. (5.10) from Table IV are generally even better, since both Eq. (5.1) and (5.10) are good fits to the high velocity data.

Although Eq. (5.11) or Eq. (5.22) are very approximate due to the poor correlation of k_1 and k_2 with material properties, the individual fits to Eq. (5.10) with constants from Table V are very good, and may therefore serve as very useful empirical expressions suitable for interpolation and prediction purposes over the whole experimental velocity range.

5.5 Extrapolation of Empirical Penetration Laws

Since there is great interest in penetration effects at velocities higher than those investigated experimentally, it is interesting to investigate the consequences of extrapolating the empirical penetration laws, Eq. (5.1) and Eq. (5.10) Table IV, to higher velocities.

Figure 5.42 shows experimental data and penetrations predicted by Eq. (5.1) and Eq. (5.10) for aluminum projectiles and targets. Original constants found from the individual least squares fit to $p/d = kV^{2/3}$, using only points in the high velocity region, were used. For the logarithmic penetration law, values of constants k_1 and k_2 found by individual least squares fits, and listed in Table V, were used. Logarithmic scales were used to accommodate a large velocity variation. Also shown are the three points obtained theoretically by Bjork¹²⁸. It should be noted that Bjork's definition of equivalent diameter has been retained. Definition of equivalent diameter on the basis of equivalent mass

would reduce the penetration predicted by Bjork by 16 per cent.

Firstly, it might be noted that both penetration laws are good fits to the experimental data in a limited velocity range. This velocity range will now be defined as the high velocity region.

Secondly, it may be seen that the predictions of penetration by the two penetration laws diverge at higher velocities. The logarithmic law predicts lower penetrations, and over a wide range of high velocities may be approximated by a law of the type $p/d = kV^{1/3}$. This velocity range will now be defined as the hypervelocity region.

It may be seen that the logarithmic law shows surprising agreement with the theoretical points, computed by Bjork. From Fig. 5.42, it is seen that the curve fitted to the soft 1100F aluminum data points fits Bjork's points almost exactly. In view of the fact that the logarithmic penetration law has limited physical significance, this agreement may be fortuitous. It may be noted that the curve fits Bjork's points better than an expression of the form $p/d = kV^{1/3}$.

Furthermore it may be seen that the logarithmic law for the much harder 2024-T3 aluminum alloy predicts lower penetrations than Bjork's analysis, the offset decreasing with increasing velocity. (This is still true on a linear scale). This behaviour is exactly what might be expected for a high strength target.

Figure 5.43 is similar to Fig. 5.42, but for steel projectiles and targets. In this case, agreement is not

quite as good. The fits to the logarithmic penetration law were obtained from points limited to quite low velocities. The steel targets had high strengths, thus all of the data used for the fits were in the transition region influenced by projectile and target strength. The transition region strength effects tend to reduce penetration, the effect being greatest at low velocities. Thus, the tendency will be to increase the initial slope, and increase the curvature, of the empirical fit. The two effects partially offset one another as may be seen from Fig. 5.43. Agreement of the logarithmic law with Bjork's points is better at 5.5 and 72 km/sec, than at 20 km/sec. Actually, one would expect that the penetration should be less than that computed by Bjork, even at 72 km/sec, particularly for the very hard 30 RC steel alloy. This extrapolation of the logarithmic fits in this case cannot be considered to be realistic.

The same effects are of course present in the logarithmic fits for the 1100F and 2024-T3 aluminum alloys, Fig. 5.42. Due to the low hardness of the 1100F alloy, and the wide velocity range in the experimental data, relatively much greater reliance may be placed on an extrapolation for this material and the agreement with Bjork's calculations may be considered to have some significance. The extrapolation for the 2024-T4 alloy however must be considered suspect, because, although data to quite high velocities is included, the transition region also extends to quite high velocities, and transition region strength effects have fairly strong influence on the fit.

5.6 Definition of Regions of Impact

Based upon the information in the previous sections, it is possible to postulate regions of impact within which certain types of behaviour may be expected. Since definition of the last two regions is necessarily based on the logarithmic penetration law (Eq. 5.10), which has no firm theoretical basis, this section is somewhat hypothetical. Nevertheless, the behaviour should be qualitatively as described. Quantitative definitions of the limits of the regions may be refined as more data becomes available at high velocities.

5.6.1 Low Velocity Region

This region is only important for projectiles which have higher strength than the target, and therefore suffer little or no deformation at low velocity. The region is of no interest in the present study, and will not be considered here. The upper limit of the region may be expected to be related to the ratio of the maximum stress induced in the projectile P^* , and the strength of the projectile, represented by H_p , but it is likely that the projectile shape will be important in producing stress concentrations leading to fracture of brittle projectile materials.

5.6.2 Transition Region

Within the transition region, the effects of target and projectile strength are dominant in determining crater shape and penetration depth. These effects have been discussed in Section 5.3.6. If attempts are made to fit the penetration in this region by a power law,

the velocity exponent varies rapidly from 2 at very low velocities down to 2/3 at the high velocity end of the region. Data for "ductile" projectiles, which show a monotonic increase in penetration with velocity, may be fitted empirically by a two parameter logarithmic fit Eq. (5.10). This is not necessarily physically significant.

The region extends from the velocity at which the projectile suffers serious deformation to a velocity such that

$$\frac{P^*}{H_t} = 30$$

or if $H_p > H_t$ (5.4)

$$\frac{P^*}{H_p} = 30$$

(See Section 5.3.6) i.e. a velocity at which the initial interface pressure is much greater than the yield strength of both the projectile and target.

5.6.3 High Velocity Region

Within this region, strength effects are no longer dominant, but are still not negligible.

Crater shapes approach hemispheres, but strength effects are sufficient to cause craters formed by low or high density projectiles, compared to the target density, to be shallower or deeper than hemispheres respectively. Cratering efficiency V_c/E is approximately constant within this region.

Within this region, the logarithmic penetration

law

$$\frac{P}{d} = k_1 K^{1/2} \log_e \left(1 + \frac{K^{1/2} B}{k_2} \right) \quad (5.23)$$

where $K = \rho_p / \rho_t$ is the density ratio and $B = \rho_t V^2 / H_t$ is the Best Number, may be approximated by

$$\frac{P}{d} = k K^{2/3} B^{1/3} \quad (5.24)$$

or Eq. (5.1). The two equations may be seen to be equivalent roughly between the limits

$$7.5 < \frac{K^{1/2} B}{k_2} < 36 \quad (5.25)$$

from Fig. 4.2. Particularly for high strength projectiles, the limit Eq. (5.4) may occur at a higher velocity than Eq. (5.25) above and Eq. (5.4) should therefore be used as the lower velocity limit.

5.6.4 Hypervelocity Region

Within this region, the strength effects are negligible, and Bjork's theory may be expected to be valid. Craters may be expected to be hemispheres. Within this region, the logarithmic penetration law may be approximated by

$$\frac{P}{d} = k K^{1/2} B^{1/6} \quad (5.26)$$

i.e. the penetration is approximately proportional to $V^{1/3}$. From Fig. 4.2 the approximate limits of the approximation are

$$64 < \frac{K^{1/2} B}{k_2} < 3600 \quad (5.27)$$

However, additional effects not considered previously may enter strongly into this region. In particular, target melting may become important. It is difficult to assess the magnitude of this effect at the present time, but it may be expected to lead to an increase in penetration and crater size. Thus, the above remarks concerning the hypervelocity region must be considered speculative at this time.

The Best Number may be seen to have the meaning of the ratio of a pressure ($\rho_t v^2$) to material strength (H_t). It can be seen that at extremely high velocities $\kappa^{2/3} \rho_t v^2 / k_2$ approximates the initial interface pressure P^* for typical values of k_2 given in Table IV. (See Section 5.4.3) It may be preferable to define a non-dimensional parameter P^*/H_t and find least squares fits to Eq. (5.16)

$$\frac{P}{d} = k_1 \log_e \left(1 + \frac{P^*}{k_2 H_t} \right) \quad (5.28)$$

This would permit redefinition of the limits of the regions of impact Eq. (5.25) and (5.26) in terms of P^*/H_t , which will be preferable from the point of view of physical interpretation.

5.7 Discussion

A quite detailed qualitative understanding of cratering has been gained from experimental studies using X-ray and high speed optical photography and other active measuring techniques, and from detailed theoretical analyses such as that carried out by Bjork¹²⁸. When data from a large variety of material combinations and over a wide velocity range

are assembled and compared, the effects of the complicated phenomena accompanying penetration on the crater depth and shape can be seen.

It is not surprising that simplified theories, presented previously, are unsuccessful, since in each case they neglect many phenomena important to the cratering process.

Even Bjork's theory, which correctly takes geometrical and compressibility effects into account, cannot be considered to be realistic in the high velocity region, except for low strength alloys, since the shear strength of the materials is neglected. The velocity region, in which strength effects are in fact negligible, is evidently much higher than previously supposed.

It is also not surprising that so much confusion and contradiction exists among previous empirical fits derived from limited sections of the data, covering different limited ranges in material properties and velocities, since nearly all of the experimental data lies in the transition region where strength effects lead to such complex behaviour, and even the limited amount of data in the high velocity region is affected by material strength to some extent.

Two empirical penetration laws have been derived in this study which are more generally applicable than previous empirical expressions. Each is strictly limited in the range of parameters covered, and in physical significance. This is a property generally associated with empirical expressions.

The empirical power law

$$\frac{P}{A} = (0.35 \pm 0.07) K^{2/3} B^{1/3} \quad (5.28)$$

where $K = \rho_p / \rho_t$ is the density ratio and $B = \rho_t V^2 / H_t$ is the Best Number, is limited to the high velocity region defined in Section 5.4.4.

On the other hand, the empirical logarithmic law

$$\frac{P}{A} = k_1 \log_e \left\{ 1 + \frac{B}{k_2} \right\} \quad (5.29)$$

with constants k_1 and k_2 tabulated in Table V may be expected to fit only those material combinations for which k_1 and k_2 are determined empirically, but over the entire experimental velocity range. The approximate equivalence of Eq. (5.28) and Eq. (5.29) where their ranges of validity coincide, has been demonstrated in Section 5.4.3 and 5.5.

Extrapolation of the empirical penetration laws Eq. (5.28) and (5.29), either to other materials or to higher velocities, has little theoretical or other justification.

In particular there is no justification whatever for extrapolating the empirical power law Eq. (5.28) to higher velocities. The argument has been advanced that the cratering efficiency V_c/E will remain constant as the velocity increases. This in effect implies that the partition of energy in the various modes such as heating, energy transmitted to other parts of the target by the stress wave system, kinetic energy carried away by the material thrown out of the crater, and energy dissipated in plastic deformation, remains constant. Such an assumption cannot be substantiated either

from experimental evidence, or from theoretical considerations, at the present time.

It appears to be fortuitous that the transition region strength effects act in such a way as to partially cancel each other, so that even in the case of high strength steel targets the extrapolated logarithmic law Eq. (5.29) shows reasonable agreement with the results of Bjork's calculation, up to 72 km/sec., Fig. 5.43. Bjork's theory may be expected to provide an upper limit to the penetration, since strength effects neglected in the theory, but operative in the high velocity region, may be expected to reduce penetration. Thus the logarithmic law Eq. (5.29) may be expected to overestimate penetration at velocities below 72 km/sec, and to underestimate penetration above 72 km/sec, for the particular steels investigated. No general conclusions about extrapolations for other materials can be drawn, and in fact some other materials may well behave in such a manner as to lead to very large errors when Eq. (5.29) is extrapolated to high velocities.

Extrapolations can only be carried out with some confidence, when the penetration law is based on sound theoretical grounds, and there is some assurance that phenomena neglected in the theory do not become operative at higher velocities.

The comparative success of the two penetration laws Eq. (5.24) and (5.25), based on elementary material properties, must be ascribed to the fact that there exists a rough correlation between dynamic compressibilities and strength properties, and static properties.

A penetration law to cover both a wide range in material properties and velocities necessarily involves a much more complex functional dependence of penetration on material properties than Eq. (5.28) and (5.29). It appears to be a hopeless task to deduce such a functional dependence from the present penetration data, both because the present data has large uncertainties associated with it, and because the data covers insufficient variation in material combinations and velocities. In particular, very few material combinations have been investigated in the high velocity region.

It seems appropriate therefore that further theoretical work be undertaken in order to guide the formulation of more realistic penetration laws. The understanding of the penetration process, provided by Bjork's analysis cannot be underestimated. It is to be strongly urged that theoretical work be directed towards extending an analysis of the type used by Bjork to include shear strength of the target and projectile. Since melting may become extensive at very high velocities, and will have the effect of reducing the shear strength, this should also be considered.

Such an analysis will provide quantitative information about the various strength effects operative in both the transition and high velocity regions, and thus aid in interpretation of experimental results and guide formulation of realistic penetration laws. Furthermore, such an analysis will provide a more rational basis for extrapolation to velocities higher than those which may be investigated experimentally.

SECTION VI

OTHER PROJECTILE-TARGET CONFIGURATIONS

6.1 Microparticle Impact

Although penetration appears to scale quite well with projectile size over the range of projectile sizes conveniently fired in guns, or by cavity charge techniques, there is a question if this scaling holds true for very small projectiles, approaching the size of the grain structure.

While several laboratories have been actively engaged in developing projection techniques for microparticles only three groups have reported cratering results by projectiles under 200 micron diameter. Anderson et al^{60,62} at Stanford Research Institute projected 100 - 150 micron stainless steel spheres at velocities up to 12,500 ft/sec. against a variety of targets. The particles were individually projected by cylindrical high explosive charges. (Fig. 6.1) Friichtenicht et al⁵⁶ at Ramo Wooldridge used an electrostatic acceleration technique to project 1 - 10 micron carbonyl iron particles at velocities up to 6000 ft/sec against lead targets. (Fig. 6.2) Gehring et al^{2,8,10} at Ballistics Research Laboratory used a specially designed shaped charge with cast iron liner to project a cloud of particles of 50 to 200 micron size, a special shutter being used to allow only particles with a velocity in the region of about 32,000 ft/sec to reach the target. The size

distribution of resultant craters (about 500 per target) was then correlated with the size distribution of particles obtained by crushing a similar cast iron liner with pestle and mortar. Although several target materials were used, only crater dimensions for lead and copper targets have been reported at this time. Crater diameters were measured. However, based on Gehring's observation that the craters were nearly hemispherical, corresponding penetrations are plotted in Fig. 6.3.

The microparticle results show a large scatter, associated partly with the experimental difficulties of accurately measuring projectile and crater sizes and projectile velocity. However some scatter is probably due to the effect of grain boundaries and local anisotropies in the target material. Gehring⁸ has shown contours of craters produced in coarse grained copper and copper single crystals by 200 micron cast iron projectiles. The penetration apparently is affected to some extent by grain orientation, and the presence of grain boundaries. Anderson⁶⁰ has observed similar effects.

On each of Fig. 6.1 to 6.3 curves representing Charters and Locke's²⁸ empirical expression

$$\frac{P}{d} = 2.78 \left(\frac{\rho_p}{\rho_t} \right)^{2/3} \left(\frac{V}{C_t} \right)^{2/3}$$

have been inserted. This expression adequately fits penetration data in lead and copper targets for large projectiles in the velocity range of interest here. The microparticles results lie consistently below the empirical curve. However, the discrepancy is probably mainly due to the fact that all of the

microparticle craters were measured to the top of the projectile material remaining in the crater (except Gehring's results, in which crater diameters were measured). Anderson's results further may be affected by mass lost by the particles during explosive acceleration and subsequent ablation.

One may conclude that within the present large experimental uncertainty it is impossible to distinguish if microparticle cratering follows a different penetration law.

6.2 Oblique Impact

Cratering due to projectiles approaching the target at oblique incidence is of great practical interest. However, oblique impact has received relatively little attention.

In the high velocity region, in which nearly hemispherical craters are formed in normal impact, several experimenters have noted that nearly hemispherical craters are also formed in oblique impact up to some critical angle. (Fig. 6.4) Beyond the critical angle, the crater becomes asymmetrical, with greater depth and steeper sides towards the direction from which the projectile approached. At grazing incidence, the crater becomes very elongated, and it has been noted that the projectile ricochets, and is capable of producing further craters in adjacent targets. Spray patterns, Fig. 6.5, and shock patterns, Fig. 6.6, also show symmetry below the critical velocity, asymmetry above. The critical velocity is clearly a function of velocity. Fig. 6.7 shows craters in lead produced by steel projectiles. At 7,000 ft/sec, a symmetrical crater

is formed at 30° incidence, but not at 60° incidence. An increase in velocity to 9800 ft/sec however results in a symmetrical crater at 60° incidence. No systematic experiments have been carried out to determine the dependence of the critical angle of incidence on velocity for various materials.

Data on cratering has been reported by Summers³⁰ for copper projectiles impacting copper targets at 7,000 and 11,000 ft/sec., (Fig. 6.8), and by Kineke⁵, (Fig. 6.9), for steel discs impacting lead targets at 16,400 ft/sec. Both experimenters noted that the data for oblique impact compared very well with that for normal impact, if penetration versus the normal component of velocity is plotted. The oblique impact data departs from the normal impact data at about the same critical angle at which the crater ceases to be hemispherical.

Anderson⁶², (Fig. 6.10), also report microparticle cratering data at oblique angles. The scatter is such that it is not possible to determine if the 60° and 30° incidence data departs from the normal incidence data when plotted on the basis of normal component of velocity.

In the high velocity region (Sect. 5.1) it has already been noted that crater volume is approximately proportional to projectile energy at normal incidence. Thus, below the critical angle one might expect that crater volume would be proportional to the normal component of projectile energy. However Bryan¹⁵³ has noted that the ratio of crater volume to projectile energy appears to be a linear function of $\cos \phi$, i.e.,

$$\frac{V_c}{E} = a \cos \phi + b \quad (6.1)$$

to angles beyond the critical angle. (Fig. 6.11)

Bryan¹³⁶ has also given a simplified theory for predicting the ratio of major to minor diameter of the crater mouth for angles of incidence beyond the critical angles. It is assumed that the projectile simply generates a spherical hole concentric with itself, which expands at constant velocity V_r . Choosing moving co-ordinates such that the projectile approaches the target vertically at velocity $V \cos \phi$, and the target moves laterally at velocity $V_s = V \sin \phi$, the crater will cease to be spherical when $V_s > V_r$. The ratio of major to minor axis is then simply

$$\beta = \frac{V_s + V_r}{2 V_r}$$

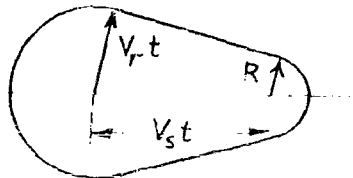
Assuming $V_r = k V \cos \phi$

$$\beta = \frac{1}{2} \left(\frac{\tan \phi}{k} + 1 \right) \quad (6.2)$$

and the critical angle at which the crater begins to elongate is (at $\beta = 1$)

$$k = \tan \phi_0 \quad (6.3)$$

A refinement was introduced to allow for the finite size of the projectile, of radius R , which by similar reasoning results in the equation



$$\beta = \frac{1}{2} \left(\frac{\tan \phi}{k} - 1 \right) + \frac{R}{D_{cm}} \left(\frac{\tan \phi}{k} - 1 \right) \quad (6.4)$$

where D_{cm} is the minor diameter of the final crater. The value of ϕ_0 must be supplied by experiment.

The theoretical curves for both cases are plotted in Fig. 6.12. Shown also are experimental points obtained by Kineke.⁵ Each point represents an average of 10 firings using 1/2 inch diameter by 0.040 inch thick steel discs accelerated by air cavity charges to 16,400 ft/sec, the angle of incidence being varied from 0° to 69° . The value of the critical angle used in the experiments was obtained from Kineke's experimental data. The projectiles spalled during acceleration, and a diameter of 0.3 inches was used in the theory. The experimental points lie between the curves neglecting the projectile size, and taking the projectile size into account. Since the projectiles tumbled in flight, and the attitude at the time of impact was not known, such scatter may be expected, and the agreement is therefore quite encouraging.

6.3 Rod Impact

Relatively little experimental work has been done with projectiles of length to diameter ratios much greater than unity, despite the evident advantage for offensive systems. Figure 6.13 graphically illustrates the greatly increased penetration per unit mass obtained by rods (moving in the direction of the longitudinal axis) as compared to

penetration obtained by spheres and cylinders of unit length/diameter ratio. Unfortunately direct comparison of penetration in the two cases is uncertain since different aluminum alloys were used as targets, and rod velocities were rather low.

No systematic study of penetration as a function of length/diameter ratio has been carried out, and, in fact, at this time, results of only three studies have been published. Summers and Niehaus³¹ used rods of L/d between 6 and 10 at velocities up to 10,000 ft/sec. against lead, copper and steel targets. Allen and Rogers⁴⁸ used rods of L/d between 6 and 12 at velocities up to 10,000 ft/sec against 7075-T6 aluminum, and Slattery and Clay²³ used rods of L/d between 8 and 15 at a constant velocity of 8,500 ft/sec against aluminum. Results are plotted in Fig. 6.14 through 6.20.

The phenomena accompanying rod impact differ somewhat from those accompanying impact of projectiles of about unit L/d ratio. It may be expected that the shock propagating upwards into the projectile is rapidly attenuated by rarefactions from the unsupported sides of the rod, which lead to rapid lateral flow of rod material. Thus the disturbance travelling back into the rod would be expected to move at sonic velocity. Two types of behaviour may then be expected according to whether the disturbance is carried above the original target surface, i.e. the impact velocity is below sonic velocity, or the disturbance is carried below the original target surface, i.e. supersonic impact velocity. In the latter case, the flow after an initial transient period may be expected to be almost pseudo-stationary until

all of the rod material has been reached by the disturbance. There would then be a final transient period during which the projectile and target material move under the action of inertial forces, resisted in the latter stages by the strength of the material involved.

The difference between rod and compact projectile behaviour therefore lies principally in the existence of the intermediate pseudo-steady flow period at supersonic velocities, which is absent in the case compact projectiles. (See Section 5.1)

Slattery²³ has noted different crater shapes, depending on whether the impact velocity was above or below the sonic velocity in the projectile. Subsonic velocities were observed to lead to cone shaped craters, while supersonic velocities lead to cylindrical craters. Such behaviour may be expected, since in the subsonic case, the disturbance reaches the back end of the rod and is able to decelerate the rod. The latter part of the penetration process then occurs at lower velocity. Hence lower lateral velocities are induced, and less expansion of the crater may be expected. Figure 6.21 shows a crater in which the impact velocity was so low that the rod was decelerated to a velocity where material strength halted the flow before gross deformation of the back end of the rod occurred.

Allen and Rogers⁴⁸ attempted to use shaped charge jet theory, (Section 3.2) essentially fitting their data to Eq. (3.34) by suitable choice of the constant $k = 1/2 \rho_p v_o^2$. The semi-empirical curves are inserted in Fig. 6.14 and 6.15. The value of the constant k was found to compare well with expected yield strength of the 7075-T6 aluminum alloy under

dynamic conditions.

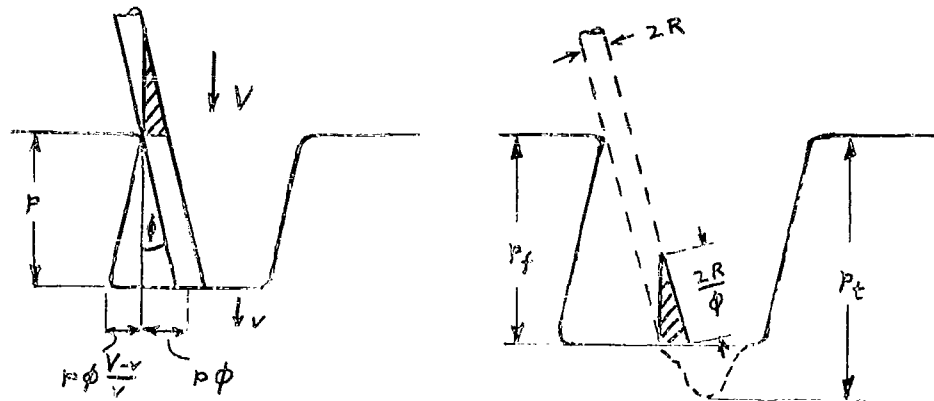
In the case of gold rods, the penetration was found to exceed the predicted values at the higher velocities. It was found that the assumed residual velocity of the projectile, $(2v - V)$ where v is the calculated velocity of the target-projectile interface, was greater than v_0 , the velocity below which no penetration occurs due to target strength. Thus it was assumed that secondary penetration was caused by the projectile material, of magnitude predicted by shaped charge jet theory, Eq. (3.34), with initial projectile velocity taken as $(2v - V)$. Results of this calculation are inserted on Fig. 6.15.

On the other hand the data of Summers and Niehaus³¹ in all cases lie well above semi-theoretical curves derived in the same manner, and in fact, at the higher velocities, lie well above the penetration predicted by simple jet theory $p/L \approx \sqrt{\rho_p/\rho_t}$ which sets an upper limit to Eq. (3.34). See Fig. 6.17 to 6.19. Secondary penetration which is only possible at these velocities in the case of tungsten carbide into copper, Fig. 6.18, and tungsten carbide into lead, Fig. 6.19, is insufficient to account for the large discrepancies. Thus it is premature at this point to place reliance on jet theory. Figure 6.20 indicates that there is little correlation on the basis of density ratio at a constant velocity of 8,500 ft/sec when the results of Allen⁴⁸ and Slattery²³ are compared.

Both Allen and Rogers⁴⁸ and Slattery and Clay²³ observed that the penetration of rods was affected very little by the angle of obliquity of the target, provided the rod remained unyawed (i.e. moved in the direction of

its axis). However Slattery and Clay* have shown that the penetration is critically dependent on the angle of yaw. Figure 6.22 shows a typical crater produced by a yawed rod in aluminum. The section was taken in the plane of the yawed rod. At right angles of this section the crater is two or three times the rod diameter in width, and is thus a narrow elongated slot.

Slattery and Clay* have suggested a simplified explanation for the crater shape



The total length of the rod does not contribute to the penetration. The crater expands radially, and thus is inclined as shown. When the rod has penetrated to a depth such that the rod intersects the crater lip, it is assumed that primary penetration ceases. The remainder of the rod then presumably continues to excavate material from the intersected side of the crater. The length of rod active in primary penetration depends on the radius of the crater. The following assumptions

* Private Communication

were made to estimate this radius

- a) the interface moves at constant velocity v .
- b) the crater on any plane parallel to the surface is cylindrical of radius r , centred at the point at which the rod penetrated the plane.
- c) the volume of the crater is proportional to the kinetic energy of the rod.

For these assumptions the radius of the crater r will be given by the equation

$$\frac{1}{2} \pi R^2 \rho_p (V-v) V^2 = K_t \pi r^2 V \quad (6.5)$$

where R is the radius of the rod, and K_t is the energy volume ratio E/V_c found for compact particle impact. Values given by Feldman ($2.6 H_t$) were used, but results have also been computed using K_t found in Section 5.3. ($3.06 (\rho_t/\rho_p)^{2/3} H_t$)

If the interference occurs at a depth p , then the portion of the rod already in the crater will continue to penetrate. The final depth of the crater is then

$$p_f = p \left(1 + \frac{v}{V-v} \right) \quad (6.6)$$

Further for a constant yaw angle ϕ , from the diagram

$$\phi p \left(1 - \frac{V-v}{v} \right) = r - R \quad (6.7)$$

which using Eq. (6.5) and (6.6) becomes

$$P_f = \frac{R}{\phi} \frac{v}{V-v} \left\{ V \sqrt{\frac{P_f}{2K_t} \frac{V-v}{v}} - 1 \right\} \quad (6.8)$$

In normal impact

$$\frac{P}{L} = \frac{v}{V-v} \quad (6.9)$$

so that Eq. (6.8) may be evaluated using empirical values of p/L found in normal impact experiments.

The crater shows a residual penetration, Fig. 6.22, assumed to be due to the cross hatched part of the rod in the diagram above, of length $2R/\phi$. This is assumed to lead to an added penetration

$$P_r = \frac{2R}{\phi} \frac{v}{V-v} \quad (6.10)$$

so that the total penetration is $P_t = P_f + P_r$. A comparison of measured penetrations and penetrations calculated on the basis of Feldman's K_t and that given in Section 5.3 are shown in the table below. Values of p/L for normal impact have been taken from Ref. 23.

Yaw	Calculated (Feldman)		Calculated (Sect. 5.3)		Measured		Rod Material
	P _t	P _f	P _t	P _f	P _t	P _f	
$\phi = 4^\circ$	0.469	0.217	0.600	0.277	0.344	0.125	Lead
6 ^o	0.312	0.145	0.400	0.185	0.250	0.156	
10 ^o	0.188	0.087	0.240	0.112	0.187	0.152	
$\phi = 3^\circ$	0.573	0.229	0.631	0.252	0.500	--	Copper
6 ^o	0.287	0.115	0.316	0.127	0.250	0.125	
10 ^o	0.173	0.069	0.190	0.076	0.156	0.120	

Penetration Depths in Inches

6.4 Finite Thickness Targets

Cratering and penetration of thin targets by high velocity projectiles has not received as much attention to date as cratering in quasi-infinite targets. While a number of studies have been reported, none of these are directly comparable since different experimental conditions were used. However, sufficient work has been done to distinguish some important phenomena in thin target cratering.

6.4.1 Relatively Thick Targets

Cratering in relatively thick targets which are not completely penetrated may give rise to damage at the rear surface of the target plate. (Fig. 6.23.) This damage may range from the appearance of a zone of slipped and deformed grains near the rear surface opposite the crater³⁴ to the appearance of internal cracks and bulging of the rear surface, to complete detachment of a segment of target material, termed spall¹². The damage is undoubtedly due to the reflection and interaction at the rear surface of the wave propagated into the target. Maiden et al¹² report spall thickness as a function target thickness at constant projectile velocity and as a function of projectile velocity at constant target thickness for steel targets at velocities up to 13,000 ft/sec.

The presence of damage at the rear surface generally is accompanied by a greater crater depth than in a corresponding quasi-infinite target. Kinard et al³⁴ have reported a study of the effect of target thickness on penetration of steel and aluminum projectiles into aluminum targets

at impact velocities between 5,000 and 13,000 ft/sec. They conclude that for the velocities used in their study, the penetration is affected by target thickness provided that the penetration is greater than 20 percent of the target thickness. It was found that a projectile could completely penetrate a target whose thickness is approximately one and one half times as great as the penetration of a similar projectile into a quasi-infinite target. Some results of this study are plotted in Fig. 6.24.

6.4.2 Thin Targets

Thinner targets which are completely penetrated exhibit different behaviour depending on the projectile velocity, target thickness, and materials involved.

At relatively low velocity, penetration is accomplished by modes familiar in armor penetration work. The resultant hole is nearly the same size as the projectile, which suffers very little deformation in the penetration process.⁷⁵ As the impact velocity increases, the projectile suffers increasingly severe damage; plastic deformation and "mushrooming" if ductile, or small pieces being spalled from the projectile if brittle. The resultant hole in the target plate consequently becomes appreciably larger than the original diameter of the projectile, and may become conical, increasing in diameter towards the rear surface as the projectile continues to mushroom, or spall during the penetration process.⁷⁵ As the impact velocity increases, more severe breakup or flow of the projectile is observed with consequent further enlargement of the target

hole, until at relatively high velocities, both target material and projectile material are ejected from the rear of the target in a spray of small particles distributed over a solid angle of 90 degrees or more, with a considerable amount of material also being ejected from the front of the target plate^{39,24}. The resultant hole in the target plate is typically several times the diameter of the original projectile. These effects are illustrated in Fig. 6.25 and 6.26 by frames from high speed framing camera records of the penetration process.

These phenomena are evidently analogous to those occurring in semi-infinite targets and have led several investigators to distinguish similar regions of impact, namely; low velocity region (undeformed projectile, armor penetration); transition region; and high velocity region, (hypervelocity or fluid impact region). Several different types of experiments have been carried out, as illustrated in Fig. 1.1 d, e, f. Each of these will be briefly discussed.

6.4.3 Complete Penetration of a Single Thin Target

Several extensive studies have been carried out involving complete penetration of a single thin target in the armor penetration region where the projectile is relatively undeformed. Of prime concern are the kinetic energy lost by the projectile during penetration and threshold velocities corresponding to certain confidence levels that the target will be just penetrated, (i.e. probability of penetration 0, 1 or 0.5, the velocity corresponding to the latter being known as the ballistic limit). This type of study is not considered here.

A preliminary study of hole diameters and spray particle distributions for single thin targets penetrated in the high velocity region have been reported at BRL⁵³ at 11,100 and 16,500 ft/sec. Results of hole diameters as a function of target thickness are replotted in Fig. 6.27.

A statistical study of hole diameters produced in thin Mylar and Testar foils by cast iron particles of less than 100 micron size at about 36,000 ft/sec has been reported by Richards and Gehring¹¹.

6.4.4 Thin Shield

Three studies of penetration in a semi-infinite target protected by a thin shield located some distance in front of the target have been reported. Olshaker²⁴ studied lead targets and shields impacted by lead and steel projectiles at about 8,000 ft/sec. Funkhauser³⁹ studied aluminum targets and shields impacted by copper projectiles at velocities ranging from 1,000 to 12,500 ft/sec. Wallace et al²² studied aluminum targets with a variety of shield and projectile materials at velocities up to about 17,000 ft/sec. Unfortunately the data for the latter study was not made available for comparison with the other two studies. Some results of the first two studies are plotted in Figs. 6.28, to 6.30.

6.4.5 Multiple Thin Targets

A number of studies of penetration of multiple spaced targets have been reported. Some of the early studies have been largely qualitative. Nysmith and Summers³³ fired glass spheres at aluminum plates, varying the number of

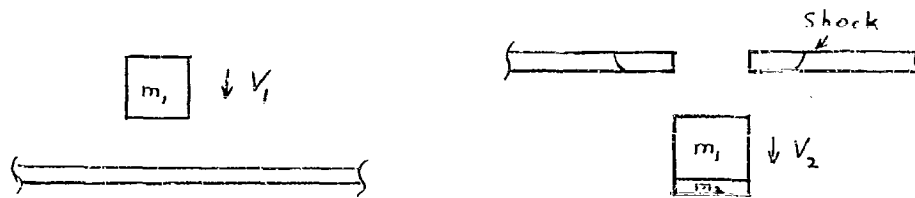
plates and plate thickness such that the total thickness of the combined plates remained constant. They found the threshold velocity to just penetrate all of the plates for each configuration, (Fig. 6.31). Halperson and Fuller⁵³ found the total number of 1/16 inch thick aluminum plates spaced 4 inches apart penetrated by 1/4 inch steel spheres as a function of velocity, (Fig. 6.32). Projectile breakup is indicated by a reduction in the number of plates penetrated as the velocity increases.

6.4.6 Thin Target Theory

The numerical solution of Bjork (Section 3.2.1) is equally applicable to thin targets as to quasi-infinite targets. All that is required is the addition of a new boundary condition, specifying the rear surface of the target. While several such cases have been computed, published results were not received for inclusion in this study.

A simplified theory for the angle of spray produced by the impact of a very high velocity projectile on a thin shield has been given by Lull¹⁰²

The projectile is assumed to punch out a section of target plate of area equal to the presented area of the projectile. Shortly after impact, the projectile and punched out section of target plate are assumed to have moved out of contact with the remaining target, and no further interaction with the remaining target is expected. At this point the only



part of the remaining target which has been affected by the impact is that behind the shock wave proceeding from the edges of the hole. Any enlargement of the hole, spall or lip formation must be a result of energy stored behind the shock. For a thin plate this energy is assumed to be negligible compared to the energy contained in the projectile and punched out segment of target.

The momentum balance then gives

$$m_1 V_1 = (m_1 + m_2) V_2 \quad (6.11)$$

The energy balance gives

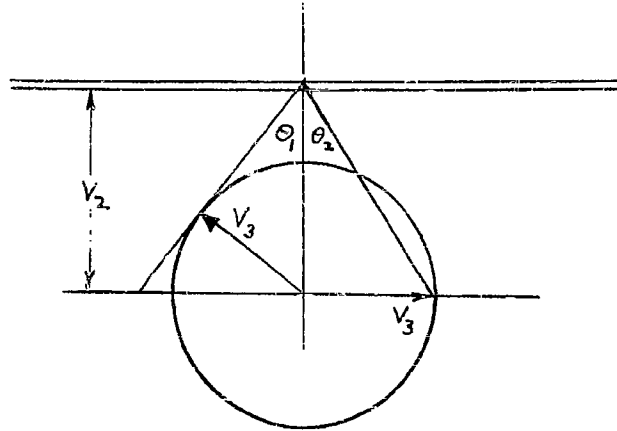
$$\frac{1}{2} m_1 V_1^2 = \frac{1}{2} (m_1 + m_2) V_2^2 + \Delta E \quad (6.12)$$

where ΔE is the increase in internal energy of the projectile and target segment. Thus

$$\Delta E = \frac{1}{2} \frac{m_1 m_2}{m_1 + m_2} V_1^2 \quad (6.13)$$

The projectile and target segment are assumed to shatter, and all of the increase in internal energy is assumed to go into acceleration of the material in a radial

direction. The projectile and shield material are therefore assumed to be distributed throughout an expanding sphere of radius R , the center of gravity of which is moving at velocity V_2 . The kinetic energy due to radial expansion of an element of the sphere is



$$\frac{1}{2} m v^2, dm = \frac{1}{2} \frac{V_3^2}{R^2} 4\pi \rho r^4 dr$$

where V_3 is the radial velocity at the surface. Hence

$$\Delta E = \frac{1}{2} \frac{V_3^2}{R^2} 4\pi \rho \int_0^R r^4 dr \quad (6.14)$$

Noting that the mass of the sphere is

$$m_1 + m_2 = \frac{4}{3} \pi R^3 \rho \quad (6.15)$$

$$\Delta E = \frac{3}{10} (m_1 + m_2) V_3^2$$

Thus from Eq. 6.13

$$V_3 = \sqrt{\frac{5}{3}} \frac{\sqrt{m_1 m_2}}{m_1 + m_2} V_1 \quad (6.16)$$

The leading hemisphere of material is moving at higher velocity than the trailing hemisphere, and contains most of the kinetic energy. It would intersect a circular area on a second target plate subtending a half angle θ_2 at the shield

$$\theta_2 = \arctan \frac{V_3}{V_2} = \arctan \sqrt{\frac{5}{3} \frac{m_2}{m_1}} \quad (6.17)$$

The trailing hemisphere would affect a larger area of target, but may be expected to produce relatively less damage since it contains less energy. The circular area intersected by the trailing hemisphere subtends a half angle θ_1 at the shield

$$\theta_1 = \arcsin \frac{V_3}{V_2} = \arcsin \sqrt{\frac{5}{3} \frac{m_2}{m_1}} \quad (6.18)$$

These are inserted in Fig. 6.30 for comparison with experimental data.

6.4.7 Discussion

None of the studies reported to date are directly comparable. The data is far too scanty to allow an attempted correlation. Some qualitative remarks may however be made.

Projectile breakup is indicated by a drop in total penetration in a given projectile-target configuration as the velocity is increased. Similarly a relatively sharp drop in total penetration occurs as the plate thickness is increased at constant velocity, indicating projectile breakup. Thus conditions roughly corresponding to projectile breakup may be estimated for several of the studies considered.

The velocity at which projectile breakup occurs appears to be a function of plate thickness as well as projectile and target material, thicker targets requiring a lower velocity for projectile breakup.

There appears to be some correlation between the diameter of the hole produced in a thin plate, and the cone angle over which the plate and projectile material is ejected from the rear of the plate (Figs. 6.27 and 6.30), both increasing with plate thickness at a given velocity. This again implies that the projectile experiences more severe breakup as the plate thickness is increased, at constant velocity. Lull's theory shows the same trend. As the plate thickness is increased further (beyond about half the length of the projectile in Fig. 6.30), the spray angle no longer increases, and later decreases. Undoubtedly the spray angle continues to decrease until the plate is so thick that it will not longer be completely penetrated. In Lull's theory the angle continues to increase with plate thickness. The discrepancy arises since his assumption that the target is thin is violated.

The total depth of penetration in a shielded target or multiple target is also a function of pellet breakup. As the shield plate thickness increases (Fig. 6.28), and the spray particles are distributed over a wider area, the penetration of the prime target is reduced. At about the shield thickness at which the spray angle becomes constant, the penetration in the prime target also becomes constant. The total penetration (shield plus prime target) therefore goes through a minimum, and increases with further increase in shield thickness. The optimum shield thickness

appears to be about 0.4 times the projectile length, from Fig. 6.28. Wallace²² states that the optimum in his study also lies at about the same shield thickness ratio.

Total penetration is seen to decrease with increase in shield spacing (Fig. 6.29) until at some optimum spacing no further reduction in penetration is achieved. It appears that beyond this spacing each particle in the spray strikes a different portion of the prime target, while at smaller spacings several spray particles may strike the same location on the prime target, leading to greater penetration. The fact that Funkhauser and Olshaker find different optimum spacings and minimum total penetration suggests that the projectiles used in the two studies suffered different degrees of breakup at the particular velocities used.

These effects are illustrated in Fig. 6.33 where it may be seen that an increase in shield thickness, or an increase in shield spacing lead to increased angle of spray and decreased penetration.

Wallace noted that the spray angle, calculated on the basis of spray diameter at the prime target and the shield spacing, appeared to decrease with increasing shield spacing, all other parameters being maintained constant. This suggests that the spray particles actually originate in an area in the projectile above the level of the shield, an effect also noted by Bjork* in his machine calculations.

It is clear that much more experimentation is required, before quantitative trends may be distinguished.

*

Private Communication

Ideally, the particle size, mass and velocity distributions in the spray ejected from a thin target should be measured as a function of target thickness and velocity, for given projectile and target materials. The effect of a given spray on a subsequent target should ideally be investigated separately. In this way the possible parametric combinations to be investigated are minimised, and comparison with possible theoretical analyses facilitated.

SECTION VII

CONCLUSIONS

Available information relating to cratering and penetration by projectiles in the velocity range where the projectile suffers major deformation or breakup has been surveyed. Much of this information is collected in this report for ready reference.

While a great deal of experimental data has been generated, most of this data shows considerable scatter, and in most cases, insufficient information about target material properties has been reported.

Most of the experimental work relates to normal impact on quasi-infinite targets. Although a very wide variety of target and projectile materials have been used, projectile velocities for most of these have been restricted to the transition region. Almost no experimental data exists above 7 km/sec. Two empirical expressions have been deduced which are more generally applicable than previous expressions. The power law (Sect. 5.3) is restricted to the high velocity region, defined in Section 5.6, while the logarithmic law (Sect. 5.4) fits the experimental data in both the transition and high velocity regions for "ductile" projectile behaviour. Both expressions are good fits to the data when constants appropriate to the projectile and target material are used, and are therefore useful for interpolation. Extrapolations to higher velocities may be expected to lead to large errors.

Only very rough correlations of the constants

in the empirical expressions with elementary material properties can be found, so that predictions of penetration for projectile and target materials other than those for which sufficient experimental data exists, may be expected to be subject to very large errors. That some correlation exists at all must be ascribed to the fact that some correlation exists between dynamic compressibility and strength properties, and elementary static properties of the materials involved. Furthermore, in the case of the logarithmic law, it may be expected that a much more complex functional dependence on material properties will be necessary in order to accommodate the many complex transition region strength effects. It appears to be a hopeless task to deduce such a functional relationship from the data, due to the large uncertainties in the data, and the limited velocity range of the data for most material combinations. An adequate functional relation must be sought on theoretical grounds.

The available theories applicable to high velocity cratering have been found to be inadequate in the experimental velocity range. Most of the theories were intended to describe cratering at much higher velocities and are therefore very simplified, generally neglecting strength effects, or introducing a simple correction for strength effects. It has been found that strength effects are important at much higher velocities than previously supposed. In particular, strength effects are important in the high velocity region, which is of prime interest for missile and space vehicle applications. A good qualitative understanding of physical phenomena involved in the cratering process has been gained. It is appropriate therefore to attempt to develop a more realistic theory at

this time. The theory will necessarily have to include realistic nonlinear compressibility, geometric and strength effects in order to provide a realistic analog to the cratering process.

For projectile-target configuration other than normal impact of compact particles on quasi-infinite targets, relatively little experimental work has been reported. In general sufficient experimental information exists to distinguish qualitative physical behaviour, but insufficient data exists to attempt empirical correlations. Theoretical work has generally been limited to simple semi-empirical treatments which have shown limited success in some cases.

It must be concluded, therefore, that at present, no reliable predictions of cratering and penetration can be made for velocities materials and configurations other than those for which experimental data exists.

Further experimental work is required, particularly for impact by projectiles of high or low length/diameter ratios, by projectiles at oblique incidence, and for impact on thin targets. Little is to be gained from further experimental work on quasi-infinite targets, except at velocities over 6 km/sec. However, care must be exercised in the design of experimental programs. Since additional independent variables have been introduced, it will clearly be impossible to carry out complete empirical surveys in which all of the experimental parameters are varied over the entire range. This would obviously lead to an experimental program of prohibitive magnitude.

It seems imperative to carry out theoretical work, so that adequate scaling laws may be deduced. Once scaling laws have been established, intelligent experimental programs may be designed to supply the necessary constants, and the experimental work may be reduced to manageable proportions.

APPENDIX A

Zaid's Theory¹⁰⁷

The fluid in the zone between the penetrator and target is at time t situated in a cylinder radius r , and height h . At time $(t + dt)$ this will be a cylinder of radius $(r + \dot{r}_a dt)$ with thickness $(h - \dot{p} dt)$, where \dot{p} is the velocity of advance of the projectile. For the conservation of mass of this incompressible fluid

$$\pi r^2 h = \pi (r + \dot{r}_a dt)(h - \dot{p} dt) \quad (\text{A.1})$$

where \dot{r}_a is the average fluid velocity over depth h . This reduces to the equation

$$\dot{r}_a = \frac{r}{2h} \dot{p} \quad (\text{A.2})$$

from which, on differentiating,

$$\ddot{r}_a \approx \frac{r}{2h^2} \left[h \ddot{p} + \frac{\dot{p}^2}{2} \right] \quad (\text{A.3})$$

An element defined by r , $r d\theta$, h in the fluid-zone will lead to the equation of motion

$$\begin{aligned} & \delta \frac{dP_a}{dr} h r d\theta dr dt + \tau_u r dr d\theta dt \\ &= - \left[\rho_t h(t+dt) dA(t+dt) (\dot{r} + \ddot{r} dt) - \rho_t h dA(t) \dot{r} \right] \end{aligned}$$

where $\gamma \frac{dP_a}{dr}$ is the average of $\frac{dP}{dr}$ over the depth of the fluid zone, P is the pressure within the fluid, τ_u is the shear at the projectile-fluid interface, and dA an element of area in the radial direction. Using the conservation of mass equation, the relation

$$\begin{aligned} h(t+dt) &= h(t) - \dot{p} dt + \dot{q} dt \\ \dot{q} &= \dot{h} + \dot{p} \end{aligned} \quad (A.4)$$

where \dot{q} is the velocity of penetration into the target, the above expression reduces to

$$\begin{aligned} \gamma h \frac{dP_a}{dr} + \tau_u &= -\rho_t h \left[\ddot{r} + \frac{\dot{r}}{h} \dot{q} \right] \\ &= \frac{\rho_t r}{2} \left[\ddot{p} + \frac{3}{2} \frac{\dot{p}^2}{h} \right] \end{aligned} \quad (A.5)$$

Integrating within the limits r and R (γ independent of r),

$$\gamma P_a(r) - \gamma P_a(R) = \frac{1}{h} \int_r^R \tau_u dr + \frac{\rho_t}{4h} (R^2 - r^2) \left(\ddot{p} + \frac{3}{2} \frac{\dot{p}^2}{h} \right) \quad (A.6)$$

Defining the ratio of the average pressure to that at the penetrator fluid zone interface as

$$P_a = \alpha P_u = \frac{\gamma'}{\gamma} P_u \quad (A.7)$$

the equation becomes

$$\gamma' P_u(r) - \gamma' P_u(R) = \frac{1}{h} \int_r^R \tau_u dr + \frac{\rho_t}{4h} (R^2 - r^2) \left(\ddot{p} + \frac{3}{2} \frac{\dot{p}^2}{h} \right) \quad (A.8)$$

The retarding force on the penetrator is

$$2 \pi \int_0^R \left\{ P_u(r) - P_u(R) \right\} r \cdot dr$$

hence, the equation of motion of the penetrator is

$$m_p \ddot{p} + \frac{2\pi}{\gamma' h} \left\{ \int_0^R \int_r^R \tau_u \cdot dz \cdot r \cdot dr + \frac{\rho_f R^4}{16} \left(\ddot{p} + \frac{3}{2} \frac{\dot{p}^2}{h} \right) \right\} = 0 \quad (\text{A.9})$$

Zaid assumed shear relationships of the form,

$$\tau_u = k \frac{\dot{r}_a}{h} \quad \tau_L = k' \frac{\dot{r}_a}{h} \quad (\text{A.10})$$

and two different fluid-zone growth relationships,

$$\dot{p} = b_n \bar{\tau}_L^n \quad \dot{p} = a_m \bar{r}_a^m \quad (\text{A.11})$$

where

$$\bar{\tau}_L = \frac{k'}{3h^2} R \dot{p} \quad \bar{r}_a = \frac{R}{3h} \dot{p} \quad (\text{A.12})$$

are the average values of τ_L , \dot{r}_a over a plane surface area of radius R .

Three cases of fluid-zone growth relationship have been considered, $n = 1, 2, m = 1$

$$\dot{q} = \frac{b_1}{3h^2} k' R \dot{p} \quad \text{I}$$

$$\dot{q} = \frac{b_2}{9h^4} k'^2 R^2 \dot{p}^2 \quad \text{II} \quad (\text{A.13})$$

$$\dot{q} = \frac{a_1}{3h} R \dot{p} \quad \text{III}$$

These lead to penetration-fluid thickness relations:

$$p = -h + \frac{b_1 k' R}{6} \log_e \left\{ \frac{\left(\frac{b_1 k' R}{3}\right)^{1/2} + h}{\left(\frac{b_1 k' R}{3}\right)^{1/2} - h} \right\} \quad \text{I} \quad (\text{A.14})$$

$$p = -h + \frac{R a_1}{3} \log_e \left\{ \frac{\frac{R a_1}{3}}{\frac{R a_1}{3} - h} \right\} \quad \text{III}$$

If the steady-state penetration dominates, a good approximation is $p \simeq \dot{p}_0 t$. Using this relation Case II has a solution

$$\dot{p}_0 t = -h + \frac{1}{4} \log_e \left\{ \frac{\left(\frac{b_2^{1/2} k' R}{3}\right)^{1/2} \dot{p}_0^{1/4} + h}{\left(\frac{b_2^{1/2} k' R}{3}\right)^{1/2} \dot{p}_0^{1/4} - h} \right\} + \frac{1}{2} \tan^{-1} \left\{ \left(\frac{3}{b_2^{1/2} k' R}\right)^{1/2} \frac{h}{\dot{p}_0^{1/4}} \right\} \quad (\text{A.15})$$

This equation estimates that 97% of the steady-state fluid-zone is established within the time the penetrator has traversed one-half the depth of that zone. Thus, with the exception of the transient effects, a reasonable solution is obtained on assuming steady-state conditions. In the above equation this would be

$$h = \left(\frac{b_z^{1/2} k' R}{3} \right)^{1/2} \dot{p}_0^{1/4} \quad (\text{A.16})$$

Generalizing this to

$$h = \left(\frac{b_z^{1/2} k' R}{3} \right)^{1/2} \dot{p}^{1/4} \quad (\text{A.17})$$

and substituting in the equation of motion of the penetrator, results, for the approximation

$$\frac{k}{\rho} \left(\frac{3}{b_z^{1/2} k' R} \right)^{1/2} \ll \frac{3}{2} \dot{p}^{5/4} \quad (\text{A.18})$$

(which Zaid considers to be valid in the range of interest), in a solution

$$p = \frac{8}{3} \dot{p}_0^{1/4} \left(\frac{b_z^{1/2} k' R}{3} \right)^{1/2} \left\{ 1 - \left(\frac{\dot{p}}{\dot{p}_0} \right)^{1/4} \right\} \quad (\text{A.19})$$

Assuming that the fluid zone was of constant thickness, the motion of the penetrator would be given by the equations

$$\frac{\dot{p}}{\dot{p}_0} = \left\{ \frac{1}{1 + \frac{B}{C} \dot{p}_0 \left[1 - \exp\left(-\frac{C}{A} t\right) \right]} \right\} \exp\left(-\frac{C}{A} t\right) \quad (\text{A.20})$$

$$\frac{\dot{P}}{\dot{P}_0} = \frac{1}{\frac{B}{C} \dot{P}_0} \left\{ \left(1 + \frac{B}{C} \dot{P}_0 \right) \exp \left(- \frac{B}{A} P \right) - 1 \right\} \quad (\text{A.20})$$

where

$$\begin{aligned} A &= \frac{m_P}{\pi R^2 h \rho_t} + \frac{1}{8 \gamma'} \left(\frac{R}{h} \right)^2 \\ B &= \frac{3}{16} \frac{1}{\gamma'} \left(\frac{R}{h} \right)^2 \frac{1}{h} \\ C &= \frac{k}{\gamma'} \frac{1}{8 h^2 \rho_t} \left(\frac{R}{h} \right)^2 \end{aligned} \quad (\text{A.21})$$

For $\frac{C}{A} t \ll 1$, these reduce to

$$P \frac{B}{A} = \log_e \left\{ 1 + \frac{B}{A} \dot{P}_0 t \right\} \quad (\text{A.22})$$

In order to evaluate these equations it is necessary to enumerate k , k' , b_1 , b_2 , a , and in the case of constant h , the value of h itself. Values of these constants have not been given.

However, Zaid does consider a hypothetical case in order to estimate the magnitude of the penetration. For this the flow is assumed to be parabolic with a shear stress relation at the projectile-fluid zone interface

$$\tau_u = \mu \frac{6 \dot{r}_u}{h}$$

where μ is the viscosity of the fluid. The estimated ranges

of material and other properties used were as follows:

$$(3 \times 10^{-3})(0.06 \times 10^{-3}) \leq \mu < .06 \times 10^{-3} \text{ slug/ft. sec.}$$

(water vapor)

(molten iron)

$$\rho_p = \rho_t = 15.2 \text{ slug/ft.}^2$$

$$R = L = 1/4 \text{ inch}$$

$$\beta = 1$$

$$1.0 \geq R/h > 10^{-3}$$

For an impact velocity of 10,000 ft/sec, the theory which assumes a fluid zone of constant height, predicts a crater depth anywhere from 3.8×10^{-4} inches to 4.5 inches, depending on the viscosity and fluid zone thickness assumed.

APPENDIX B

Opik's Meteoritic Impact Theory¹²¹

In solving the equations set out in Section III, it is easier to introduce the dimensional variables $p_m = p/2R$, $\bar{p}_m = \bar{p}/2R$, $r_m = r/R$ and $\delta = \sqrt{\rho_t/(\rho_t + \rho_p)}$. The problem is now reduced to solving the equation

$$\ddot{r}_m = -\frac{1}{4} \frac{\delta}{1-\delta^2} \frac{r_m^2 \dot{r}_m^2}{\left(1 + \frac{2\delta}{r_m^3}\right)} \left\{ 1 - \frac{24(1-\delta^2)}{r_m^6} + \frac{\phi}{\dot{r}_m^2} \right\} \quad (B.1)$$

for the initial condition $t = 0$, $r_m = 1$, $\dot{p} = V/2R$, and

$$\begin{aligned} \dot{r}_m(0) &= \frac{2\delta \dot{p}_m(0)}{1 + \frac{2\delta}{r_m^3}} \\ &= \frac{V}{R} \frac{\delta}{1 + 2\delta} \end{aligned} \quad (B.2)$$

where

$$\begin{aligned} \phi &= \frac{2k}{\rho_t} \left(\frac{\delta}{R}\right)^2 \\ &= \frac{2k}{R^2} \frac{1}{(\rho_p + \rho_t)^2} \end{aligned} \quad (B.3)$$

The nonlinear differential equation could not be integrated

directly. However, the reverse differential equation obtained by the transformation,

$$\frac{dr_m}{dt} = \frac{1}{\psi} \quad \frac{d^2 r_m}{dt^2} = - \frac{1}{\psi^3} \frac{d\psi}{dr_m} \quad (\text{B.4})$$

is easier to handle. The transformed equation will be

$$\frac{d\psi}{dr_m} = \frac{1}{4} \left(\frac{\delta}{1-\delta^2} \right) \left(\frac{r_m^2 \psi}{1 + \frac{2\delta}{r_m^3}} \right) \left\{ 1 - \frac{24(1-\delta^2)}{r_m^6} + \phi \psi^2 \right\} \quad (\text{B.5})$$

for the initial conditions

$$r_m = 1 \quad \psi(1) = \frac{R}{V} \frac{1+2\delta}{\delta} \quad (\text{B.6})$$

This has the solution

$$\frac{1}{\psi} = \dot{r}_m = \frac{\dot{r}_m(0)}{f(r_m)} \left\{ \left[1 - \frac{(1+2\delta)^2}{2\delta} \left(\frac{V_0}{V} \right)^2 \right] g(r_m) \right\}^{1/2} \quad (\text{B.7})$$

where

$$f(r_m) = \frac{1}{r_m^3} \left(\frac{r_m^3 + 2\delta}{1 + 2\delta} \right)^n \exp \left\{ \frac{1}{12} \frac{\delta}{1-\delta^2} (r_m^3 - 1) \right\} \quad (\text{B.8})$$

$$n = 1 - \frac{1}{6} \left(\frac{\delta^2}{1-\delta^2} \right)$$

$$g(r_m) = \int_0^{r_m} \frac{x^2 f^2(x)}{1 + \frac{2\delta}{x^2}} dx \quad (\text{B.8})$$

$$V_0 = \left(\frac{2k}{\rho_p} \right)^{1/2}$$

The maximum penetration is obtained when $\dot{r}_m = \dot{p}_m = 0$. The radius of the meteorite at this time, R_1 is obtained by placing $\dot{r}_m = 0$, hence

$$g\left(\frac{r_{\max}}{R}\right) = \frac{2\delta}{(1+2\delta)^2} \left(\frac{V}{V_0}\right)^2 \quad (\text{B.9})$$

and the maximum penetration, p_{\max} , is obtained from r_{\max}

$$\frac{p_{\max}}{2R} = \frac{\frac{r_{\max}}{R} - 1}{2\delta} \quad (\text{B.10})$$

APPENDIX C

Stanyukovitch Equivalent Explosive Analogy¹³³

It is assumed that a powerful shock wave emanates from the point of impact of a projectile onto a target which is capable of completely destroying the solid media within a certain volume, and converting it into a strongly compressed gas. The pressure at the front of the shock will be given by the relation

$$\frac{m_p V^2}{2} = \frac{4\pi}{n-1} \eta P r^3 \quad (C.1)$$

where r is the distance from the point of impact, n the polytropic index of the expanding gas; P the pressure on the front of the shock wave, and η a parameter depending on n such that at $n = 1, 7/5, 3$ or 5 , η is equal to $1/3, 1/5, 1/6$ and $1/7$ respectively. For strong condensations of a gas at pressures above a megabar over a wide range of pressure, it is assumed that $n = 3$.

The Rankine-Hugoniot relations across the shock are

$$\begin{aligned} e &= \frac{P}{\rho(n-1)} = \frac{P}{2} \left(\frac{1}{\rho_{ot}} - \frac{1}{\rho_t} \right) \\ U^2 &= \frac{P}{\rho_{ot} - \rho_t} \\ V^2 &= P \left(\frac{1}{\rho_{ot}} - \frac{1}{\rho_t} \right) \end{aligned} \quad (C.2)$$

where e is the internal energy, ρ_t the target density behind the shock, ρ_{ot} the target density in front of the shock, U the velocity of the shock wave front, and v the velocity of the gas behind the shock wave front. This mode of cratering will continue until the energy on the shock wave front is less than ζ ,

$$\zeta \leq e + \frac{V^2}{2} = V^2 \quad (C.3)$$

where ζ is the internal energy required to disintegrate the target material. For the earth's crust Stanyukovitch estimates ζ as approximately 3 cal/gm. From these equations, the radius r of the hemispherical crater formed during this mode may be found,

$$\frac{m_p V^2}{2} = \frac{4}{3} \pi r^3 \rho_{ot} \left(\frac{3}{2} \frac{n+1}{n-1} \eta \zeta \right) \quad (C.4)$$

Now the mean density of the energy throughout this crater is

$$\langle \zeta \rangle = \frac{3}{2} \eta \frac{n+1}{n-1} \zeta \quad (C.5)$$

which for $n = 3$ ($\eta = 1/6$), gives $\langle \zeta \rangle = \zeta/2$. This energy density for impact into the earth is of the order of the initial density of high explosives, therefore the entire mass of the substance in this crater is comparable to an equal weight of high explosive.

Empirically, it has been found that the radius of a crater p formed in the earth by the detonation of a mass M of high explosive at the surface is given by

$$p^3 = k M \quad (C.6)$$

that is

$$p^3 = \frac{4}{3} \frac{k}{\eta} \frac{n-1}{n+1} \frac{m_p V^2}{\xi} \quad (C.7)$$

For $n = 3$

$$p^3 = k \frac{m_p V^2}{\xi} \quad (C.8)$$

APPENDIX D

SHOCK RELATIONS

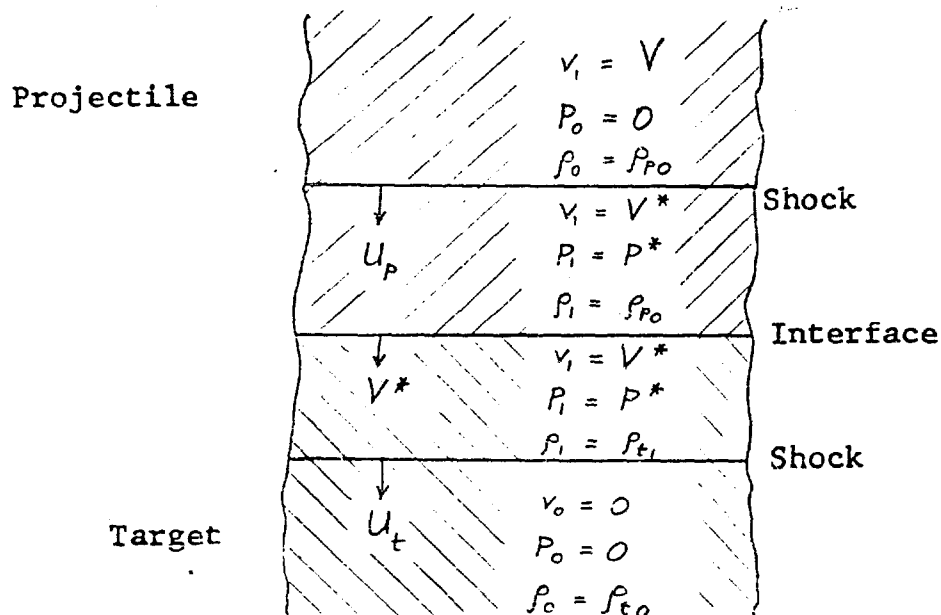
The mechanical shock relations, derived from the laws of conservation of mass and momentum are

$$U = v_o \pm v_o \sqrt{\frac{P_1 - P_o}{v_o - v_1}} \quad (D.1)$$

and

$$v_1 = v_o \pm \sqrt{(v_o - v_1)(P_1 - P_o)} \quad (D.2)$$

where U is the shock velocity, v the particle velocity
 v the specific volume and P the pressure respectively,
and $()_o$ refers to condition ahead of the shock, $()_1$ to
conditions behind the shock.



Experiments^{137 to 151} have shown that the relation between shock velocity and particle velocity behind the shock relative to the particle velocity ahead of the shock may be represented by a simple linear relation to surprising accuracy

$$U - v_0 = c + S(v_1 - v_0) \quad (D.3)$$

where c may be identified as the adiabatic bulk sonic velocity, and S is related to the change in compressibility with pressure.

Eliminating v_1 between Eq. (D.1) and (D.2) and using Eq. (D.3), a relation between interface pressure P^* and velocity V^* may be devised by considering the shock moving into the stationary undisturbed target.

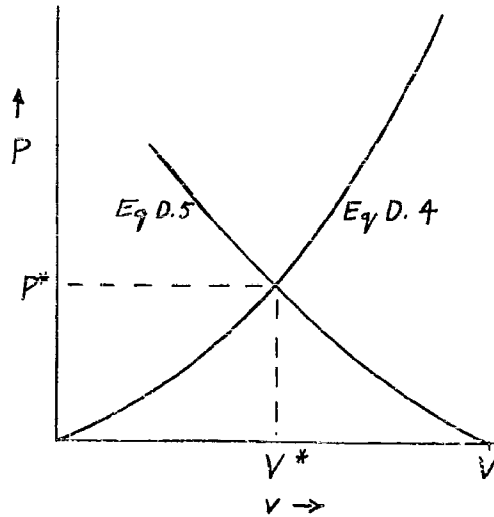
$$P^* = \rho_{t0} V^* (c_t + S_t V^*) \quad (D.4)$$

where $\rho = 1/v$ represents density. Similarly by considering the shock moving into the undisturbed projectile material which has a velocity V

$$P^* = \rho_{p0} (V - V^*) \left[c_p + S_p (V - V^*) \right] \quad (D.5)$$

Equation (D.4) and (D.5) are two simultaneous equations for interface pressure and velocity.

Explicit solutions for P^* and V^* are difficult to obtain, but the solution can be obtained very simply by plotting Eq. (D.4) and (D.5) and obtaining the solution graphically. Since the intercept of Eq. (D.5) on the abscissa is the projectile velocity V , it is customary to draw the two



curves on overlays, so that they may be positioned to obtain solutions for any projectile velocity.

For the acoustic approximation, i.e. neglecting the change of compressibility with pressure, $S = 0$ and the above curves become straight lines. An explicit solution may be found

$$P^* = V \frac{\rho_{p0} c_p \cdot \rho_{t0} c_t}{\rho_{p0} c_p + \rho_{t0} c_t} \quad (D.6)$$

$$V^* = V \frac{\rho_{p0} c_p}{\rho_{p0} c_p + \rho_{t0} c_t} \quad (D.7)$$

The condition that the shock in the projectile moves below the original target surface is $U_p > 0$. Applying Eq. (D.1), (D.2) and (D.3) to the shocks in the projectile and target, and eliminating the specific volume, the condition reduces to

$$V > \frac{1}{\rho_{p0}} \frac{P^*}{(V - V^*)} \quad (D.8)$$

which may be evaluated with the use of Eq. (D.4) and (D.5). Again a semi-graphical method is useful. Using Eq. (D.5)

$$V > c_p + S_p (V - V^*) \quad (D.9)$$

and a simple trial and error procedure employing the curves previously used to find P^* and V^* may be used.

When the projectile and target materials are identical, $V^* = \frac{1}{2}V$ by symmetry, and

$$V > \frac{c_p}{1 - \frac{1}{2} S_p} \quad (D.10)$$

In the acoustic approximation, $S_p = 0$ and Eq. (D.9) and (D.10) reduce to

$$V > c_p \quad (D.11)$$

as may be expected.

Interface velocities and pressures obtained graphically from $P - v$ plots are plotted in Fig. 5.1a and b as a function of projectile velocity. The V^* vs. V curves are very nearly straight lines, over the velocity range shown. In fact they may be approximated by straight lines given by

$$V^* \approx \frac{1}{2} \left(\frac{\rho_p}{\rho_t} \right)^{1/2} V \quad (D.12)$$

above a projectile velocity of about 3 km/sec with a maximum error of about 20% for most materials. Corresponding approximate values of P^* may then be obtained from Eq. (D.4).

While the approximation is not too accurate, it does afford a simple means of estimating interface pressures and densities rapidly.

Bibliography

Experimental Work in Cratering

Ballistic Research Laboratory

1. J. W. Gehring, Jr.; Observations on High Speed Pellets and their Impact upon Target Pellets
B.R.L. Memorandum Report No. 704, July 1953.
2. J. W. Gehring, Jr.; An Analysis of Micro-particle Cratering in a Variety of Target Materials
Third Hypervelocity Impact Symposium, Vol. 1, October 1958.
3. J. H. Kineke, Jr.; An Experimental Study of Crater Formation in Lead
Third Hypervelocity Impact Symposium, Vol. 1, October 1958.
4. J. B. Feldman, Jr.; Volume-Energy Relation from Shaped Charge Jet Penetrations
Third Hypervelocity Impact Symposium, Vol. 1, October 1958.
5. J. H. Kineke, Jr.; An Experimental Study of Crater Formation in Metallic Targets
Fourth Hypervelocity Impact Symposium, Vol. 1, April 1960.

6. J. B. Feldman, Jr.; Volume-Energy Relation from Shaped Charge Jet Penetrations
Fourth Hypervelocity Impact Symposium, Vol. 2,
April 1960.
7. J. W. Gehring, Jr.; Observations of the Phenomena of Hypervelocity Impact
Fourth Hypervelocity Impact Symposium, Vol. 2,
April 1960.
8. J. W. Gehring Jr., and L. G. Richards; Further Studies of Micro-Particle Cratering in a Variety of Target Materials
Fourth Hypervelocity Impact Symposium,
Vol. 3, April 1960.
9. C. M. Glass, and R. B. Pond; A Metallurgical Approach to the Hypervelocity Problem
Fourth Hypervelocity Impact Symposium, Vol. 3,
April 1960.
10. L. G. Richards, and L. S. Holloway; Study of Hypervelocity Micro-Particle Cratering
B.R.L. Memo Report No. 1280, June 1960.
11. L. G. Richards, and J. W. Gehring Jr ; Hypervelocity Micro-Particle Impact on Thin Foils
B.R.L. Technical Note No. 1380, Feb. 1961.

Canadian Armament Research and Development Establishment

12. C. J. Maiden, J. Charest, and H. P. Tardif, An Investigation of Spalling and Crater Formation

by Hypervelocity Projectiles

Fourth Hypervelocity Impact Symposium, Vol. 3,
April 1960; also CARDE Tech Memo. AB 62,
May 1960.

Carnegie Institute of Technology

13. R. J. Eichelberger, F. E. Allison, and W. F. Donaldson;
Craters formed by High-Velocity Fragments--Funda-
mentals of Shaped Charges
Contract No. DA-36-061-ORD-394. Status Report 3,
July 1954.
14. E. M. Pugh and R. J. Eichelberger; Crater Formation
in Metals by High Velocity Fragments
(Title Unclassified)
First Hypervelocity Impact Symposium, Santa
Monica 1955 (Secret).
15. R. J. Eichelberger; Experimental Test of the Theory
of Penetration by Metallic Jets
Journal of Applied Physics, Vol. 27, 1956, p. 63.
16. F. E. Allison and G. M. Bryan; Cratering by a Train
of Hypervelocity Fragments
Second Hypervelocity Impact Symposium, Vol. 1,
May 1957.
17. F. L. Culp; Volume-Energy Relation for Craters
formed by High Velocity Projectiles
Third Hypervelocity Impact Symposium,
Vol. 1, October 1958.

18. F. E. Allison, K. R. Becker and R. Vitali; Effects of Target Temperature on Hypervelocity Cratering
Fourth Hypervelocity Impact Symposium, Vol. 1,
April 1960.

Colorado School of Mines

19. J. S. Rinehart and W. C. Maurer; Impact Formation in Rock
Fourth Hypervelocity Impact Symposium, Vol. 3,
April 1960; also Journal of Applied Physics,
Vol. 31, July 1960, p. 1247-1253.

General Electric Corporation

20. M. Kornhauser; Prediction of Cratering Caused by Meteoroid Impacts
Journal of Astronautical Sciences, Vol. 5, 1958.
21. M. Kornhauser; Surface Roughness Caused by Meteoroid Impacts
Third Hypervelocity Impact Symposium, Vol. 1,
October 1958.
22. R. R. Wallace Jr., J. R. Vinson, and M. Kornhauser,
Effects of Hypervelocity Particles on Shielded Structures
American Rocket Society: Lifting Re-entry
Vehicles: Structures, Materials and Design
Conference, Palm Springs, California,
April 4-6, 1961.

Lincoln Laboratory, M.I.T.

23. R. E. Slattery and W. G. Clay; The Penetration of Thin Rods into Aluminum
Fourth Hypervelocity Impact Symposium, Vol. 3,
April 1960.

Massachusetts Institute of Technology

24. A. Olshaker; An Experimental Investigation in Lead of the Whipple "Meteor Bumper";
Fourth Hypervelocity Impact Symposium, Vol. 2,
April 1960; S.M. Thesis, Massachusetts
Institute of Technology, June 1960, also
Journal of Applied Physics, Vol. 31, 1960
p. 2118-2120.
25. A. H. Jones; High Velocity Impact;
S.M. Thesis, Massachusetts Institute of
Technology, January 1960.
26. A. W. Peck; Some Material Effects in Cratering in Hypervelocity Impact;
S.M. Thesis, Massachusetts Institute of
Technology, June 1961.

National Aeronautics and Space Administration, AMES

27. J. L. Summers and A. C. Charters; High-Speed Impact of Metal Projectiles in Targets of Various Materials
Third Hypervelocity Symposium, Vol. 1,
October 1958.

28. A. C. Charters and G. S. Locke Jr.; A Preliminary Investigation of High-Speed Impact: the Penetration of Small Spheres into Thick Copper Targets
NACA RM A 58 B 26 May 1958.
Declassified December 1958.
29. A. C. Charters and J. L. Summers; Some Comments on the Phenomena of High-Speed Impact
Paper Presented at Decennial Symposium on
May 26, 1959 at U. S. Naval Ordnance Laboratory,
White Oak, Silver Spring, Maryland.
30. J. L. Summers; Investigation of High Speed Impact: Regions of Impact and Impact at Oblique Angles
NASA TN D-94 October 1959.
31. J. L. Summers and W. R. Niehaus; A preliminary Investigation of the Penetration of Slender Metal Rods in Thick Metal Targets
NASA TN D-137 December 1959.
32. A. C. Charters; High Speed Impact
Scientific American, Vol. 203 No. 4, October 1960
p. 128.
33. C. R. Nysmith and J. L. Summers; Preliminary Investigation of Impact on Multiple Sheet Structures and Evaluation of the Meteoroid Hazard to Space Vehicles
NASA TN D-1039, July 1961.

National Aeronautics and Space Administration, Langley

34. W. H. Kinard, C. H. Lambert, D. R. Schryer, and F. W. Casey, Jr.; Effect of Target Thickness on Cratering and Penetration of Projectiles Impacting at Velocities to 13,000 feet per second.
NASA Memo 10-18-58 L, December 1958.
Declassified April 12, 1961.
35. R. D. Collins, Jr., and W. H. Kinard; The Dependency of Penetration on the Momentum per Unit Area of the Impacting Projectile and the Resistance of Materials to Penetration.
NASA TN D-238, May 1960.
36. D. J. Carter, Jr.; A Preliminary Investigation on the Destruction of Solid-Propellant Rocket Motors by Impact from Small Particles.
NASA TN D-442, September 1960.
37. W. H. Kinard and R. D. Collins, Jr.; A Technique for Obtaining Hypervelocity Impact Data by using the Relative Velocities of Two Projectiles.
NASA TN D-724, February 1961.
38. W. H. Kinard and R. H. Hopko; An Investigation of High-Velocity Cratering into Metallic Targets and Correlations for Metallic and Non-Metallic Targets.
NASA TN D-726, February 1961.

39. J. O. Funkhauser; A Preliminary Investigation of the Effect of Bumpers as a Means of Reducing Projectile Penetration
NASA TN D-802, April 1961.

National Bureau of Standards

40. O. G. Engel; Pits in Metals Caused by Collisions with Liquid Drops and Soft Metal Spheres
Journal of Research of the N.B.S., Vol. 62, No. 6, June 1959, p. 229-246.
41. O. G. Engel; Collisions of Liquid Drops with Liquids. Part 1. A Review with Some Preliminary Data.
WADD Tech. Rept. 60-475, Part 1.

Naval Ordnance Test Station

42. J. S. Rinehart; Some Observations on High Speed Impact
Tech. Memo. R R B-50, October 1949.
43. E. B. Mayfield and J. W. Rogers; Craters Produced by the Hypervelocity Impact of Aluminum Cylinders on Steel Plates
N.O.T.S. 1366, NAVORD Report 5025, February 1956.
44. W. A. Allen, E. B. Mayfield, and H. L. Morrison; Dynamics of a Projectile Penetrating Sand. Part I
Journal of Applied Physics, Vol. 28, 1957, p. 370.
45. W. A. Allen, E. B. Mayfield and H. L. Morrison; Dynamics of a Projectile Penetrating Sand. Part II
Journal of Applied Physics. Vol. 28, 1957. p. 1331-1335.

46. M. E. Blackman; Elastic and Plastic Behaviour in the Impact of Cylinders against Plates
Journal of Applied Physics, Vol. 30, 1959
p. 1397-1403.
47. E. B. Mayfield and J. W. Rogers; Cratering and Shock Wave Phenomena in Steel Plates at High Impact Speeds
Journal of Applied Physics, Vol. 31, No. 3,
March 1960, p. 472.
48. W. Allen and J. W. Rogers; Penetration of a Rod into a Thick Aluminum Target
NAWEPs Report 7597, NOTS TP 2587,
December 1960.

Naval Research Laboratory

49. J. M. Krafft; Surface Friction in Ballistic Penetration
Journal of Applied Physics, Vol. 26, 1955. p. 1248
50. W. W. Atkins; Hypervelocity Penetration Studies
Third Hypervelocity Impact Symposium, Vol. 1,
October 1958.
51. W. W. Atkins; Hypervelocity Penetration Studies
Fourth Hypervelocity Impact Symposium, Vol. 1,
April 1960.
52. W. W. Atkins and H. F. Swift; Hypervelocity Capability and Impact Research
ARPA Order 70-59, NRL Memo Rept 1115
December 1960

53. Project Defender Progress Report No. 1 (U)
N.E. L. Memo. Report 1136, January 1961 (Secret)
54. E. N. Clark and A. MacKenzie; Some Results of Hypervelocity Explosive Charge Investigation
Third Hypervelocity Impact Symposium, Vol. 1,
October 7-9, 1958.

Picatinny Arsenal

55. E. N. Clark, A. MacKenzie, F. H. Schmitt, and I. L. Kintish;
Studies of Hypervelocity Impact on Lead
Fourth Hypervelocity Impact Symposium, Vol. 1,
April 1960.

Thompson Ramo-Wooldridge Corporation

56. J. F. Friichtenicht, and B. Hamermesh; Ballistic Impacts by Microscopic Projectiles
Fourth Hypervelocity Impact Symposium, Vol. 3,
April 1960.

Rheem Manufacturing Company

57. R. J. McKenzie, F. F. Martin, and H. M. Kenworthy,
High Velocity Impact of Small Metal Spheres upon Flat Metal Targets
Third Hypervelocity Impact Symposium, Vol. 1,
October 1958.

Stanford Research Institute

58. G. E. Duvall; Penetration of Matter by Solid Projectiles
Internal Report No. 002-55, 1955.
59. S. Katz and G. D. Anderson; Penetration of Metal and Lucite Targets by Small Particles
S.R.I. Project No. Gu-1722, Scientific Report No. 1, February 1957.
60. G. D. Anderson, D. G. Doran, F. S. Hempy, and M. C. Kells; Cratering by High Velocity Microparticles
Third Hypervelocity Impact Symposium, Vol. 1, October 1958.
61. M. C. Kells and D. D. Keough; Impact of High Speed Particles with Solids and Gases
Poulter Lab. Tech. Report 017-58, December 1958.
62. G. D. Anderson; Studies in Hypervelocity Impact
Poulter Lab. Tech. Report 018-59, December 1959.

University of Utah

63. M. E. van Valkenburg; Modeling of High-Speed Impact through the use of Plastics
OSR Tech. Rept. No. 1, Contract AF 18(600)-1217, March 1955
64. M. E. van Valkenburg, W. G. Clay, F. W. Langson, and W. Mayeda; Some Characteristics of Craters from High-Speed Pellets Impacting into Semi-Infinite Targets
OSR Tech. Rept. Contract AF 18(600)-1217.

65. W. G. Clay and W. S. Partridge; Wax Modeling Studies of High Speed Impact
OSR Tech. Rept. No. 5, Contract AF 18(600)-1217,
June 1956.
66. W. S. Partridge, H. B. Vanfleet, and C. R. Whited;
An Investigation of Craters formed by High Speed Pellets
OSR Tech. Rept. No. 9, Contract AF 18(600)-1217.
67. M. E. van Valkenburg, W. G. Clay, and J. H. Huth;
Impact Phenomena at High Speeds
Journal of Applied Physics, Vol. 27, 1956.
p. 1123-1129.
68. M. E. van Valkenburg, J. S. Thompson, and J. H. Huth;
Some New Data on High-Speed Impact Phenomena
Journal of Applied Mechanics, Vol. 24, March 1957,
p. 65-63.
69. W. S. Partridge; High-Velocity Impact Studies at the University of Utah
Second Hypervelocity Impact Symposium, Vol. 1,
May 1957.
70. H. B. Vanfleet, C. R. Whited, and W. S. Partridge;
High Velocity Impact Craters in Lead-Tin Alloys
OSR Tech. Rept. No. 13, Contract AF 18(600)-1217,
January 1958.

71. W. S. Partridge and W. G. Clay; Studies of High-Velocity Impact in Wax
Journal of Applied Physics, Vol. 29, 1958,
p. 939-942.
72. W. S. Partridge, H. B. Vanfleet, and C. R. Whited;
Crater Formation in Metallic Targets
Journal of Applied Physics, Vol. 29, 1958,
p. 1332.
73. C. R. Morris, W. S. Partridge, and E. T. Cannon;
Perforation of Thin Aluminum Targets
Tech. Report UU-1, August 1958, Utah University.
74. M. D. Fullmer, W. S. Partridge, E. T. Cannon;
Penetration and Perforation Studies of Thin Glass Targets
Tech. Report UU-2, August 1958, Utah University.
75. W. S. Partridge, C. R. Morris, and M. D. Fullmer;
Perforation and Penetration Effects of Thin Targets
Third Hypervelocity Impact Symposium, Vol. 1,
October 1958.
76. H. B. Vanfleet, W. S. Partridge and E. T. Cannon;
The Anomalous Behaviour of Lead-to-Lead Impact
Third Hypervelocity Impact Symposium, Vol. 1,
October 1958.

77. M. A. Cook and R. T. Keyes; Microsecond Framing Camera Observations of High Velocity Impact. Third Hypervelocity Impact Symposium, Vol. 1, October 1958.
78. C. E. McDermott, E. T. Cannon, and R. W. Grow; Temperature Studies and Effects in Perforation of Thin Aluminum Targets. Technical Report UU-3, May 15, 1959. University of Utah.
79. D. K. Johnson, E. T. Cannon, E. P. Palmer, and R. W. Grow; Cratering Produced in Metals by High-Velocity Impact. Tech. Rept. No. UU-4, Contract AF 04(647)-176, July 1959.
80. J. S. Clark, R. R. Kadesch, and R. W. Grow, Spectral Analysis of the Impact of Ultra Velocity Copper Spheres into Copper Targets. OSR Tech. Rept. No. 16, Contract AF 18(600)-1217, September 1959.
81. R. T. Keyes, R. W. Bartlett, and M. A. Cook; Framing Camera Observations of Ultra High Velocity Penetration in Transparent Targets and a Mechanism for Crater Expansion. Fourth Hypervelocity Impact Symposium, Vol. 3, April 1960; also AFOSR-TN-60-851, March 1960.

82. E. P. Palmer, R. W. Grow, D. K. Johnson, and G. H. Turner; Cratering; Experiment and Theory
Fourth Hypervelocity Impact Symposium, Vol. 1,
April 1960.
83. R. W. Grow, R. R. Kadesch, E. P. Palmer, W. H. Clark,
J. S. Clark, and R. E. Blake; Experimental
Investigation of Spray Particles Producing the
Impact Flash
Fourth Hypervelocity Impact Symposium, Vol. 3,
April 1960.
84. W. H. Clark, R. R. Kadesch, and R. W. Grow; Hyper-
velocity Impact Spray Particles
OSR Tech. Rept. No. 18, Contract AF 49(638)-462,
May 1960.
85. R. E. Blake, R. W. Grow, and E. P. Palmer; Velocity
and Size Distribution of Impact Spray Particles
OSR Tech. Rept. No. 19, Contract AF 04(647)-176,
May 1960.
86. G. H. Turner, E. P. Palmer, and R. W. Grow; Projectile
Effects and Subsurface Disturbance in High-Velocity-
Impact Cratering in Lead
Tech. Rept. No. UU-5, Contract AF 04(647)-176,
August 1960.

Watertown Arsenal

87. J. P. McDonough and E. N. Hegge; Observations of
Projectile Impacts of Sand Particles Ranging
from 2400 f.p.s. to 7,000 f.p.s.
Third Hypervelocity Impact Symposium, Vol. 1,
October 1958.

88. J. P. McDonough and E. N. Hegge; Observation of Metallic Projectile Impacts of Small Particles at Velocities Ranging from 5000 f.p.s. to 7500 f.p.s. Part 2.
First Hypervelocity Technique Symposium,
October 1960.

89. K. H. Abbot; Metallurgical Observations of High Speed Impact
Fourth Hypervelocity Impact Symposium, Vol. 2,
April 1960.

Others

90. J. S. Rinehart; Some Observations on High-Speed Impact
Popular Astronomy, Vol. 58, 1950, p. 458-464.

91. J. S. Rinehart and W. C. White; Shapes of Craters formed in Plaster of Paris by Ultra-Speed Pellets
American Journal of Physics, Vol. 20, 1952, p. 14.

92. J. S. Rinehart; Surface Energy, a Mode for Energy Absorption during Impact
American Journal of Physics, Vol. 21, 1953,
p. 305-307.

93. J. S. Rinehart and J. Pearson; Behavior of Metals under Impulsive Loads
American Society for Metals, Cleveland, 1954.

94. D. C. Jenkins; Erosion of Surface by Liquid Drops
Nature, Vol. 176, 1955, p. 303.

95. R. J. Charles; High Velocity Impact in Comminution Mining Engineering, Vol. 8, 1956.
96. S. Singh and P. N. Gandhi; Effects Produced by Explosives with Lined Cavities in Steel Research, Vol. 9, 1956; p. 55.
97. F. P. Bowden and J. H. Brunton; Damage to Solids by Liquid Impact at Supersonic Speeds Nature Vol. 181, 1958; p. 873-875.
98. H. A. Cohen, A. Corman, and M. Dubin; Calibration of Micrometeorite Detectors used in Satellite and Rockets Third Hypervelocity Impact Symposium, Vol. 1, October, 1958.
99. R. Graham; Impact Physics (Bibliography) Sandia Corporation, SCR, December 1958.
100. P. A. Franken; Preliminary Survey of High-Speed Impact Information WADC Tech. Rept. 58-577, ASTIA D 216-029, June 1959.
101. A. Soundrarag; Studies of Copper Targets Attacked by Shaped Charges Acta Met. Vol. 7, 1959, p. 752.
102. D. B. Lull; Analysis of Impact of Hypervelocity Pellet with a Thin Shield Memo., A. D. Little Corp., December 1959.

103. H. G. Hopkins and H. Kolsky; Mechanics of Hypervelocity Impact of Solids
Fourth Hypervelocity Impact Symposium, Vol. 1,
April 1960.

Theory

104. Encyclopedia Britannica; Armour Plate; Resistance to Penetration
1959 Edition.
105. G. R. Irwin; Review of Missile Penetration Mechanics
Unclassified Preprint, also First Hypervelocity Impact Symposium, Santa Monica, 1955 (Secret).
106. H. A. Bethe; An Attempt at a Theory of Armor Penetration
Ordnance Laboratory Report, Frankford Arsenal, May 23, 1941
107. G. I. Taylor; The Formation and Enlargement of a Circular Hole in a Thin Plastic Plate
Quart. J. Mechanics and Applied Mathematics, Vol. 1, 1948, p. 103.
108. W. T. Thomson; Approximate Theory of Armor Penetration
Journal of Applied Physics, Vol. 26, 1955, p. 30, also Vol. 26, 1955, p. 919.

109. M. Zaid and B. Paul; Armor Penetration
Ordnance, Vol. 41, 1956-57, p. 609-611.
110. M. Zaid and B. Paul; Mechanics of Thin Plate
Perforation (Unclassified Title)
Proc. Second Fuze Symposium, Diamond
Ordnance Fuze Laboratories, March 1956
(Secret)
111. M. Zaid and B. Paul; Mechanics of High Speed
Projectile Perforation
J. of the Franklin Institute, Vol. 264,
1957, p. 117-126.
112. M. Zaid and B. Paul; Normal Perforation of a
Thin Plate by a Truncated Projectile
Journal of the Franklin Institute, Vol. 265,
1958, p. 317-335.
113. M. Zaid and B. Paul; Oblique Perforation of a
Thin Plate by a Truncated Conical Projectile
Journal of the Franklin Institute, Vol. 268,
1959, p. 24-45.
114. W. S. Partridge and H. B. Vanfleet; Similarities
between Lunar and High-Velocity-Impact
Craters
The Astrophysical Journal, Vol. 128, 1958,
p. 416-419.

115. F. E. Allison; A Review of the Theories Concerning Crater Formation by Hypervelocity Impact
Third Hypervelocity Impact Symposium, Vol. 1,
October 1958.
116. D. Rodriguez; Meteor Shielding for Space Vehicles
Aerospace Engineering, Vol. 19, December 1960,
p. 20.
117. G. Grimmer; Probability that a Meteorite will Hit or Penetrate a Body Situated in the Vicinity of the Earth
Journal of Applied Physics, Vol. 19, 1948,
p. 947.
118. J. L. Bohm and O. P. Fuchs; High Velocity Impact Studies Directed towards the Determination of the Spatial Density, Mass and Velocity of Micrometeorites at High Altitudes
Contract AF 19(604)-1894, Scientific Report
No. 1, ASTIA AD 243 106.
119. M. Zaid; An Analytical Approach to Hypervelocity Impact Mechanics
Fourth Hypervelocity Impact Symposium, Vol. 3,
April 1960. Also Technik Incorporated,
Research Analysis Development, Garden City,
New York, April 1960. Contract DA-30-069-507-
ORD-2674.

120. M. Zaid; Penetration by Hypervelocity Particles
Technik Incorporated, Research Analysis
Development, Garden City, New York,
November 1960, Contract DA-30-069-507-
ORD-2674.
121. E. Opik; Researches on the Physical Theory of
Meteor Phenomena: I Theory of the Formation
of Meteor Craters
Acta et Comm. Univ. Tartuensis 1936.
122. G. Birkhoff, D. P. MacDougall, E. M. Pugh, and
G. I. Taylor; Explosives with Lined
Cavities
Journal of Applied Physics, Vol. 19, 1948,
p. 563.
123. D. C. Pack and W. M. Evans; Penetration by High
Velocity ('Munroe') Jets. I
Proc. of the Physical Society, London,
Vol. B 64, 1951.
124. N. Rostoker; The Formation of Craters by High
Speed Particles
Meteoritics, Vol. 1, 1953, p. 11.
125. M. A. Cook; Mechanism of Cratering in Ultra-
High Velocity Impact
Explosives Research Group, Univ. of Utah,
1957, AFOSR-TN-57-486, AD 136 479, Contract
AF-18(603)100.

126. O. G. Engel; Waterdrop Collisions with Solid Surface
Journal of Research of the N.B.S., Vol. 54,
1955, p. 281-298.
127. O. G. Engel; Erosion Damage to Solids caused by High-Speed Collisions with Rain
Journal of Research of the N.B.S., Vol. 61,
1958, p. 47.
128. R. L. Bjork; Effect of Meteoroid Impact on Steel and Aluminum in Space
Rand Paper No. P-1662, also the 10th International Astronautical Congress, London, England, August 1959.
129. F. L. Whipple; Vistas in Astronautics 1958; The Meteoric Risk to Space Vehicles
pp. 115-124, Pergamon Press, New York, 1958.
130. N. H. Langton; The Thermal Dissipation of Meteorites by a Bumper Screen
Bericht über den V. Internationalen Astronautischen Kongres, August 1954.
131. C. E. McDermott, E. T. Cannon, and R. W. Grow; Temperature Studies and Effects in Perforation of Thin Aluminum Targets
Tech. Rept. UU-3, Univ. of Utah, May 1959.

132. M. A. Lavrent'yev; The Problems of Piercing at Cosmic Velocities
NASA TT F-40, May 1960
Translated from 'Artificial Earth Satellites',
No. 3, Academy of Sciences, USSR (Moscow)
1959.
133. K. P. Stanyukovitch and V. V. Fedynskiy; The Destructive action of Meteorite Impacts
Doklady Akademii Nauk SSSR, Vol. 57,
No. 2, 1947, p. 129-132, (Translation
ASTIA AD 124 240).
134. K. P. Stanyukovitch; Concerning the Impact of Solids at High Velocities
Soviet Physics JETP Vol. 9, 1959, p. 1141.
135. D. B. Beard; Interplanetary Dust Distribution and Erosion Effects
Third Hypervelocity Impact Symposium,
Vol. 1, October 1958.
136. G. M. Bryan; A Model of Oblique Impact
Fourth Hypervelocity Impact Symposium
Vol. 3, April 1960
137. J. M. Walsh and R. H. Christian; Equation of State of Metals from Shock Wave Measurements
Physical Review, Vol. 97, 1955. p. 1544-1556.

138. R. W. Goranson, D. Bancroft, B. L. Burton,
T. Blechar, E. E. Houston, E. F. Gittings,
and S. A. Landeen; Dynamic Determination
of the Compressibility of Metals
Journal of Applied Physics, Vol. 26, 1955,
p. 1472-1479.
139. J. M. Walsh and R. H. Christian; Equations of
State of Metals from Shock Wave Measurements
Physical Review, Vol. 97, 1955, p. 1544-1556.
140. D. Bancroft, E. L. Peterson, and S. Minshall,
Polymorphism of Iron at High Pressures
Journal of Applied Physics, Vol. 27, 1956,
p. 291-298.
141. J. M. Walsh, M. H. Rice, R. G. McQueen, and
F. L. Yarger; Shock Wave Compression of
Twenty-Seven Metals Equation of State of
Metals
Physical Review, Vol. 108, 1957, p. 196-216.
142. S. Katz, D. R. Curran, and D. G. Doran; Hugoniot
Equation of Aluminum and Steel from Oblique
Shock Measurement
Poulter Lab. Tech. Rept. O25-57, December 1957:
Also Journal of Applied Physics, Vol. 30,
p. 568-576, 1959.
143. M. H. Rice, R. G. McQueen, and J. M. Walsh;
Compression of Solids by Strong Shock Waves
pp. 1-63, Solid State Physics, Vol. 6,
Academic Press, New York, 1958.

144. W. A. Allen, H. L. Morrison, D. B. Ray, and J. W. Rogers; Fluid Mechanics of Copper Third Hypervelocity Impact Symposium, October 1958.
145. L. V. Al'tshuler, K. K. Krupnikov, B. N. Ledenev, V. I. Zhuchikhin, and M. I. Brazhnik; Dynamic Compressibility and Equation of State of Iron under High Pressures Soviet Physics JETP, Vol. 34, 1958, p. 606-614.
146. L. V. Al'tshuler, K. K. Krupnikov, and M. I. Brazhnik; Dynamic Compressibility of Metals under Pressures from 400,000 to 4,000,000 Atmospheres Soviet Physics JETP, Vol. 34, 1958, p. 614-619.
147. F. S. Minshall; The Dynamic Response of Iron and Iron Alloys to Shock Waves A.I.M.E. Conference on "Response of Materials to High-Velocity Deformation", Colorado, July 1960.
148. R. R. McQueen and S. P. Marsh; Equation of State for Nineteen Metallic Elements from Shock-Wave Measurements to Two Megabars Journal of Applied Physics, Vol. 31, 1960, p. 1253-1269.
149. G. R. Fowles; Shock Wave Compression of Hardened and Annealed 2024 Aluminum Poulter Lab. Tech. Rept. O11-60, October 1960.

150. D. S. Hughes, L. E. Gourley and M. F. Gourley; Shock-Wave Compression of Iron and Bismuth Journal of Applied Physics, Vol. 32, 1961, p. 624-629.
151. K. L. DeVries, G. S. Baker, and P. Gibbs; A Survey of High Pressure Effects of Solids Univ. of Utah, WADD TR 59-341, Contract AF 33(616)-5016, Project 7021.
152. R. L. Bjork; Analysis of the Formation of Meteor Crater, Arizona; a Preliminary Report Rand Corporation, p. 2370, July 6, 1961.
153. G. M. Bryan; Cratering of Lead by Oblique Impacts of Hypervelocity Steel Pellets Carnegie Institute of Technology, Department of Physics, Twenty-second Quarterly Progress Report, Contract No. DA-36-061.

TABLE I ESTABLISHMENTS ACTIVE IN HIGH VELOCITY RESEARCH																						
LABORATORY	ACCELERATORS										TARGETS								PROJECTILES			
	SHAPED CHARGES	AIR CAVITY CHARGES	POWDER GUN	HIGH EXPLOSIVE GUN	EXPLODING WIRE	SHOCK TUBE	LIGHT GAS GUN	ELECTRICALLY HEATED GAS GUN	ELECTRO-MAGNETIC GUN	ELECTRO-STATIC ACCELERATOR	PROTON CHARGE PARTICLE ACCELERATOR	SEMI-INFINITE TARGETS	FINITE TARGETS	THIN TARGETS	SPACE THIN PLATE TARGETS	BUMPERS	HEATED TARGETS	NON-METAL TARGETS	OBlique IMPACTS	DISC SPHERES CYLINDERS	MICROPARTICLES	RODS
AEROJET GENERAL CORPORATION	X	X					X	X						X					X	X		
AR DE, FORT HALSTEAD, UNITED KINGDOM	X						X					X								X		
A.R.O. INCORPORATED			X				X	X														
ARMOUR RESEARCH FOUNDATION (CHICAGO)						X	X															
AVCO, WILMINGTON							X	X									X			X		
BALLISTIC RESEARCH LABORATORY	X	X					X					X		X				X	X	X	X	
C.A.R.D.E.			X				X					X	X					X		X		
CARNEGIE INSTITUTE OF TECHNOLOGY	X	X										X		X			X		X	X		
COLORADO SCHOOL OF MINES			X									X						X		X		
CONVAIR, SAN DIEGO		X					X								X					X		
DENVER RESEARCH INSTITUTE	X	X													X					X		
EGLIN AFB.							X					X	X				X	X		X		
FRANKFORD ARSENAL				X																		
GENERAL ELECTRIC COMPANY	X			X					X							X				X		
GRIMMAN AIRCRAFT											X										X	
LINCOLN LABORATORY, MIT			X				X					X										X
MIT, A.S.R.L.			X									X				X				X		
NASA, AMES			X				X					X			X			X	X	X		X
NASA, LANGLEY			X				X					X				X	X	X		X		
NAVAL ORDNANCE TEST STATION			X				X						X							X		X
NAVAL RESEARCH LABORATORY			X				X	X				X	X		X			X		X		
NORTH AMERICAN					X																	
PICATINNY ARSENAL		X										X						X		X		
THOMPSON RAMO WOOLDRIDGE CORPORATION										X		X		X							X	
BRIDGES AND BLOSSOM INCORPORATED								X				X						X		X		
SRI FOURIER LABORATORIES	X	X										X						X	X		X	
TECHNICAL OPERATIONS					X																	
UNIVERSITY OF UTAH	X	X	X				X		X			X		X			X	X		X		
UTAH RESEARCH AND DEVELOPMENT COMPANY INCORPORATED							X					X								X		
WATERTOWN ARSENAL			X				X					X								X		

TABLE III POSTULATED EMPIRICAL EQUATIONS

PENETRATION LAW	TARGET	PROJECTILE	SHAPE	SIZE	VELOCITY	INVESTIGATOR
$\bar{p} = \left(\frac{3K_1 K_2}{2\pi} \right) V_0^{1/3} \left(\frac{\rho_p}{\rho_t} \right)^{1/3} \left(\frac{V}{c_t} \right)^{-1} \frac{1}{(3-K_2 V_{c_t})}$	ALUMINUM WAX (10°C) BRASS LEAD MAGNESIUM STEEL ZINC	ALUMINUM BRASS LEAD MAGNESIUM STEEL ZINC	SPHERES	$\frac{1}{8}$ "	$\frac{V}{c_t} \approx 1$	VAN VALKENBURG et al (67)
$\frac{\bar{p}}{d} = 2.5 \left(\frac{V}{c_t} \right)^{1.4}$	ALUMINUM BRASS LEAD MAGNESIUM MAGNESIUM-LITHIUM LEAD	ALUMINUM BRASS LEAD MAGNESIUM MAGNESIUM-LITHIUM LEAD	SPHERES CYLINDERS	$\frac{1}{8}$ "	$0.1 \leq \frac{V}{c_t} \leq 1.0$	HUTII et al (68)
$p = 1.25 \frac{m_p^{1/3} V^{1/3}}{\rho_t^{1/3} H^{1/4}}$	ALUMINUM BRASS BRONZE COPPER MALLORY STEEL TITANIUM	—	JET	—	10,540 f.p.s.	PUGH AND EICHELEFGER (14)
—	LEAD	STEEL	DISC	—	1300 to 15400 f.p.s.	KINEKE (3)
$\bar{p} = \frac{V_p (1 - e^{-K_4 E})}{K_1 K_2 (2m_p E)^{1/2} + K_3}$	LEAD	LEAD	SPHERES	$\frac{1}{8}$ " $\frac{3}{16}$ " $\frac{3}{8}$ "	< 5900 f.p.s.	VANFLEET et al (66)
$p = K m_p^{1/3} \frac{(V - V_0)}{c_t}$ $\frac{V_0}{c_t} < \frac{V}{c_t} < 2$	WAX (23°C)	WAX (4°C)	SPHERES CYLINDERS	0.177 ins [d=0.22 ins L=0.33 ins d=0.22 ins L=0.388 ins]	$0.3 < \frac{V}{c_t} < 2.2$	PARTRIDGE AND CLAY (71)
$\frac{\bar{p}}{d} = K \left(\frac{V}{c_p} \right)^{c_k} c_p$	ALUMINUM COPPER LEAD STEEL TIN	ALUMINUM COPPER MALLORY 1000 STEEL	FRAGMENTS	—	1000 to 6000 f.p.s.	McKENZIE et al (57)
$\frac{p}{d} = \frac{1.2 c_p \rho_p}{c_t \rho_t + c_p \rho_p} \left(\frac{V}{c_p} \right)$ $= 136.8 V_1 \rho_p^{1/2}$ $c_t^2 \rho_p$ 1.5 d ≤ target thickness ≤ 5 d	ALUMINUM 1100 ALUMINUM 2024-O COPPER LEAD STEEL ALUMINUM 2024-O COPPER LEAD ALUMINUM COPPER IRON LEAD ZINC	MERCURY WATER ALUMINUM COPPER IRON LEAD ZINC	SPHERES	—	< 6500 f.p.s.	ENGEL (40)
$\frac{p}{d} = 2.2 H \left(\frac{\rho_p}{\rho_t} \right)^{2/3} \left(\frac{V}{c_t} \right)^{2/3}$	COPPER LEAD	ALUMINUM COPPER LEAD MAGNESIUM LITHIUM STEEL TUNGSTEN	SPHERES	0.125", 0.178" 0.125", 0.119" 0.125", 0.109" 0.125", 0.218" 0.125", 0.125", 0.096"	$\leq 11,000$ f.p.s.	CHARTERS AND LOCKE (28)
$\frac{p}{d} = 1.9 \left(\frac{\rho_p}{\rho_t} \right) \left(\frac{V}{c_t} \right)$	ALUMINUM STEEL STEEL	ALUMINUM MAGNESIUM NICKEL POLYETHYLENE STAINLESS-STEEL	MICROPARTICLES	100μ AND 150μ	2,300 - 13,200 f.p.s.	ANDERSON (62)
$p = 2.0 \left(\frac{\rho_p}{\rho_t} \right)^{0.8} \left(\frac{V}{c_t} \right)^{0.7}$	STEEL	STEEL	SPHERES	0.2"	$\approx 17,700$ f.p.s.	MADINE et al (12)
$p = 2.0 \left(\frac{\rho_p}{\rho_t} \right)^{0.8} \left(\frac{V}{c_t} \right)^{0.7}$	COPPER LEAD	ALUMINUM	SPHERES	0.2", 0.4"	—	—
$p = \frac{309.6 (\rho_p V L K)}{(\rho_p)^{0.778} (t + 2.8 K K)^{0.778}}$	ALUMINUM COPPER LEAD STEEL	ALUMINUM COPPER LEAD STEEL	SPHERES CYLINDER (L/d=1)	0.0625" 0.22" 0.50" 0.22" 0.50"	≤ 13000 f.p.s.	COLLINS AND FARRAR (35)
$p = \frac{K}{2} m_p^{1/3} V^{2/3}$	CADMIUM COPPER LEAD ZINC	—	—	—	—	BRI (52)
$p = \left(\frac{3}{4\pi K} \right)^{1/3} \frac{m_p^{1/3} V^{2/3}}{H^{1/3}}$	ALUMINUM COPPER STEEL	—	—	—	—	BRI (52)

TABLE IV
EMPIRICAL FITS TO THE PENETRATION LAW

$$p/d = k \left(\frac{\rho_p}{\rho_t} \right)^{2/3} \left(\frac{\rho_t v^2}{H_t} \right)^{1/3}$$

Target	ρ_t (gm/cc)	H_t (kg/mm ²)	Max. Vel (km/sec)	$k = \left(\frac{\rho_t}{\rho_p} \right)^{2/3} \left(\frac{H_t}{\rho_t v^2} \right)^{1/3} \left(\frac{p}{d} \right)$
Al. 1100F	2.79	*	4.37	*
Al. 2024 & 24ST	2.68	114-120	3.98	0.413 ± 0.007
Cu. (36)	8.88	36	3.33	0.366 ± 0.009
Cu. (65)	8.88	65	5.27	0.419 ± 0.031
Pb.	11.34	4	5.00	0.312 ± 0.020
Stl. 1020	7.69	111	3.95	0.378 ± 0.010
Stl. 1030	7.69	123	3.96	0.371 ± 0.012
Stl. 30 RC	7.74	302	3.52	0.279 ± 0.004
Cd.	8.66	23	5.01	0.309 ± 0.046
Ag.	10.45	*	2.54	*
Zn.	7.13	45	2.51	0.371 ± 0.014

* H_t for these materials is unknown. The values of $k/H_t^{1/3}$ for these are: (i) 1100F Al. target, $(0.287 \pm 0.008) \times 10^{-3}$ cm/dyne^{1/3}, and (ii) Ag. target $(0.277 \pm 0.024) \times 10^{-3}$ cm/dyne^{1/3}.

TABLE V
EMPIRICAL FITS TO THE LOGARITHMIC PENETRATION LAW

$$p/d = k_1 \log \left(1 + \frac{\rho_T v^2}{k_2 H_t} \right)$$

Proj.	Target	H _t	ρ _p /ρ _t	Max. Impact Vel. (km/sec)	k ₁	k ₂	Deviation (p/d)
Al.	1100F Al.	*	1.0	4.37	0.603	*	0.043
Al.	2024 Al.	120	1.0	2.00	0.602	3.815	0.091
Al.	24ST Al.	114	1.0	3.98	0.694	4.863	0.049
Fe.	2024 Al.	120	2.93	1.65	0.672	0.765	0.099
Cu.	2024 Al.	120	3.32	1.86	1.096	1.649	0.146
Sn.	Sn.	5.3	1.0	2.27	0.421	9.261	0.102
Al.	1020 Stl.	111	0.342	2.19	0.182	6.089	0.040
Fe.	1020 Stl.	111	1.0	1.71	0.521	4.305	0.106
Cu.	1020 Stl.	111	1.13	1.64	0.550	4.874	0.067
Pb.	1020 Stl.	111	1.46	1.29	1.116	11.639	0.049
Mg.	1030 Stl.	123	0.226	3.70	0.270	17.795	0.032
Al.	1030 Stl.	123	0.360	4.00	0.287	4.181	0.028
Fe.	1030 Stl.	123	1.0	3.96	0.501	3.416	0.043
Fe.	4140 Stl.	245	1.0	2.30	0.359	1.137	0.062
Fe.	30RC Stl.	302	1.0	2.26	0.632	3.730	0.020
Cu.	Cu.	36	1.0	3.33	0.535	4.145	0.029
Al.	Cu.	65	0.301	5.27	0.427	14.695	0.058
Cu.	Cu.	65	1.0	3.06	0.421	1.555	0.080
Al.	Pb.	4	0.237	5.00	0.454	63.909	0.108
Cu.	Pb.	4	0.786	2.19	0.539	6.847	0.102

* H_t for this material is unknown. The value of (k₂H_t) from the least squares fit is 122.5 × 10⁸ dynes/cm².

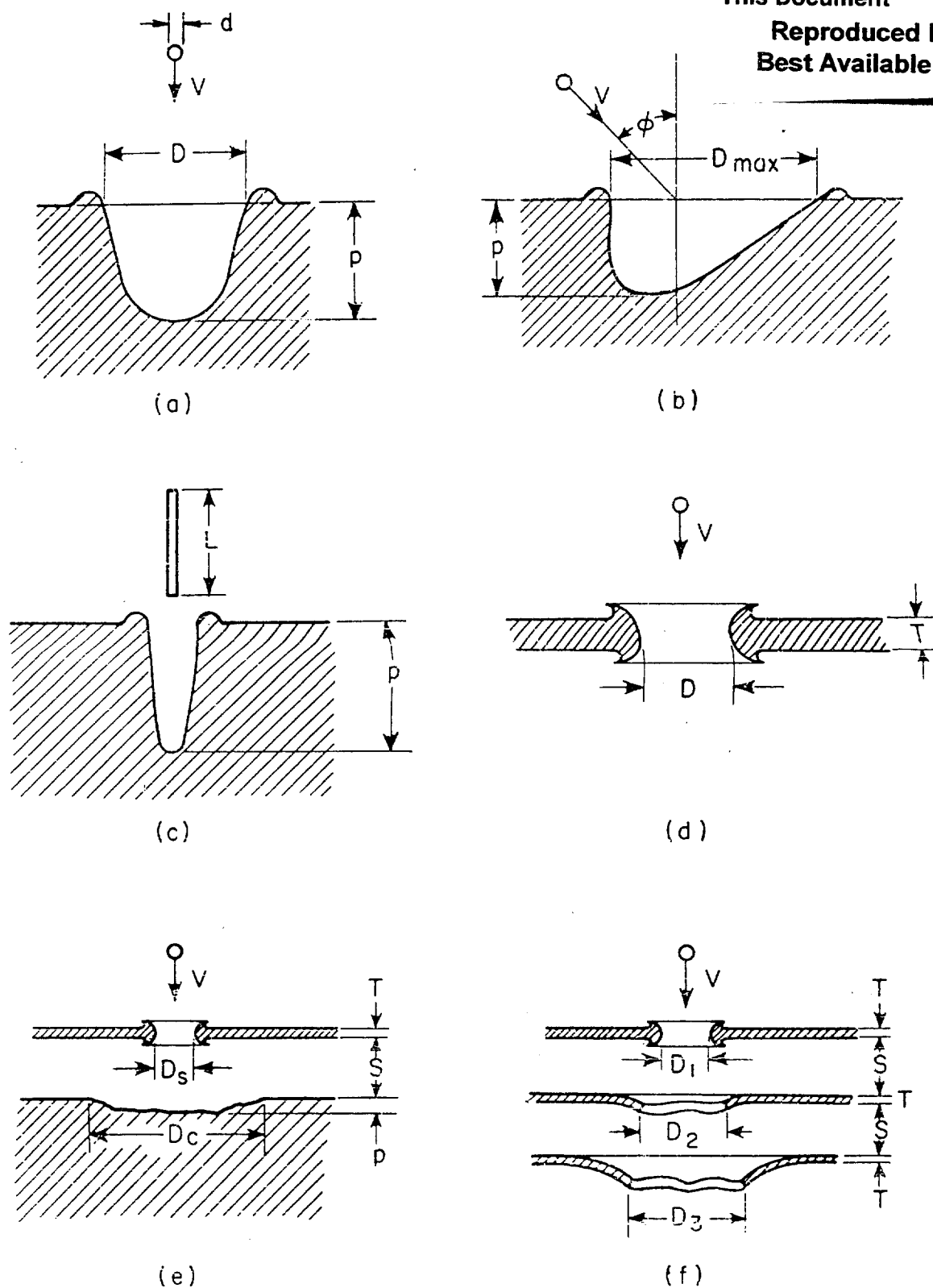


Fig. 1.1 Projectile-Target Configurations

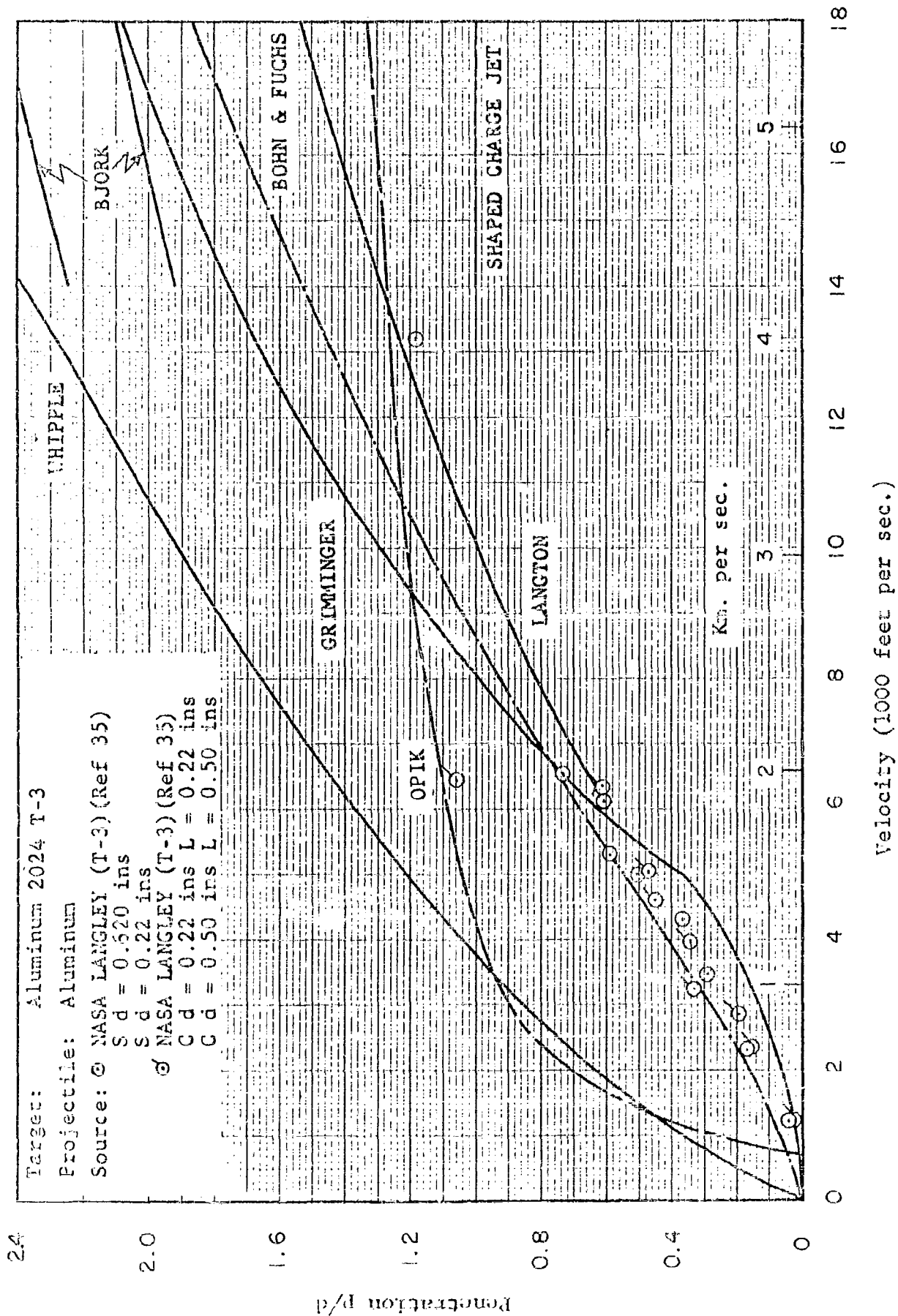


Fig. 1.2 The Penetration of Aluminum into Aluminum 2024 T-3 Targets

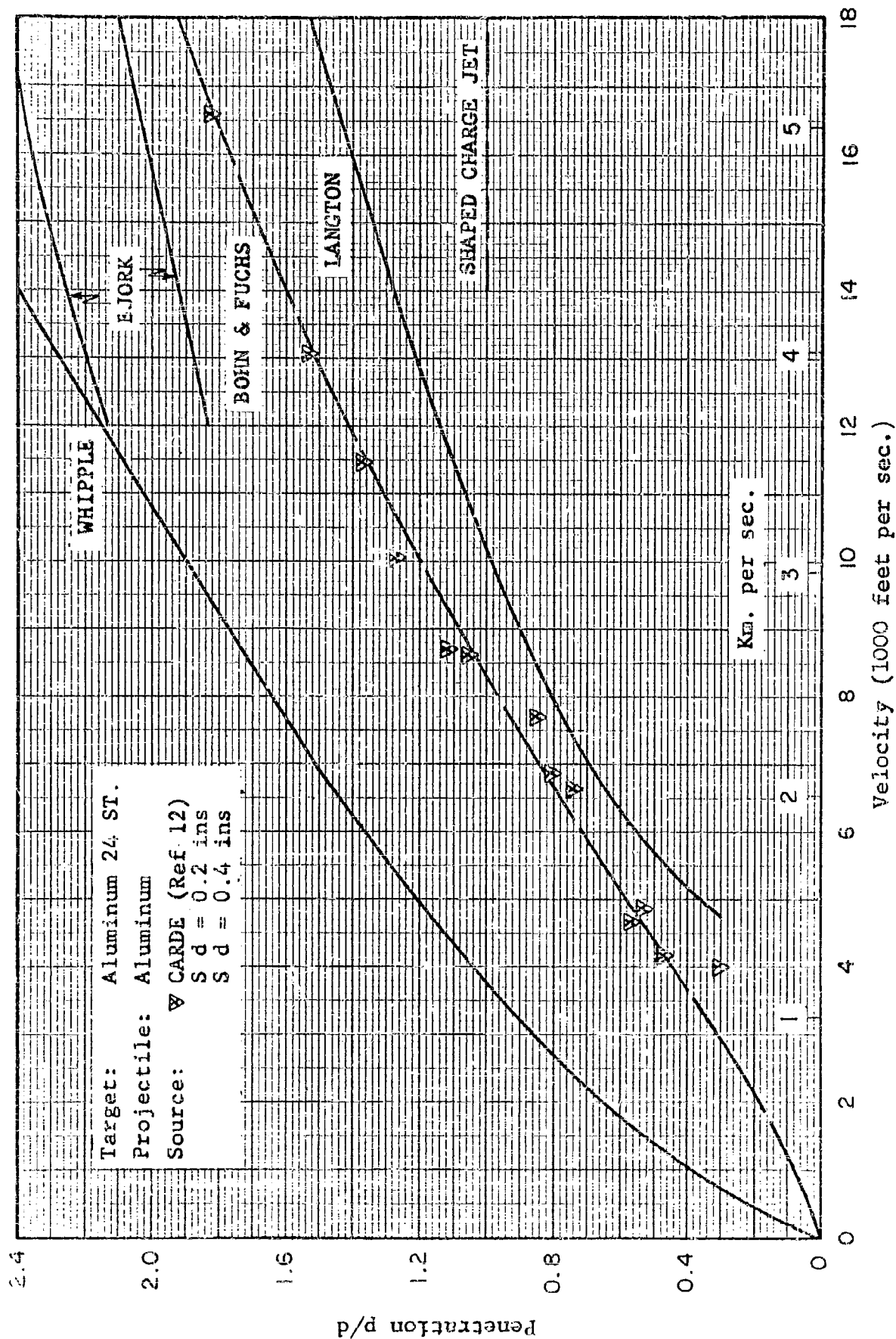


Fig. 1.3 The Penetration of Aluminum Spheres into 24 ST Aluminum Targets

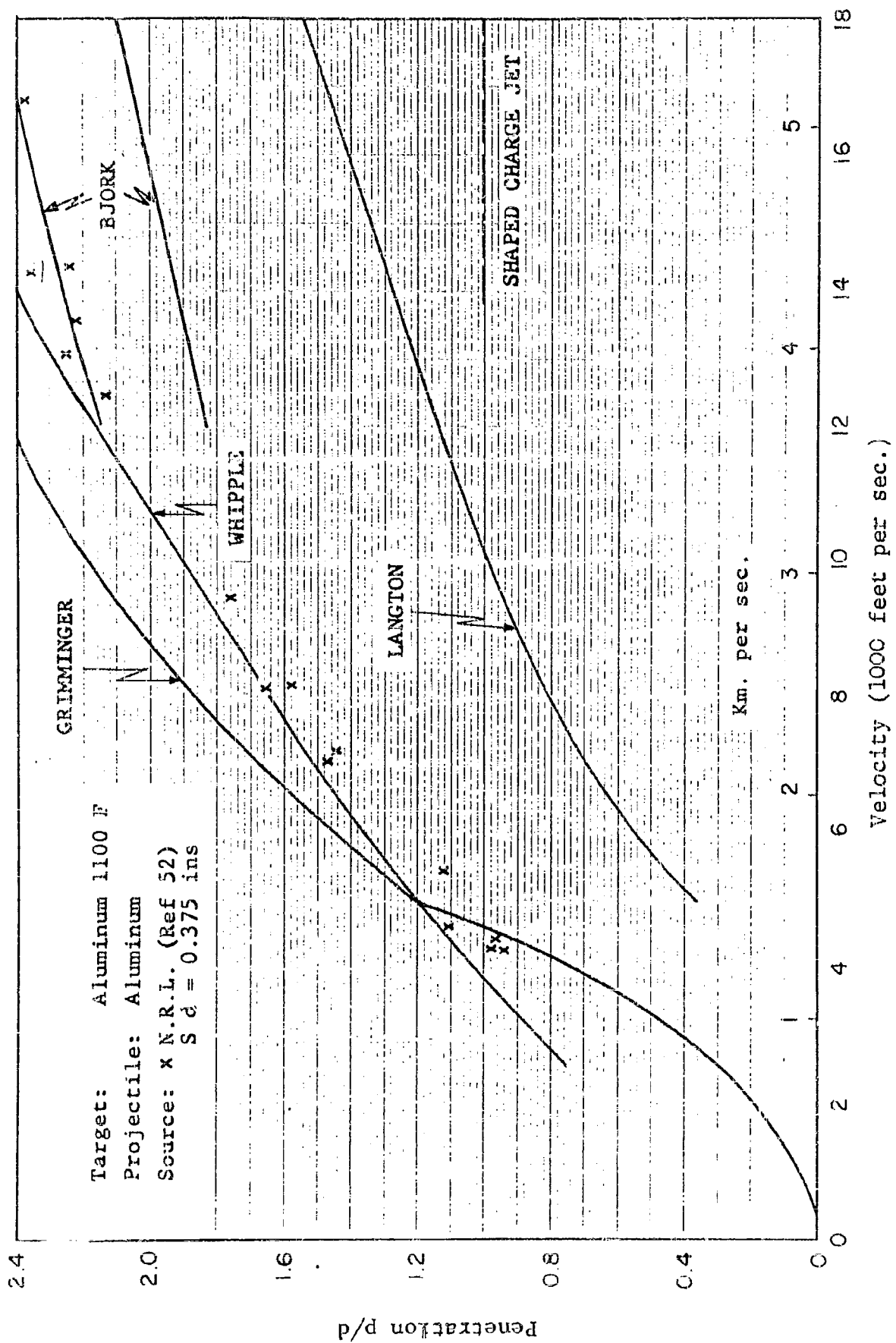


Fig. 1.4 The Penetration of Aluminum Spheres into 1100 F Aluminum Targets

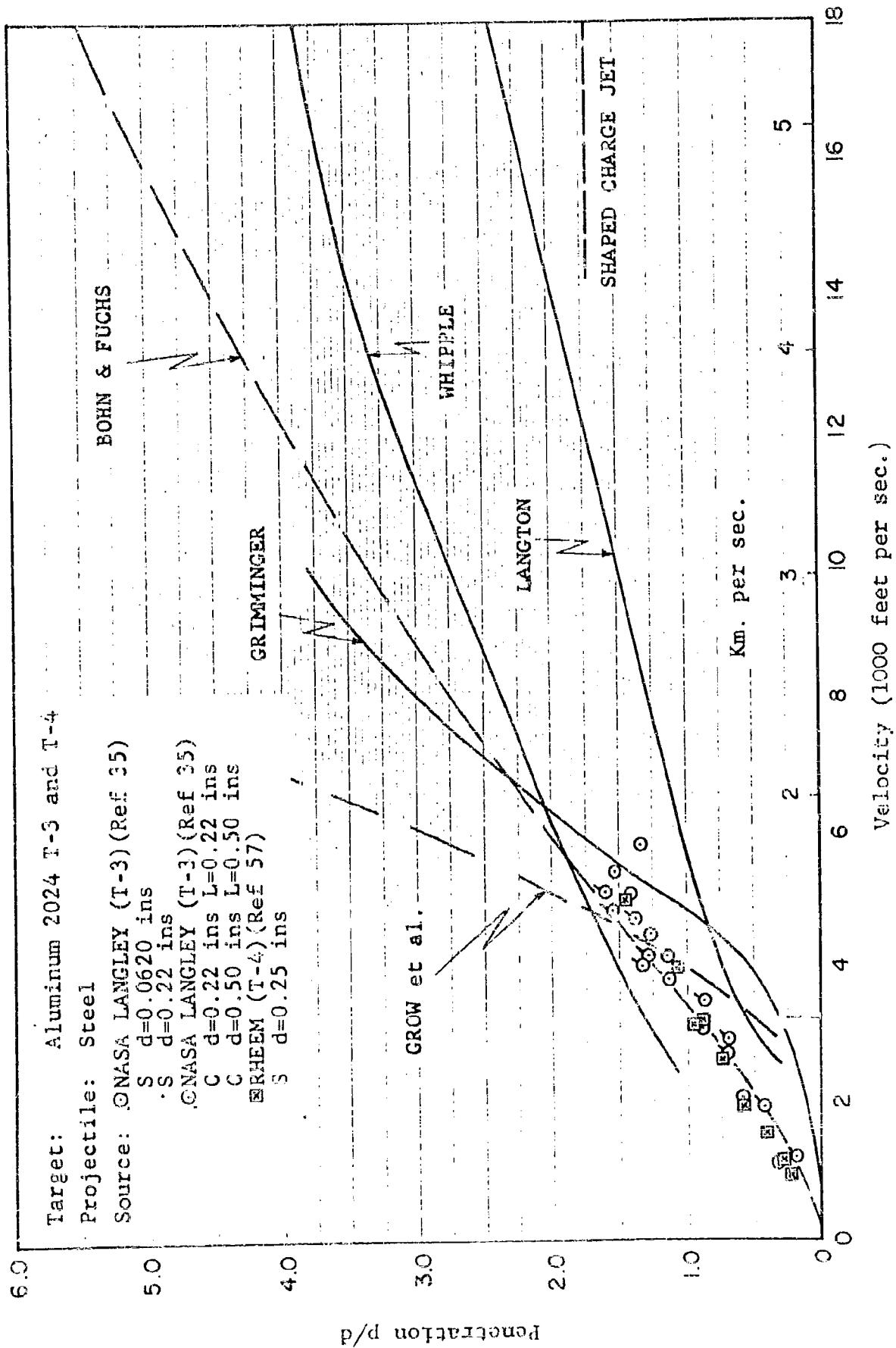


Fig. 1.5 The Penetration of Copper Projectiles into Aluminum 2024 T-3 and T-4 Targets

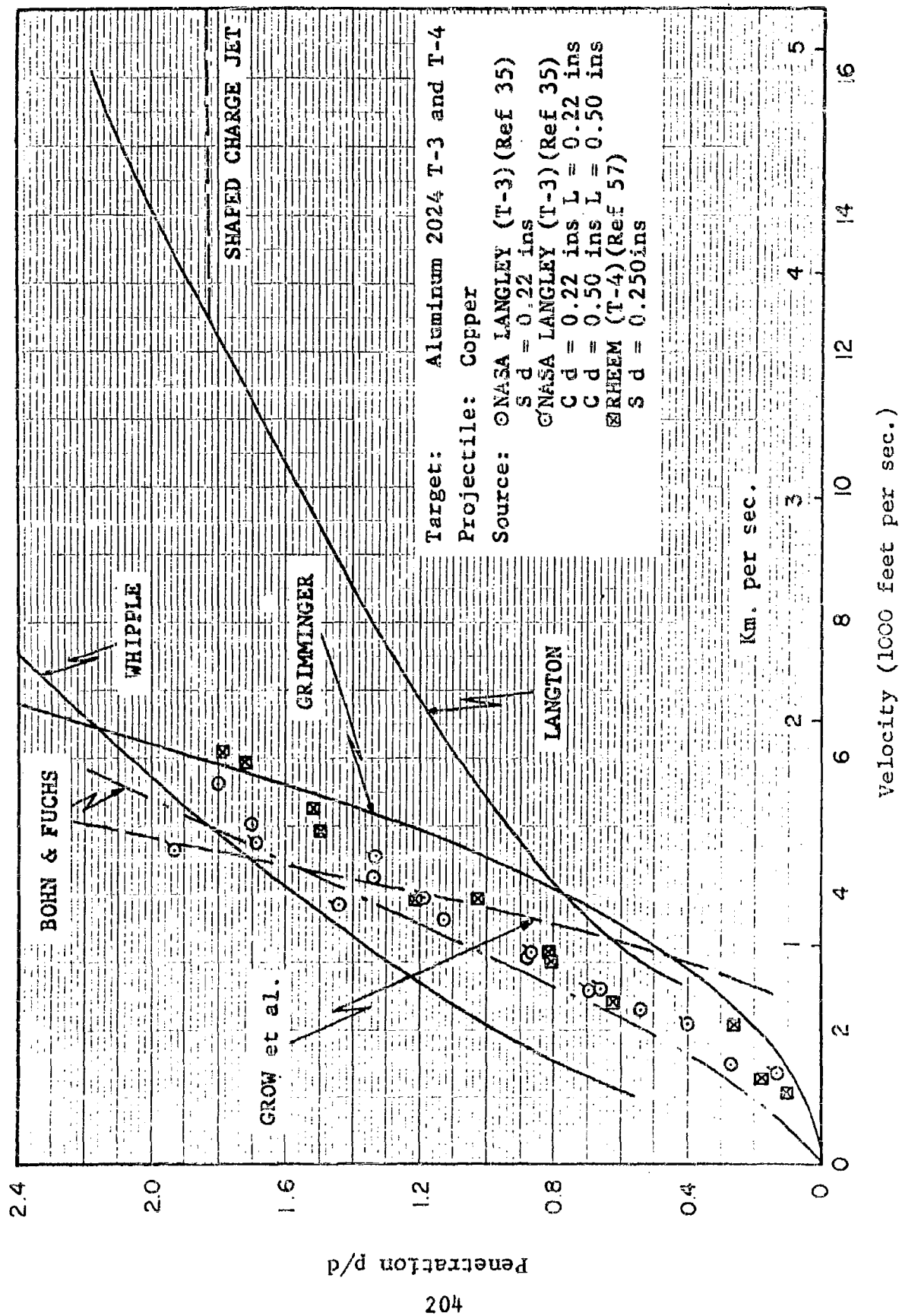


Fig. 1.6 The Penetration of Copper into Aluminum 2024 T-3 and T-4 Targets

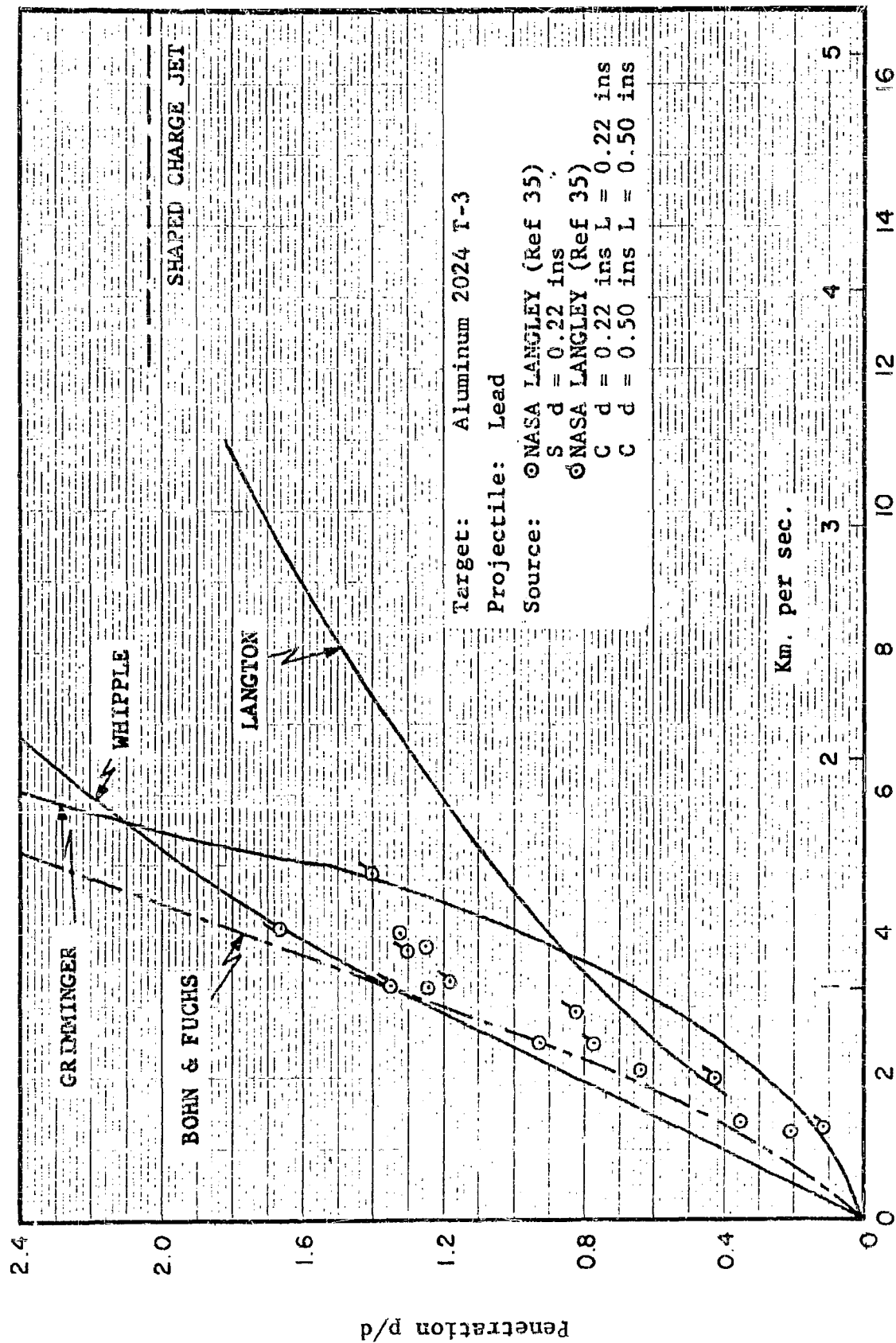


Fig. 1.7 The Penetration of Lead into Aluminum 2024 T-3 Targets

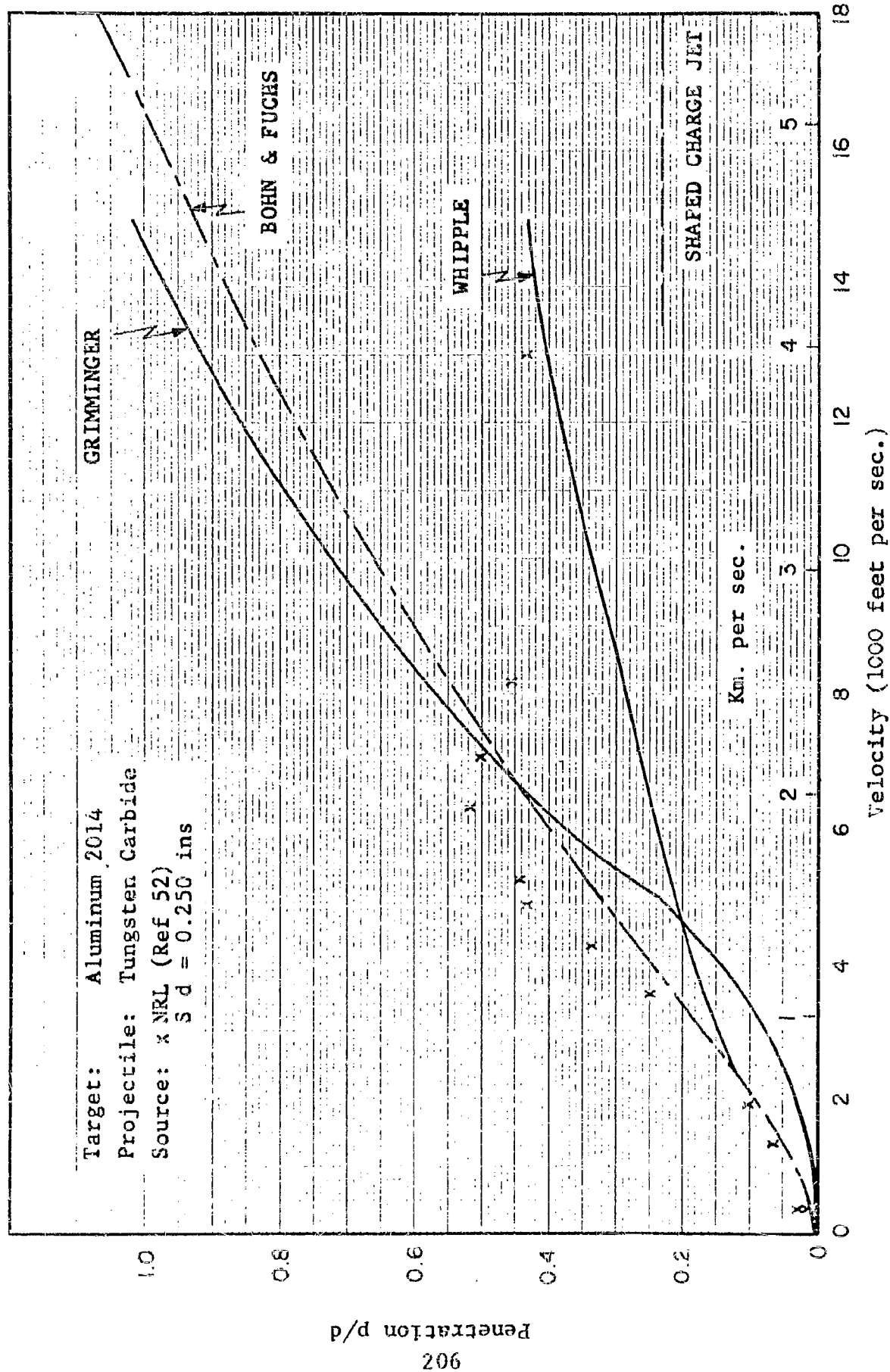


Fig. 1.8 The Penetration of Tungsten Carbide Spheres into Aluminum 2014 Targets

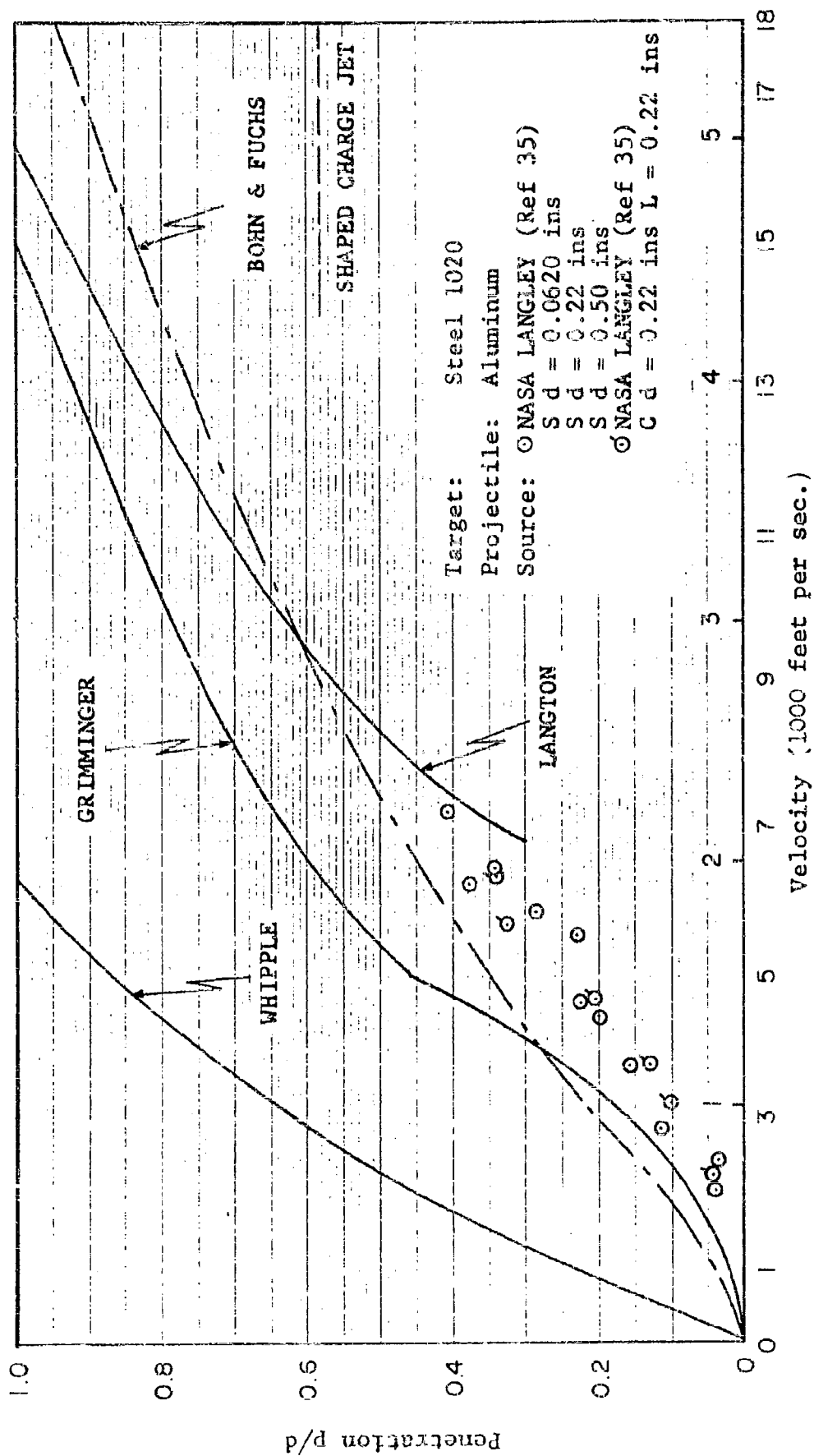


Fig. 1.9 The Penetration of Aluminum Projectiles into 1020 Steel Targets

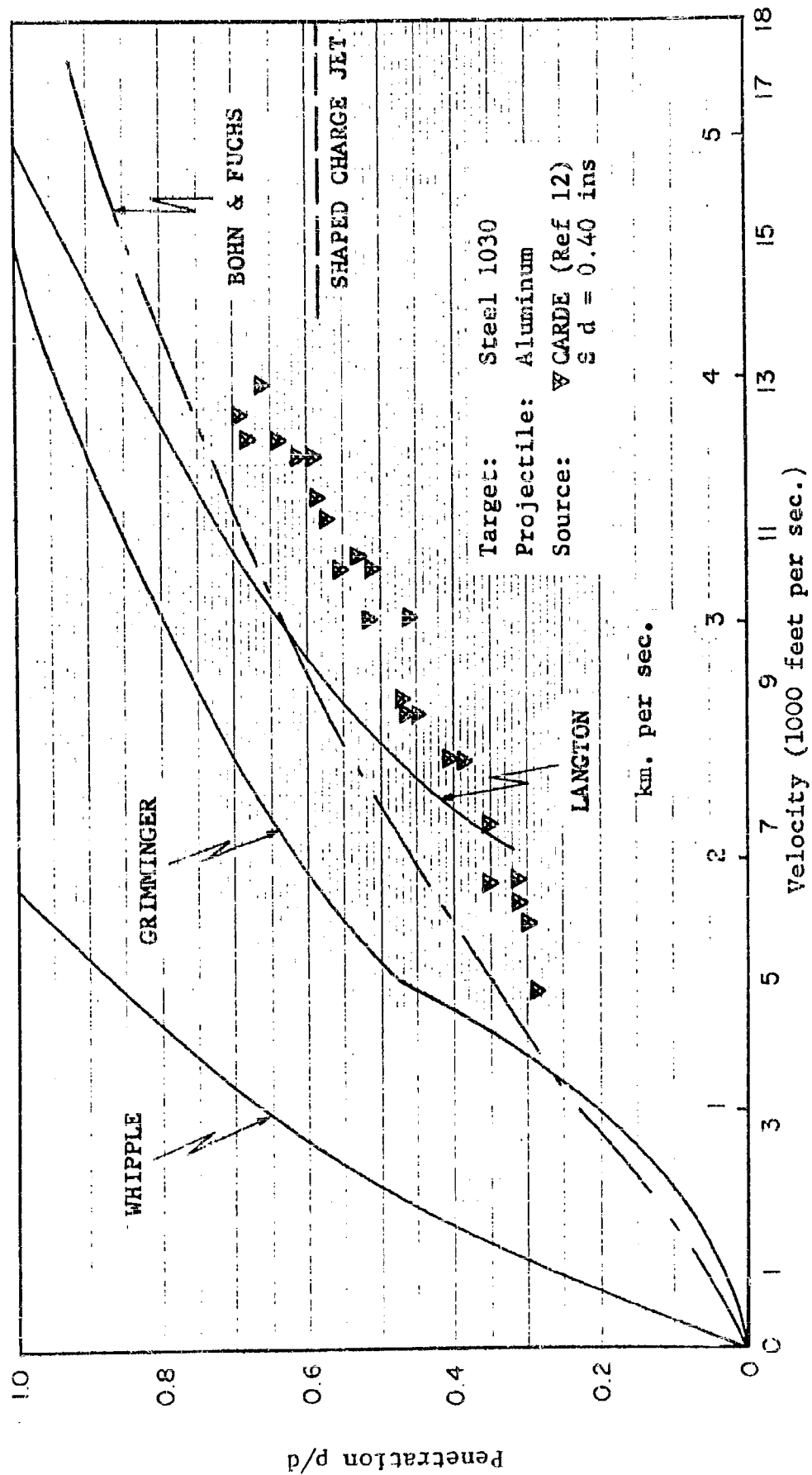


Fig. 1.10 The Penetration of Aluminum Projectiles into 1030 Steel Targets

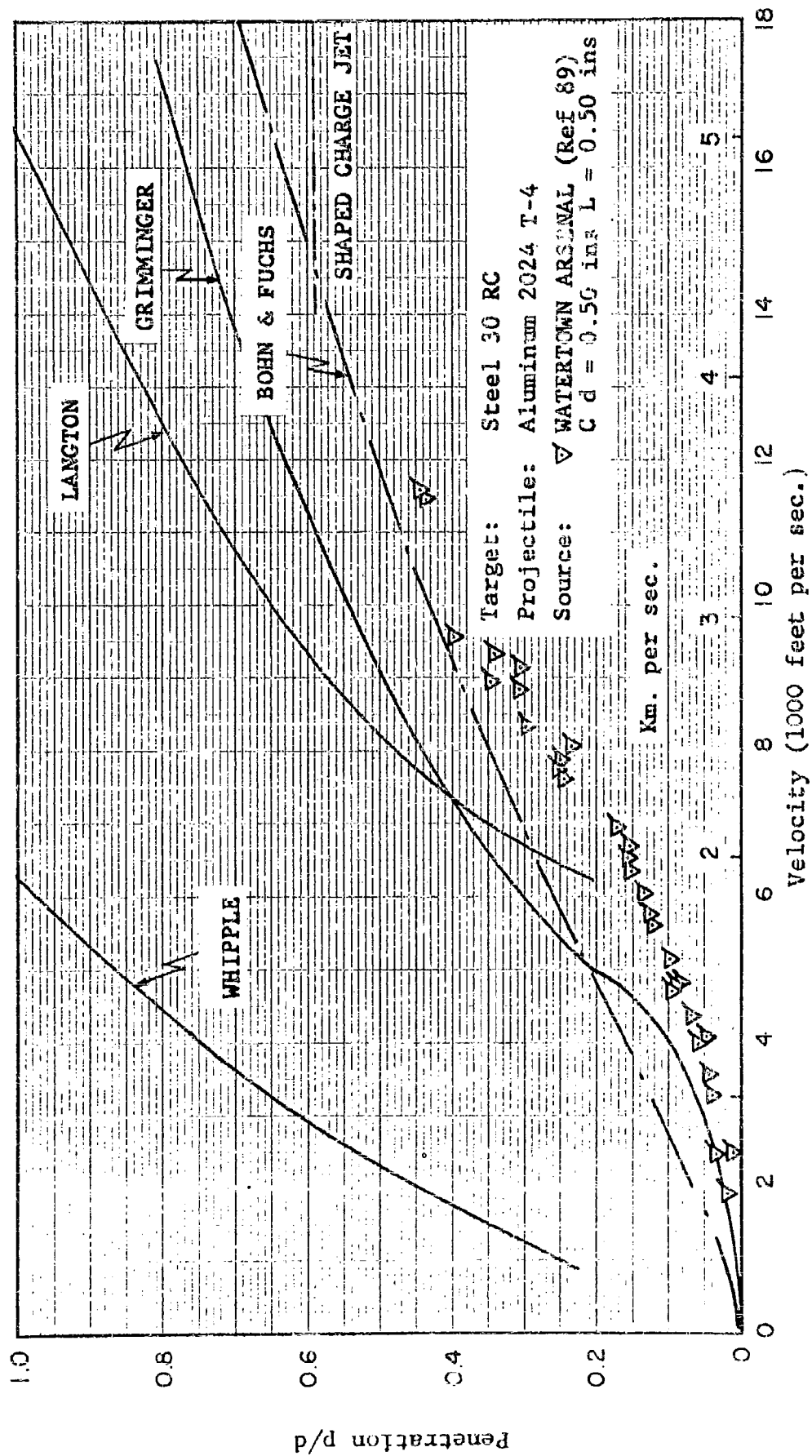


Fig. 1.11 The Penetration of 2024 T-4 Aluminum Projectiles into 30RC Steel Targets

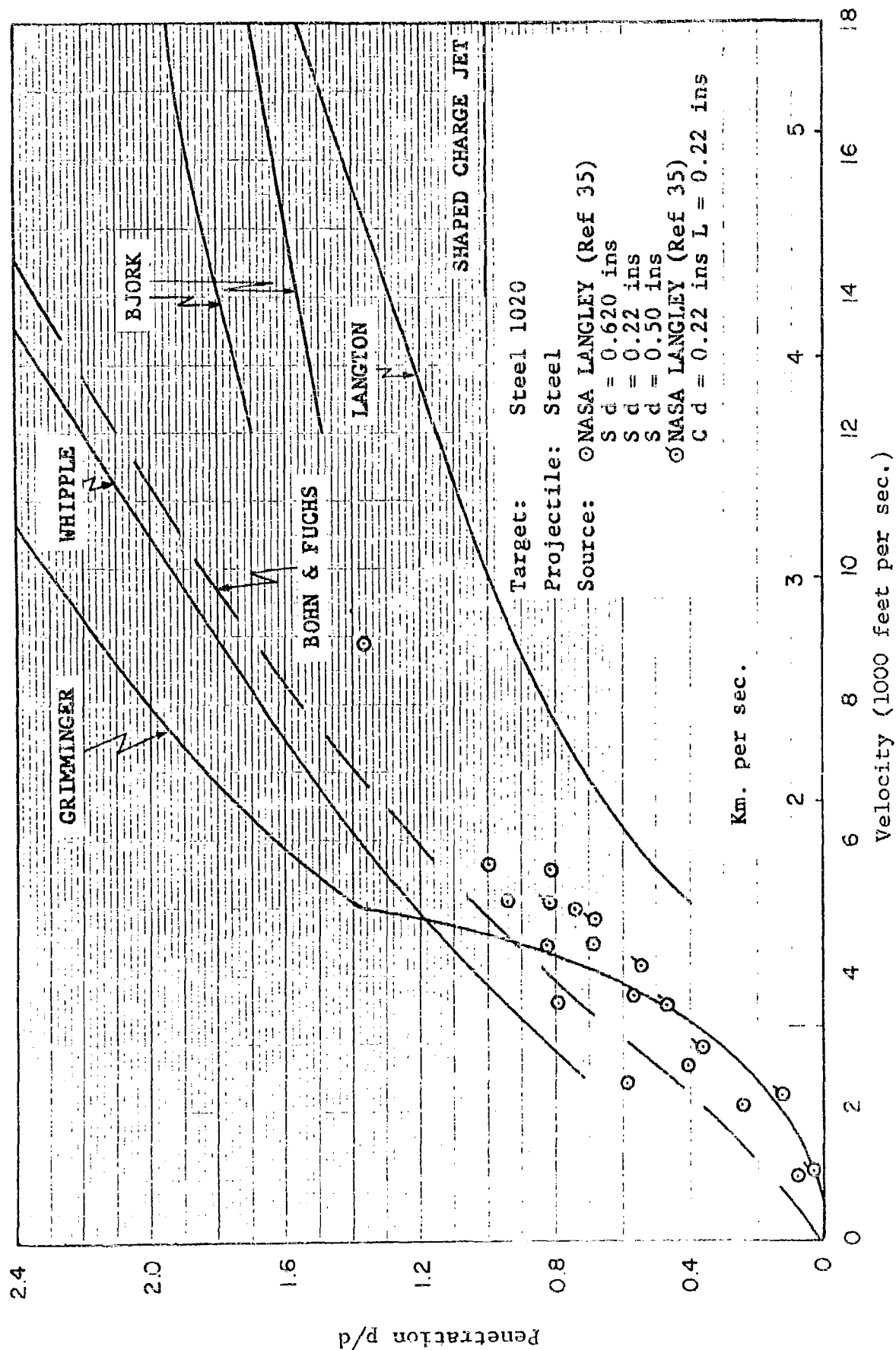


Fig. 1.12 The Penetration of Steel Projectiles into 1020 Steel Targets

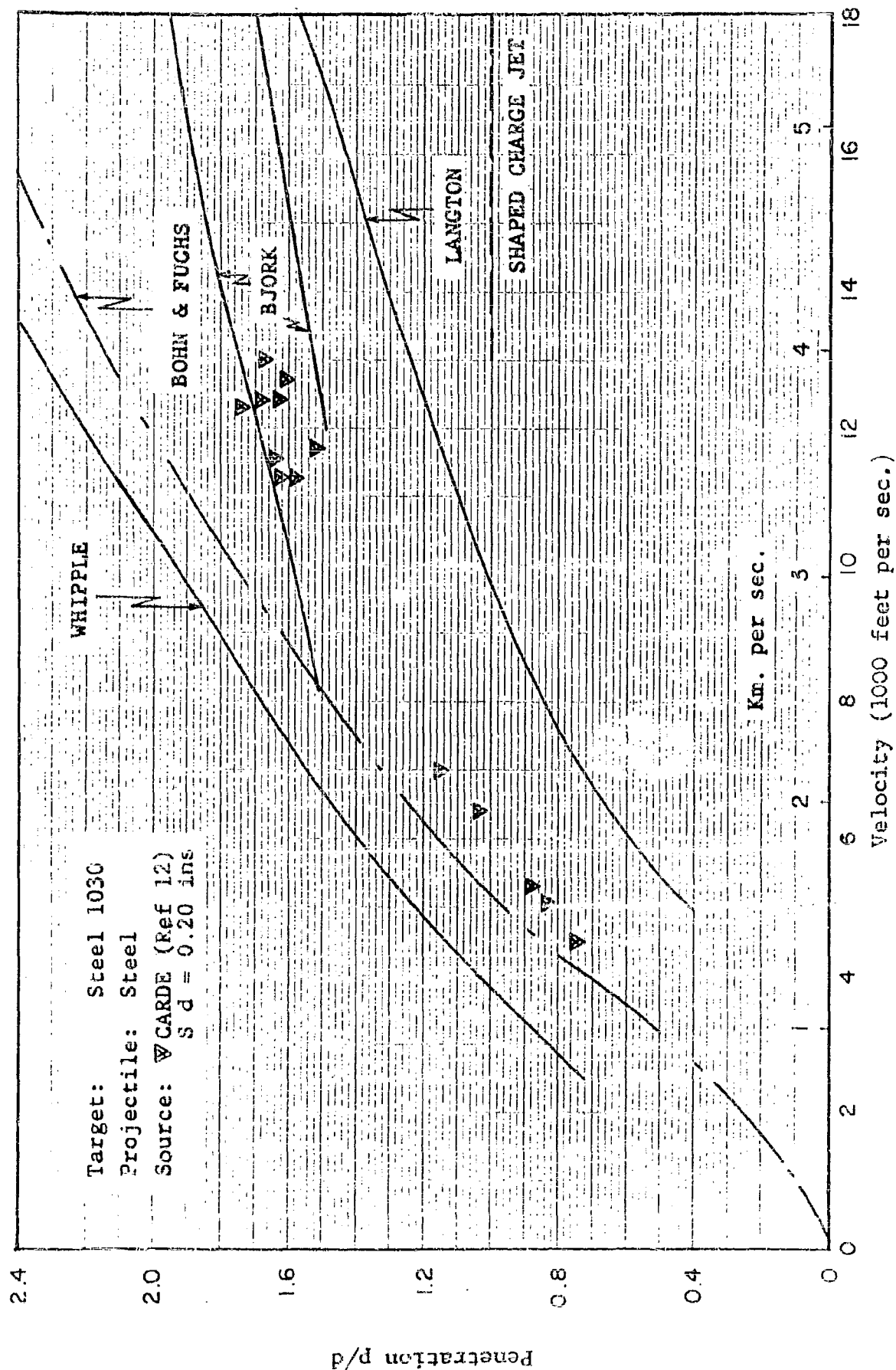


Fig. 1.13 The Penetration of Steel Projectiles into 1030 Steel Targets

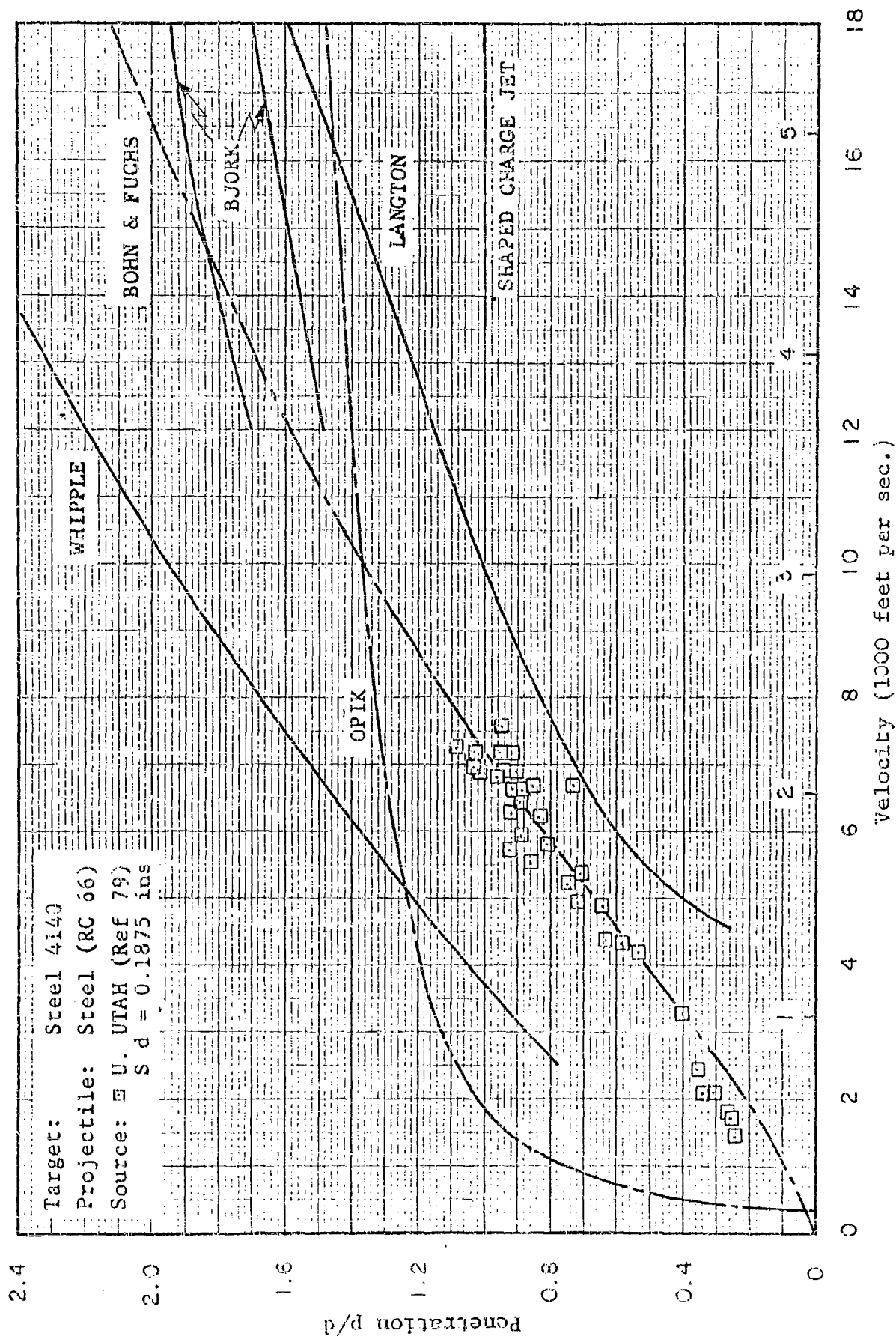
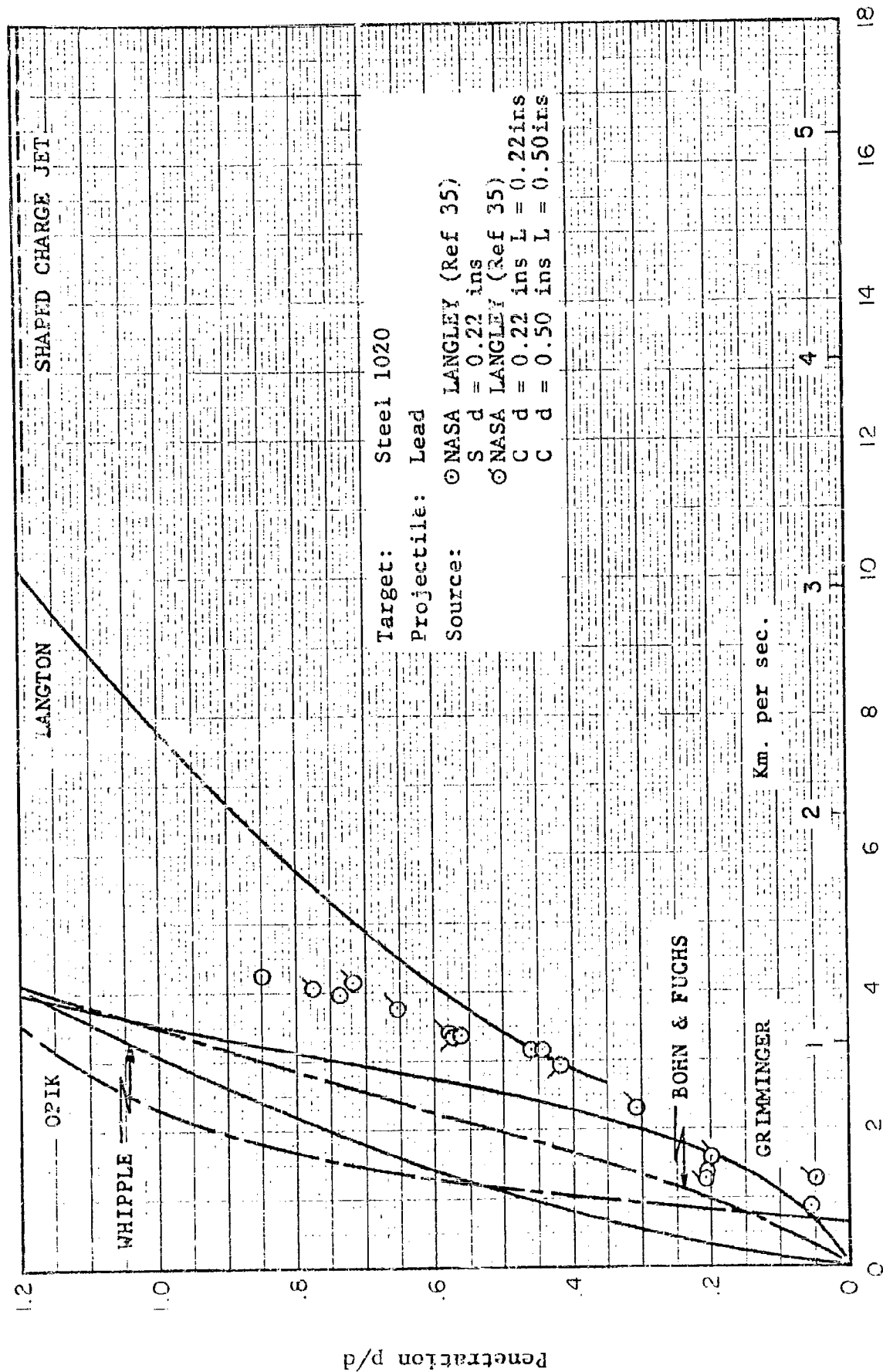


Fig. 1.14 The Penetration of RC-66 Steel Projectiles into 4140 Steel Targets



Velocity (1000 feet per sec.)

Fig. 1.15 The Penetration of Lead Projectiles into 1020 Steel Targets

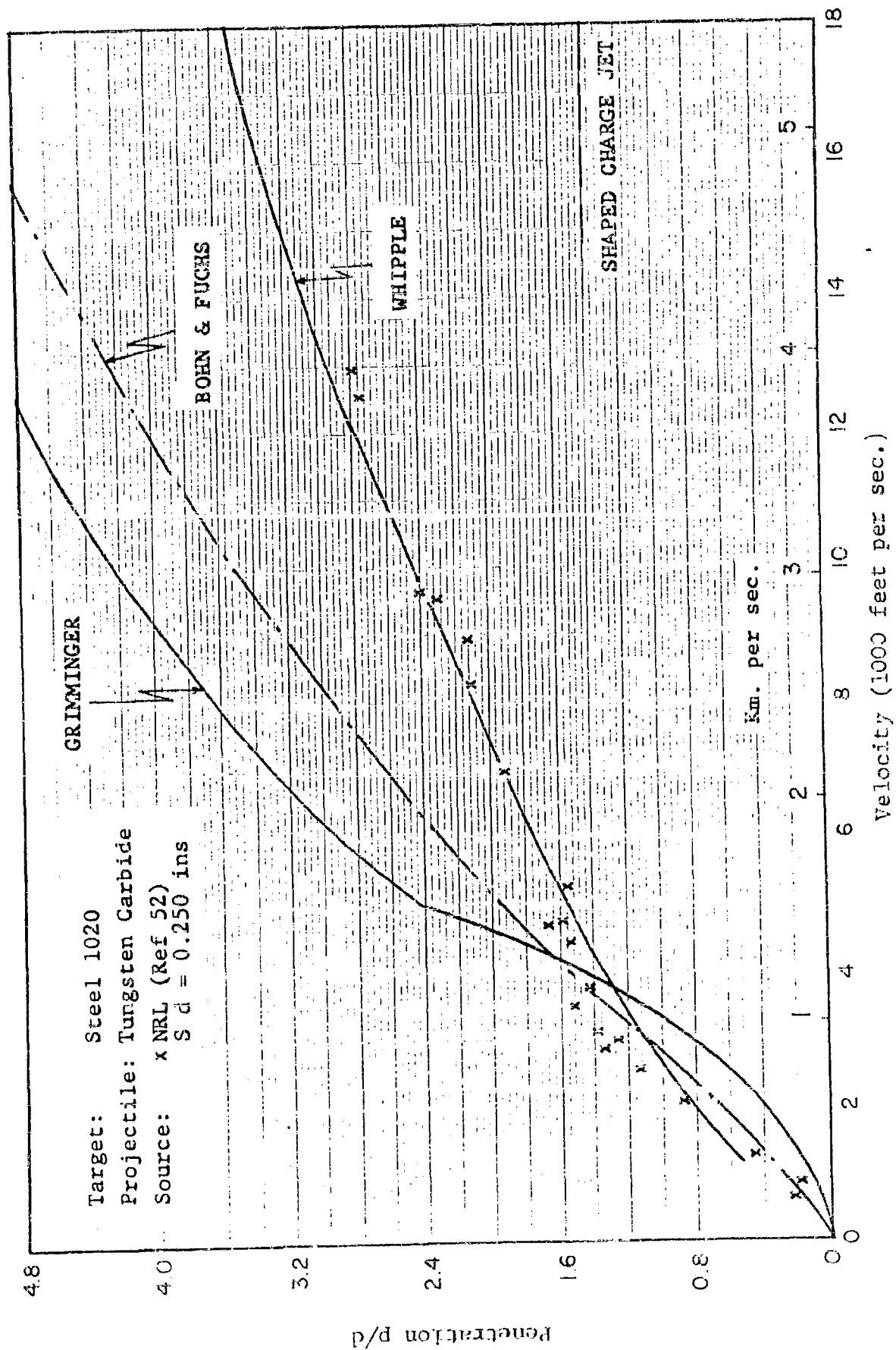


Fig. 1.16 The Penetration of Tungsten Carbide Projectiles into 1020 Steel Targets

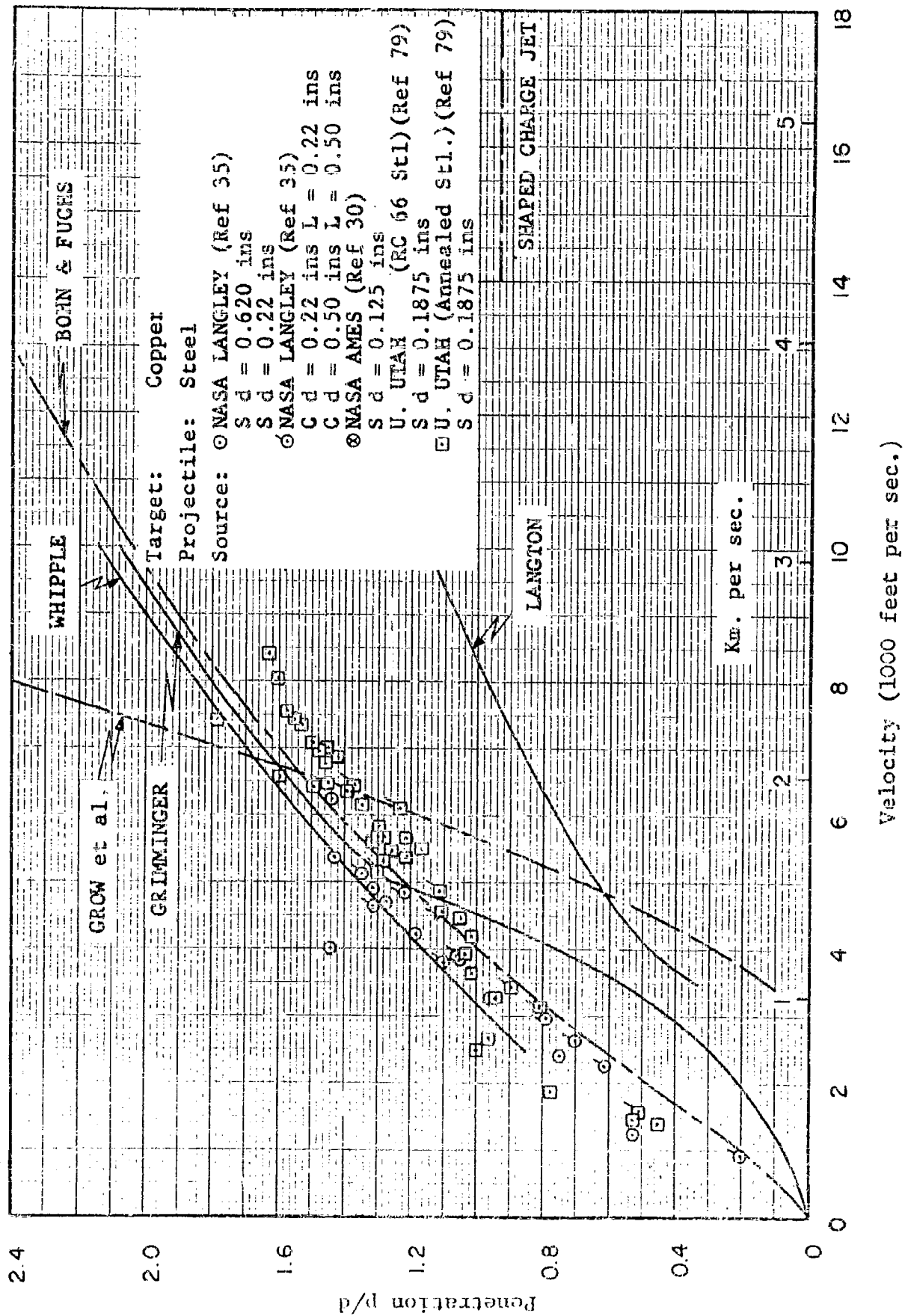


Fig. 1.17 The Penetration of Steel Projectiles into Copper Targets

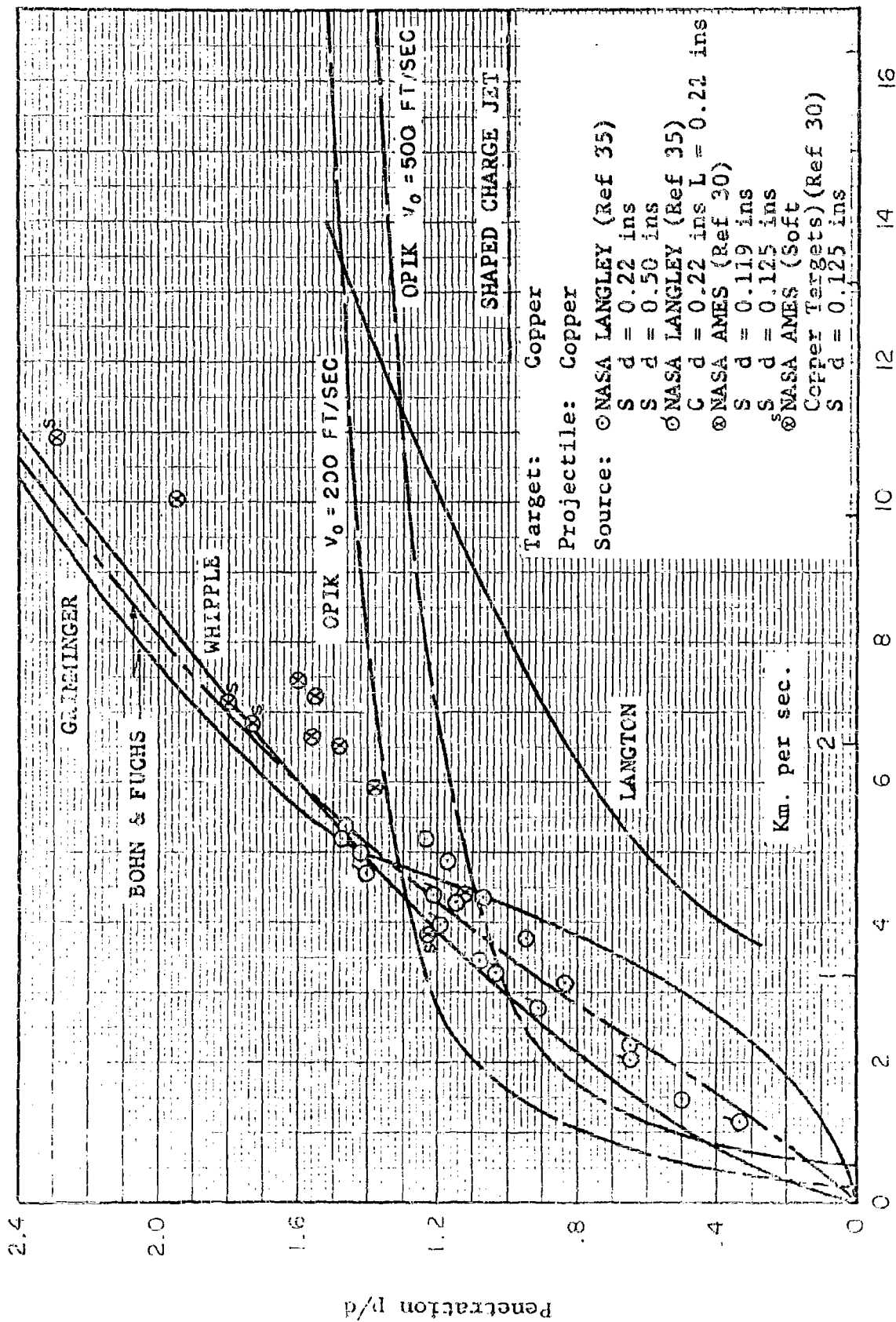


Fig.1.13 Penetration of Copper Projectiles into Copper Targets

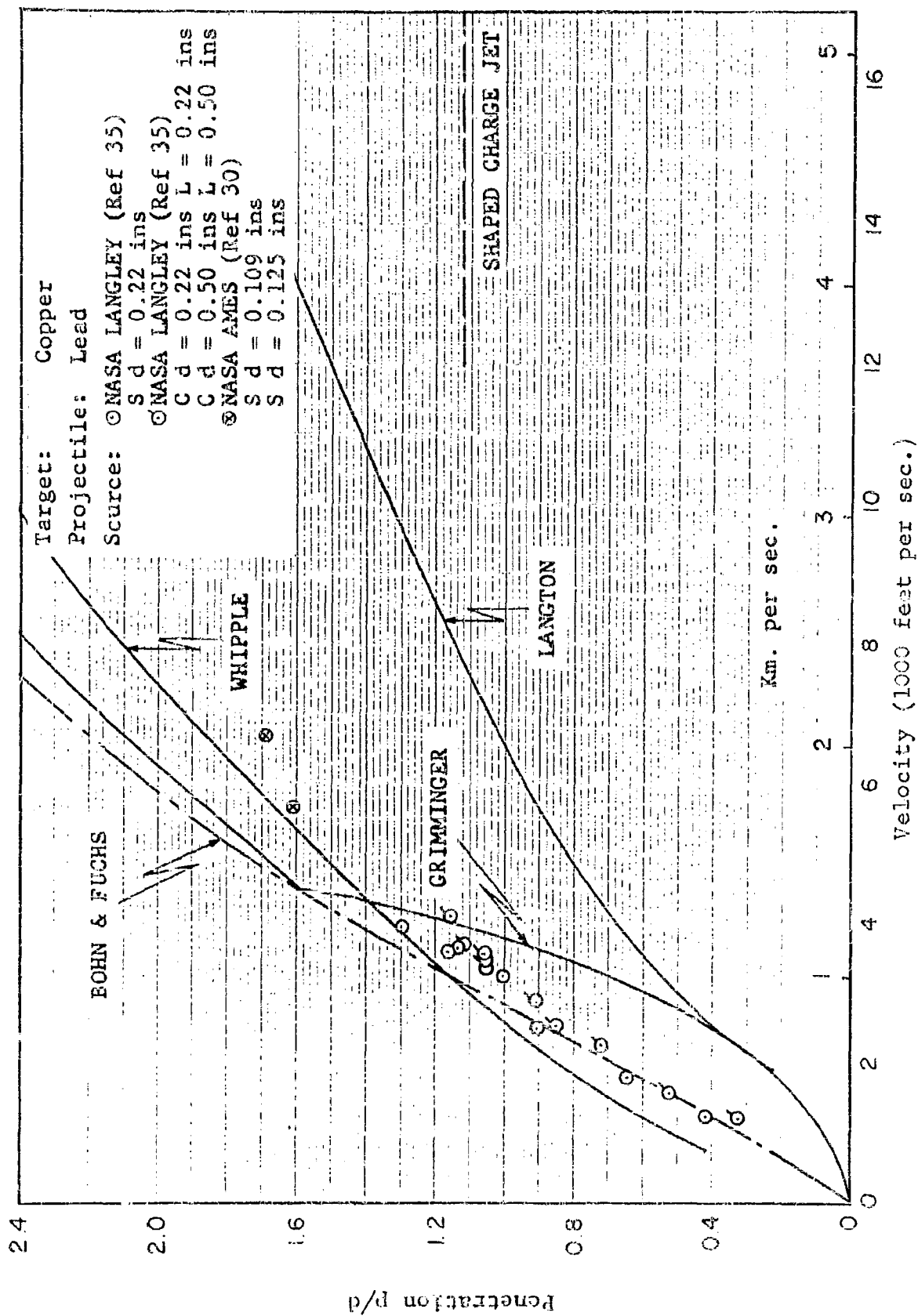


Fig. 1.19 The Penetration of Lead Projectiles into Copper Targets

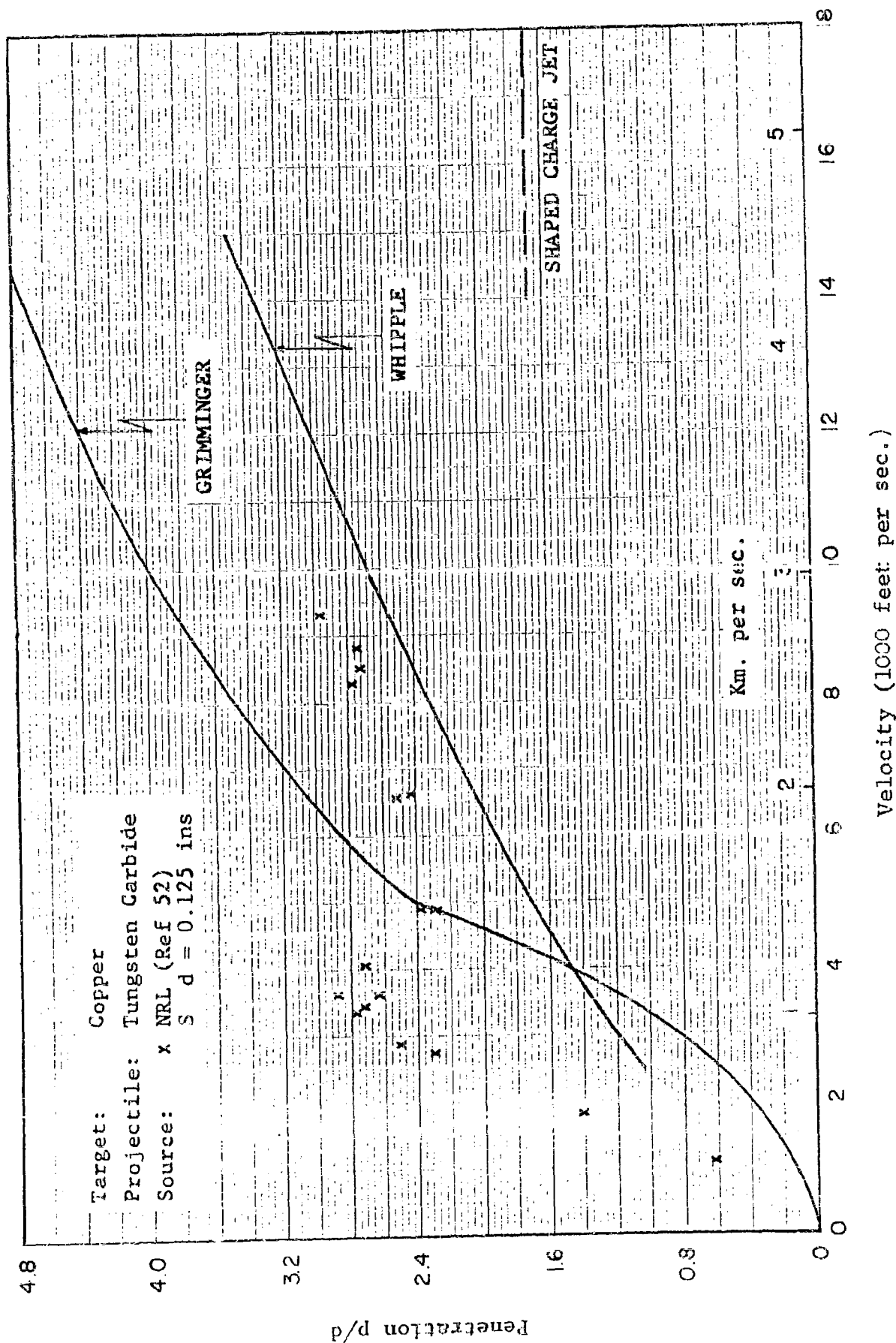


Fig. 1.20 The Penetration of Tungsten Carbide Projectiles into Copper Targets

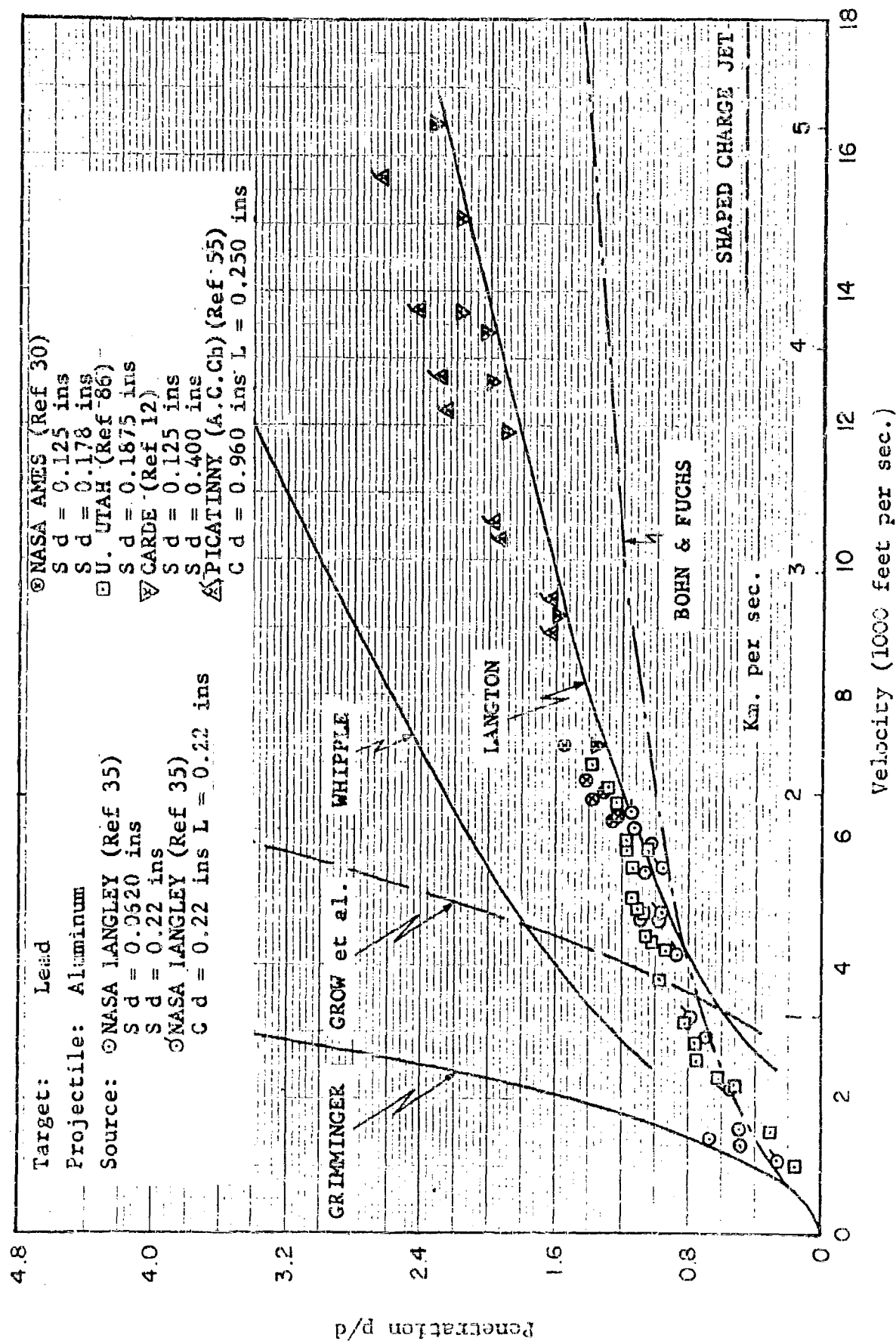


Fig. 1.21 The Penetration of Aluminum Projectiles into Lead Targets

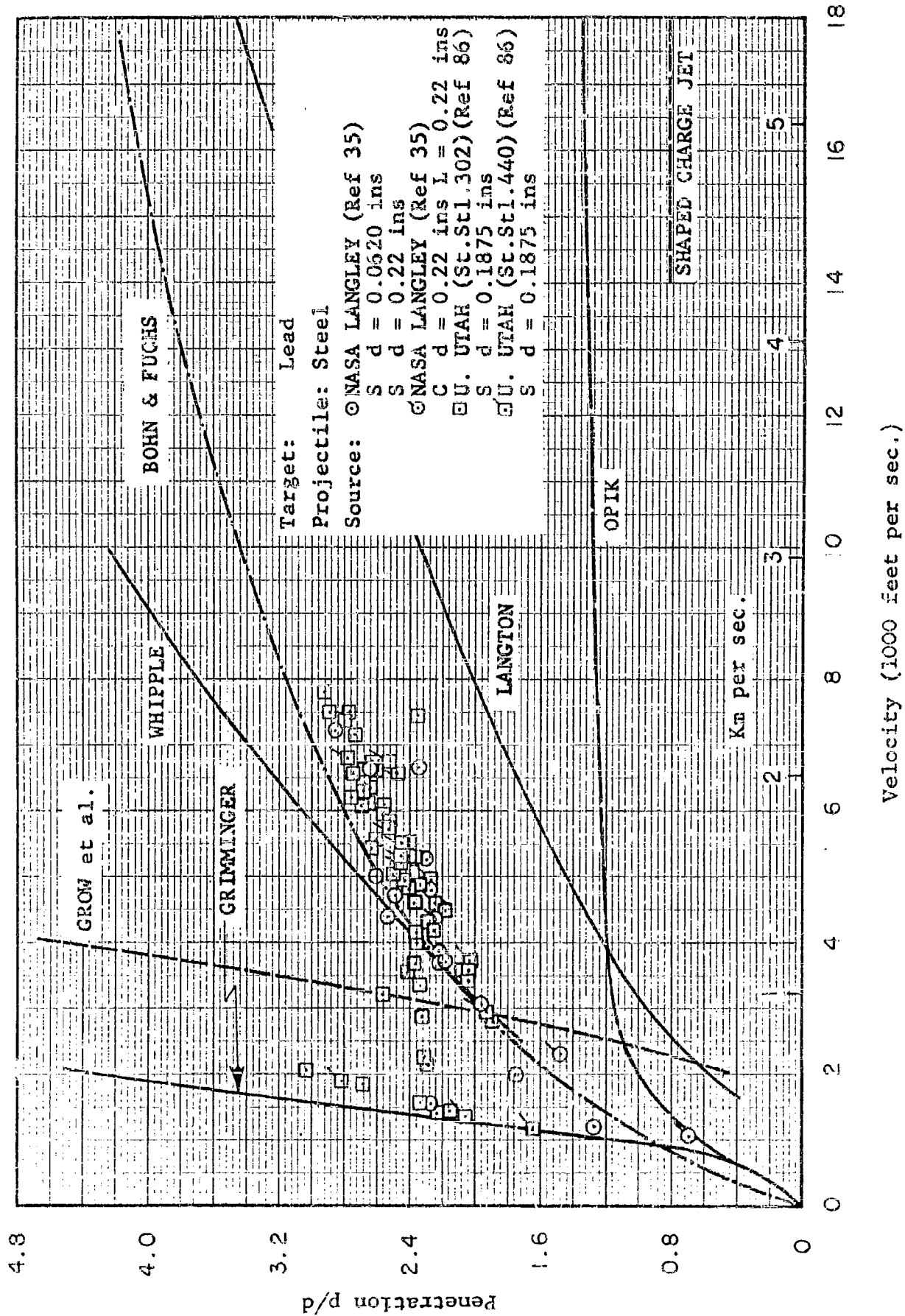


Fig. 1.22 The Penetration of Steel Projectiles into Lead Targets

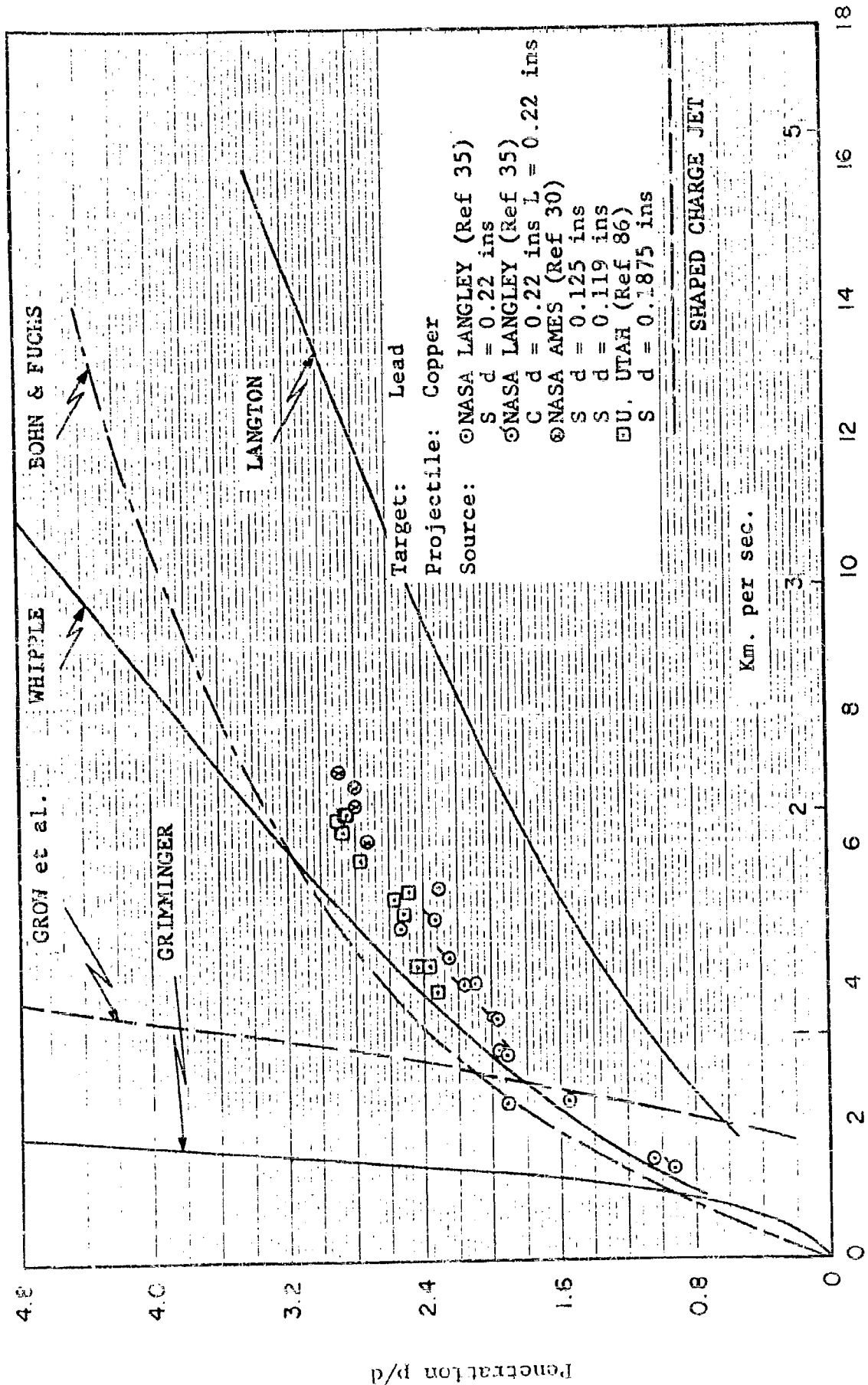


Fig. 1.23 The Penetration of Copper Projectiles into Lead Targets

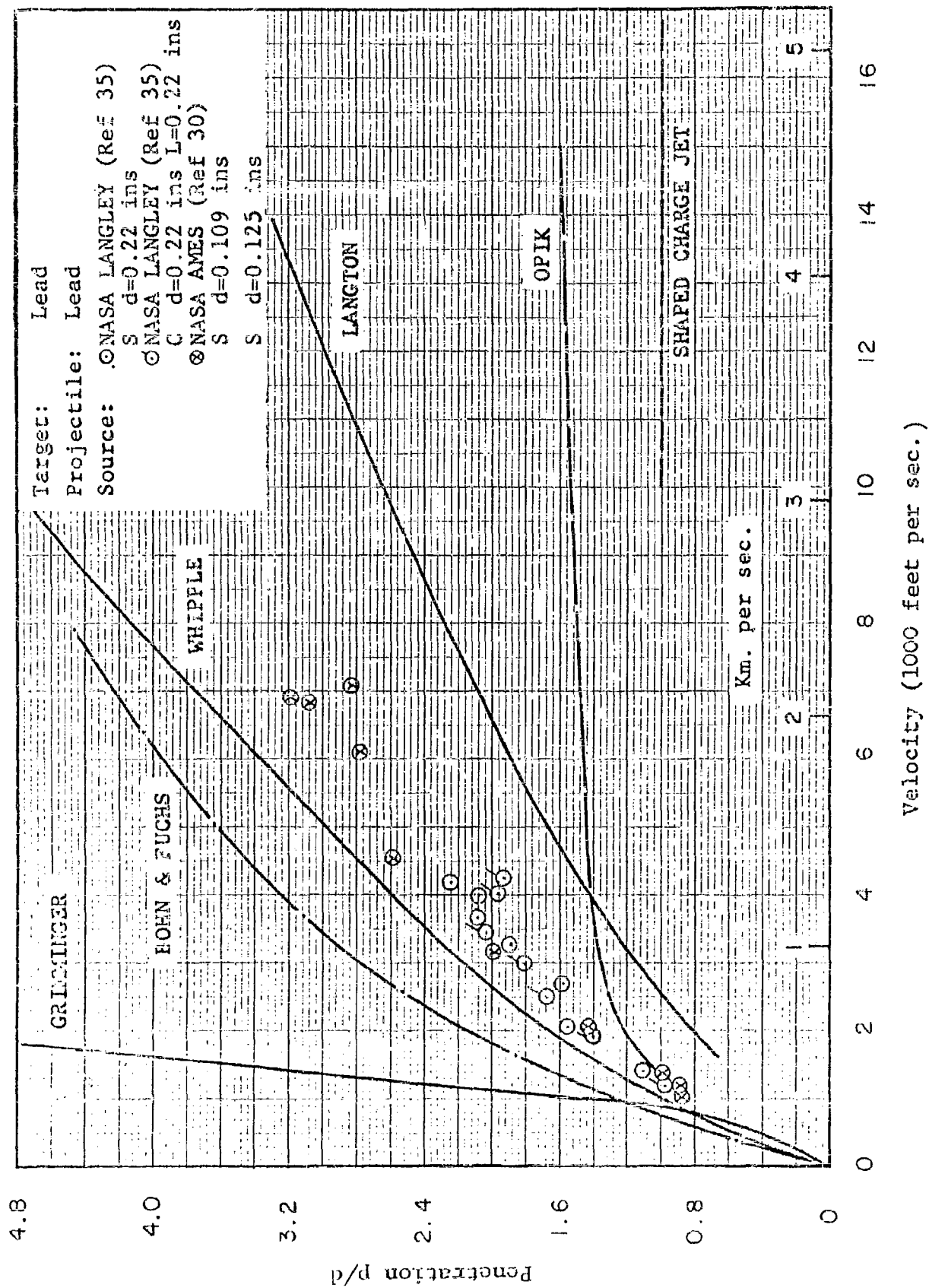


Fig. 1.24 The Penetration of Lead Projectiles into Lead Targets

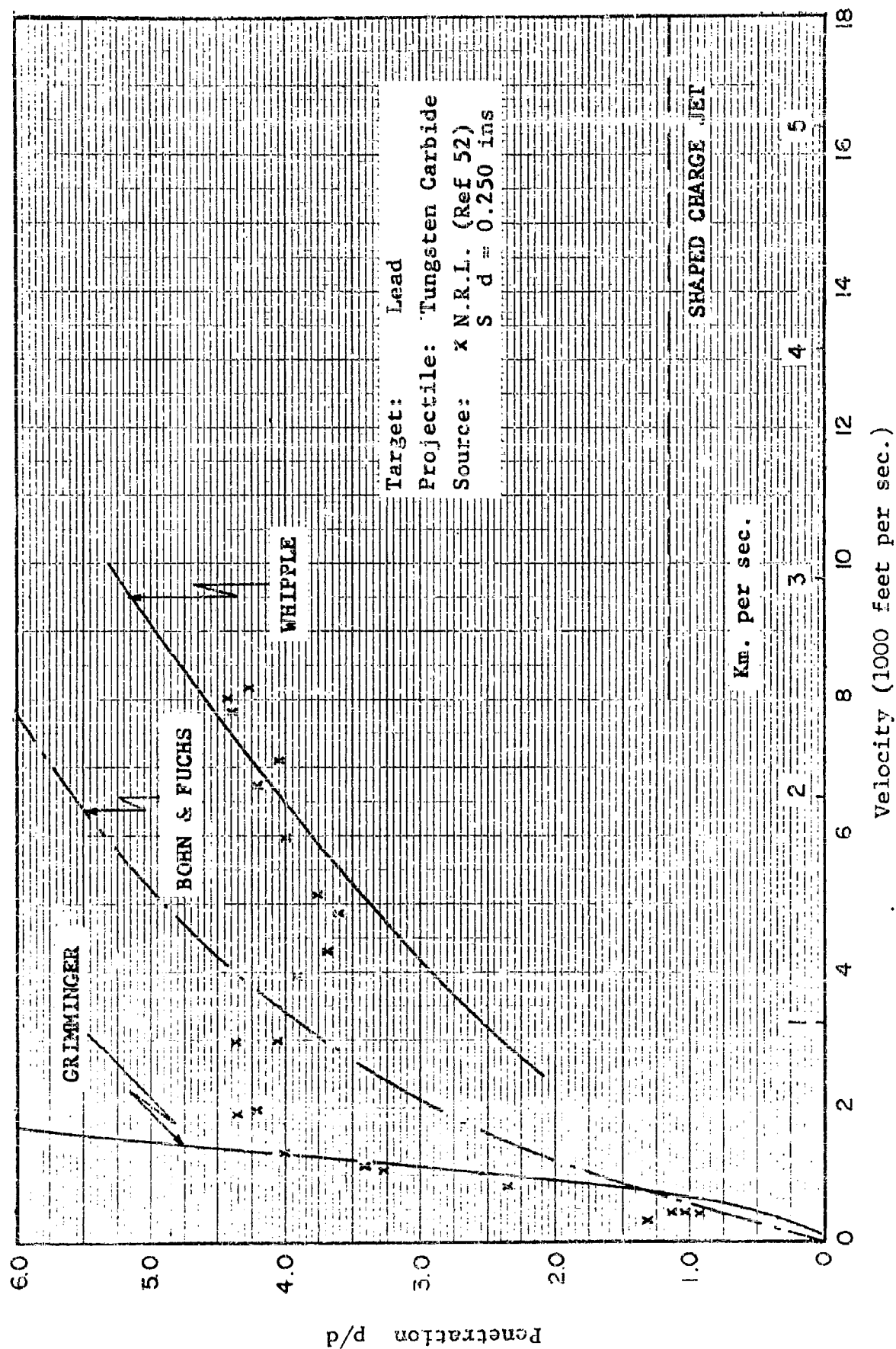


Fig. 1.25 The Penetration of Tungsten Carbide Projectiles into Lead Targets

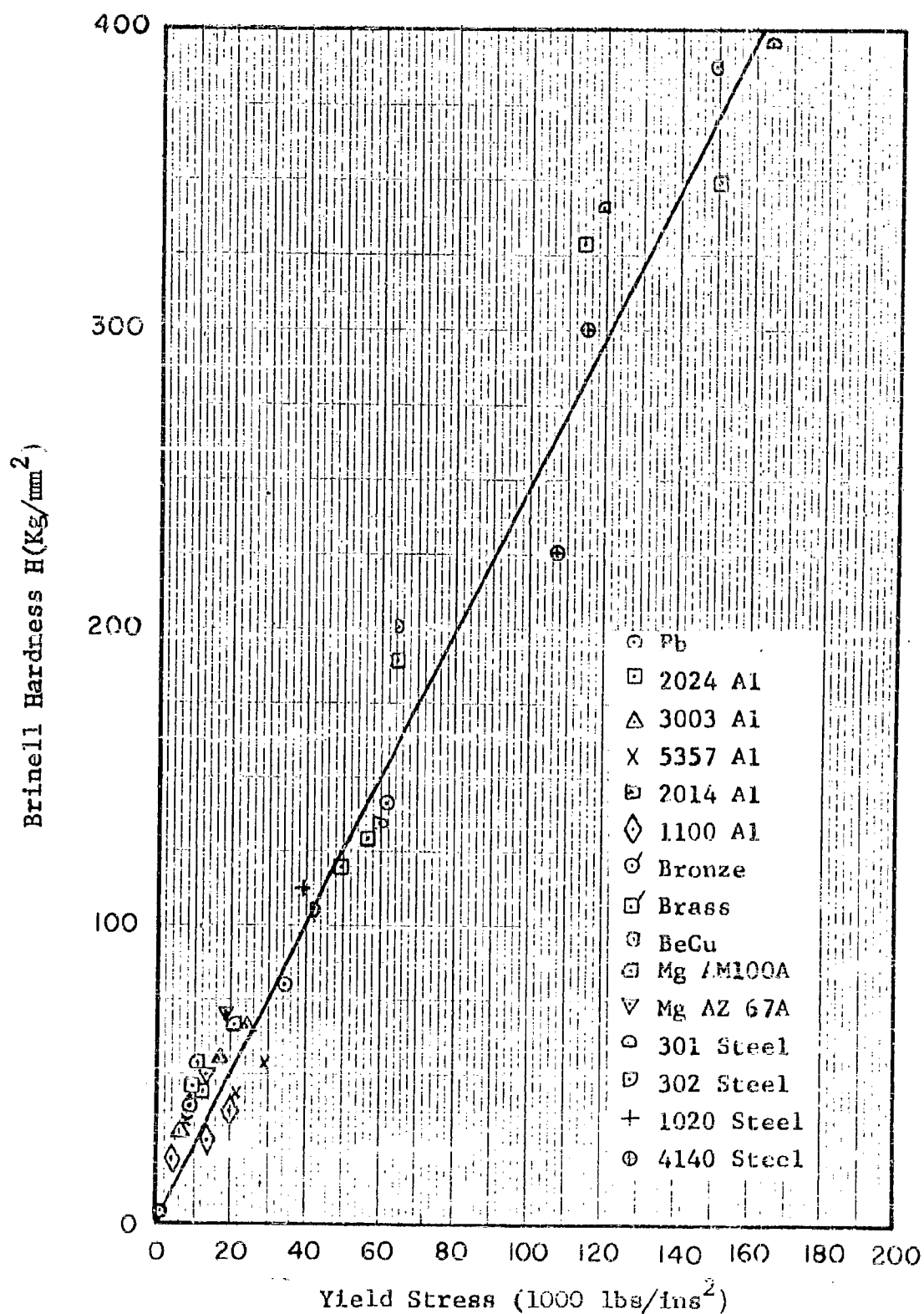


Fig. 4.1 Brinell Hardness versus Yield Strength for a Number of Representative Target Materials

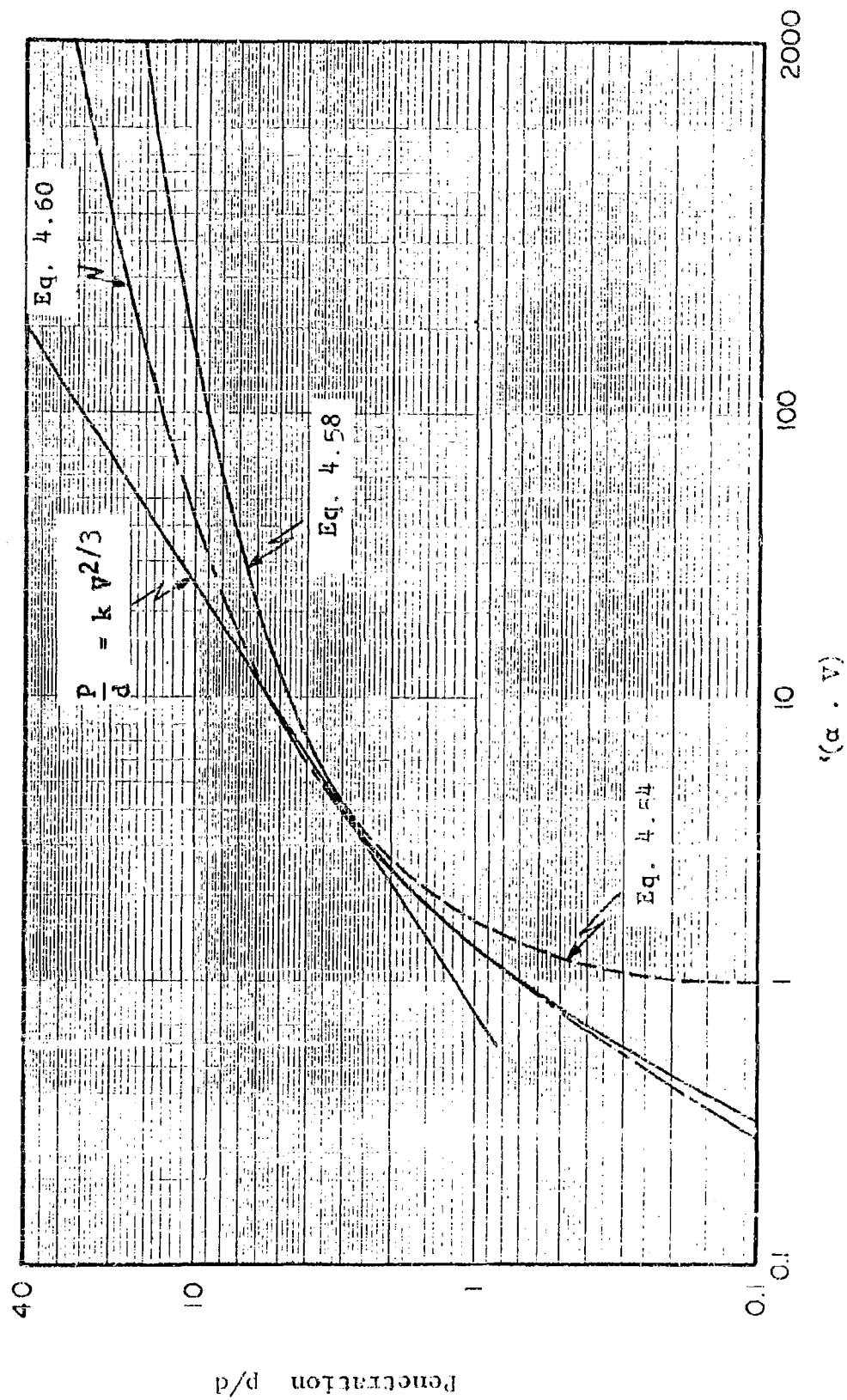
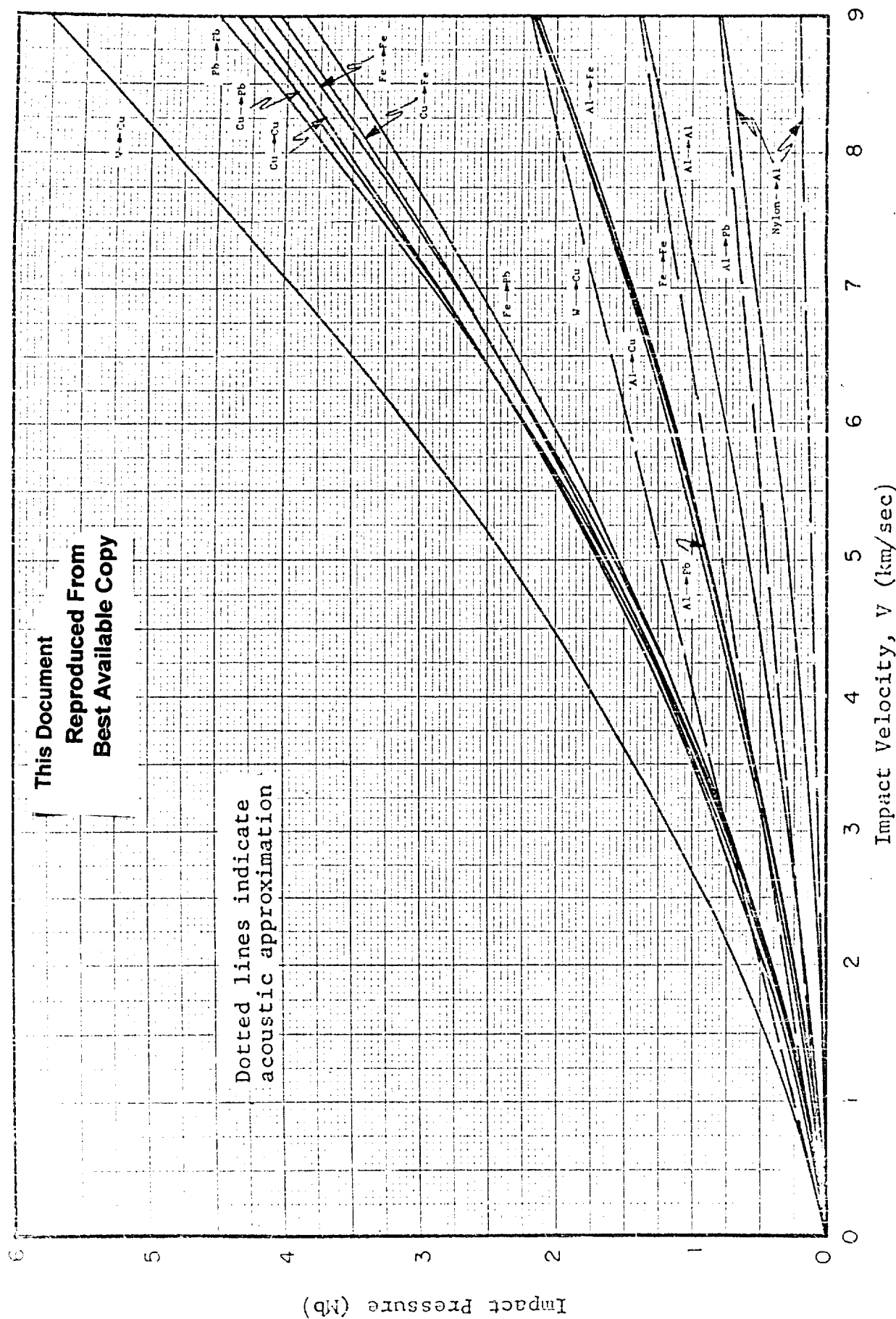


Fig. 4.2 Behaviour of Logarithmic Penetration Laws



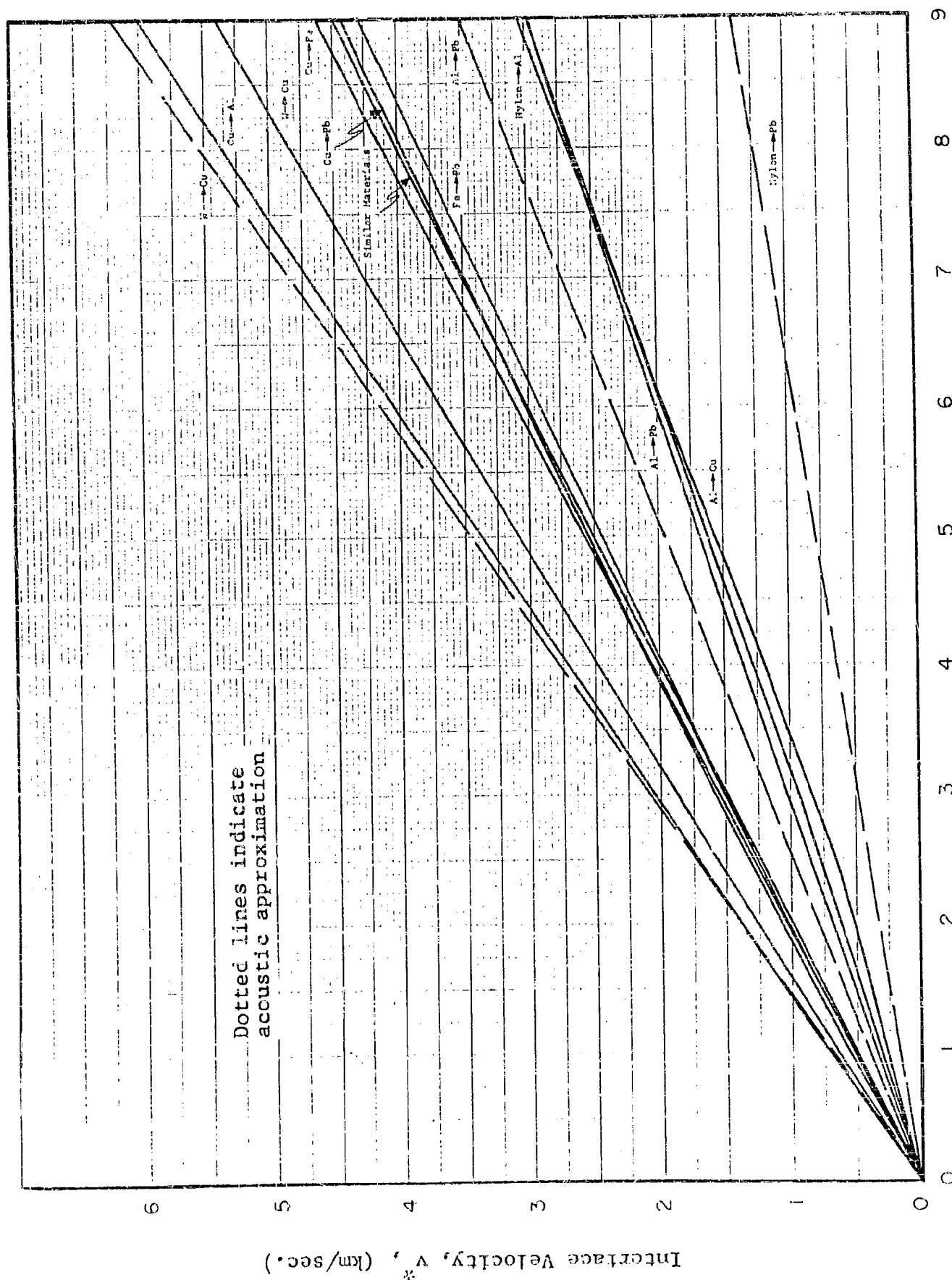


Fig. 5.1.b Initial Interface Velocities in One Dimensional Impact

Lead
Projectile



Copper
Projectile



Steel
Projectile



Revised for Publication by
AERONAUTIC AND STRUCTURES RESEARCH LABORATORY
MASSACHUSETTS INSTITUTE OF TECHNOLOGY

Fig. 5.2 Craters in Lead Targets formed by 1/8" Spheres
at Approximately 700 ft/sec

Lead
Projectile



Copper
Projectile



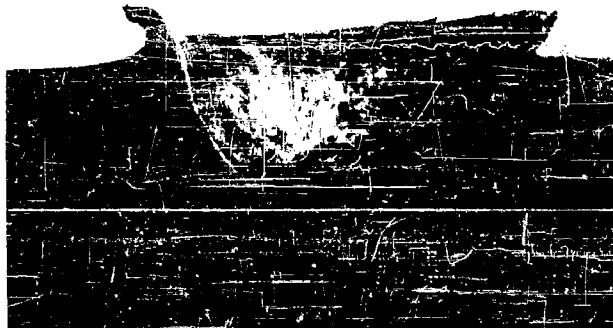
Steel
Projectile



MANUSCRIPT FOR PUBLICATION BY
AERONAUTIC AND STRUCTURES RESEARCH LABORATORY
MASSACHUSETTS INSTITUTE OF TECHNOLOGY

Fig. 5.2 continued Craters in Lead Targets formed by
1/8" Spheres at Approximately 1500 ft/sec

Lead
Projectile



Copper
Projectile



Steel
Projectile



Released for Publication by
AERONAUTIC AND STRUCTURES RESEARCH LABORATORY
MASSACHUSETTS INSTITUTE OF TECHNOLOGY

Fig. 5.2 continued Craters in Lead Targets formed by
1/8" Spheres at Approximately 2000 ft/sec.

Lead
Projectile



Copper
Projectile



Steel
Projectile



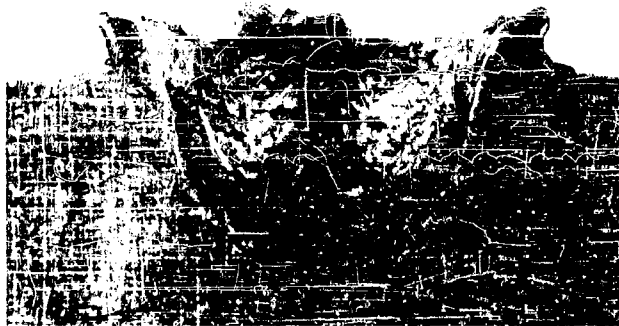
Released for Publication by
AERONAUTIC AND STRUCTURES RESEARCH LABORATORY
MASSACHUSETTS INSTITUTE OF TECHNOLOGY

Fig. 5.2 continued Craters in Lead Targets formed by
1/8" Spheres at Approximately 3000 ft/sec

Lead
Projectile



Copper
Projectile

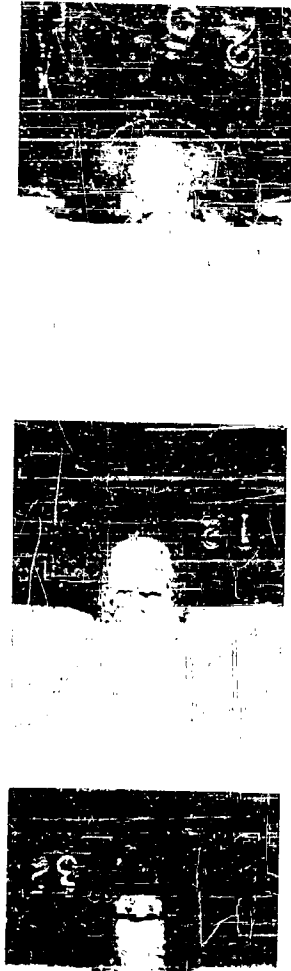


Steel
Projectile

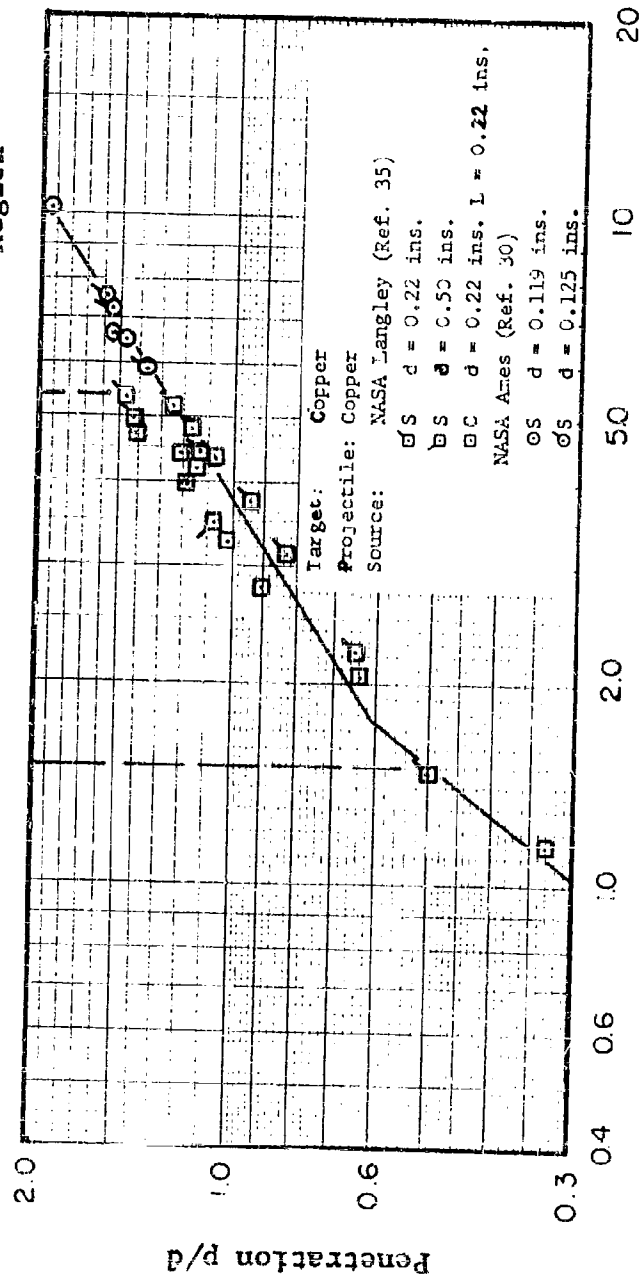


Revised for Publication by
ARMED AND ARMED STUDIES OF CRATER FORMATION
MASSACHUSETTS INSTITUTE OF TECHNOLOGY

Fig. 5.2 concluded Craters in Lead Targets formed by
1/8" Spheres at Approximately 5000 ft/sec

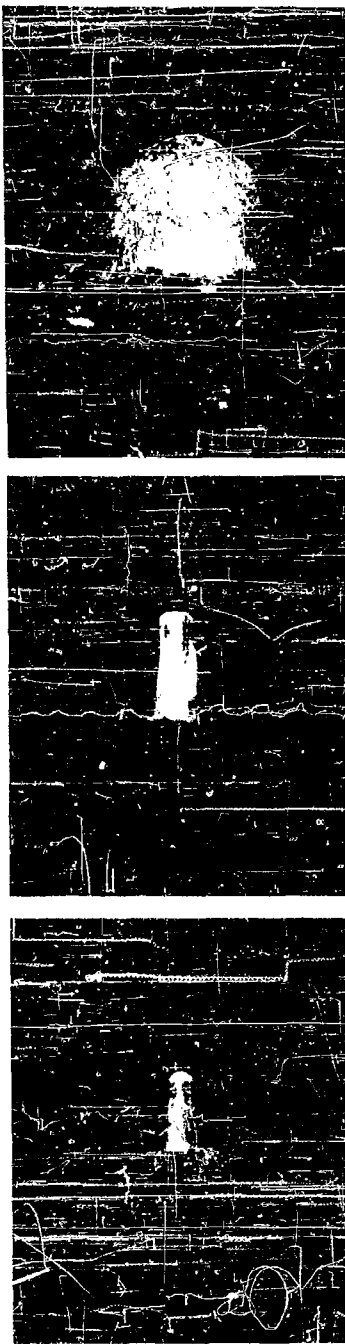


Undeformed Projectile Transition Region High Velocity Region



Prepared for publication by
 NATIONAL AERONAUTICS AND SPACE ADMINISTRATION
 LANGLEY RESEARCH CENTER, LANGLEY FIELD, VIRGINIA

Fig. 5.3 Illustration of Regions of Impact for a Ductile Projectile



Undeformed Projectile Region Transition Region High Velocity Region

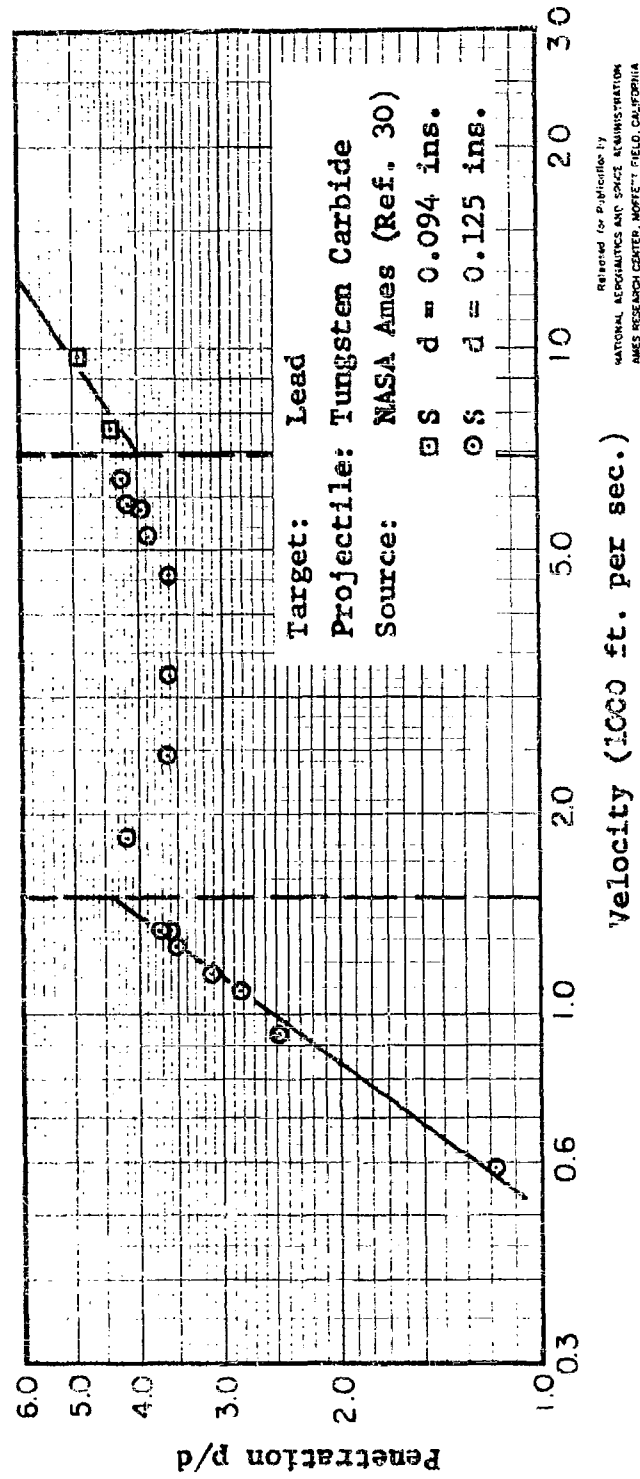
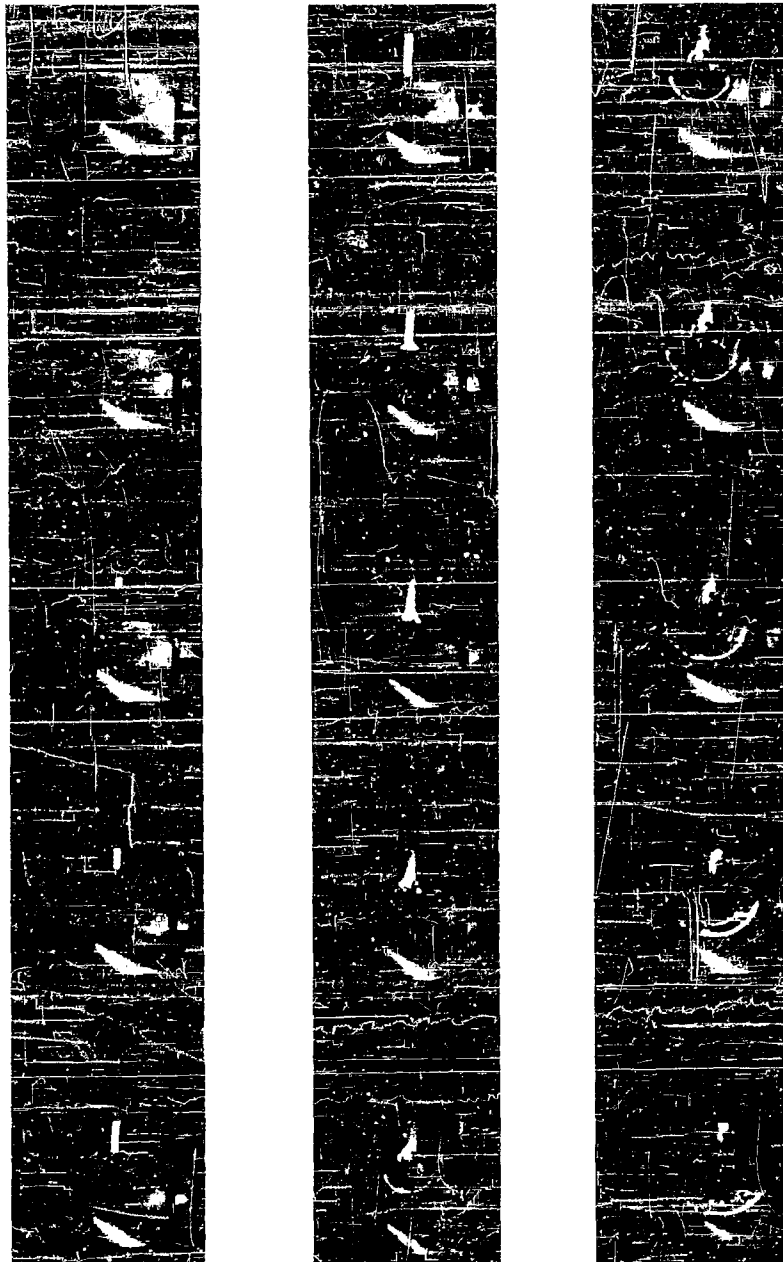


Fig. 5.4 Illustration of Regions of Impact for a High Strength Projectile



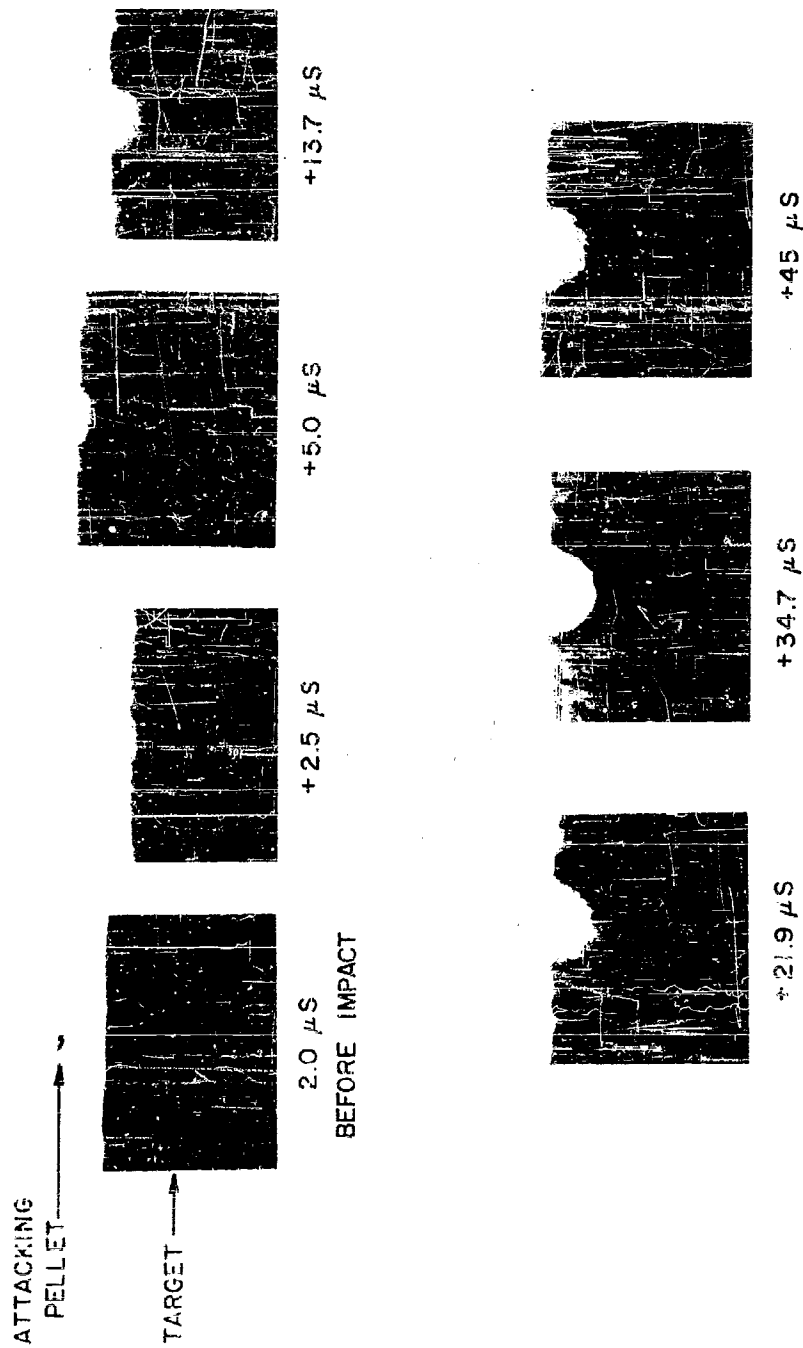
Released for Publication by
NATIONAL AERONAUTICS AND SPACE ADMINISTRATION
AMES RESEARCH CENTER, MOFFETT FIELD, CALIFORNIA

Fig. 5.5 Illustration of Cratering in the High Velocity Region. Copper Target Struck by Copper Sphere. The Projectile Material has been Lifted to Illustrate the Plating Effect. (Ref. 30)



Released for Publication by
 BALLISTICS RESEARCH LABORATORY
 ARMY PROOFING GROUND, MARYLAND

Fig. 5.6 High Speed Framing Camera Pictures of Penetration
 of a Lucite Target by a Steel Projectile (from Ref. 7)



Released for Publication by
 BALLISTICS RESEARCH LABORATORY
 ABERDEEN PROVING GROUND, MARIETTA, GA

Fig. 5.7 Flash X-radiographs of the Formation of a Crater in a 2-SO Aluminum Target
 by a 0.18 gm Steel Projectile at 15,000 ft/sec. (from Ref. 7)



a. $\sim 20 \mu \text{ SEC}$



b. $\sim 65 \mu \text{ SEC}$



c. $\sim 165 \mu \text{ SEC}$

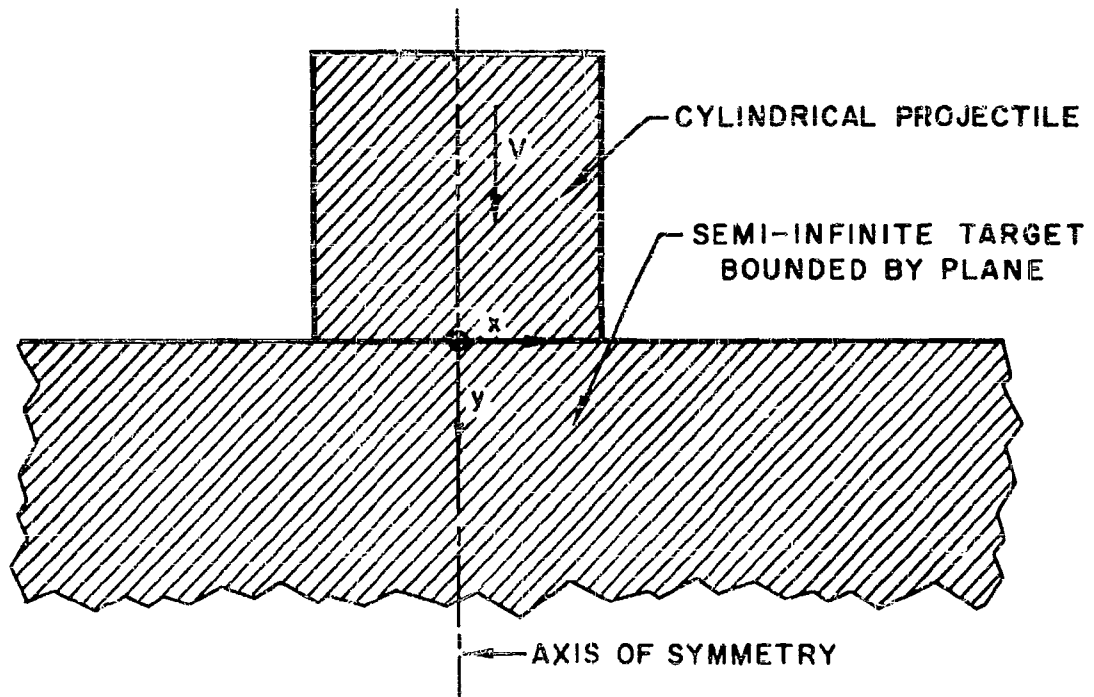


d. $\sim 280 \mu \text{ SEC}$

Released for Publication by
BALISTICS RESEARCH LABORATORY
AMERIDEN PROVING GROUND, MARYLAND

Fig. 5.8 Flash X-Radiograph of the Spray Issuing from a Crater in the Process of Formation in a Lead Target (from Ref. 7)

INITIAL CONDITIONS



$P = e = 0$ EVERYWHERE

$\rho = \rho_0$ EVERYWHERE

$t = 0$

VELOCITY = 0 IN TARGET

VELOCITY = V IN Y DIRECTION IN PROJECTILE

PROJECTILE HAS JUST CONTACTED TARGET

Fig. 5.9 Numerical Solution of the Penetration of an Iron Projectile into an Iron Target, Neglecting Material Strength (from Ref. 128)

PRESSURE CONTOURS AND VELOCITY FIELD

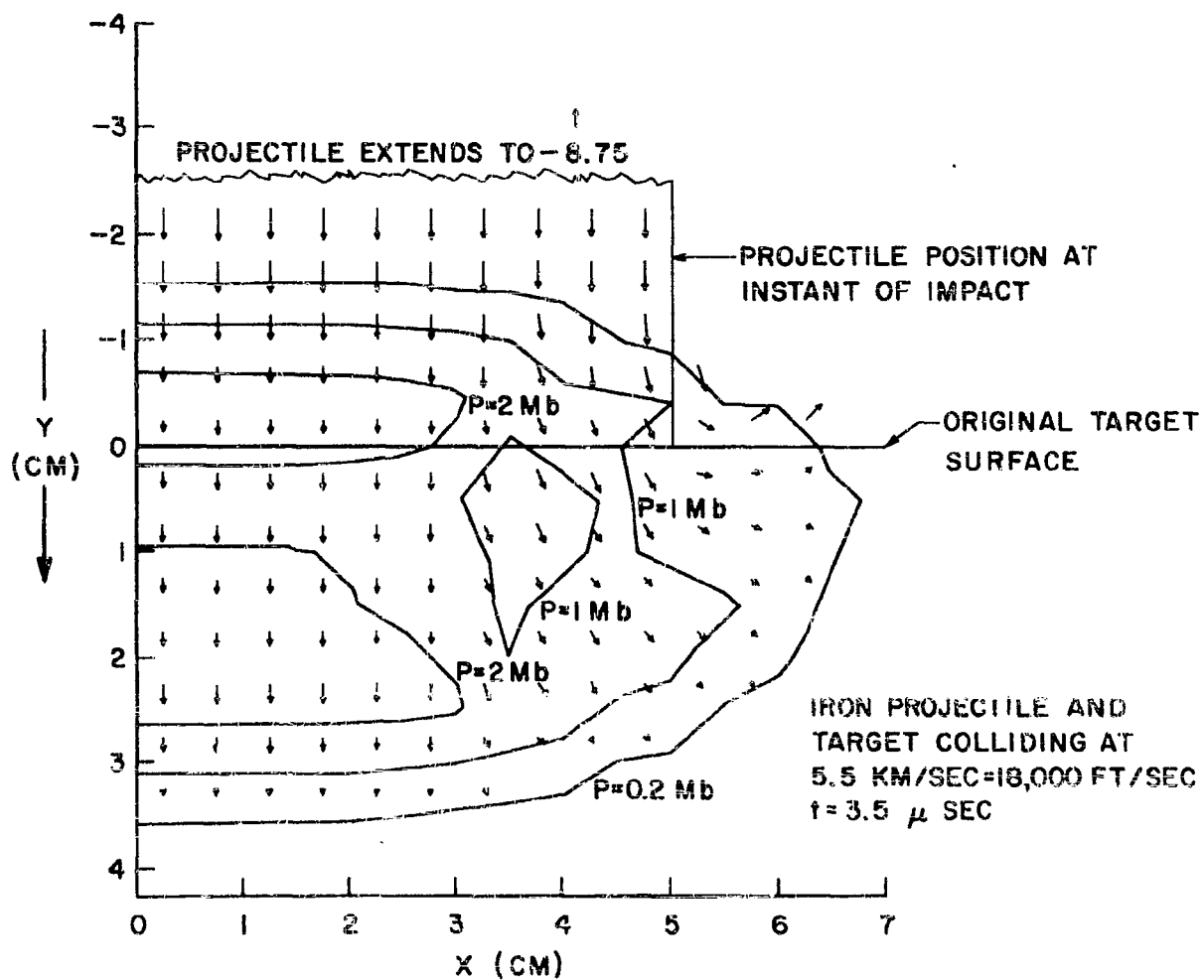


Fig. 5.9 Continued, (Note Changing Scale)

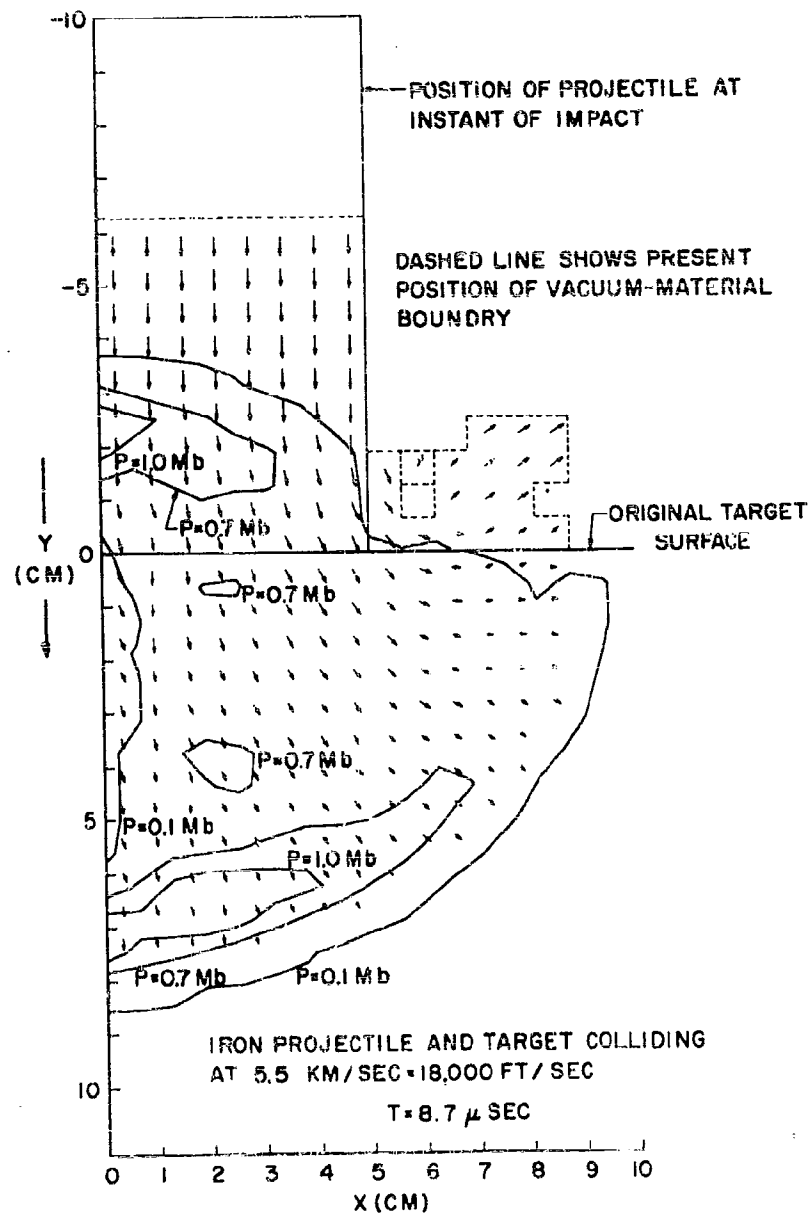


Fig. 5.9 Continued, (Note Changing Scale)

VELOCITY AND PRESSURE CONTOURS

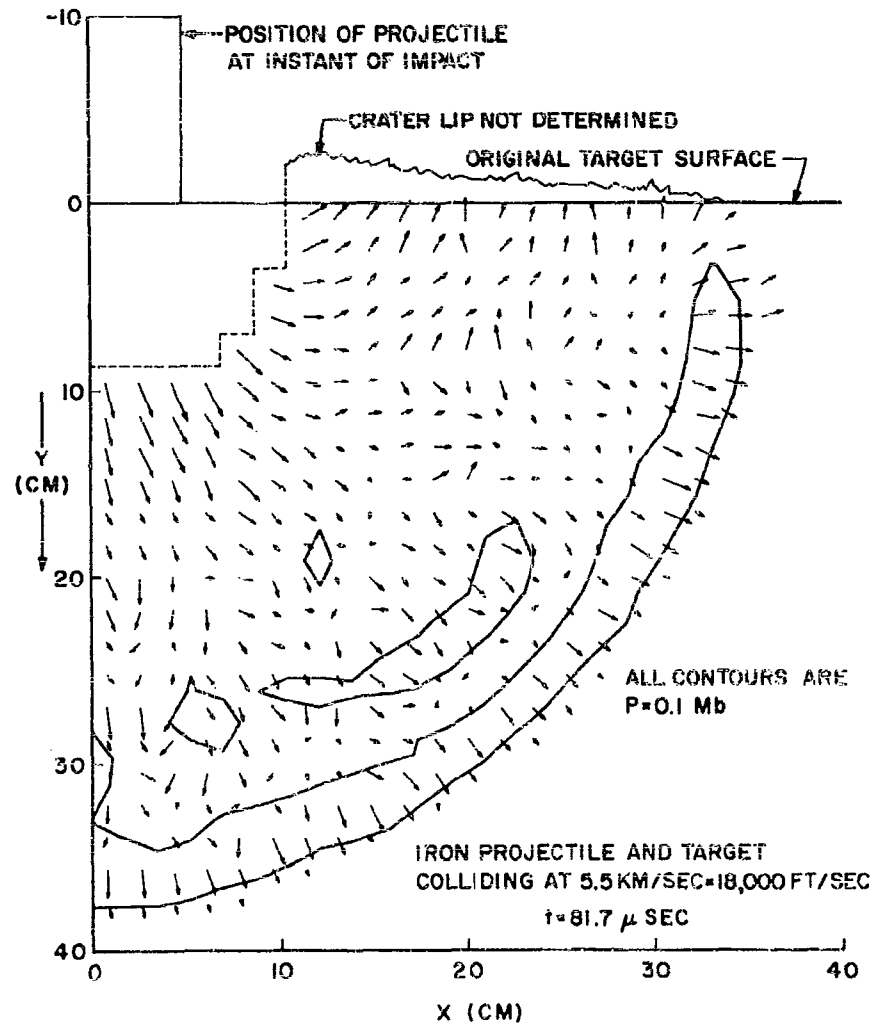


Fig. 5.9 Concluded, (Note Changing Scale)

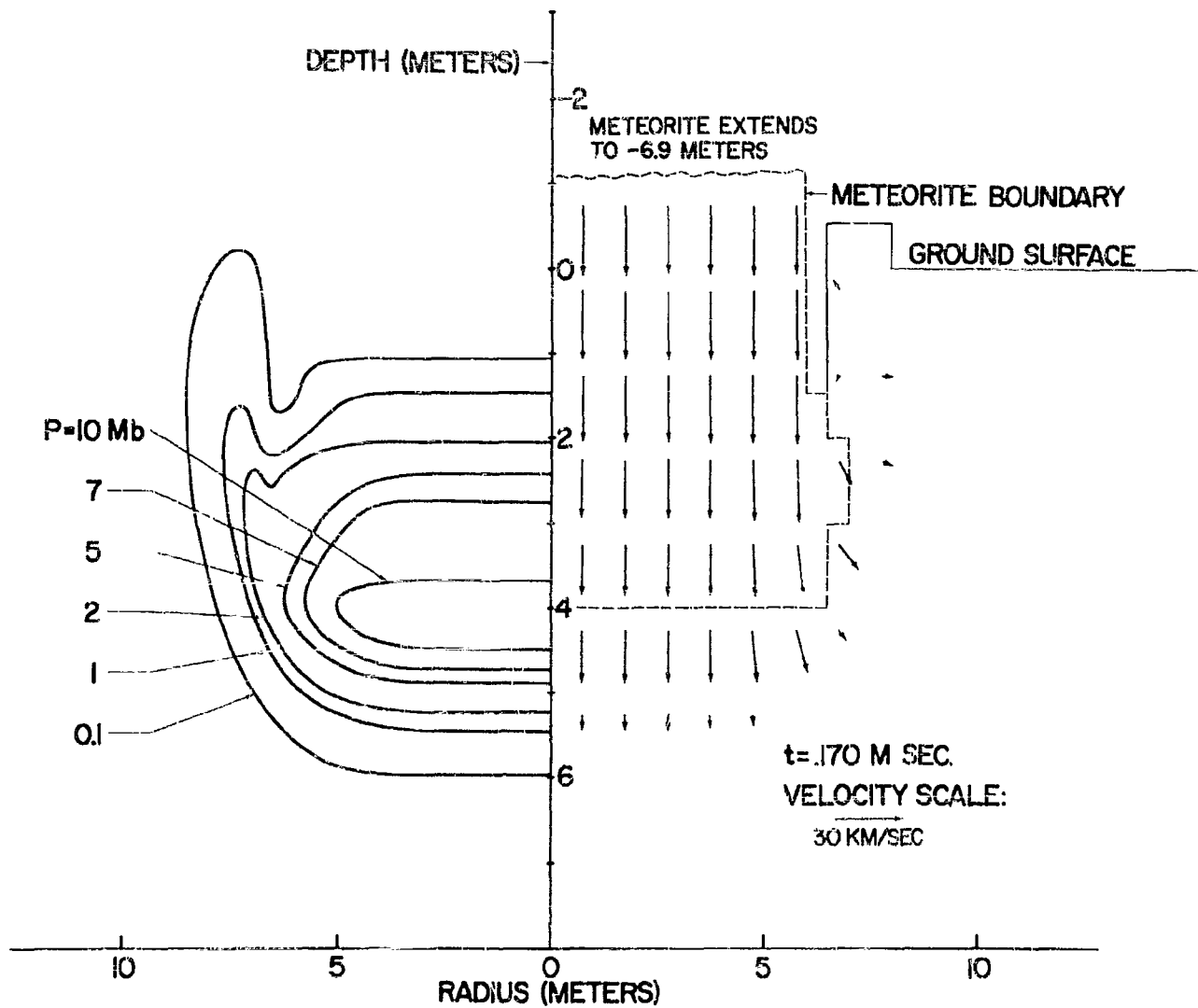


Fig. 5.10 Numerical Solution for the Penetration of a Meteorite into Tuff (from Ref. 152)

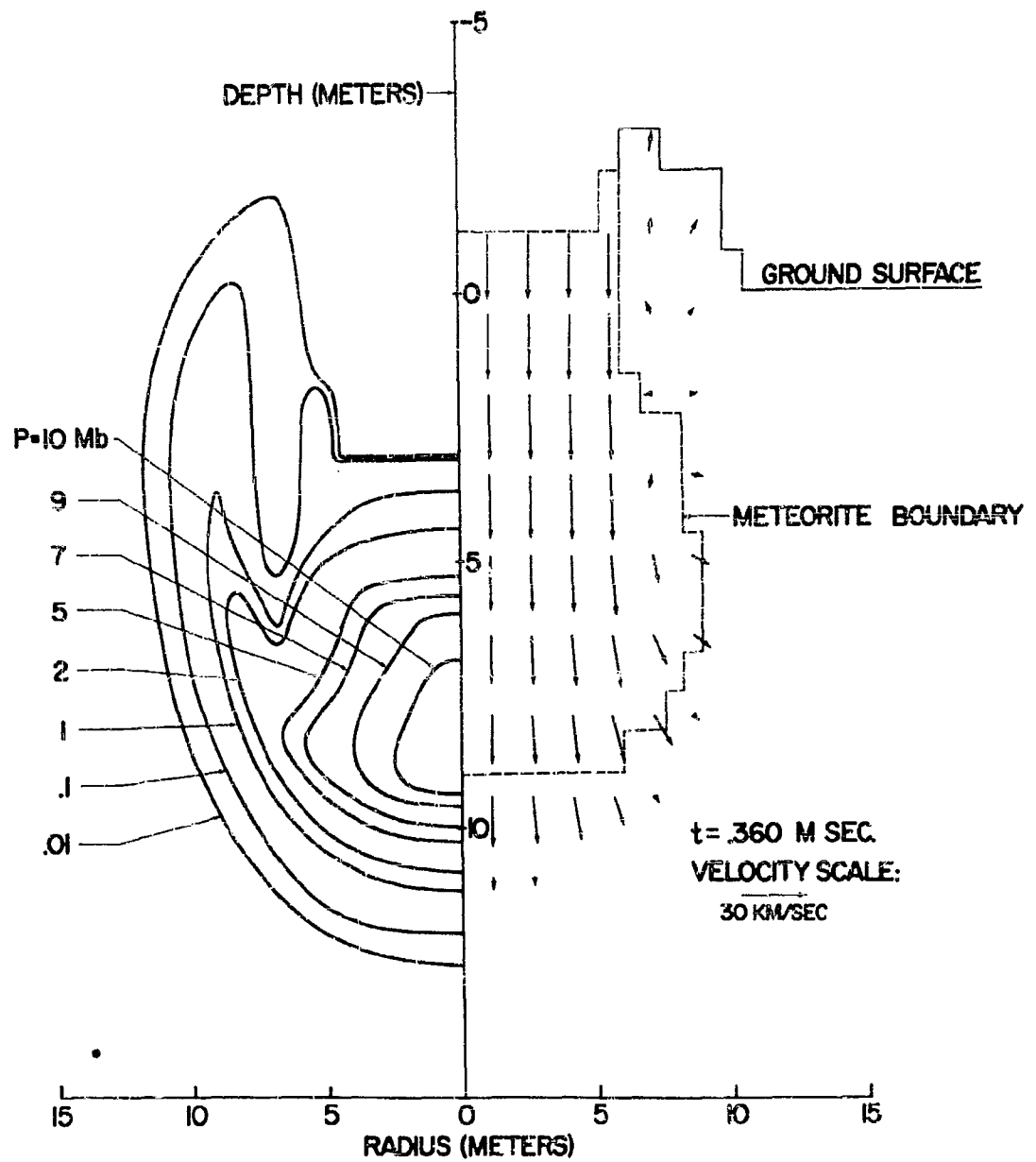


Fig. 5.10 Continued (Note Changing Scale)

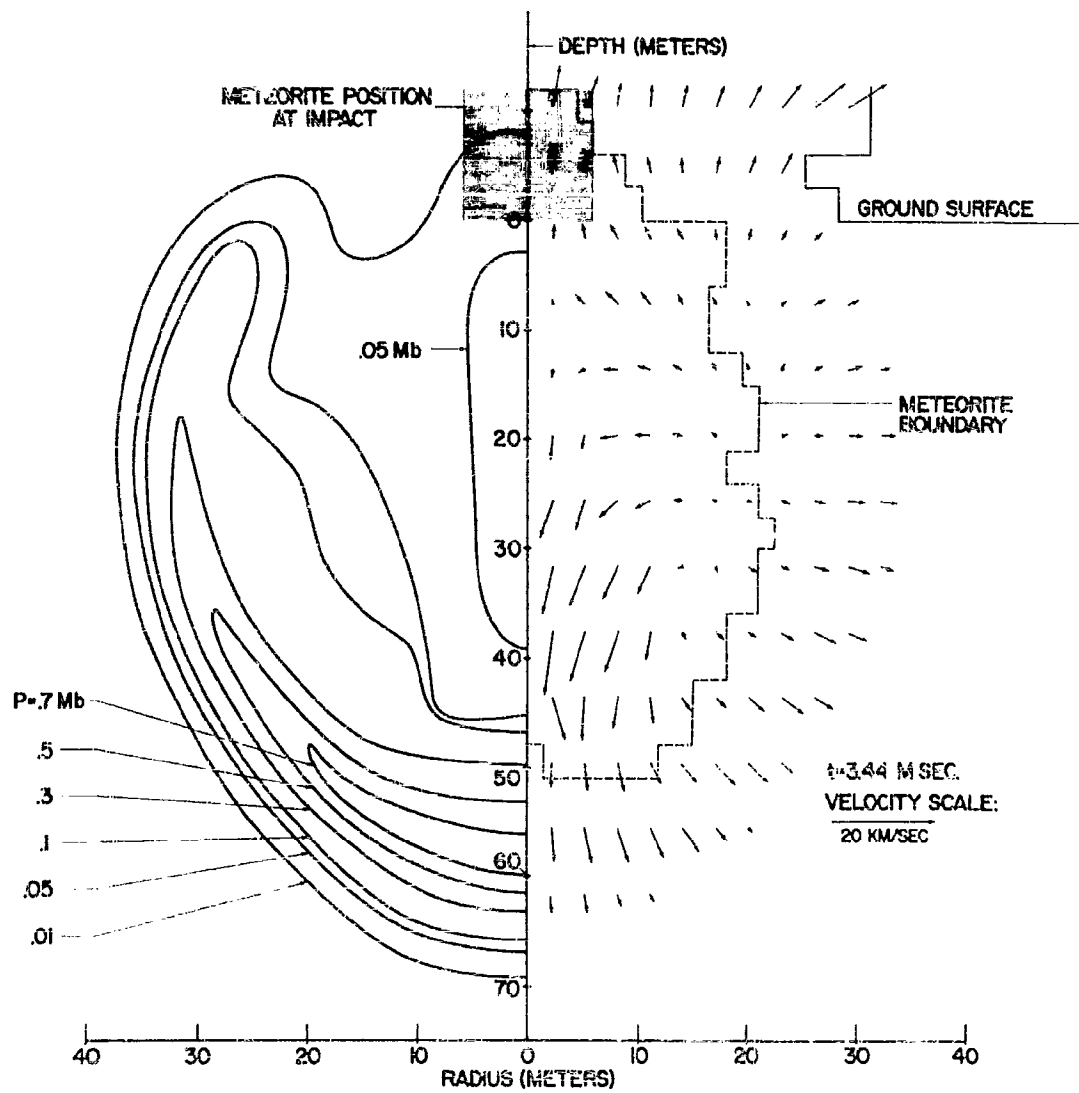


Fig. 5.10 Continued (Note Changing Scale)

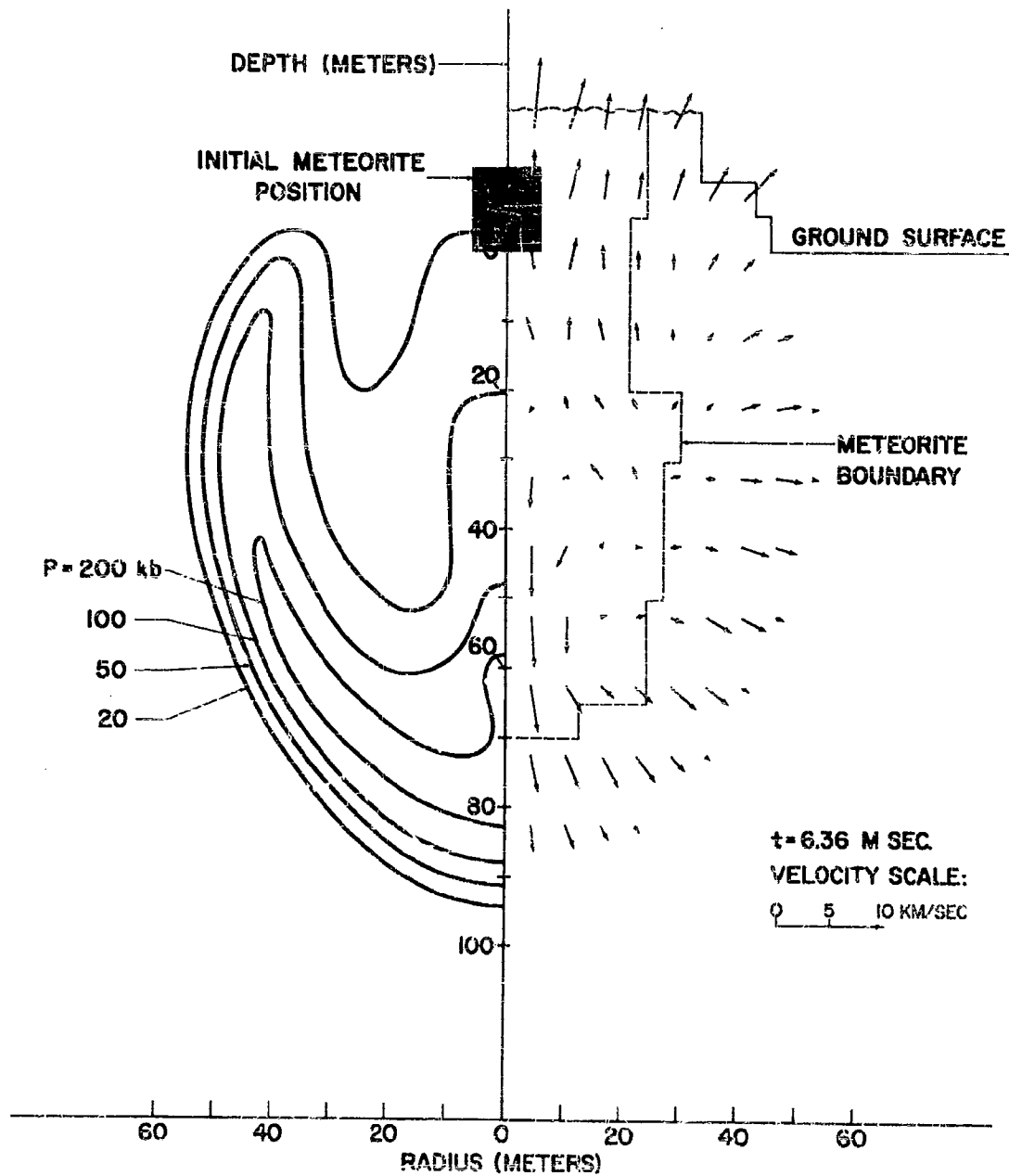


Fig. 5.10 Continued (Note Changing Scale)

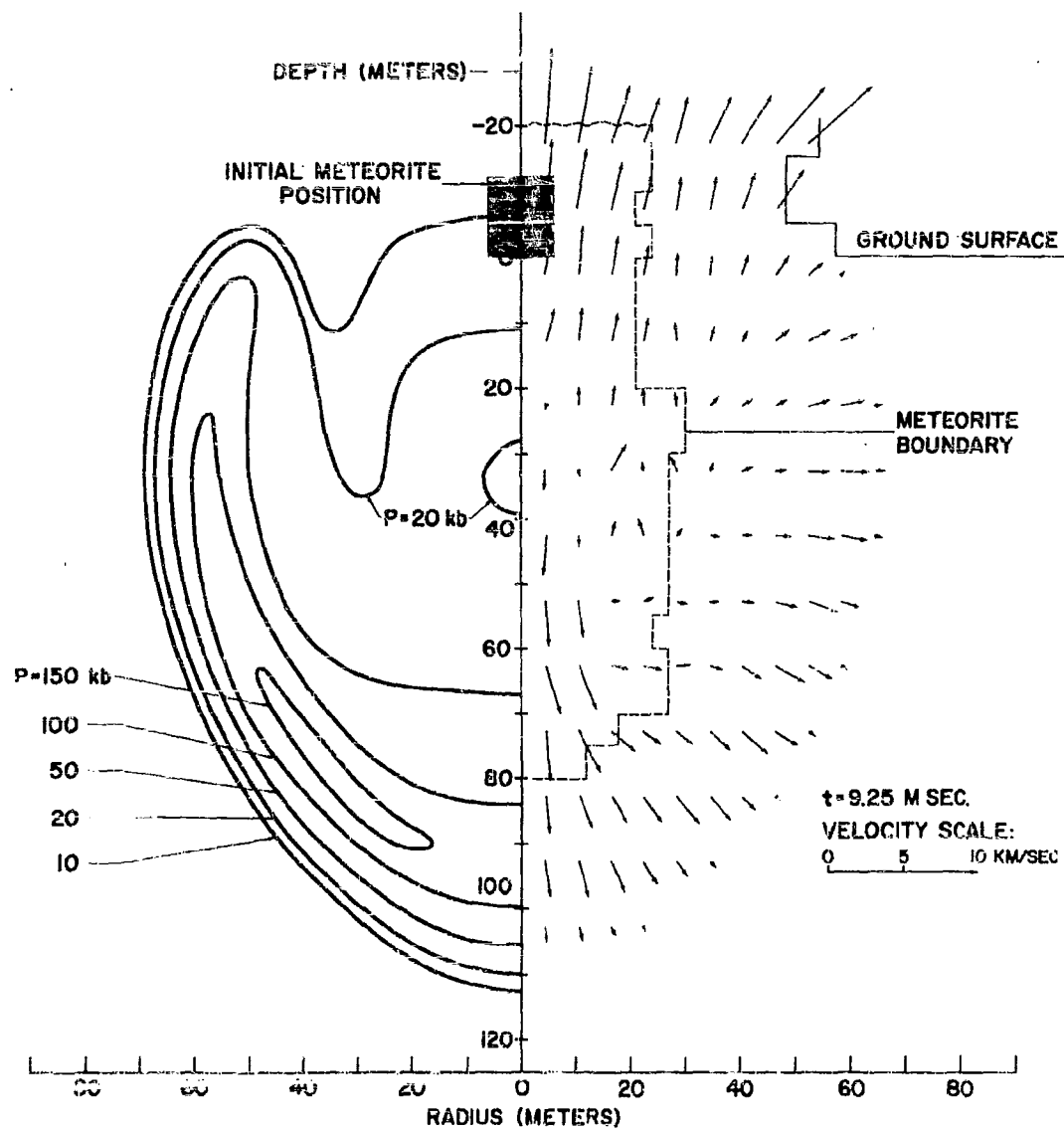


Fig. 5.10 Continued (Note Changing Scale)

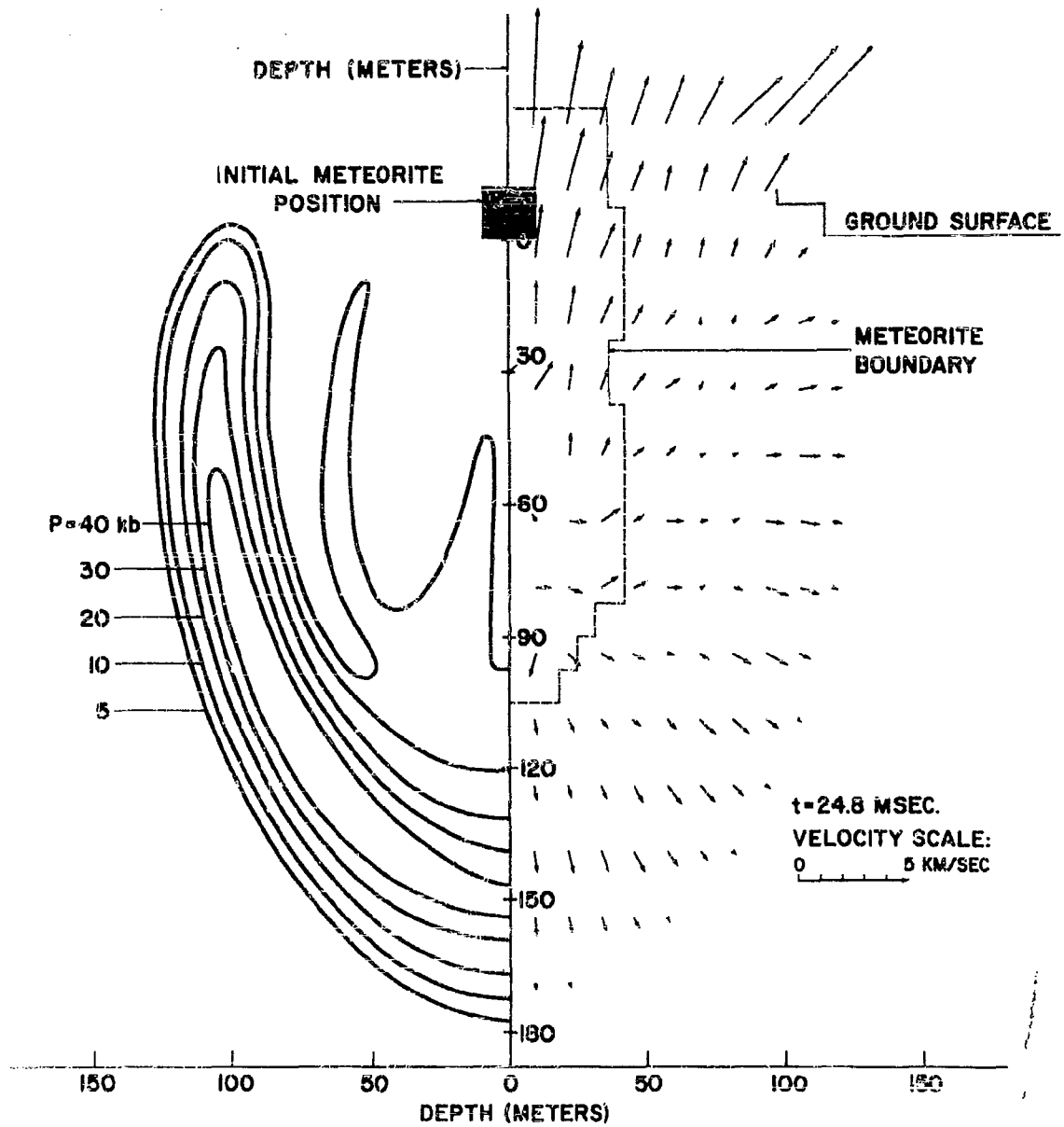


Fig. 5.10 Continued (Note Changing Scale)

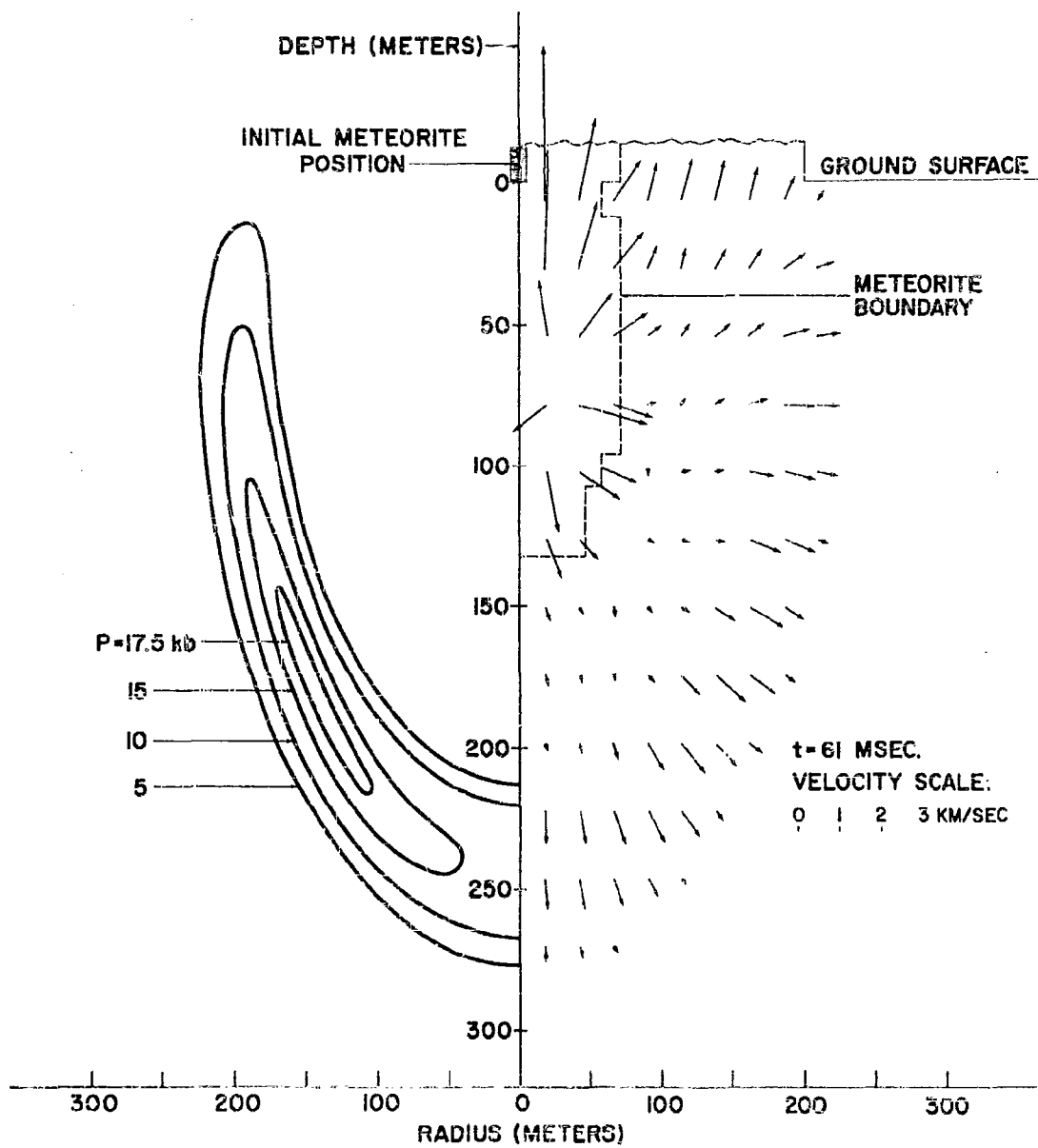


Fig. 5.10 Concluded (Note Changing Scale)



At Crater Boundary



1 mm from Crater Boundary



2.5 mm from Crater Boundary



Undisturbed Crystal Structure

Fig. 5.11 Crystallographic Changes in a 70:30 Brass Target in the Vicinity of the Crater x 500 (from Ref. 25)

Revised for publication by
AERONAUTIC AND STRUCTURES RESEARCH LABORATORY
MASSACHUSETTS INSTITUTE OF TECHNOLOGY

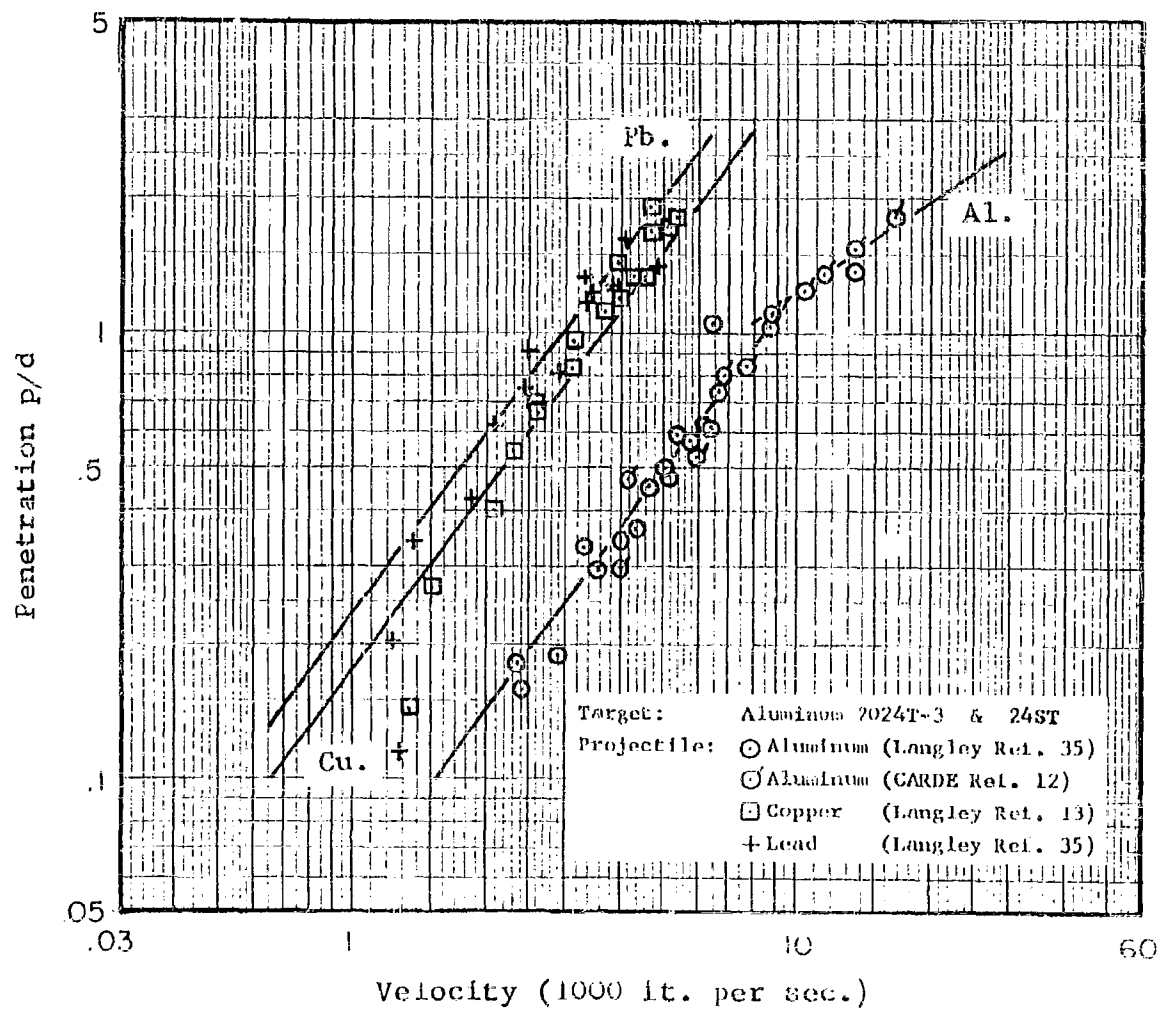


Fig. 5.12 Penetration in Aluminum Targets

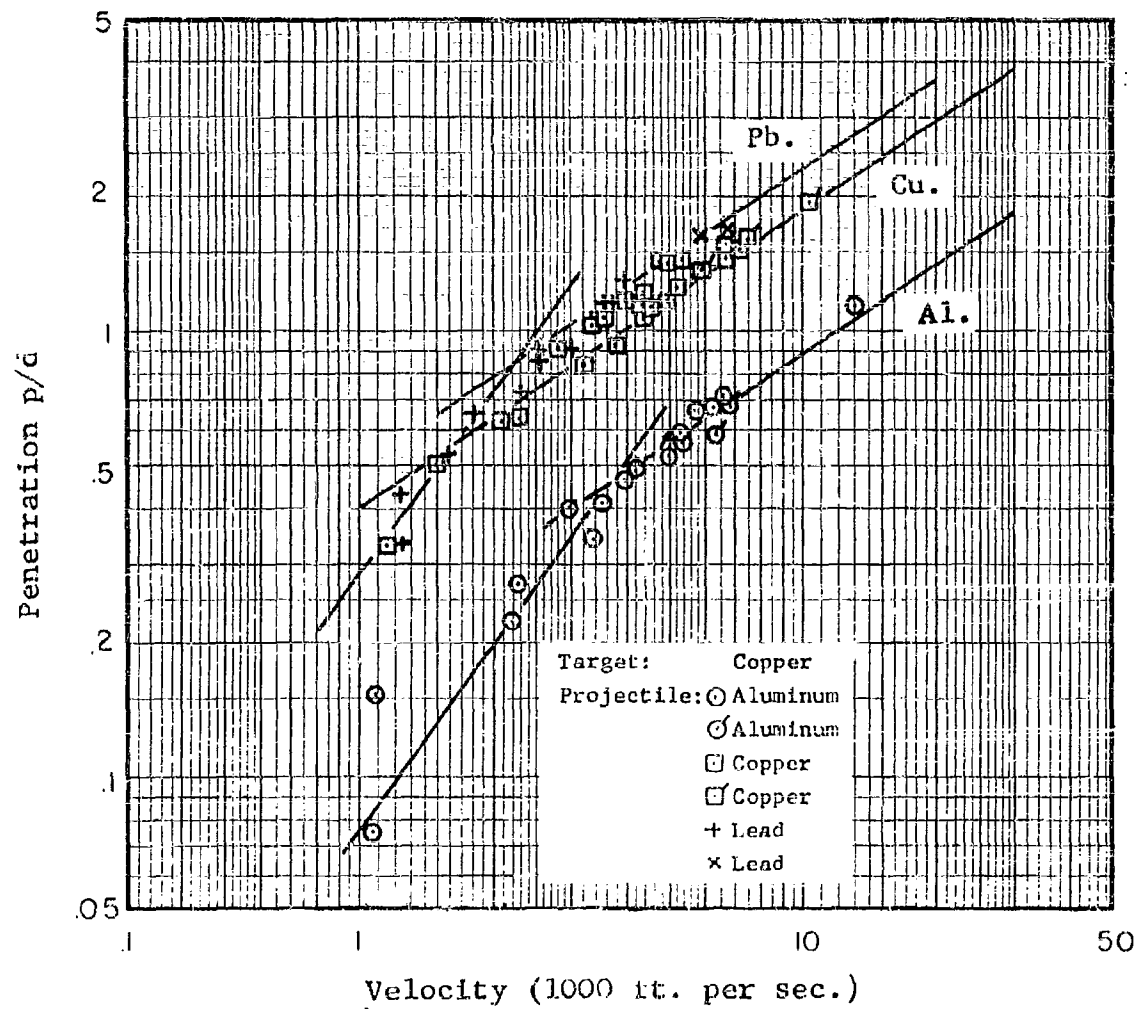


Fig. 5.13 Penetration in Copper Targets

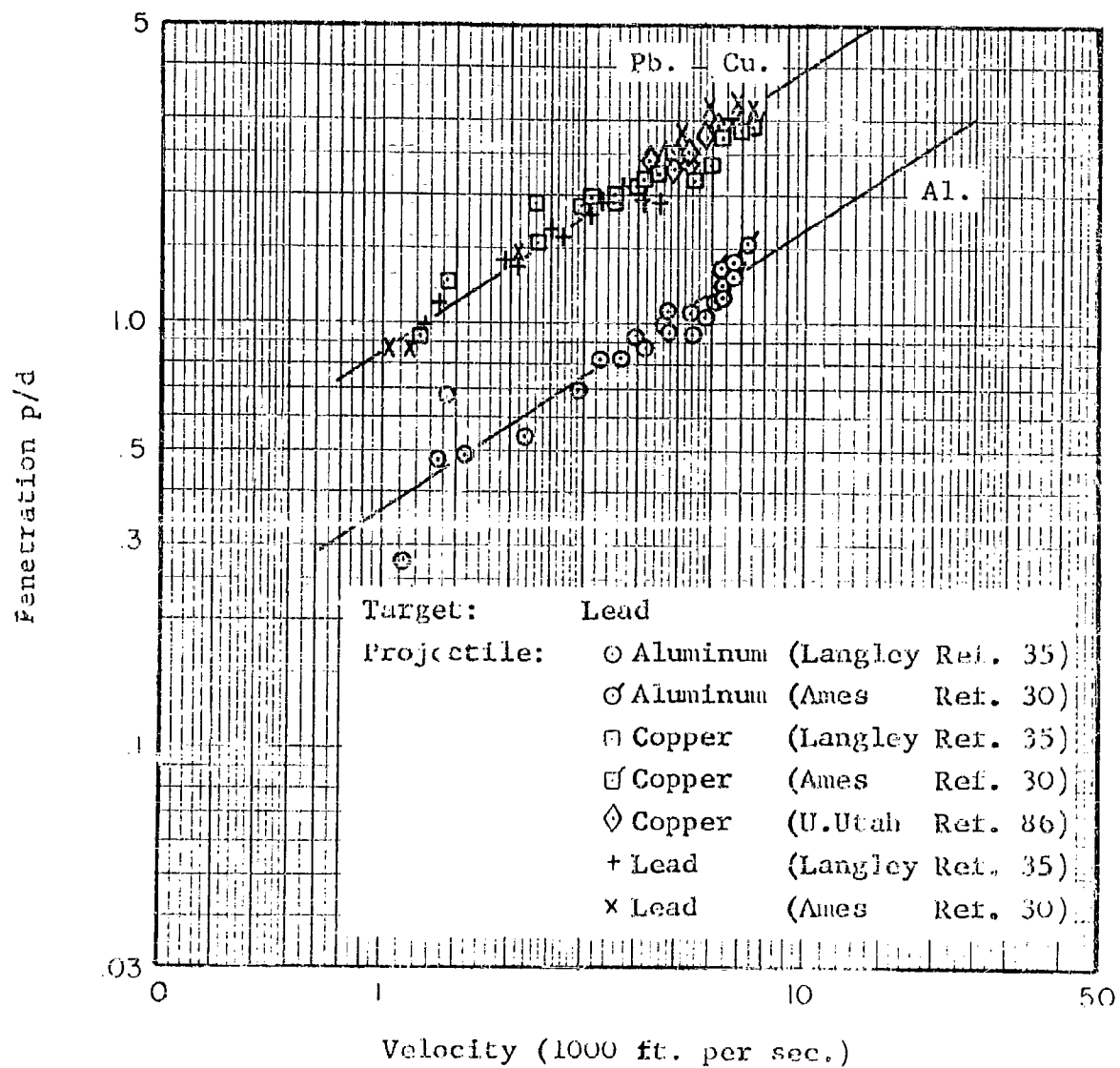


Fig. 5.14 Penetration in Lead Targets

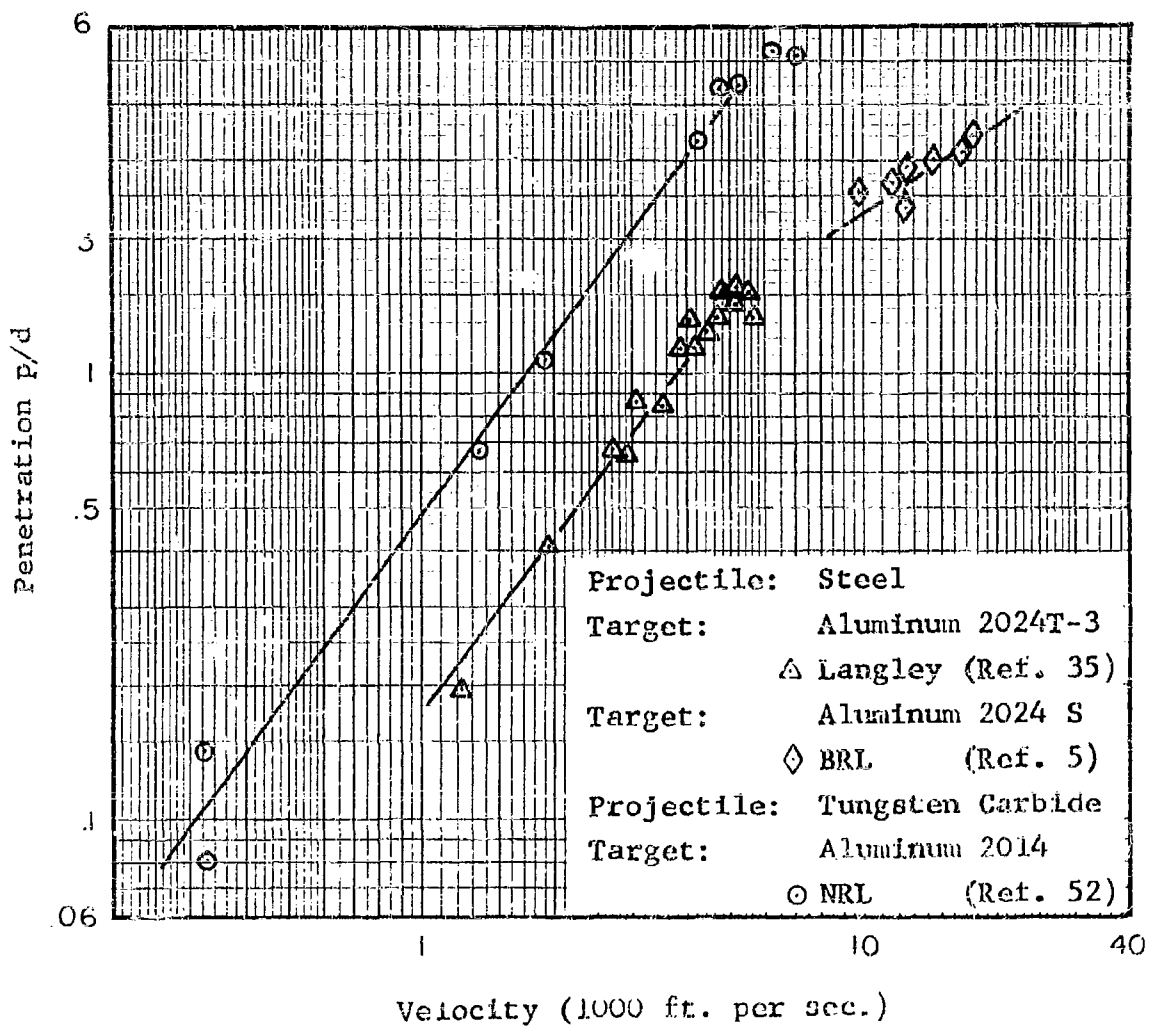


Fig. 5.15 Penetration in Aluminum Targets

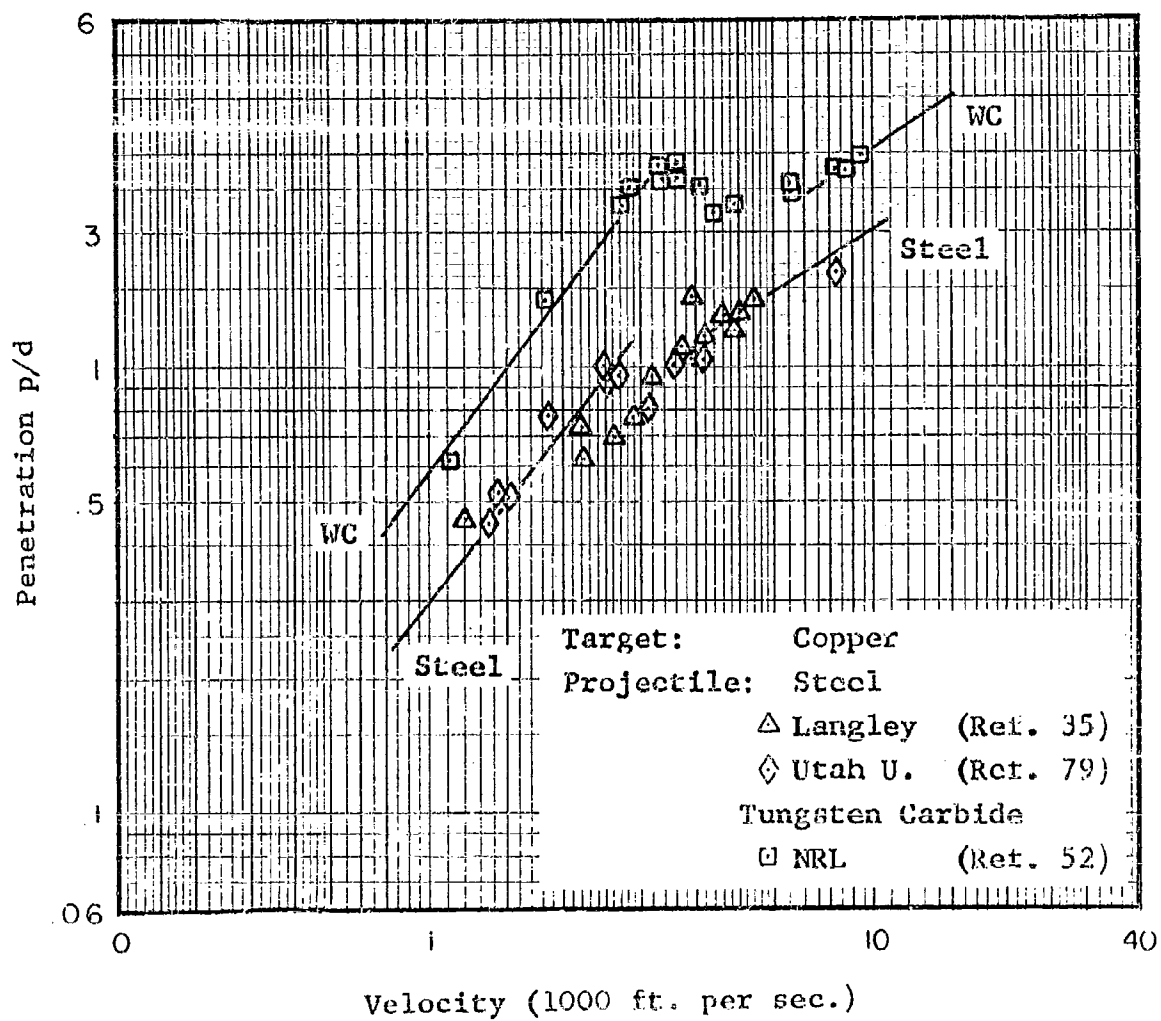


Fig. 5.16 Penetration in Copper Targets

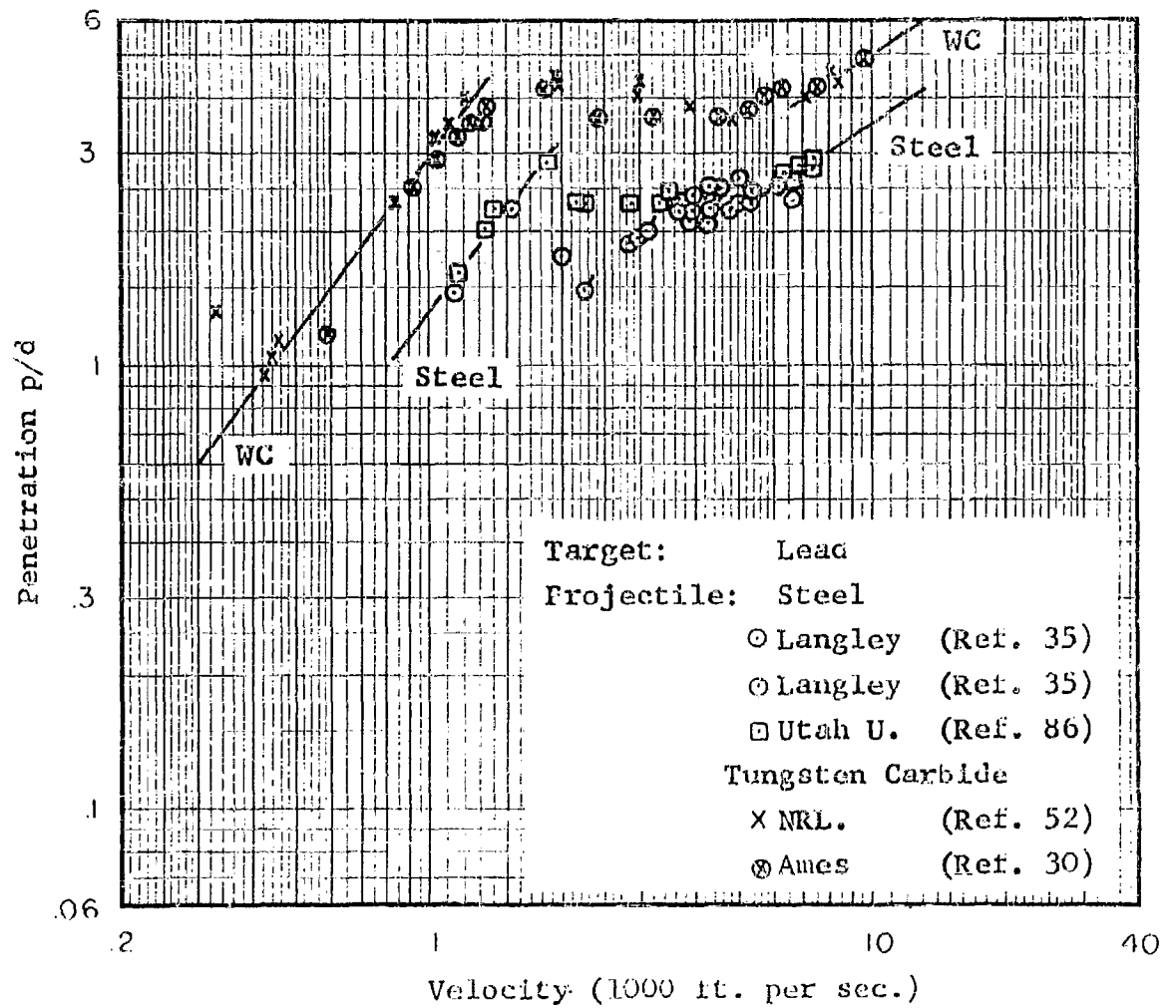


Fig. 5.17 Penetration in Lead Targets

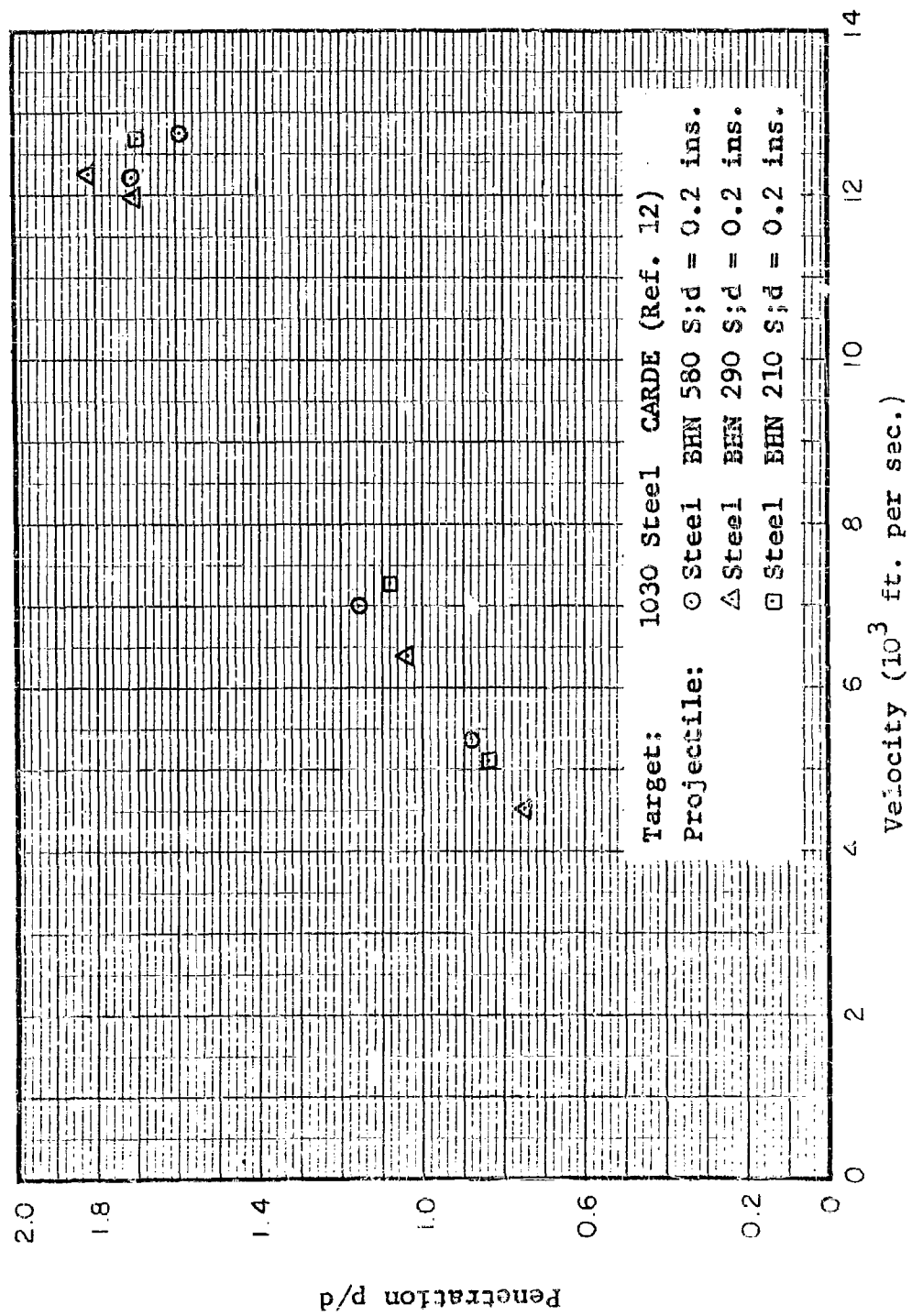


Fig. 5.13 Penetration by Various Heat Treated Steel Spheres in 1030 Steel Targets

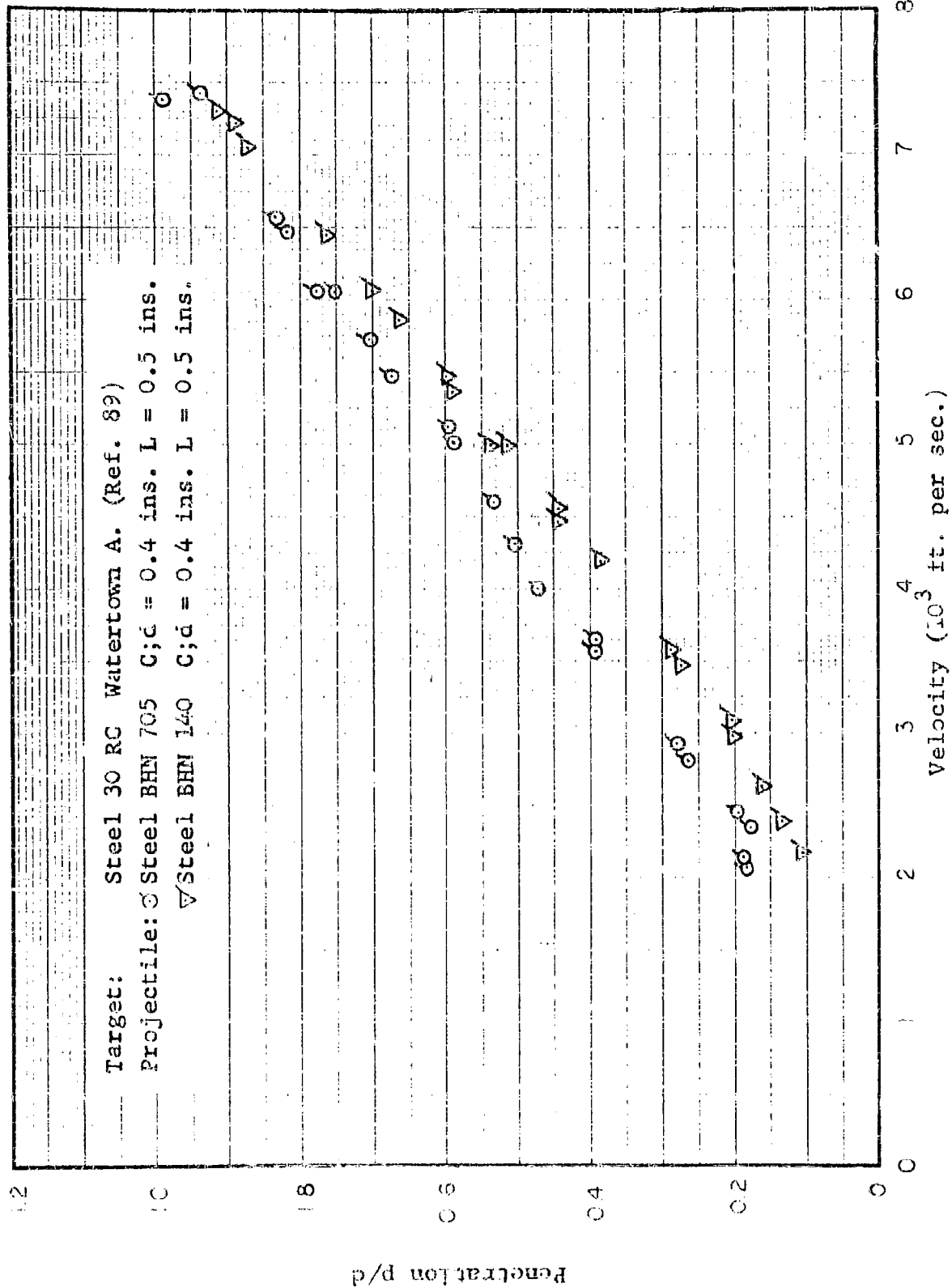


Fig. 5.19 Penetration by Two Different Hardness Steel Cylinders in 30 RC Steel Targets

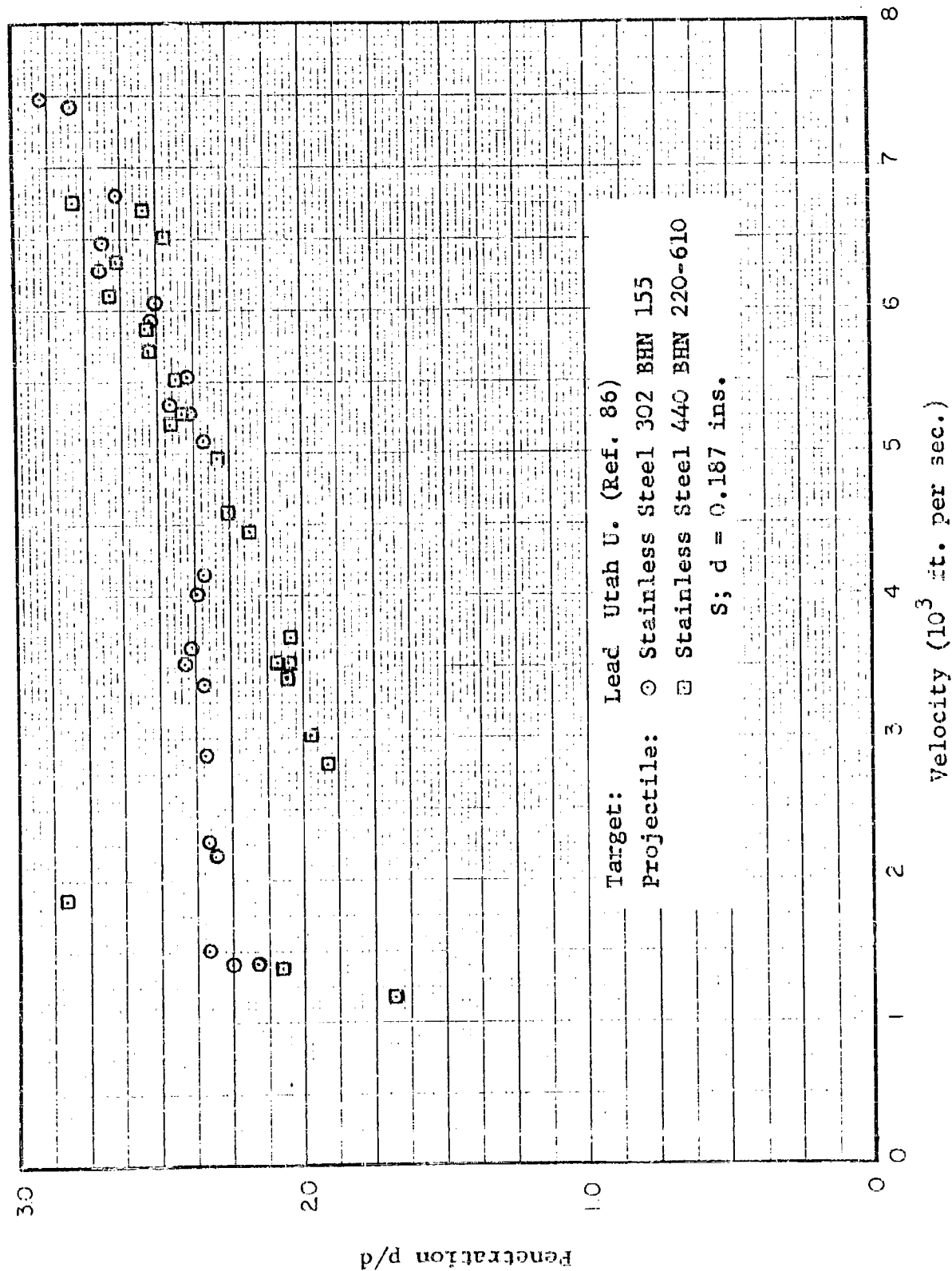


Fig. 5.20 Penetration by 302 Stainless Steel and 440 Stainless Steel Spheres in Lead Targets

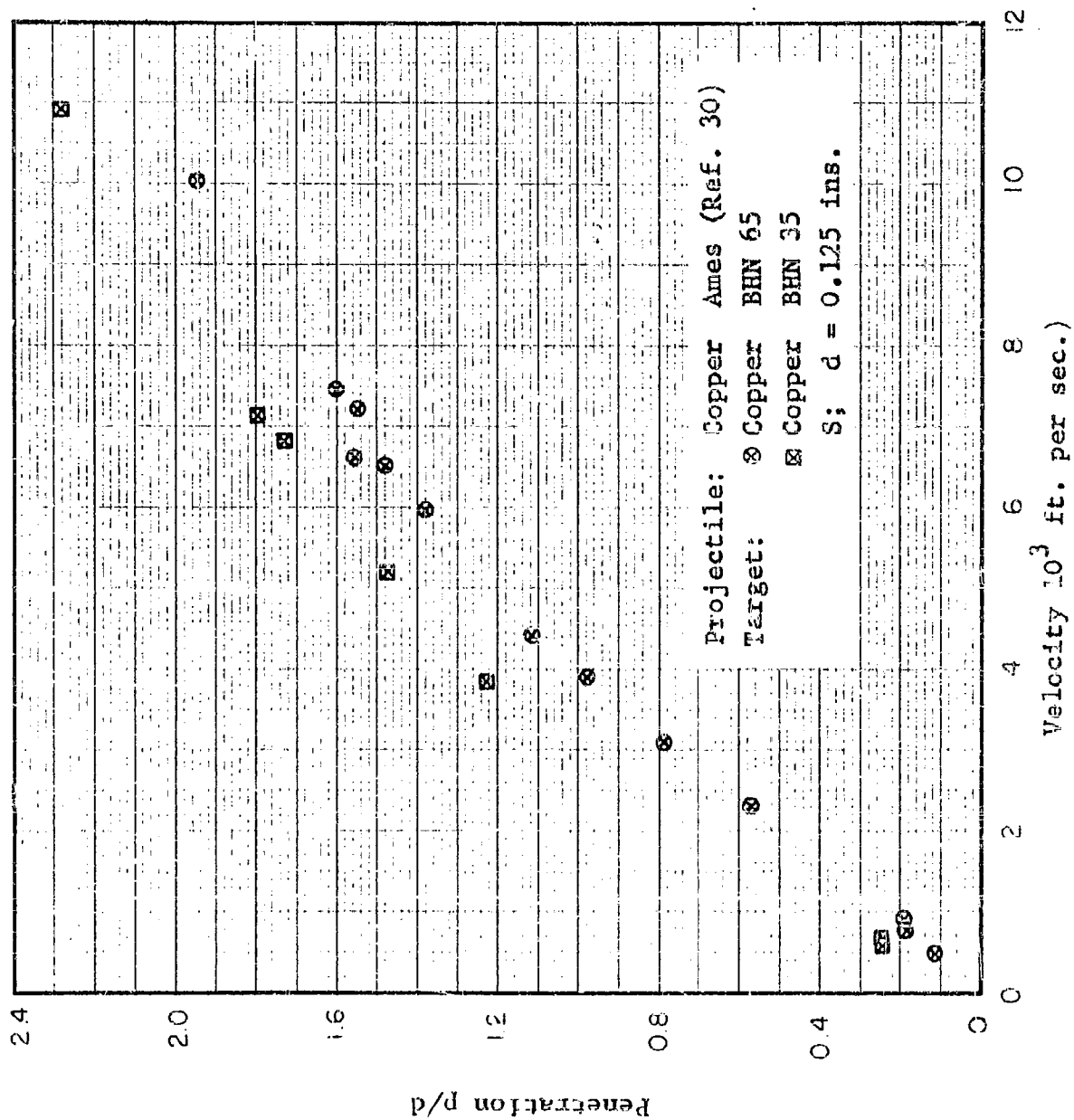


Fig. 5.21 Penetration by Copper Spheres in Copper Targets
 BHN 65 and BHN 36

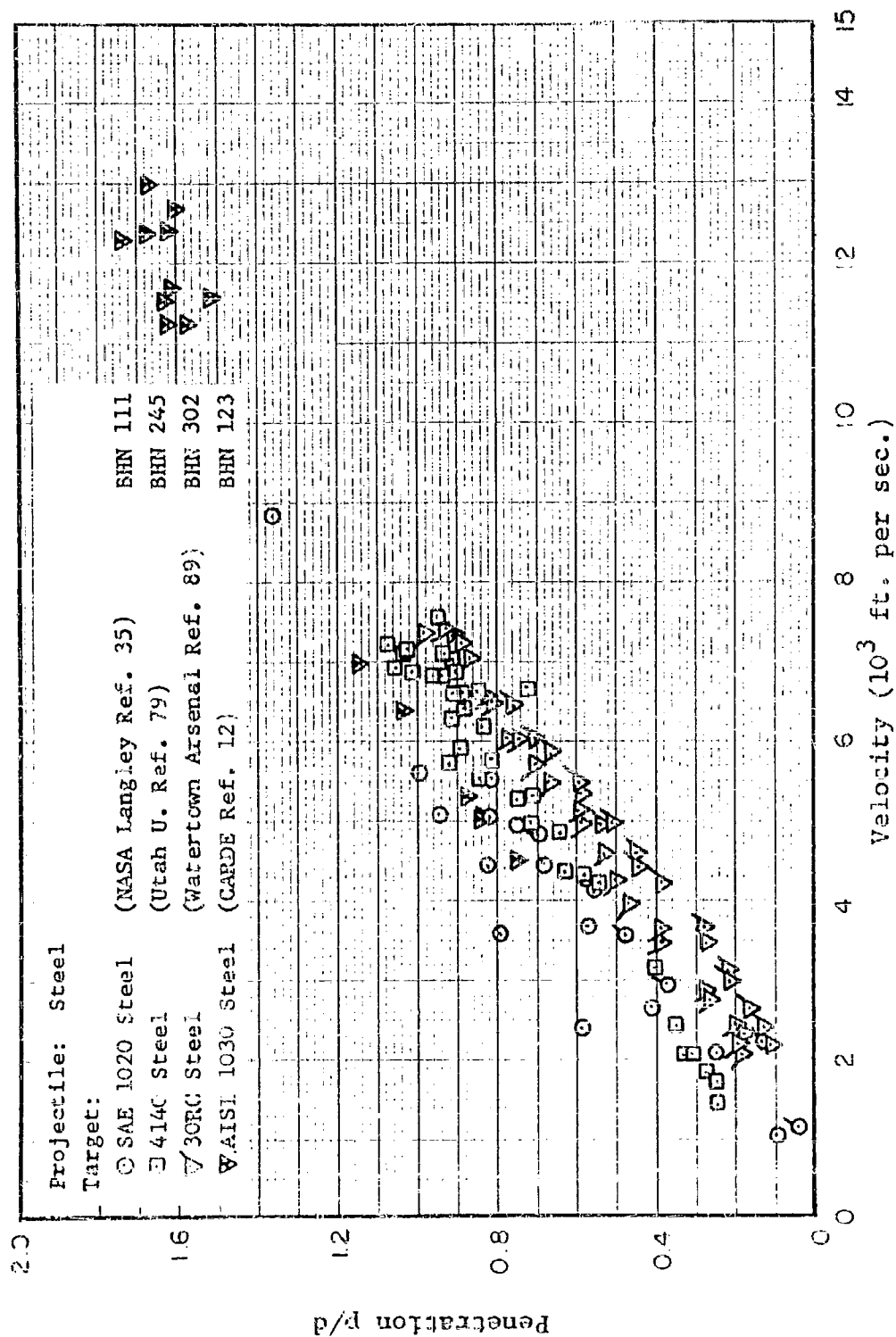


Fig. 5.22 Penetration by Steel Projectiles in SAE 1020 Steel, 4140 Steel, 30 RC Steel, and AISI 1030 Steel Targets

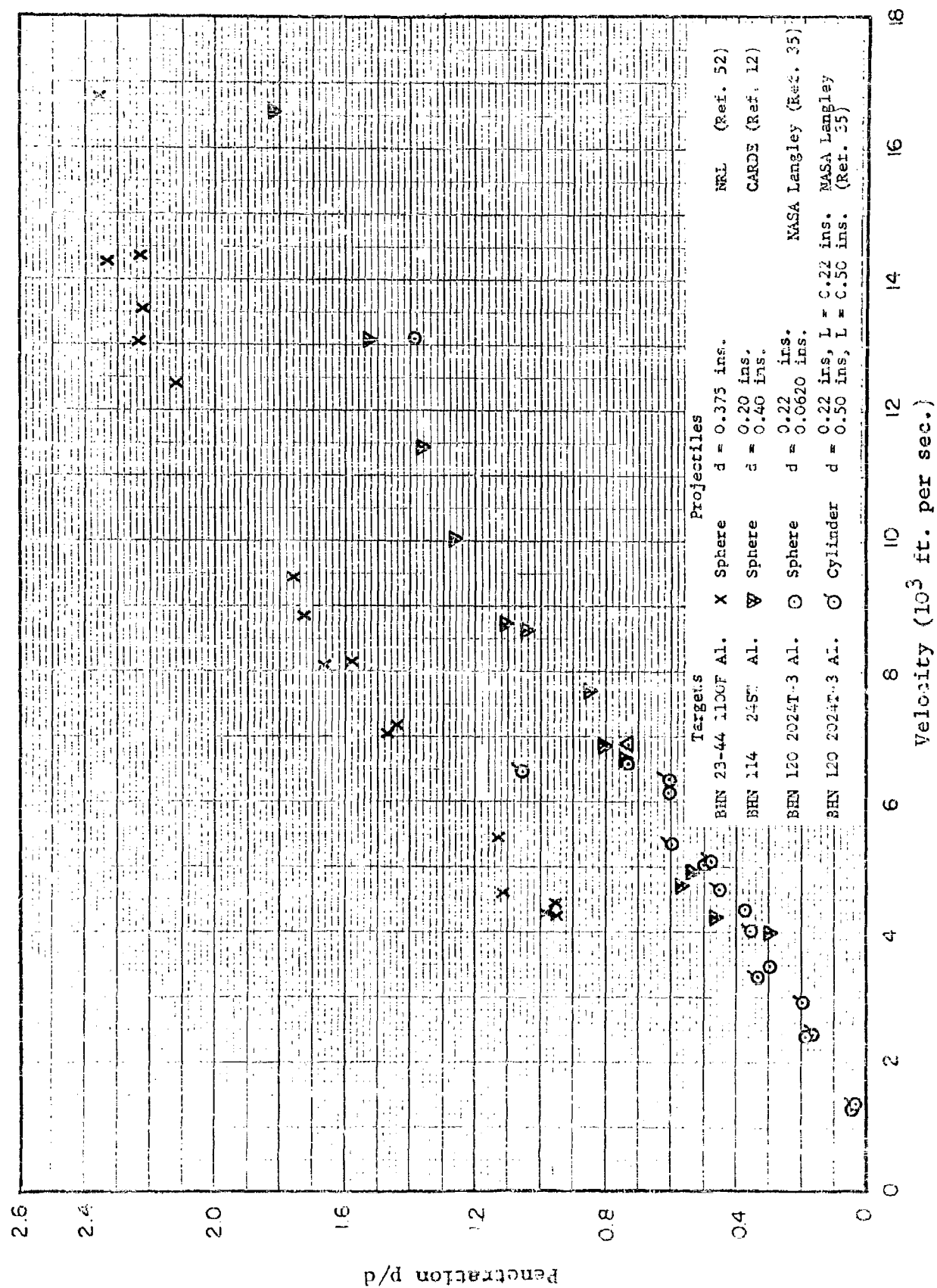


Fig. 3.23 Penetration by Aluminum Projectiles in 1100F Aluminum and 2024 Aluminum Targets

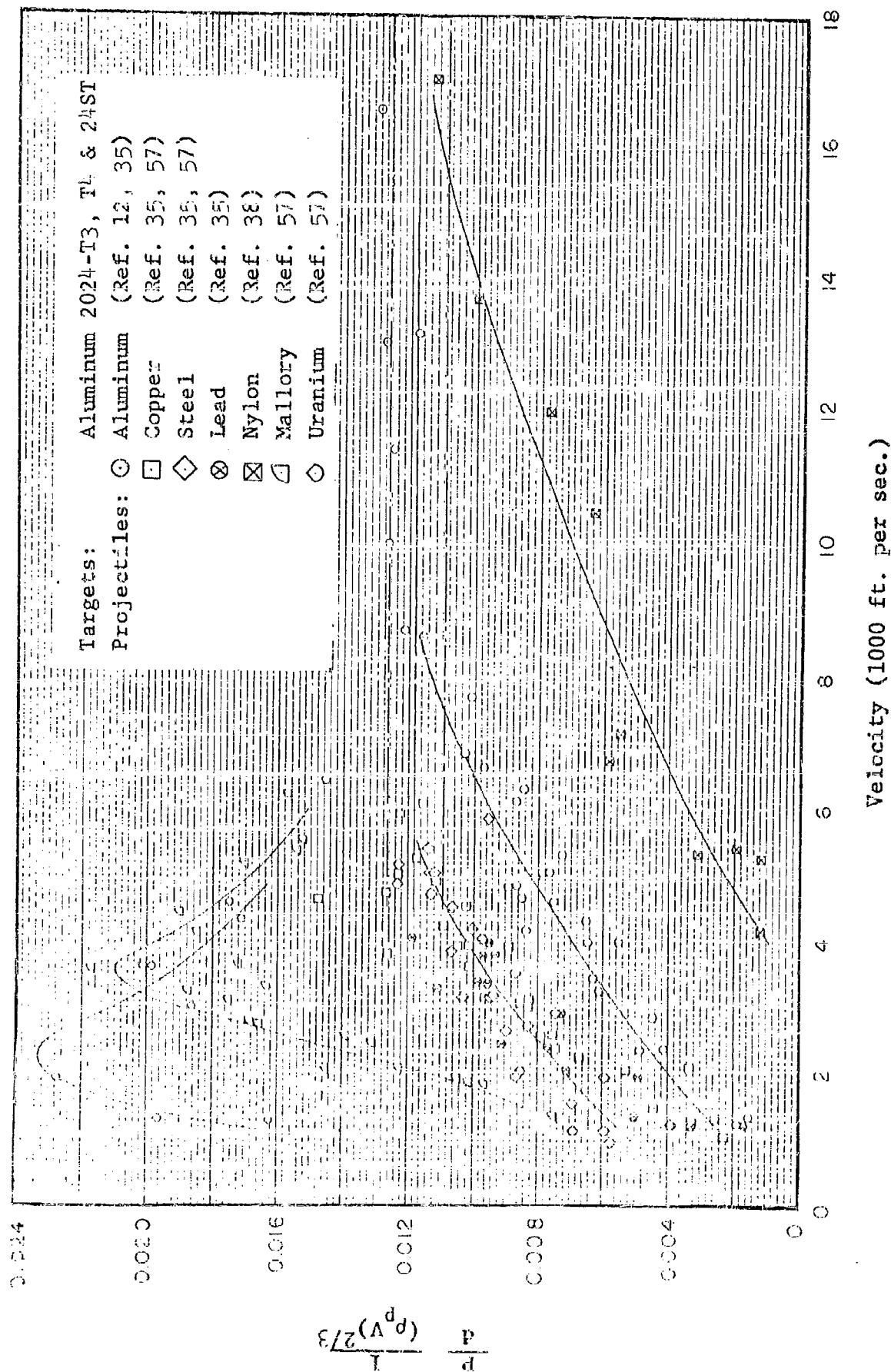


Fig. 5.24 Penetration Ratio in Aluminum Targets

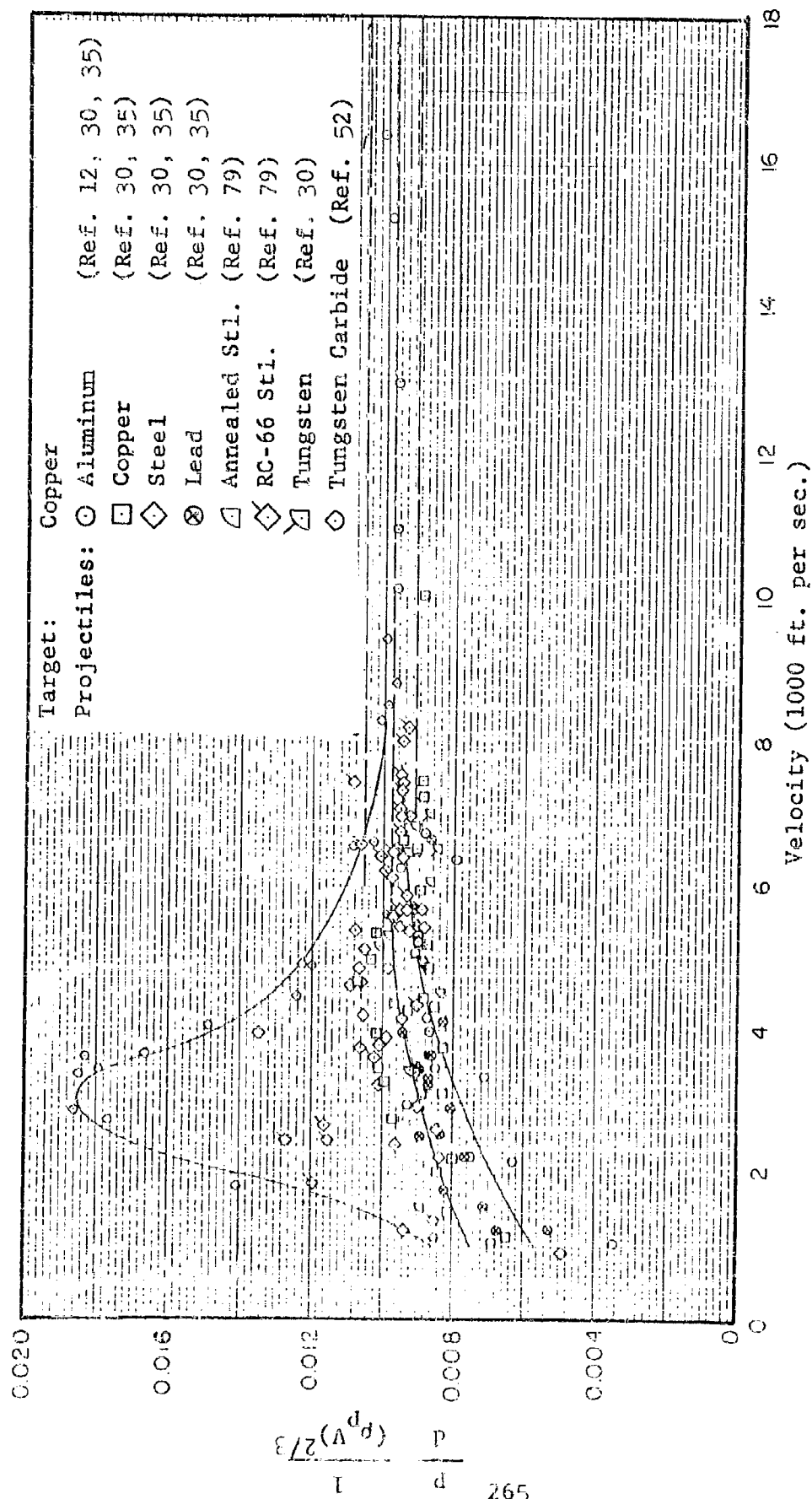


Fig. 5.25 Penetration Ratio in Copper Targets

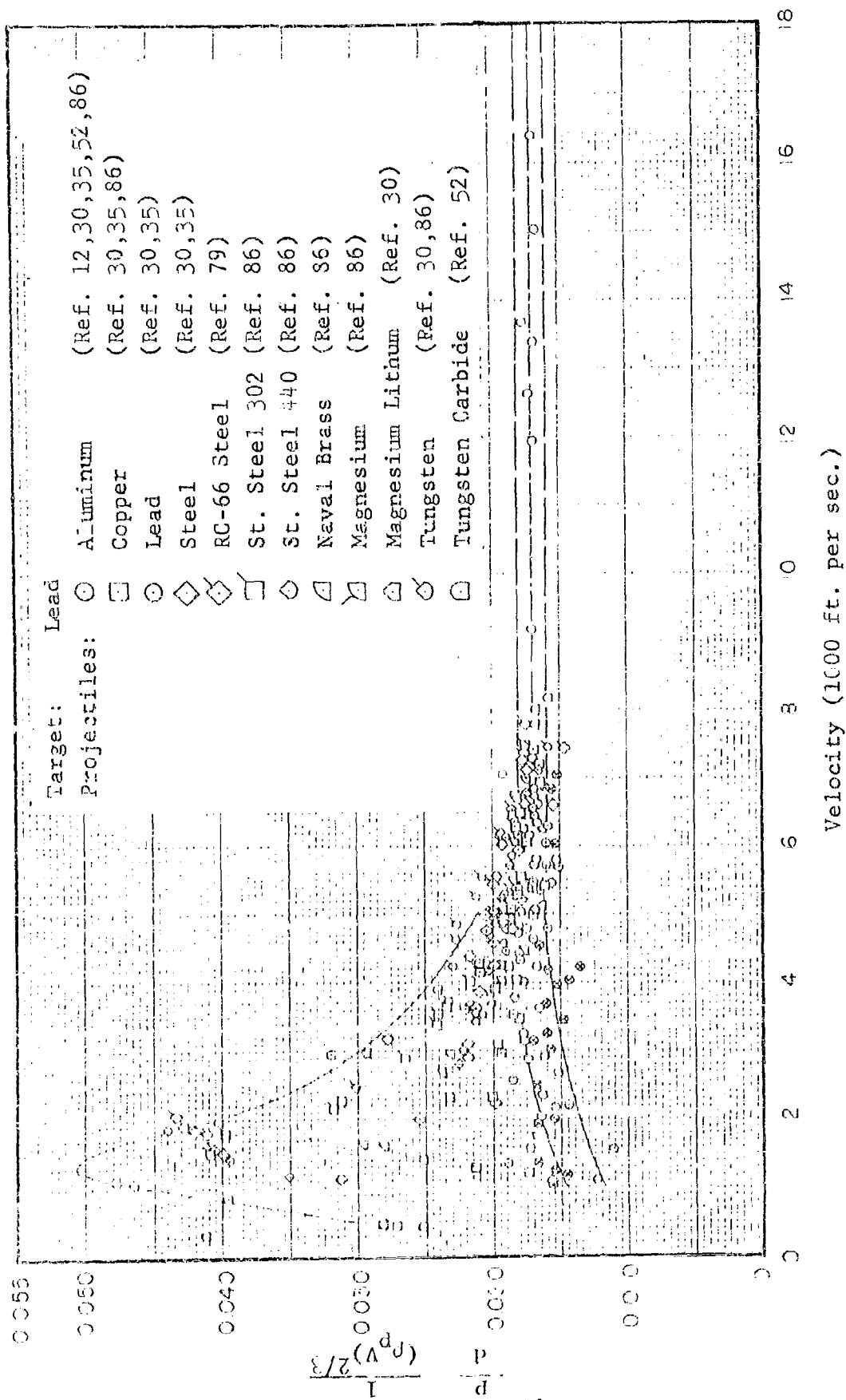


Fig. 5.26 Penetration Ratio in Lead Targets

$$k_1 = \frac{P}{d} \frac{1}{(\rho_p V)^{2/3}} (10^{-4})$$

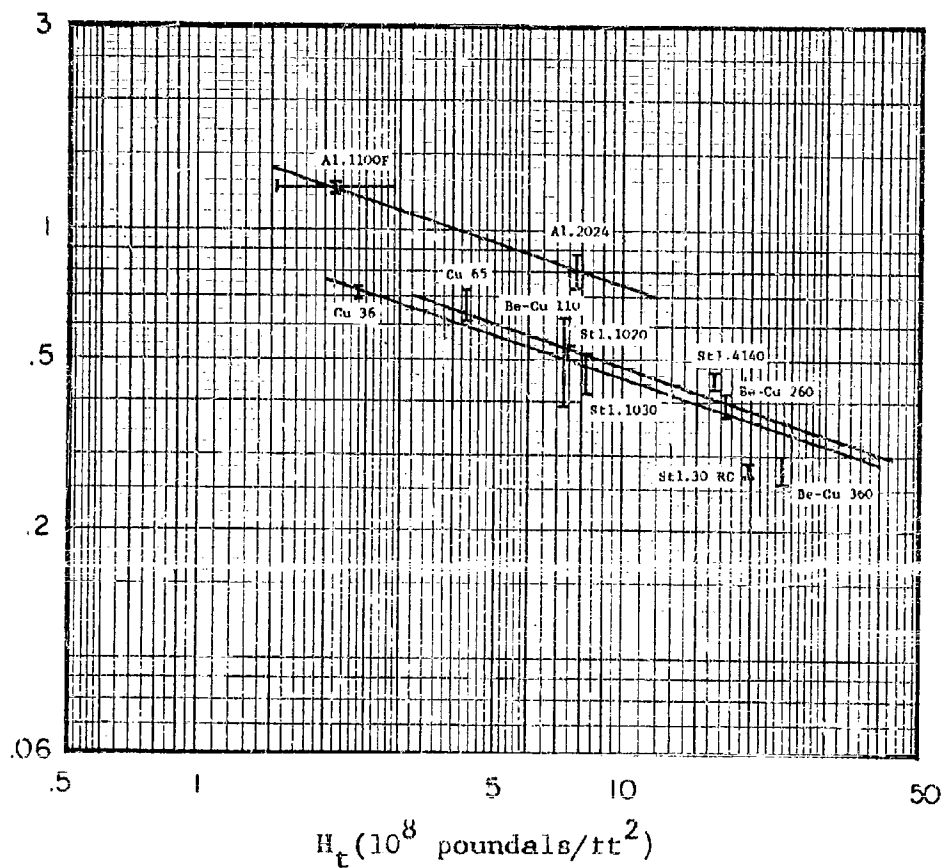


Fig. 5.27 Penetration Dependence on Target Hardness

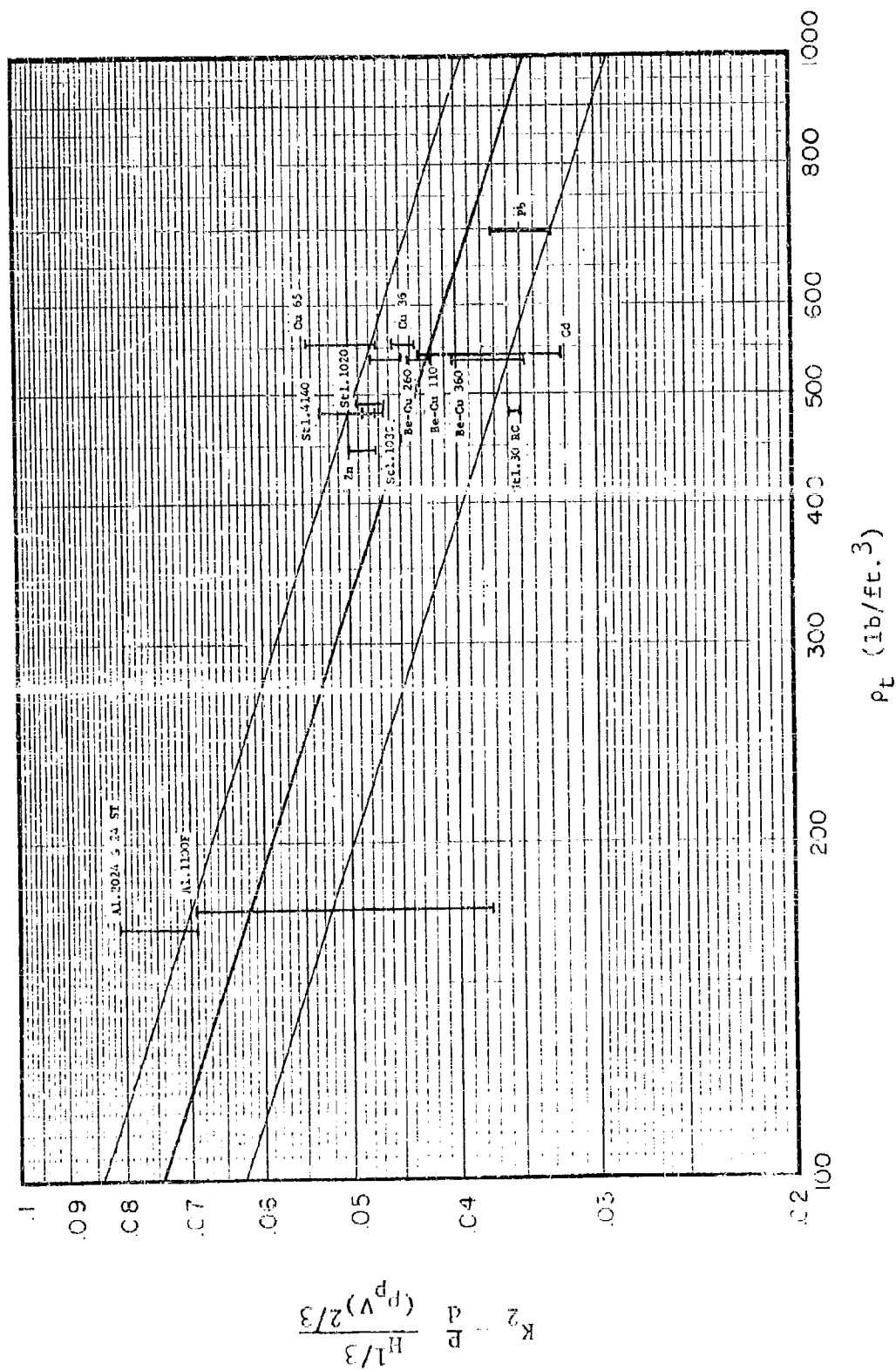
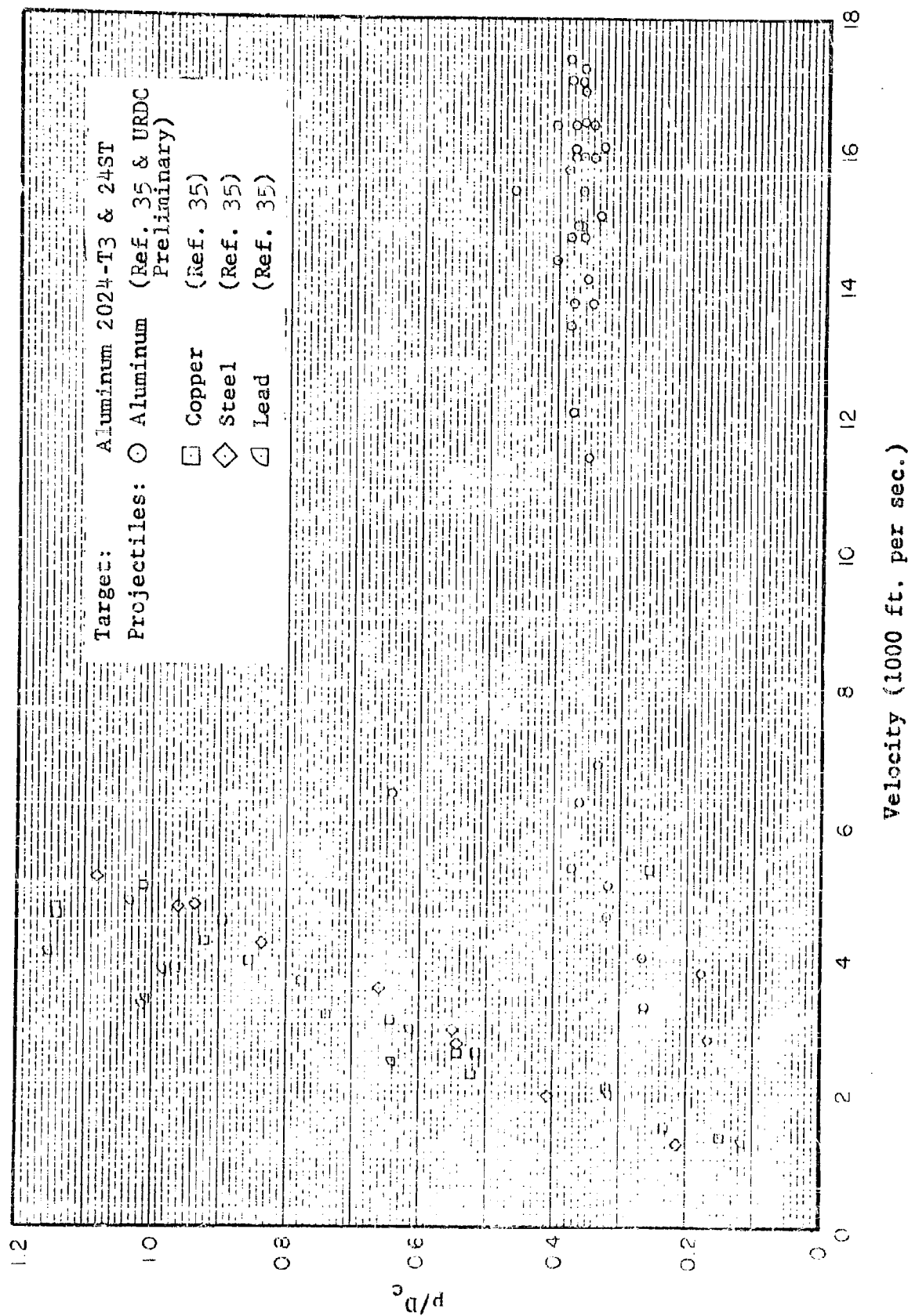


Fig. 5.26 Penetration Dependence on Target Density



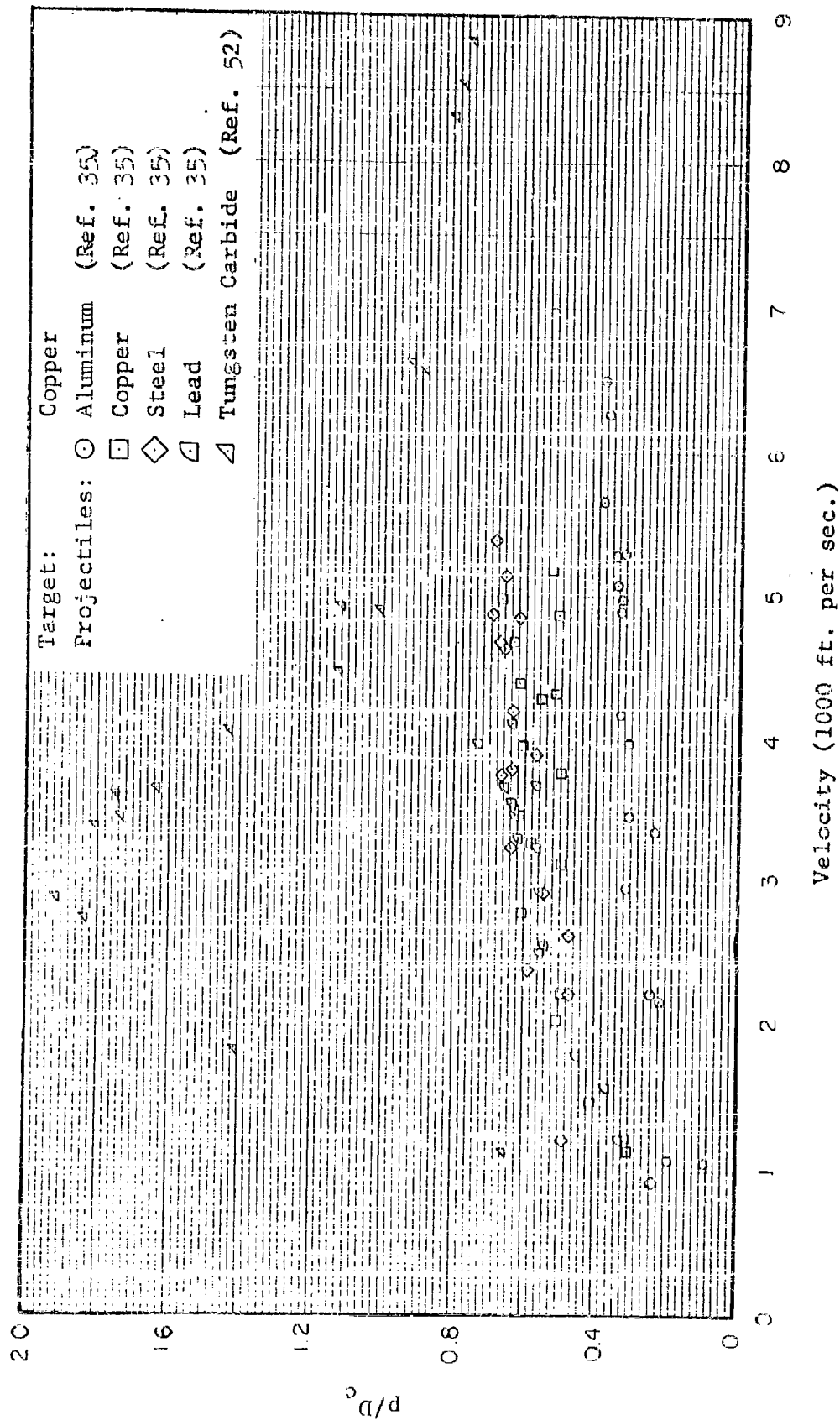


Fig. 5.30 Depth-Diameter Ratios for Craters in Copper Targets

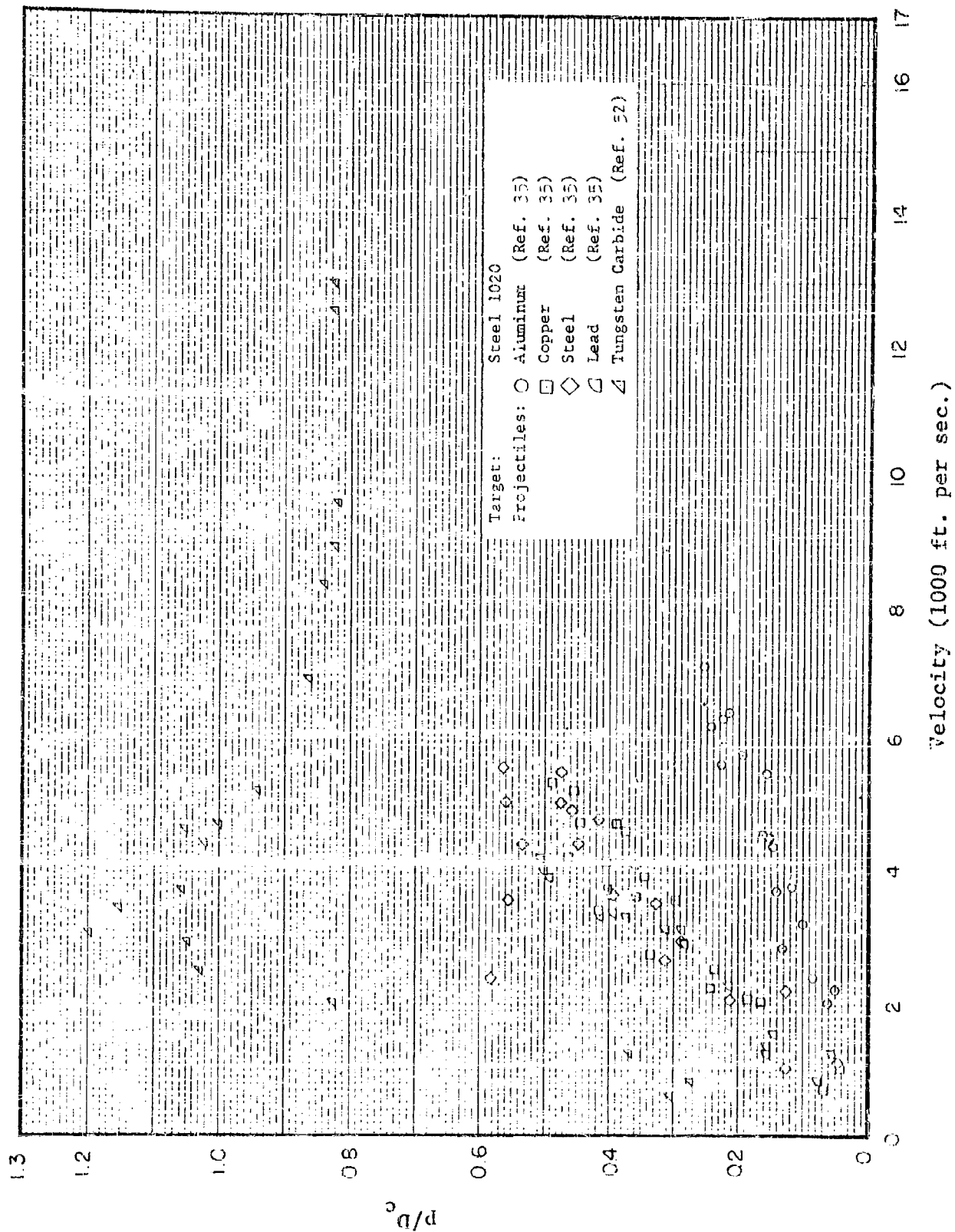


Fig. 5.31 Depth-Diameter Ratios for Craters in 1020 Steel Targets

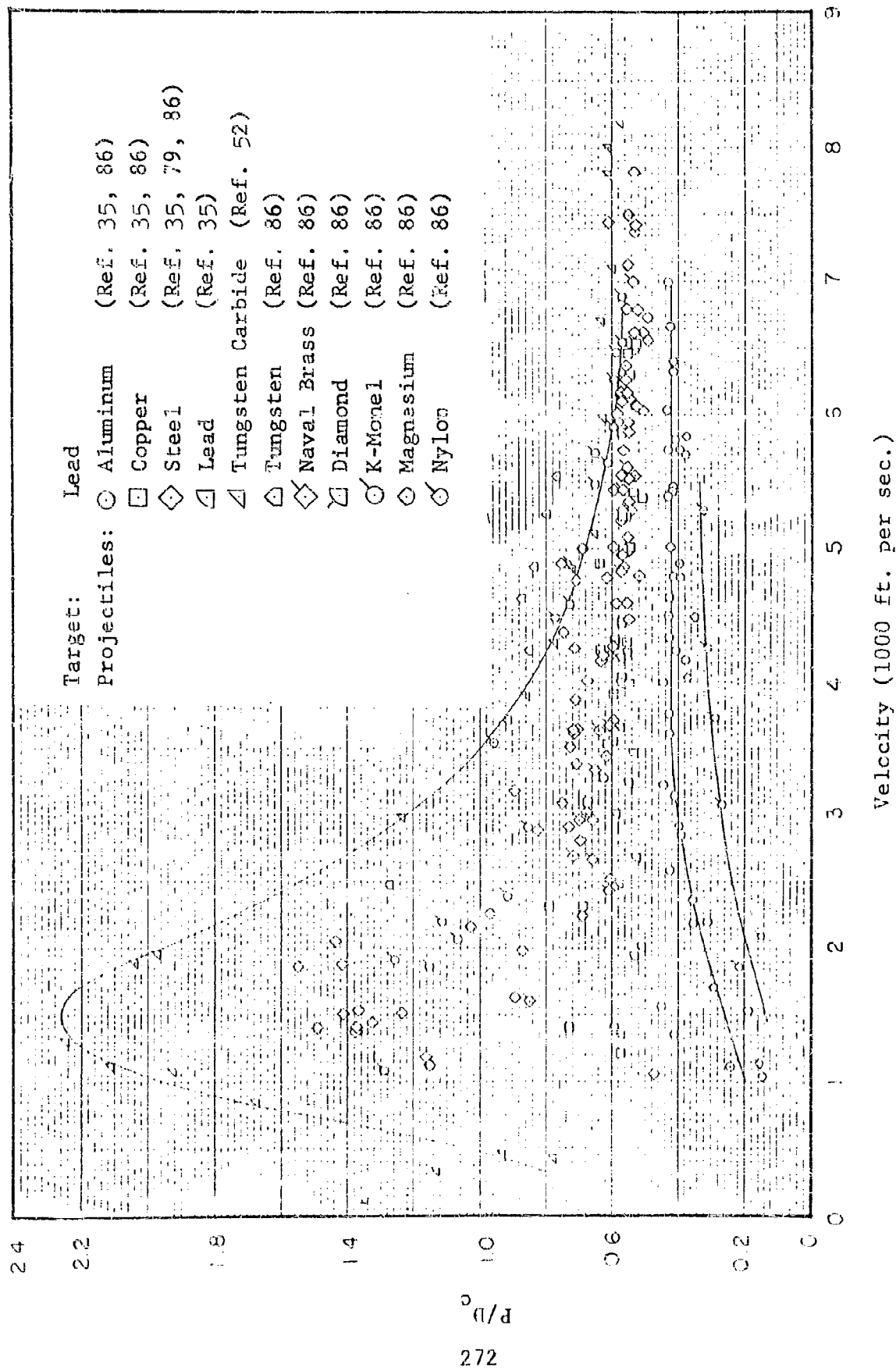


Fig. 5.32 Depth-Diameter Ratios for Craters in Lead Targets

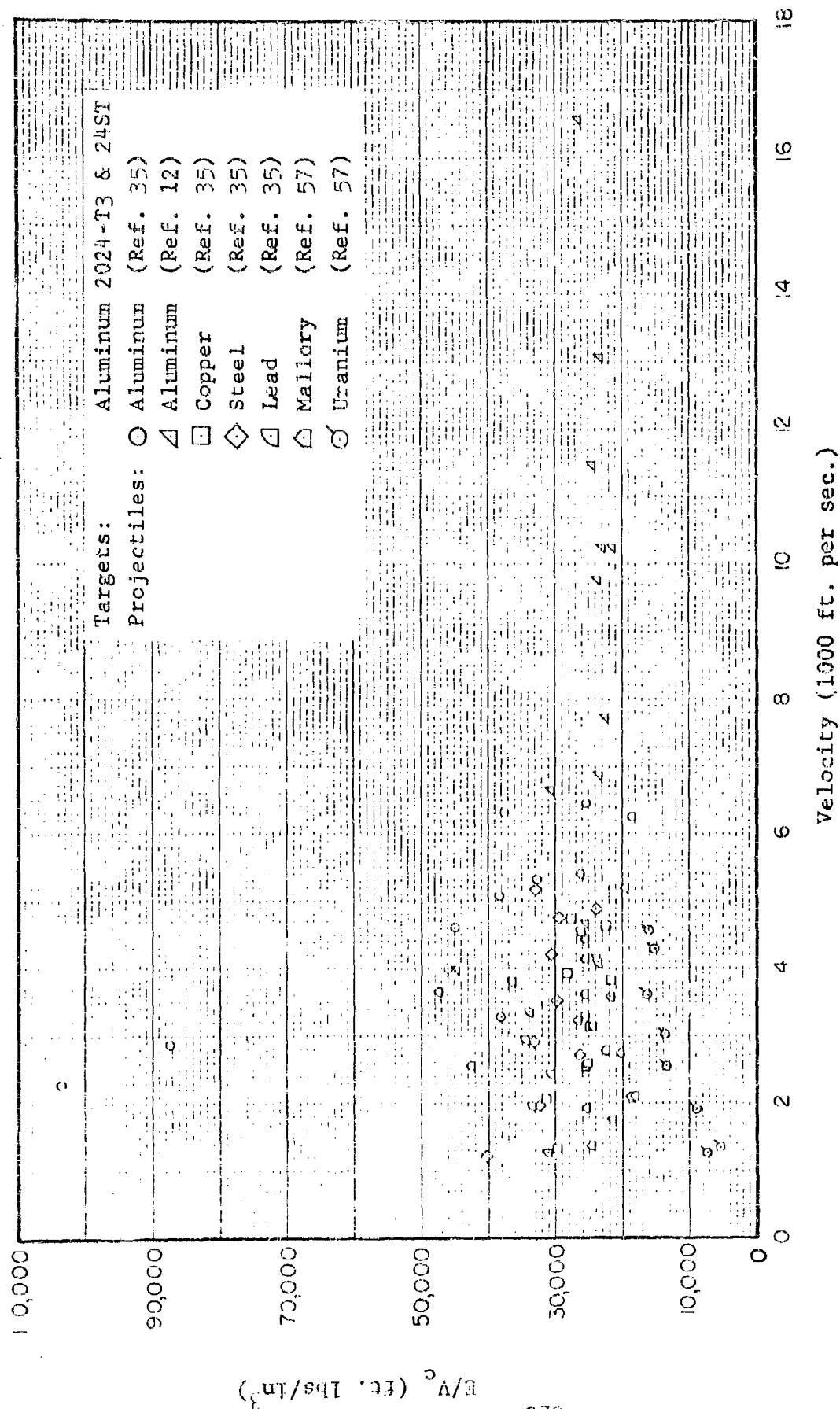


Fig. 5.33 Energy-Volume Ratios for Aluminum Targets

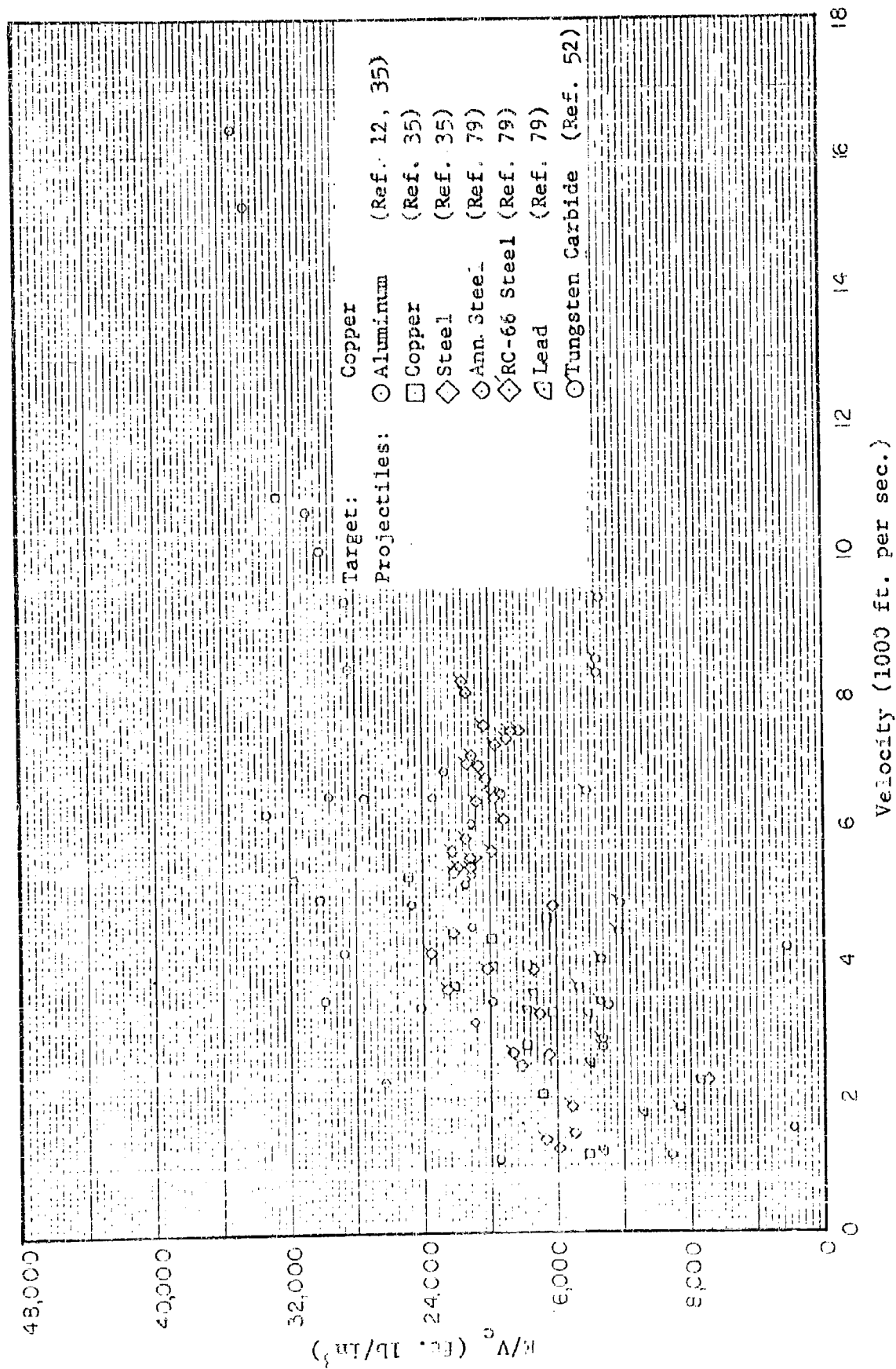


Fig. 5.3- Energy-Volume Ratios for Copper Targets

Figure 5.15 Energy-Volume Ratios for 1020 Steel Targets

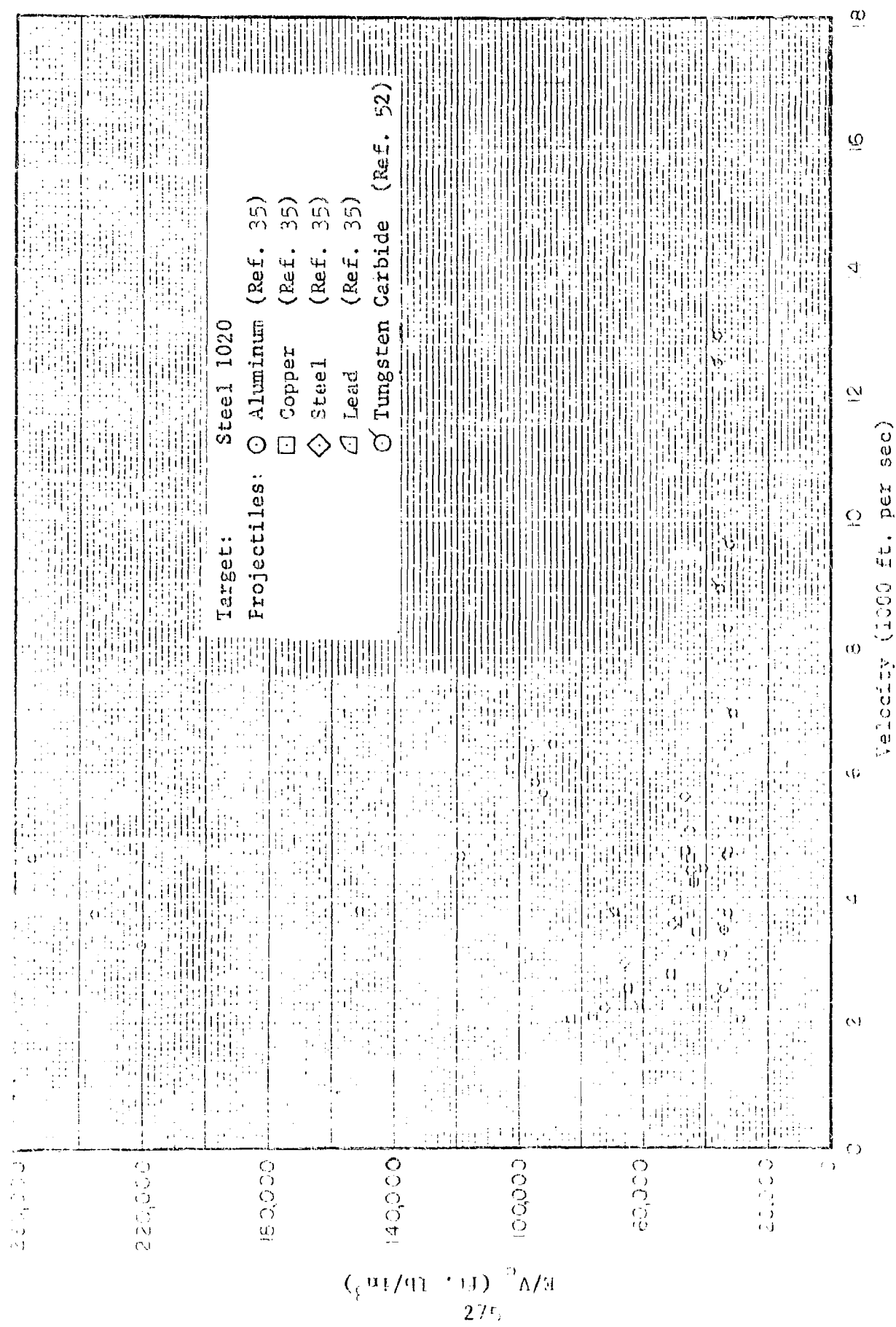


Fig. 5.15 Energy-Volume Ratios for 1020 Steel Targets

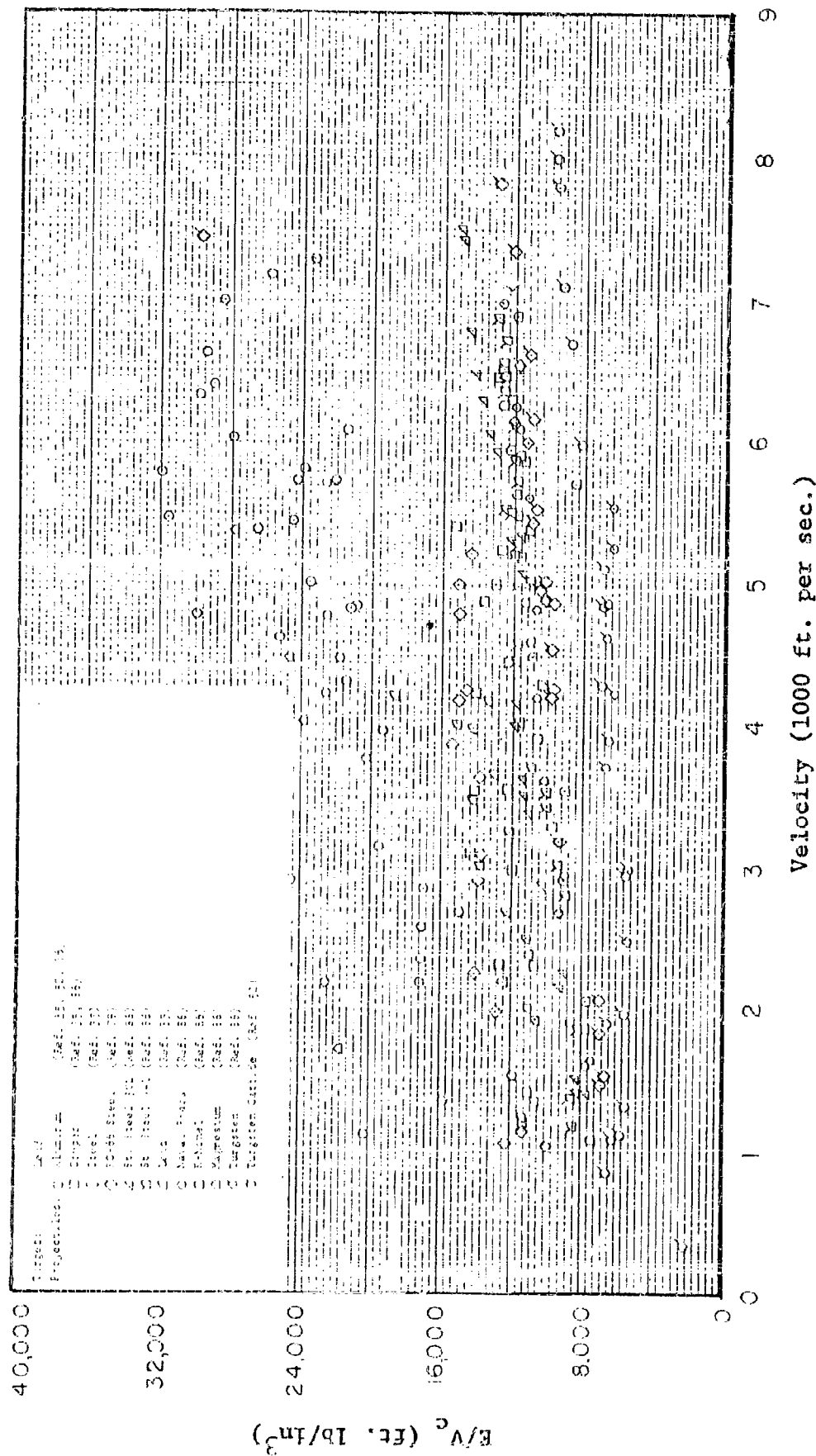


Fig. 5.36 Energy--Volume Ratios for Lead Targets

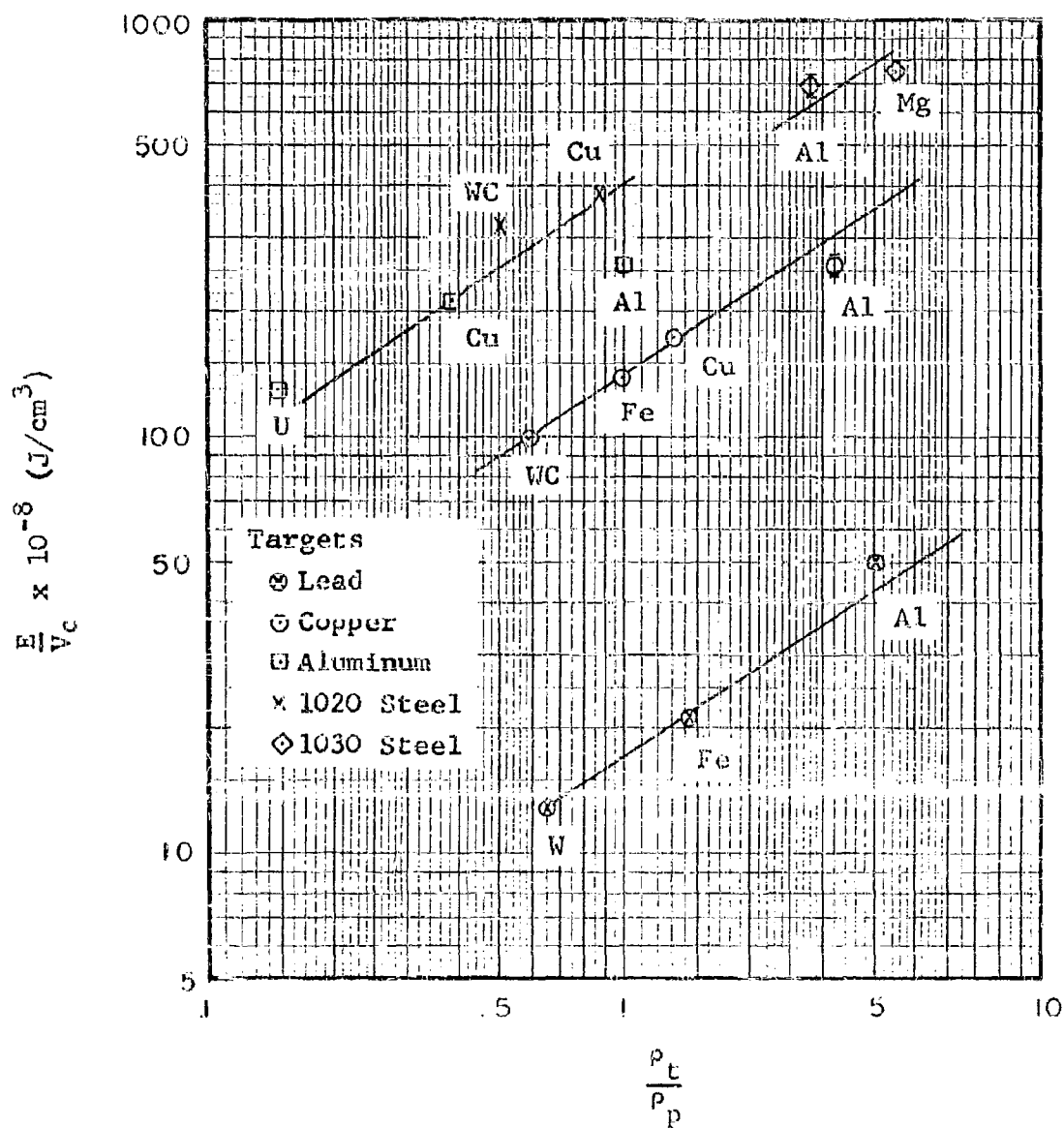


Fig. 5.37 Energy-Volume Ratio Dependence on Density Ratio

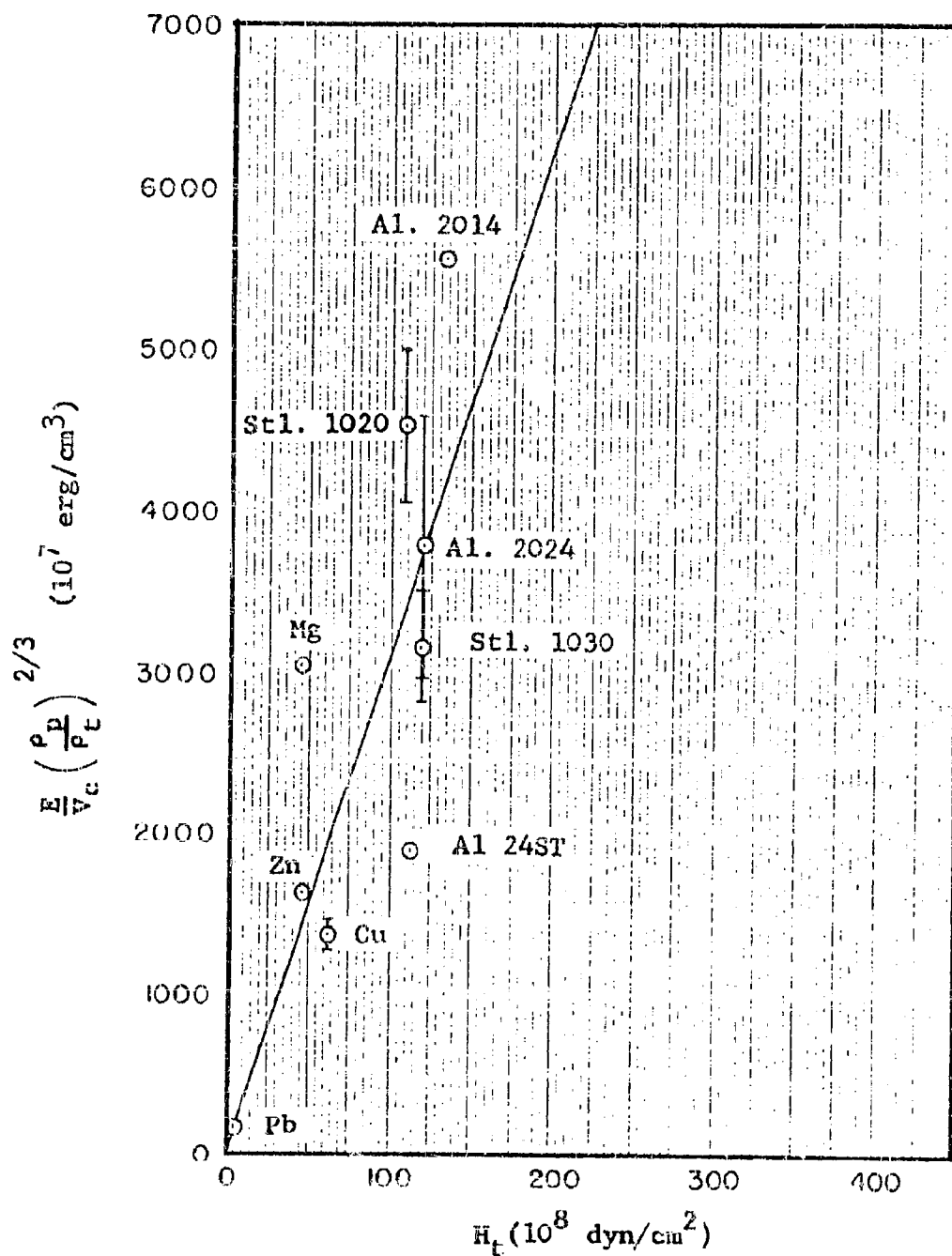


Fig. 5.38 Energy-Volume Ratio Dependence on Target Hardness

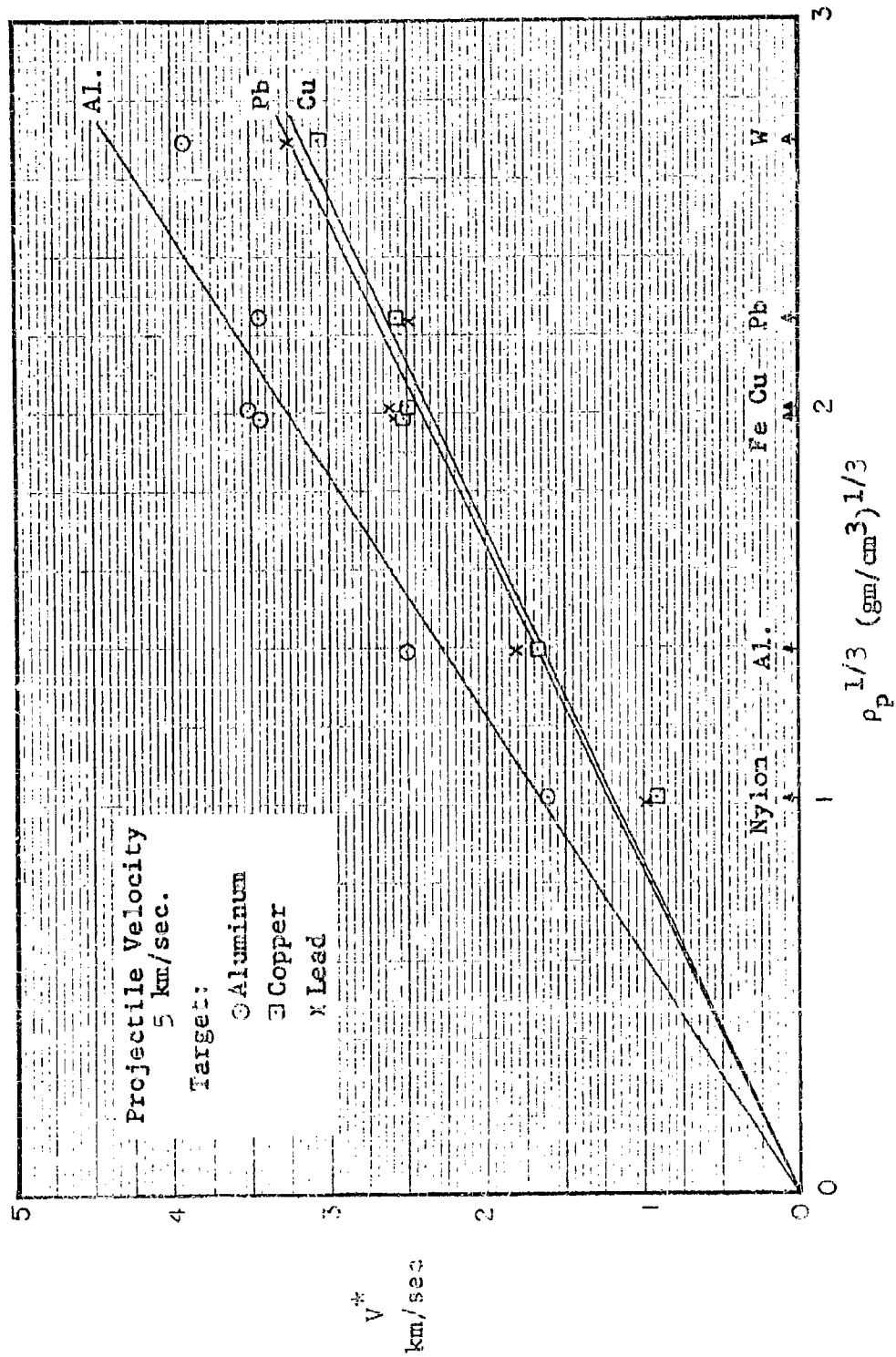


Fig. 5.39 Initial Interface Velocity Dependence on Projectile Density
at Constant Projectile Mass and Velocity

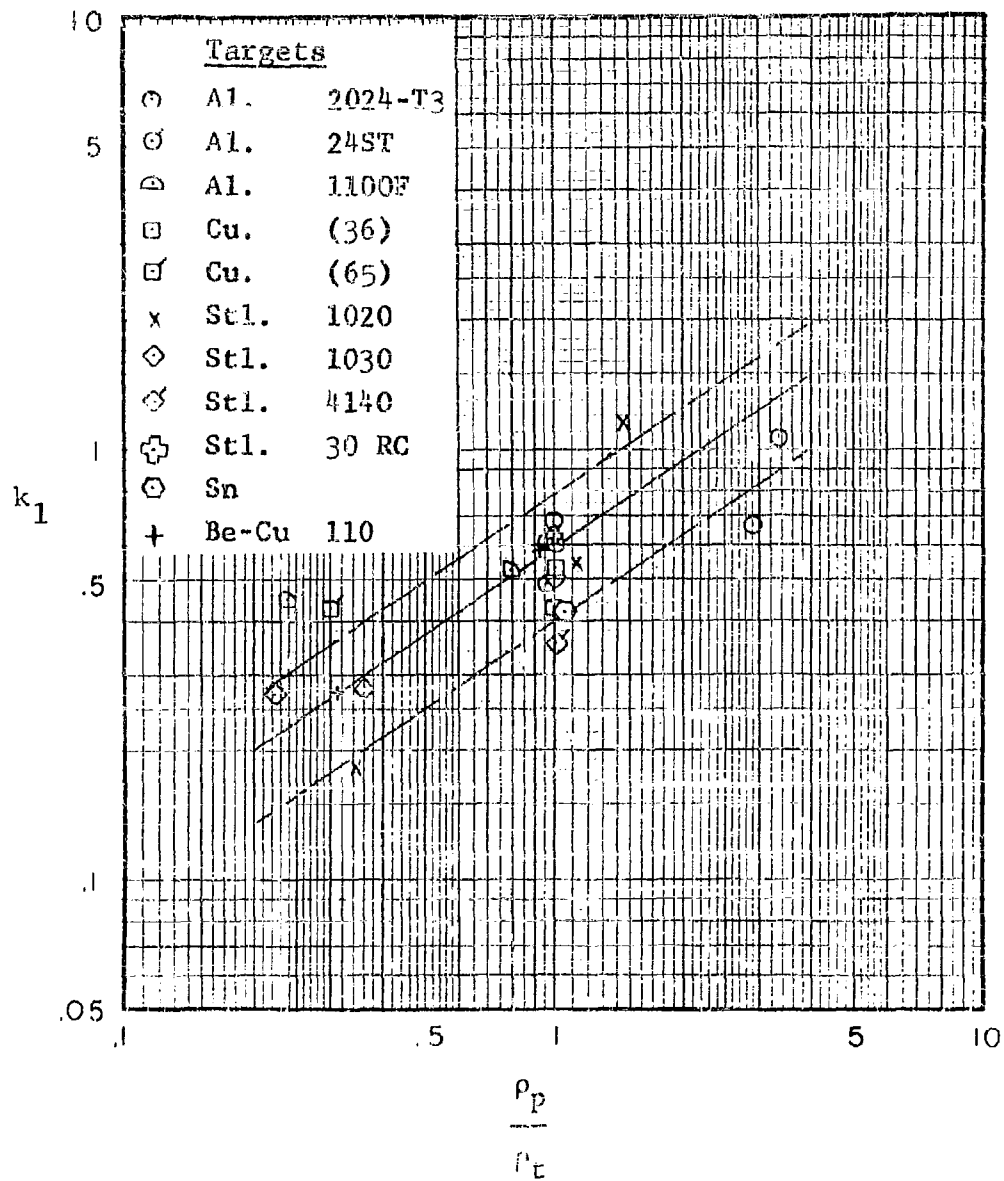


Fig. 5.40 Correlation of Logarithmic Penetration Law Parameters with Density Ratio

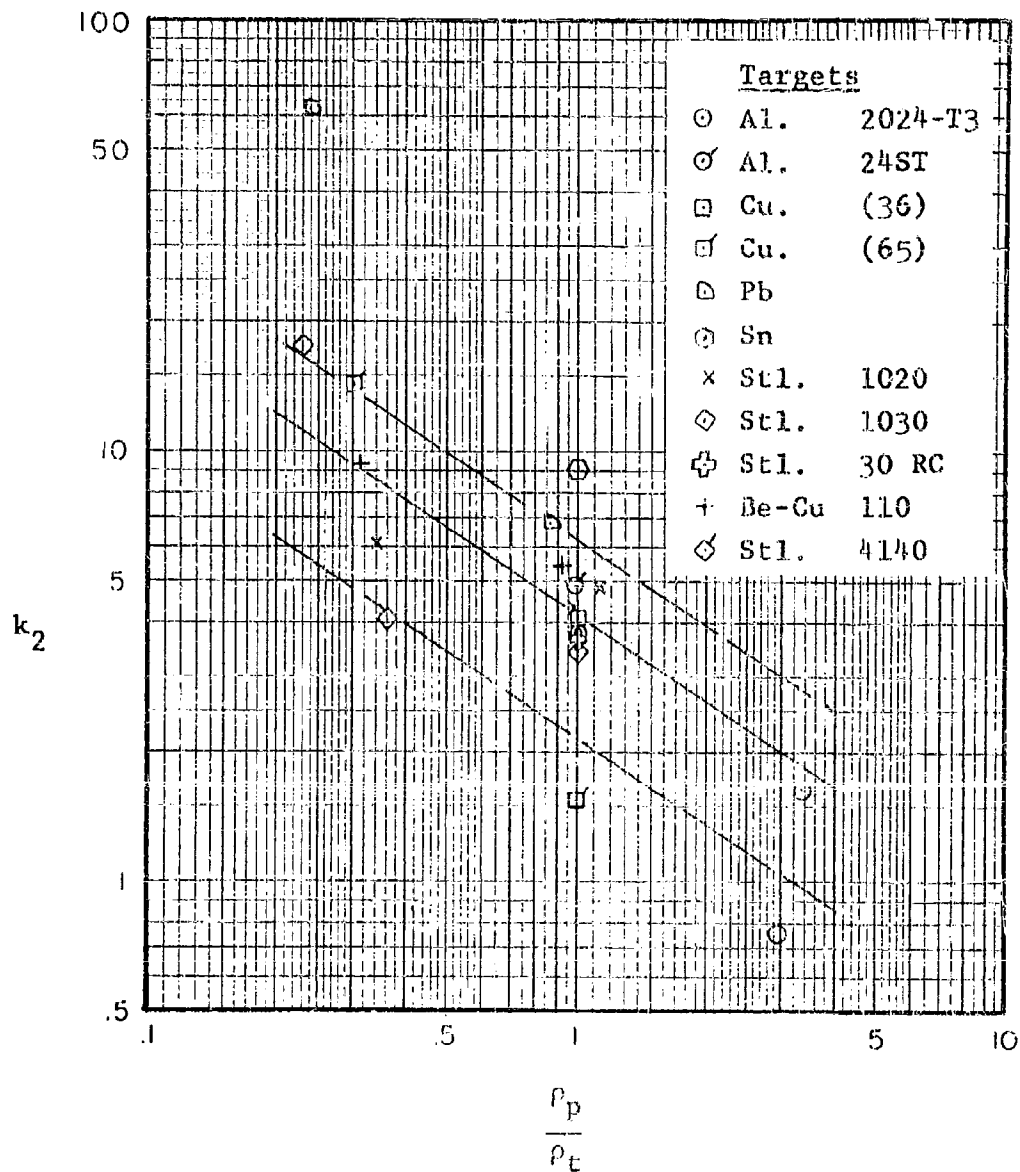


Fig. 5.41 Correlation of Logarithmic Penetration Law Parameters with Density Ratio

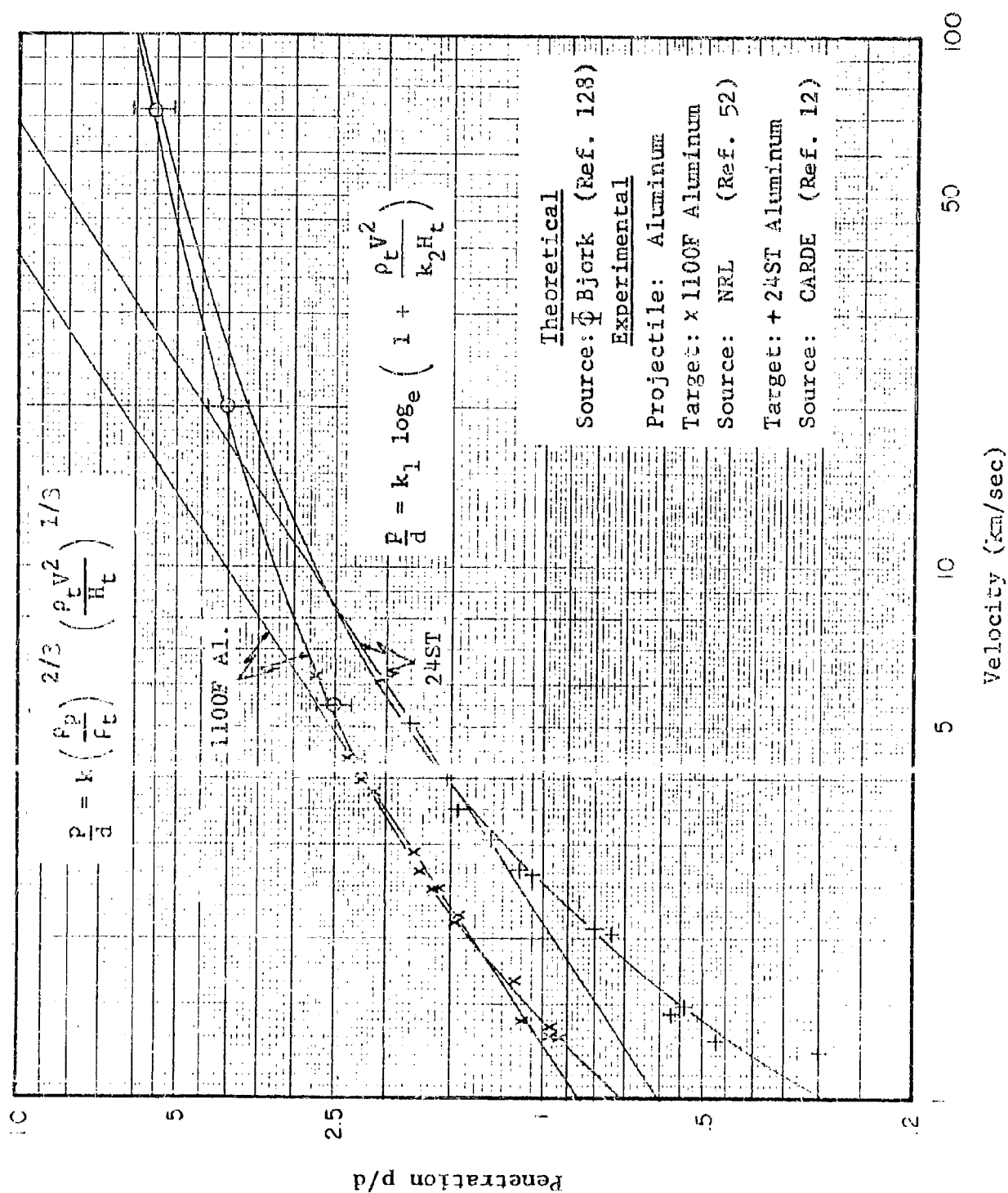


Fig. 1.12 Extrapolation of Empirical Penetration Laws for Aluminum Projectiles and Targets

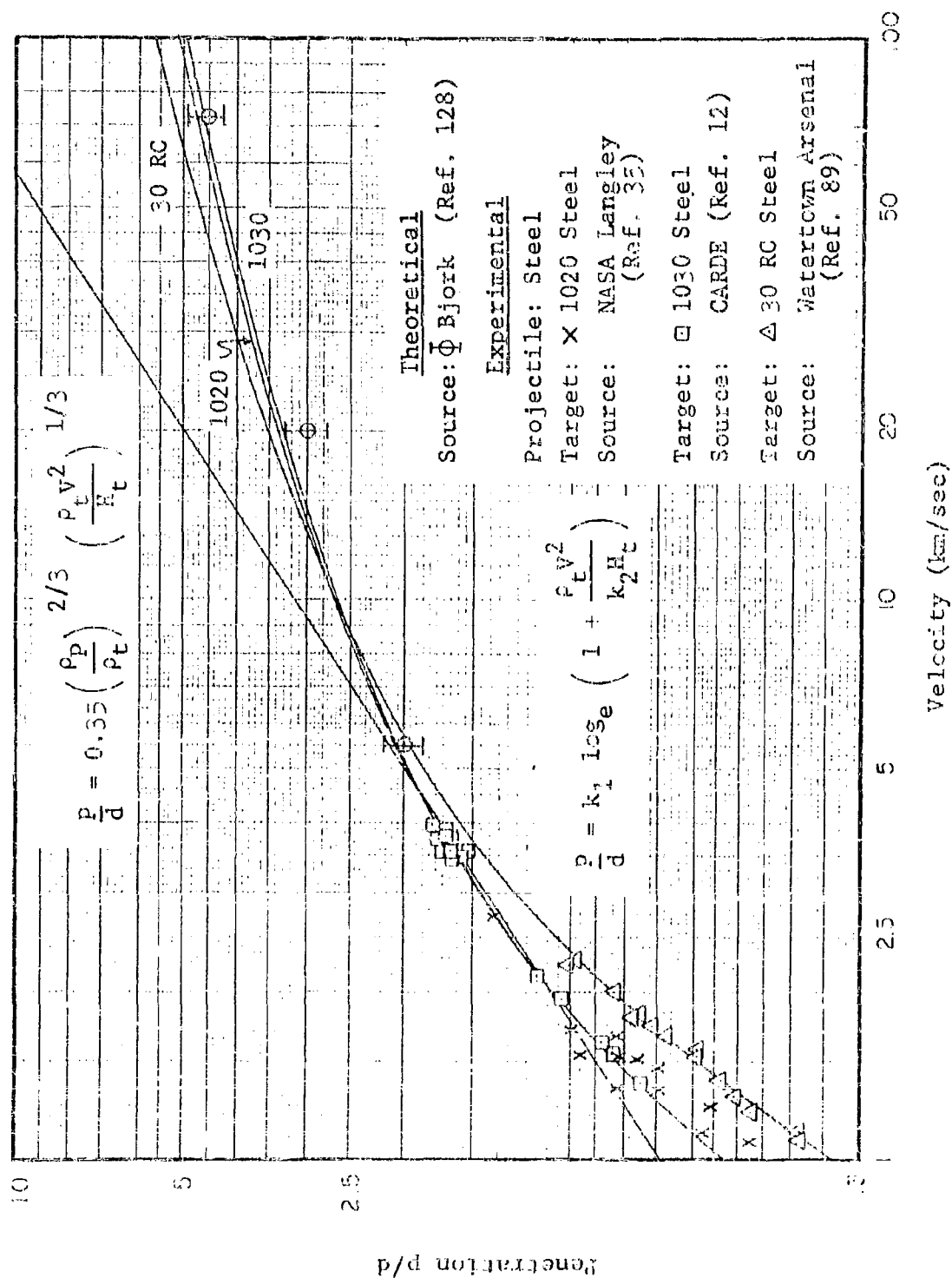


Fig. 5.1: Extrapolation of Empirical Penetration Laws for Steel Projectiles and Targets

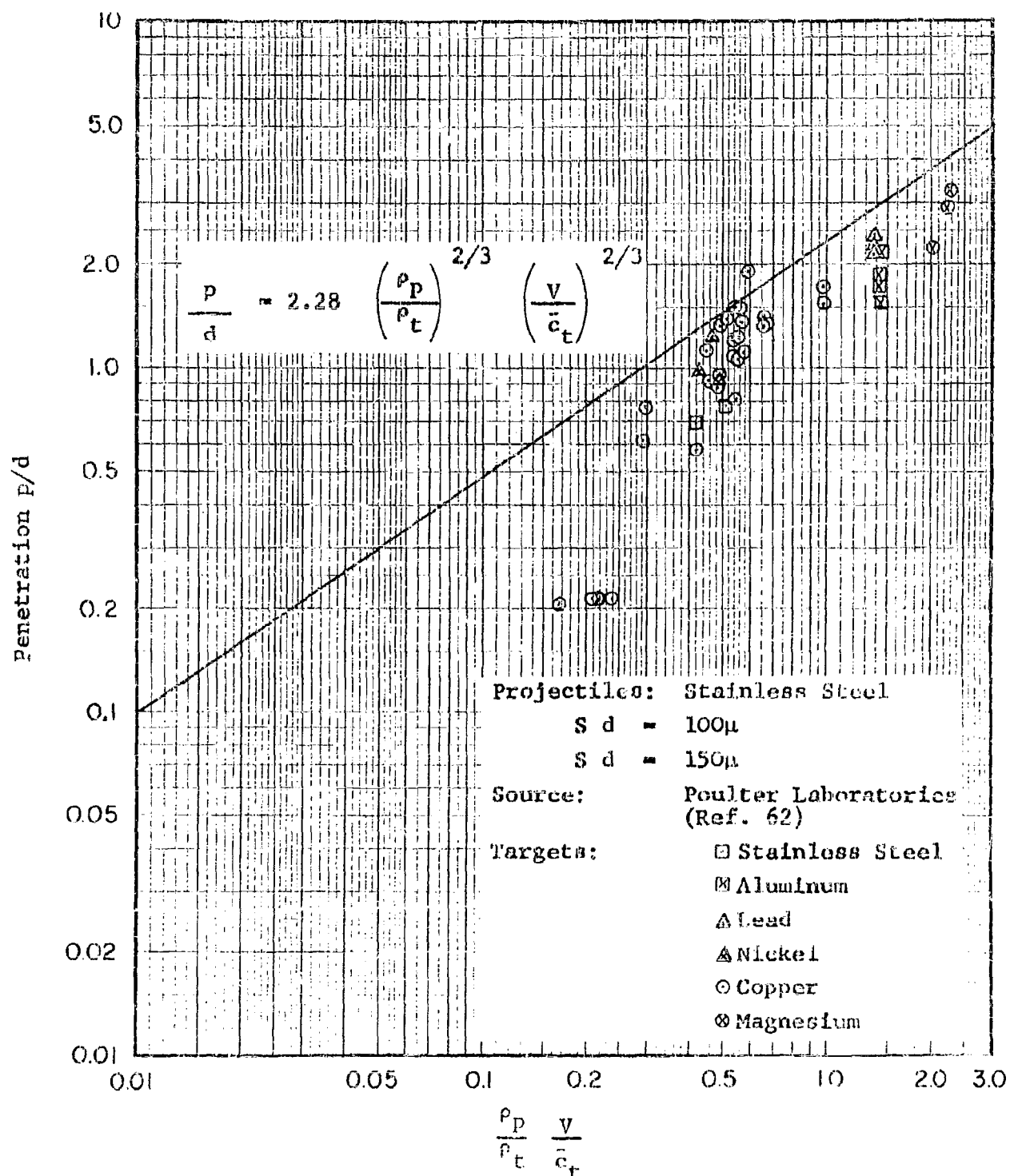


Fig. 6.1 The Penetration of Stainless Steel Spheres (100 μ and 150 μ diameter) into Various Targets

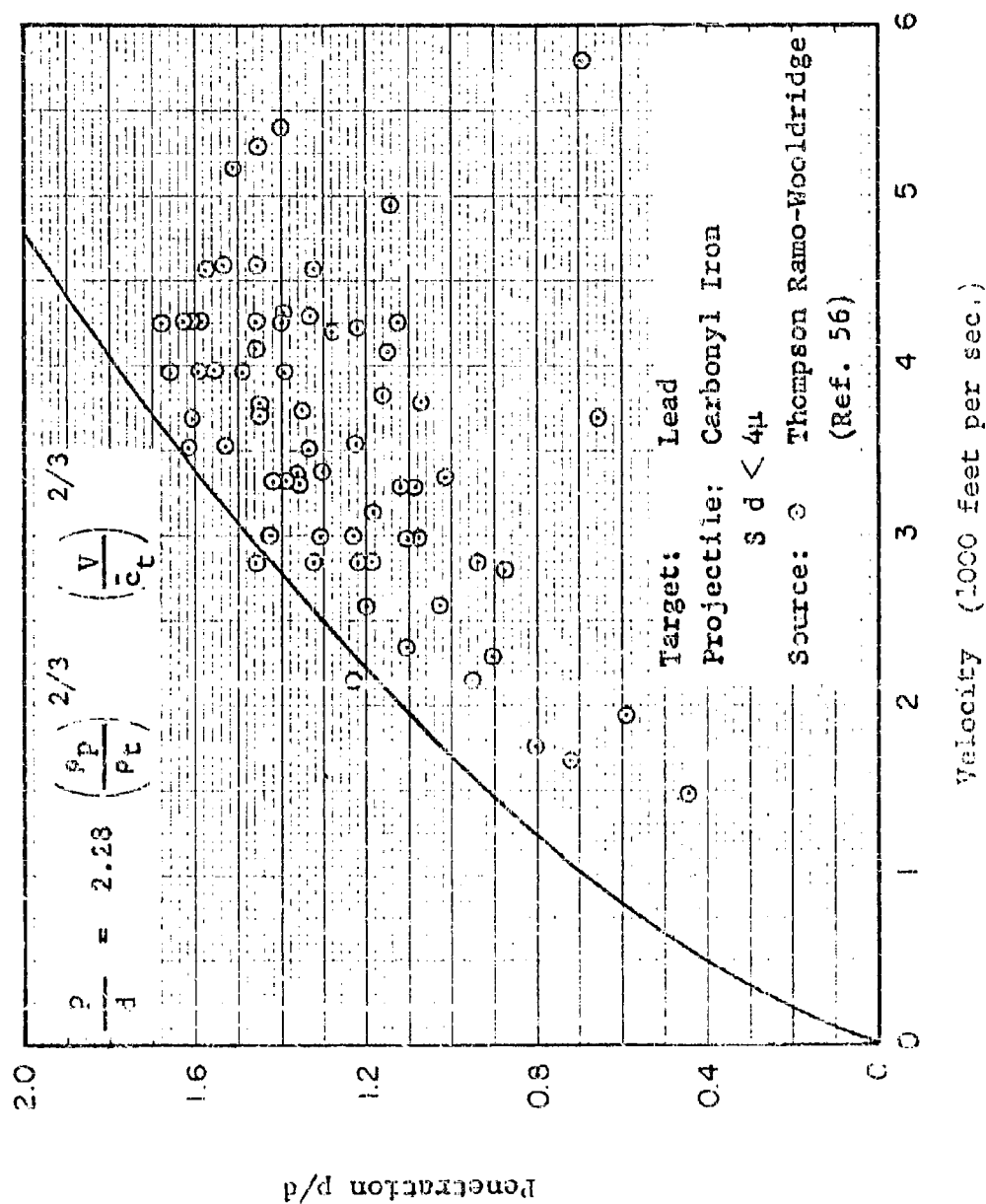


Fig. 6.2 The Penetration of Carbonyl Iron Microparticles into Lead

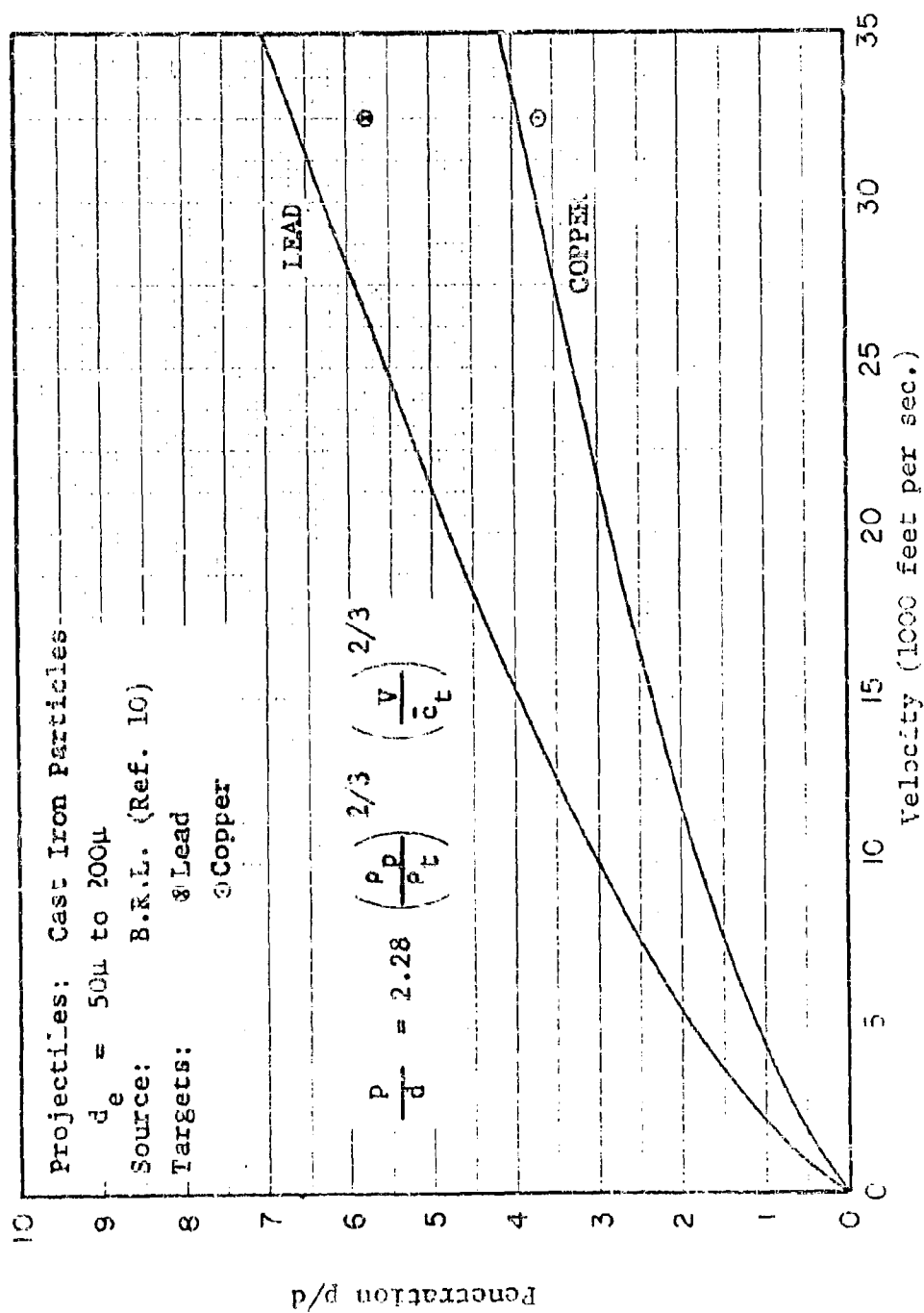


Fig. 6.3 Microparticle Gratering by 50 - 200 micron
 Cast Iron Particles

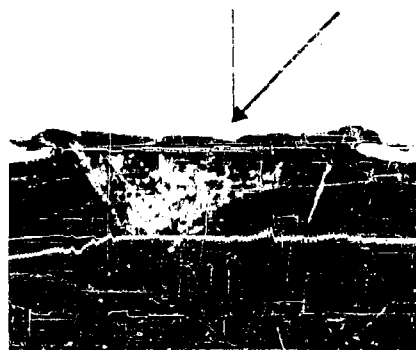
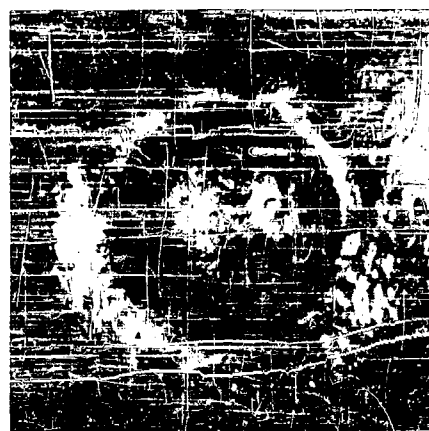
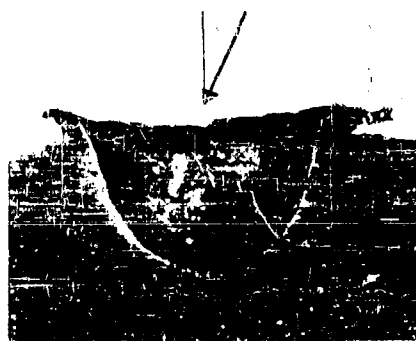
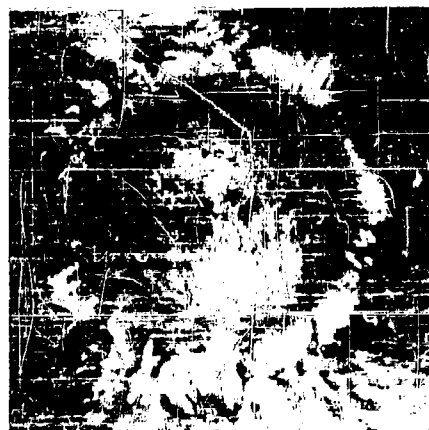
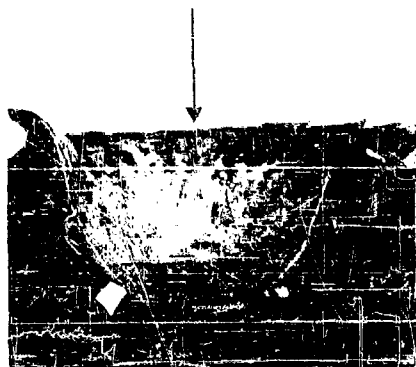
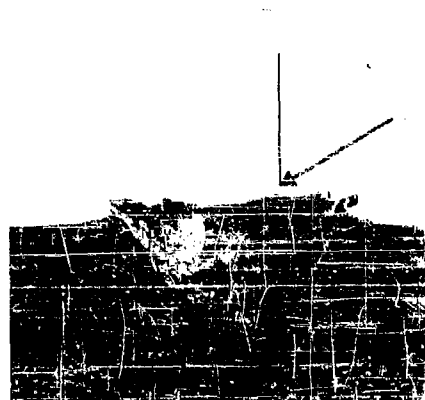
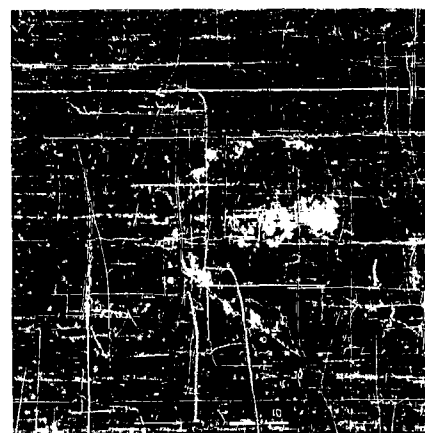
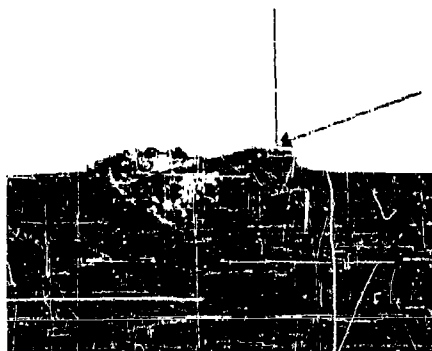


Fig. 6.4 Craters formed by Lead Spheres in Lead Targets at 7000 ft/sec at Oblique Angles of Impact



60°



70°



80°

Fig. 6.4 concluded Craters formed by Lead Spheres in Lead Targets at 7000 ft/sec at Oblique Angles of Impact

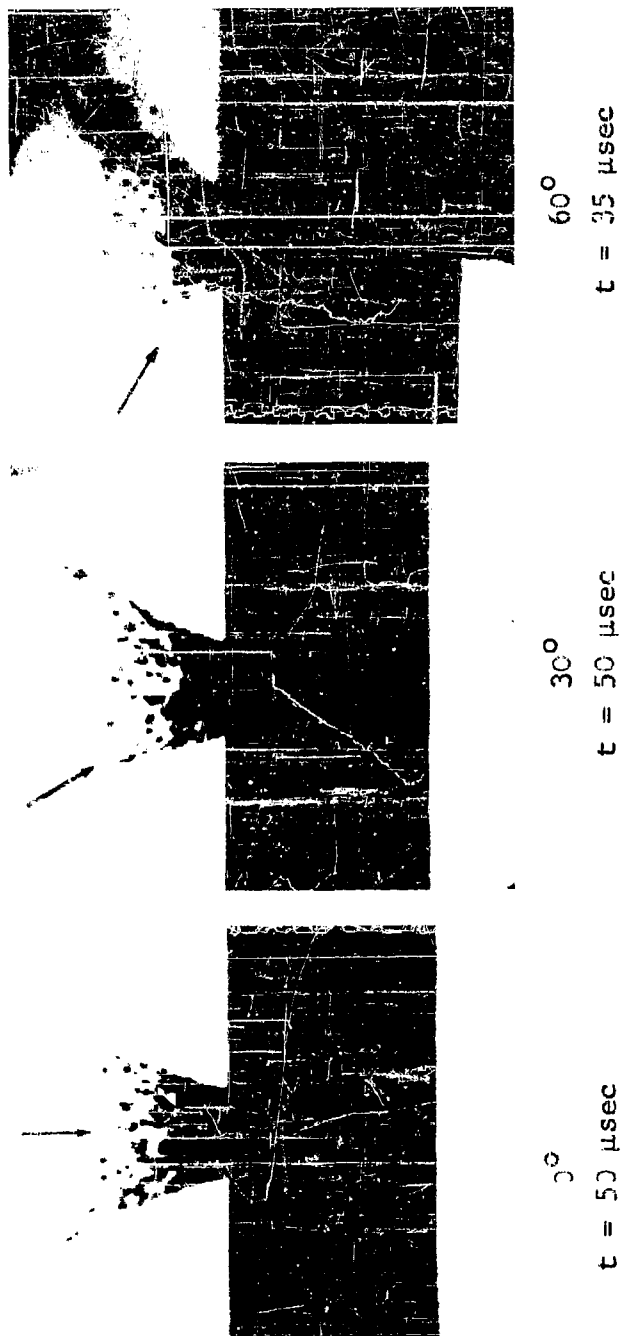
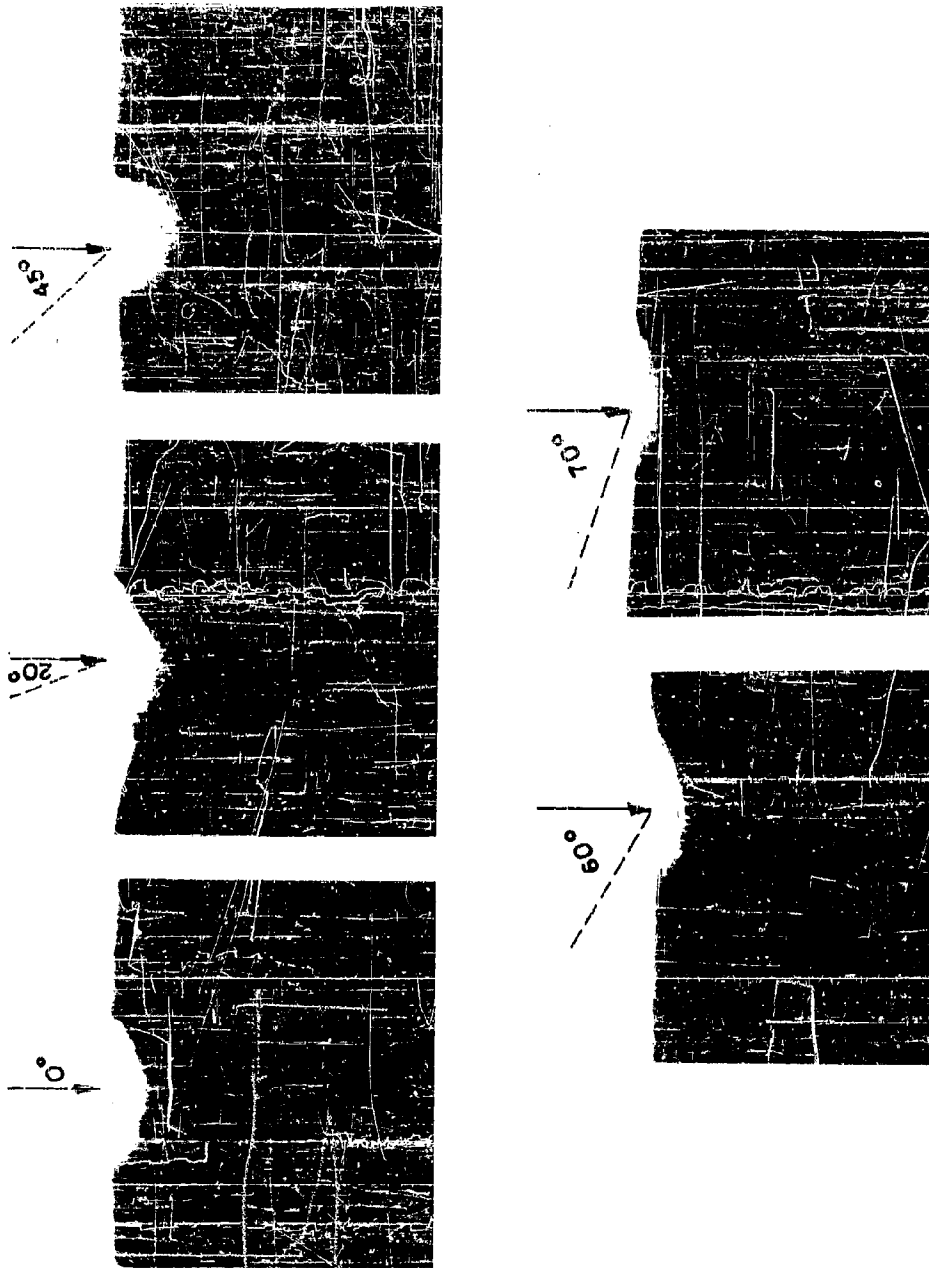


Fig. 6.5 Flash X-Radiographs of the Spray formed by Lead Projectile Impacting a Lead Target at about 7000 ft/sec. t is the Approximate Time after Impact (from Ref. 153)

Released for Publication by
 CARNEGIE INSTITUTE OF TECHNOLOGY
 PITTSBURGH, PENNSYLVANIA



Selected for Publication by
 BALLISTICS RESEARCH LABORATORY
 ZEPHYRUS PROVING GROUND, MARYLAND

Fig. 6.6 Flash X-Radiographs of Crater Formation in Aluminum
 Targets at 15,000 ft/sec. Radiographs at 50 μ /sec.
 after Impact

30°
2.32 KM/SEC



60°
2.32 KM/SEC



60°
3.22 KM/SEC



Released for Publication by
BALISTICS RESEARCH LABORATORY
FEDERAL BUREAU OF INVESTIGATION, WASHINGTON, D.C.

Fig. 6.7 Craters formed in Lead Targets by Steel
Projectiles at Oblique Angles of Impact
(from Ref. 7)

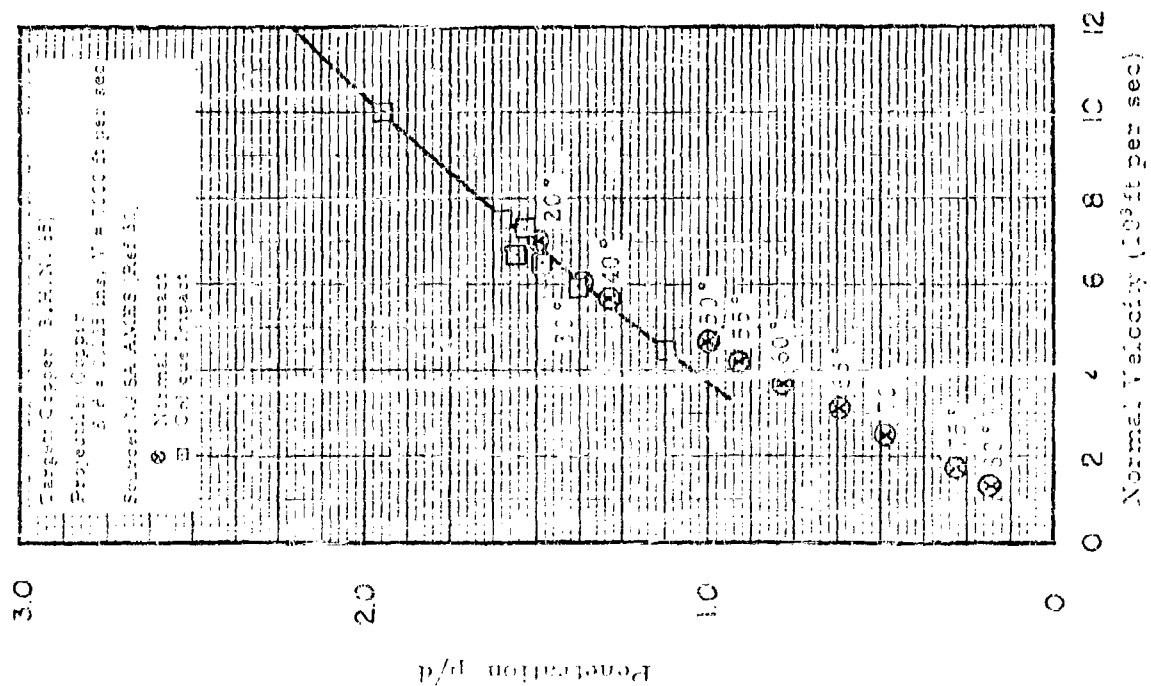
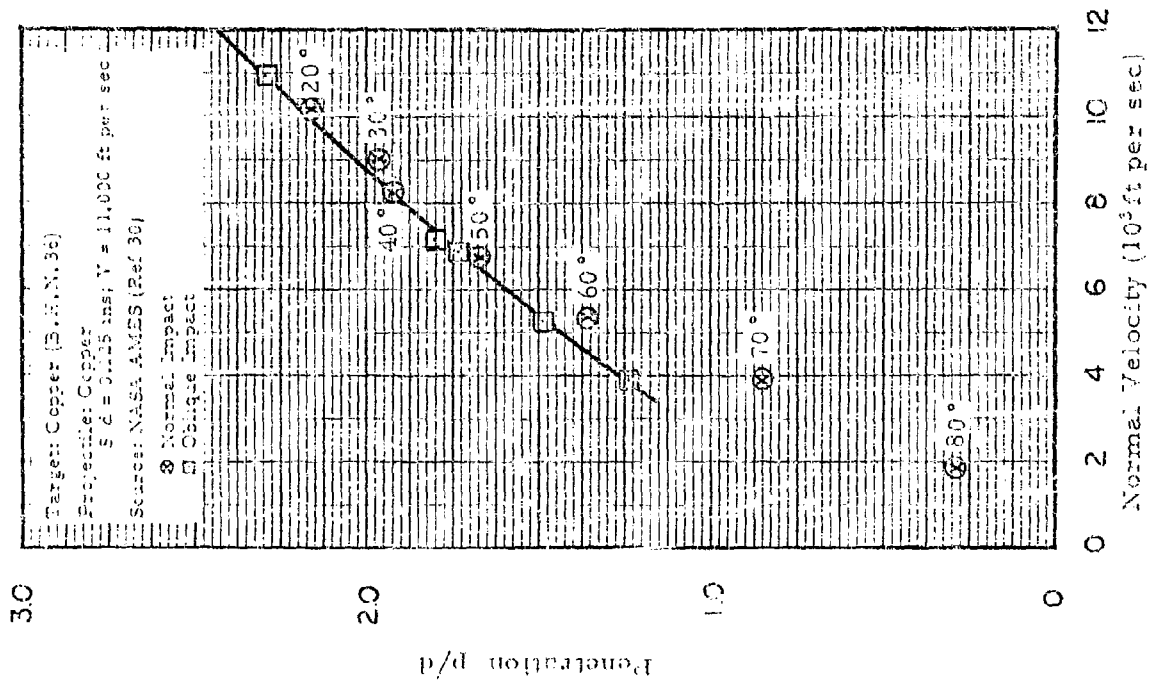


Fig. 6.8 Penetration at Oblique Incidence

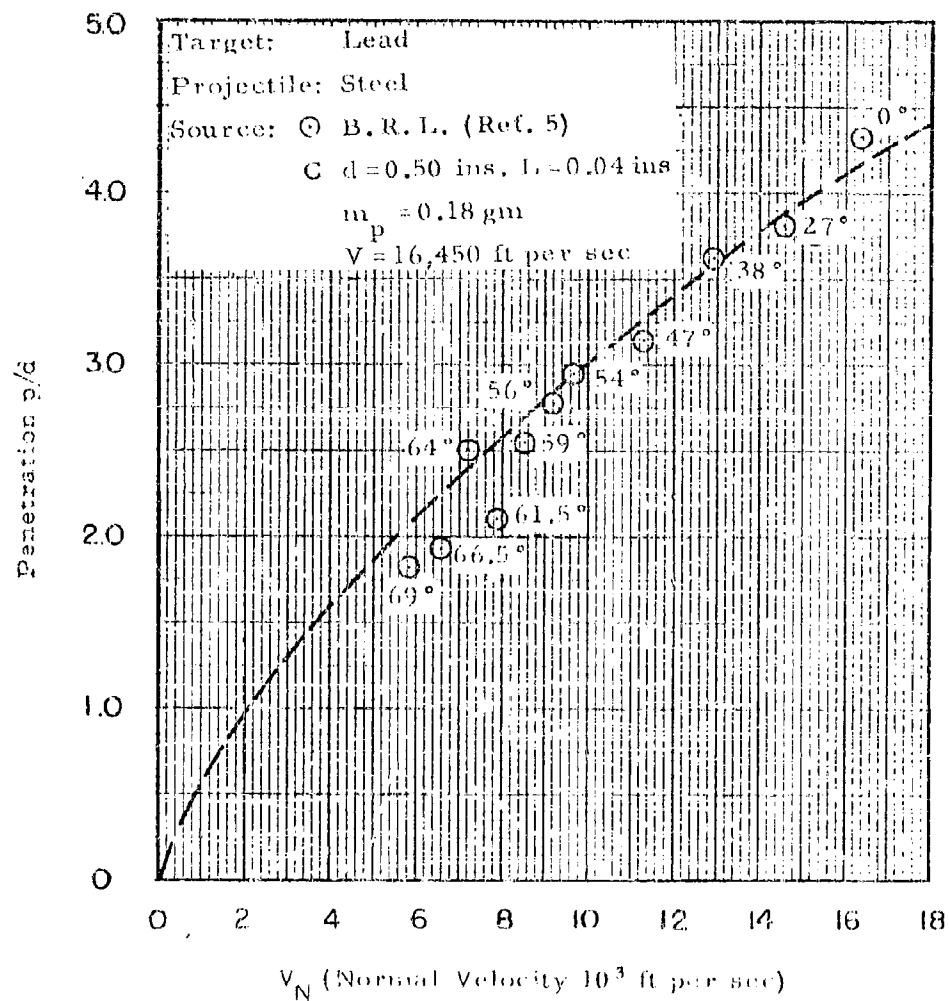


Fig. 6.9 Penetration at Oblique Incidence

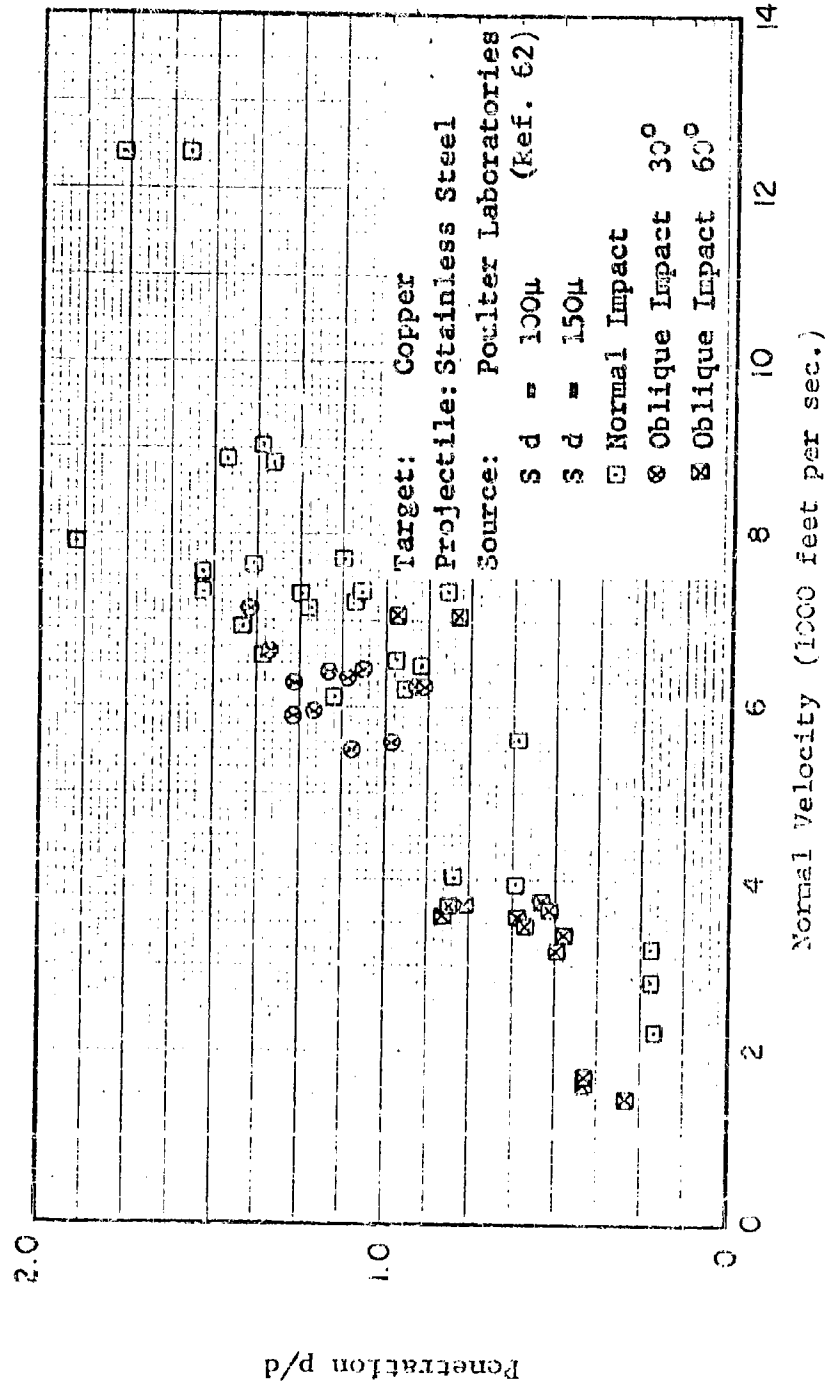


Fig. 5.10 Microparticle Penetration at Oblique Incidence

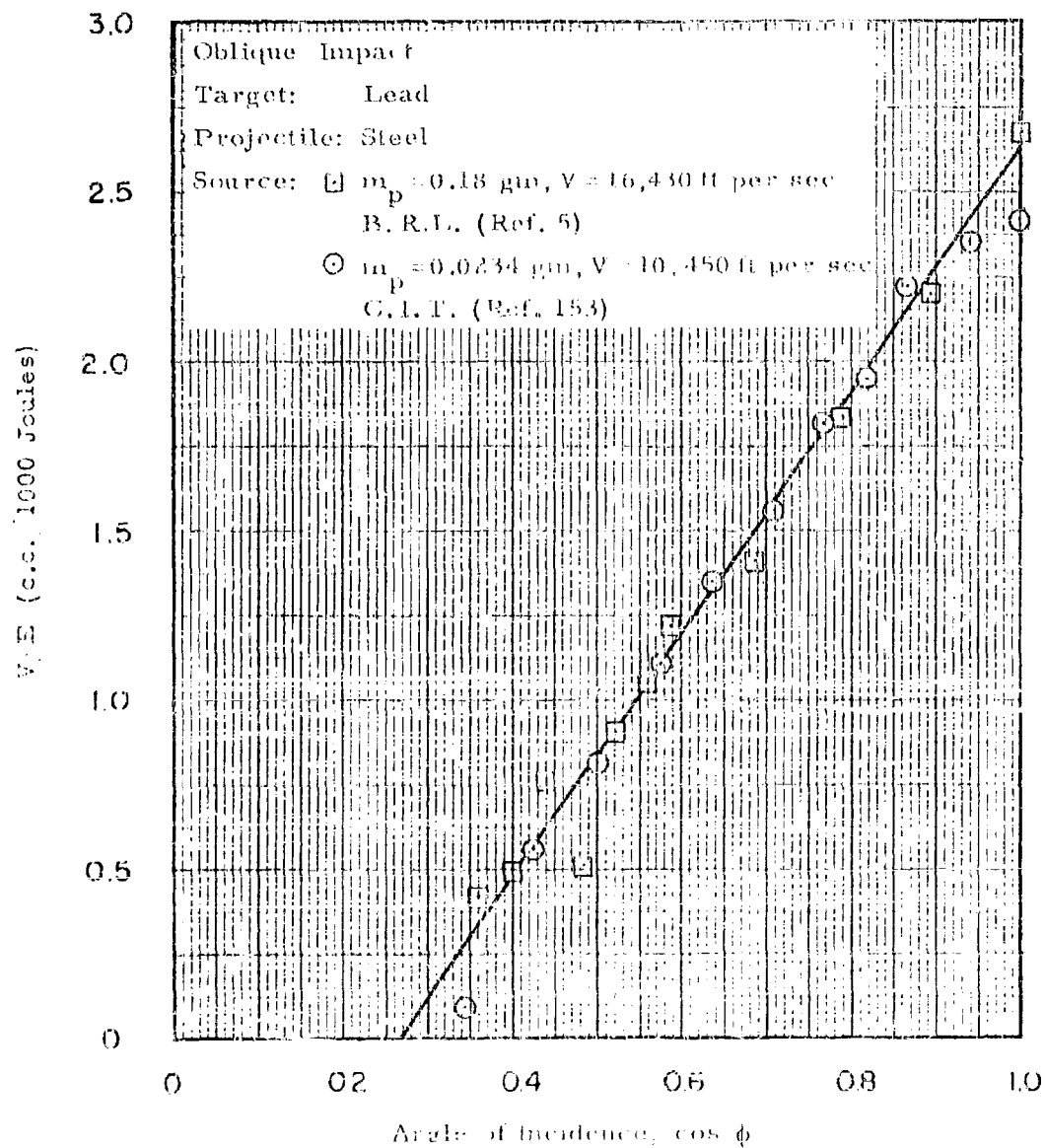


Fig. 6.11 Crater Volume at Oblique Incidence

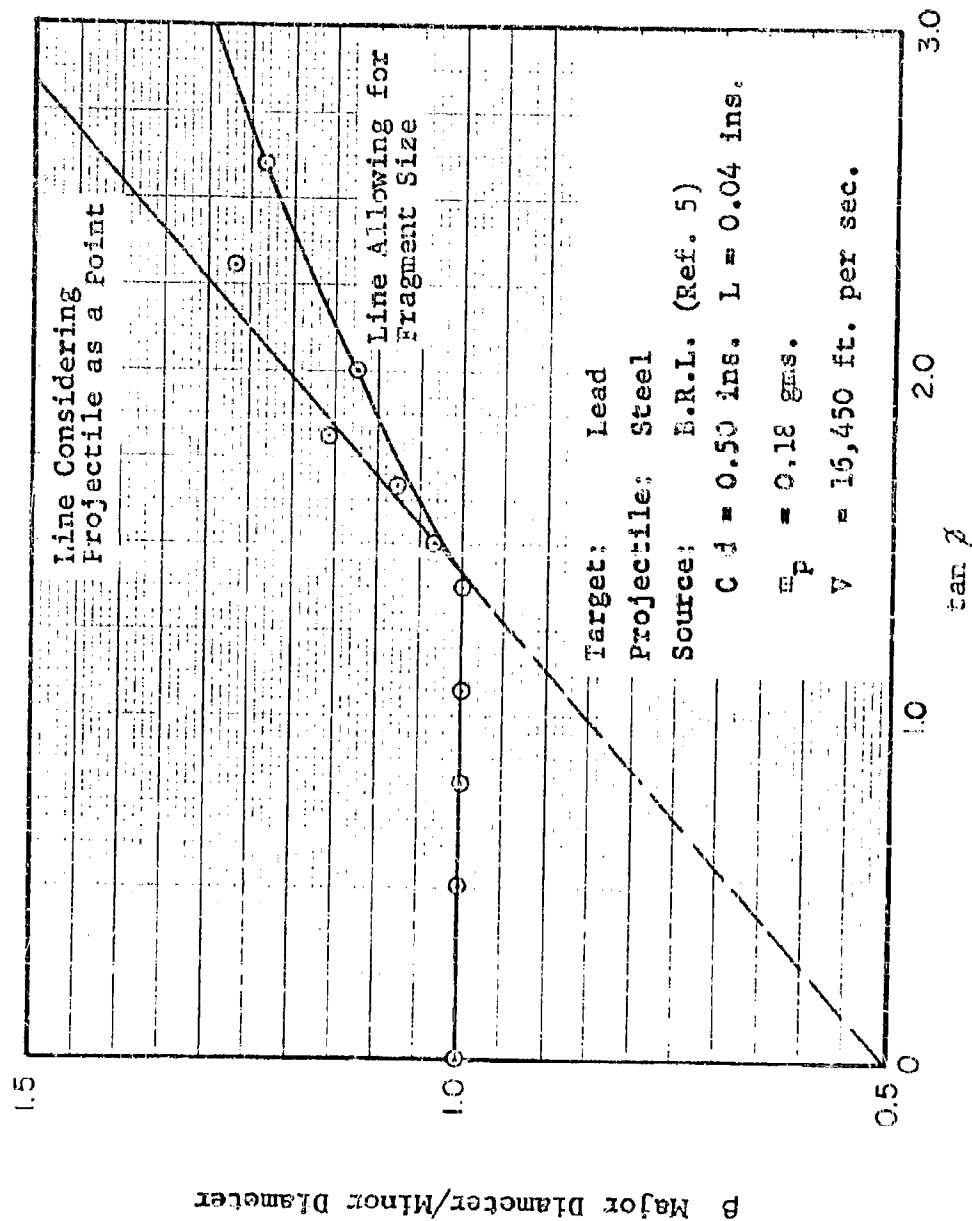


Fig. 6.12 Crater Mouth Dimensions for Oblique Impact

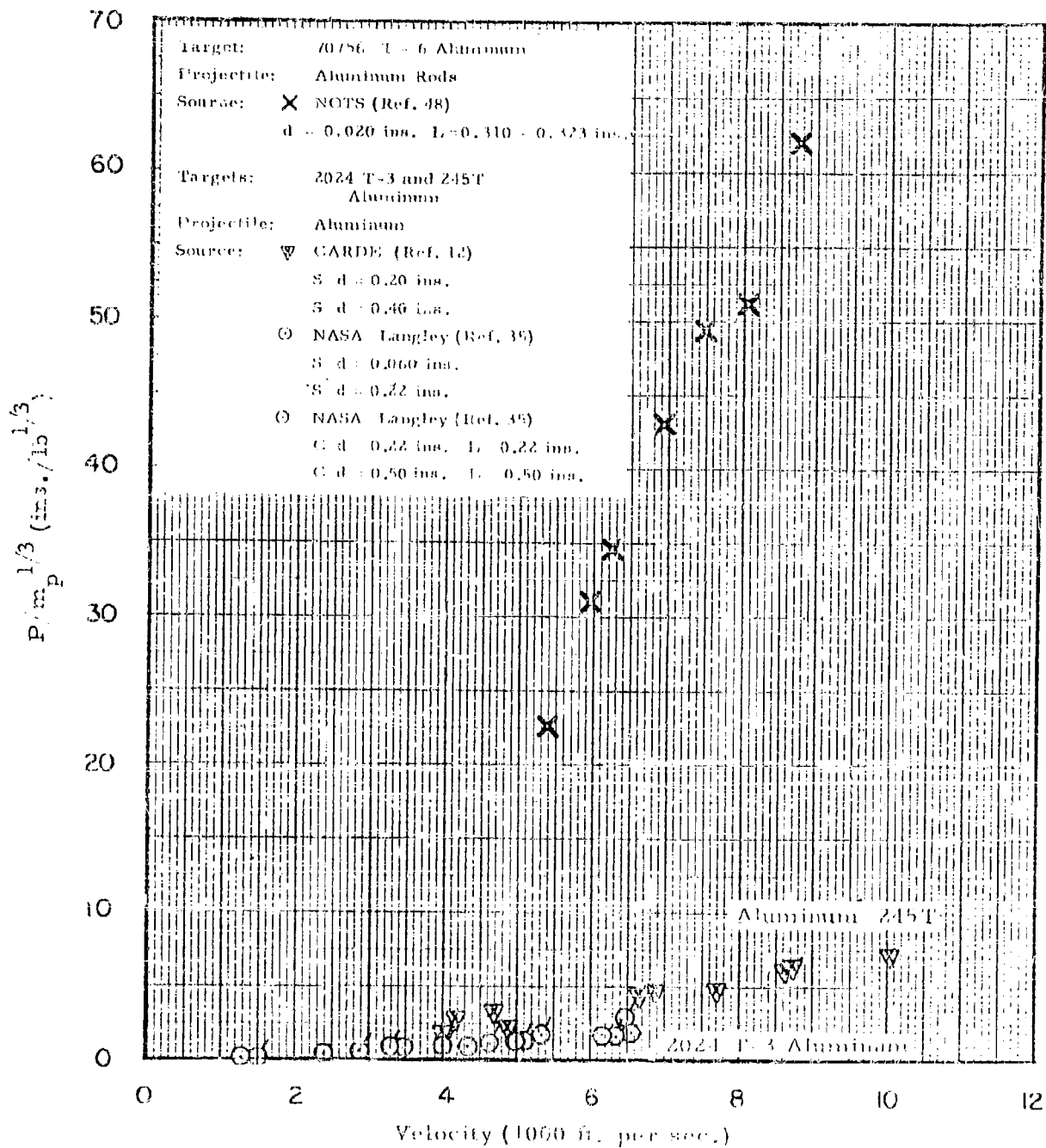


Fig. 6.13 Penetration of Slender Rods Compared to that of Spheres in Aluminum

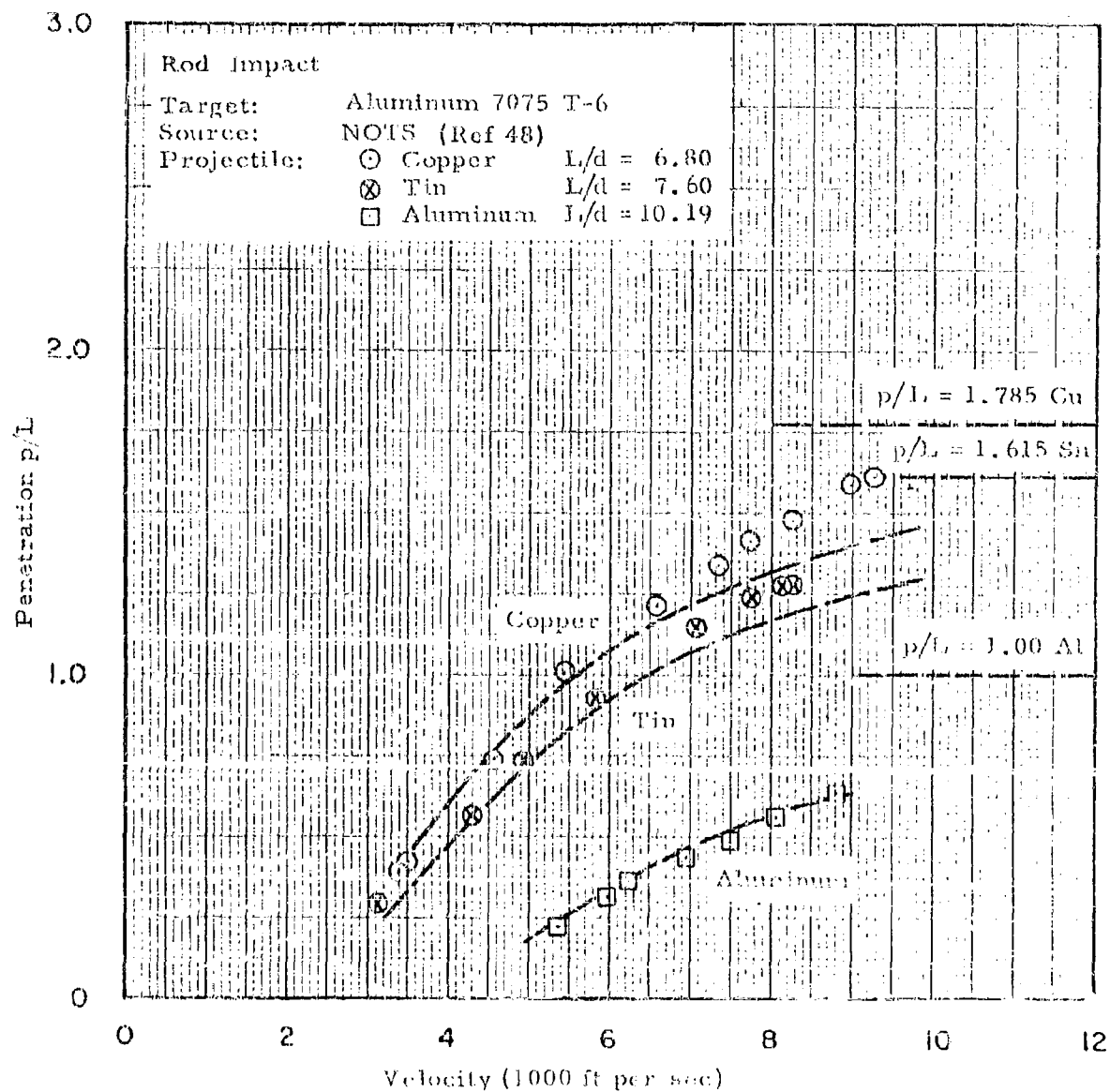


Fig. 6.14 The Penetration of Aluminum Targets by Aluminum, Copper and Tin Rods

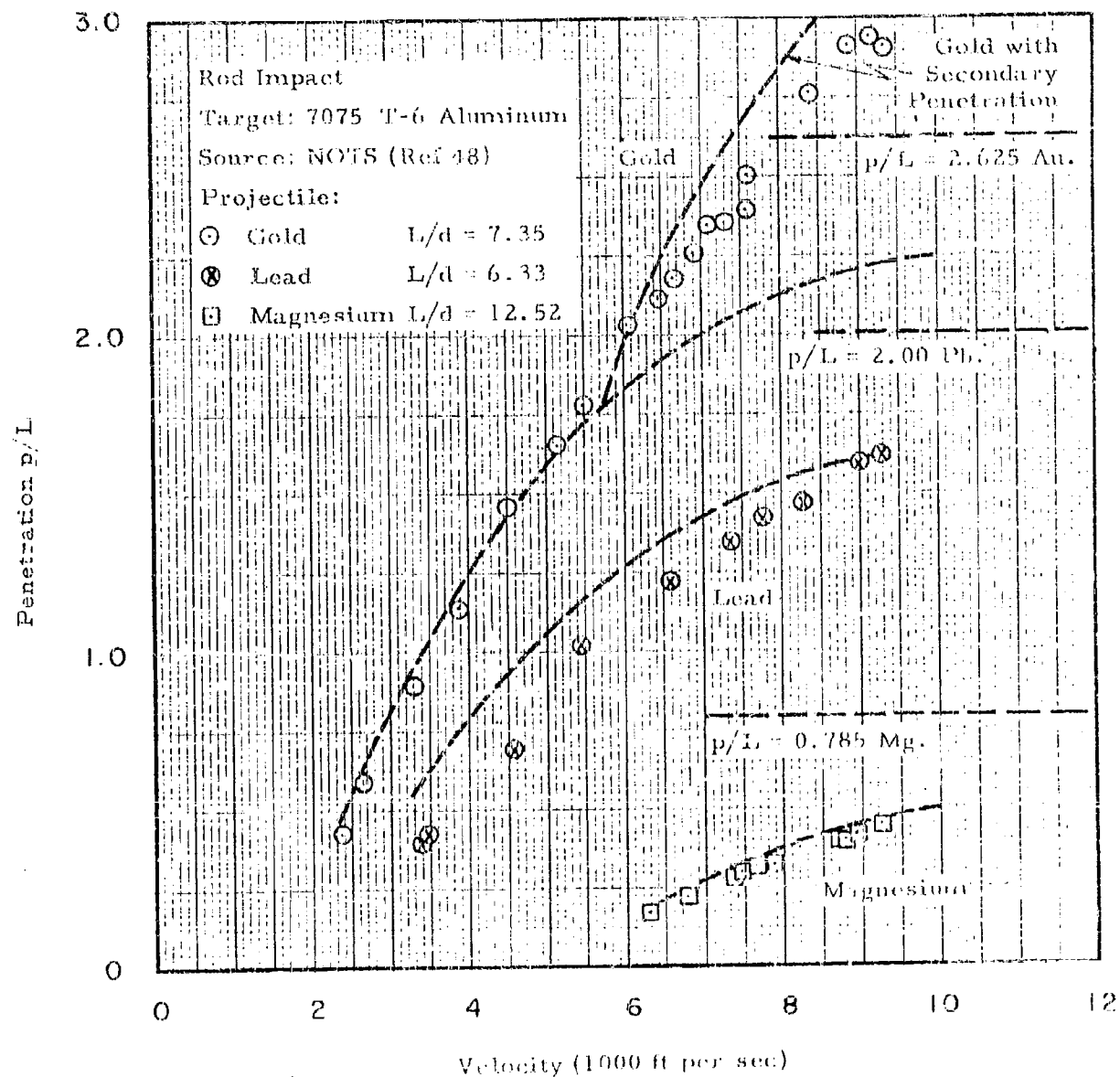


Fig. 6.15 The Penetration of Aluminum Targets by Gold, Lead and Magnesium Rods

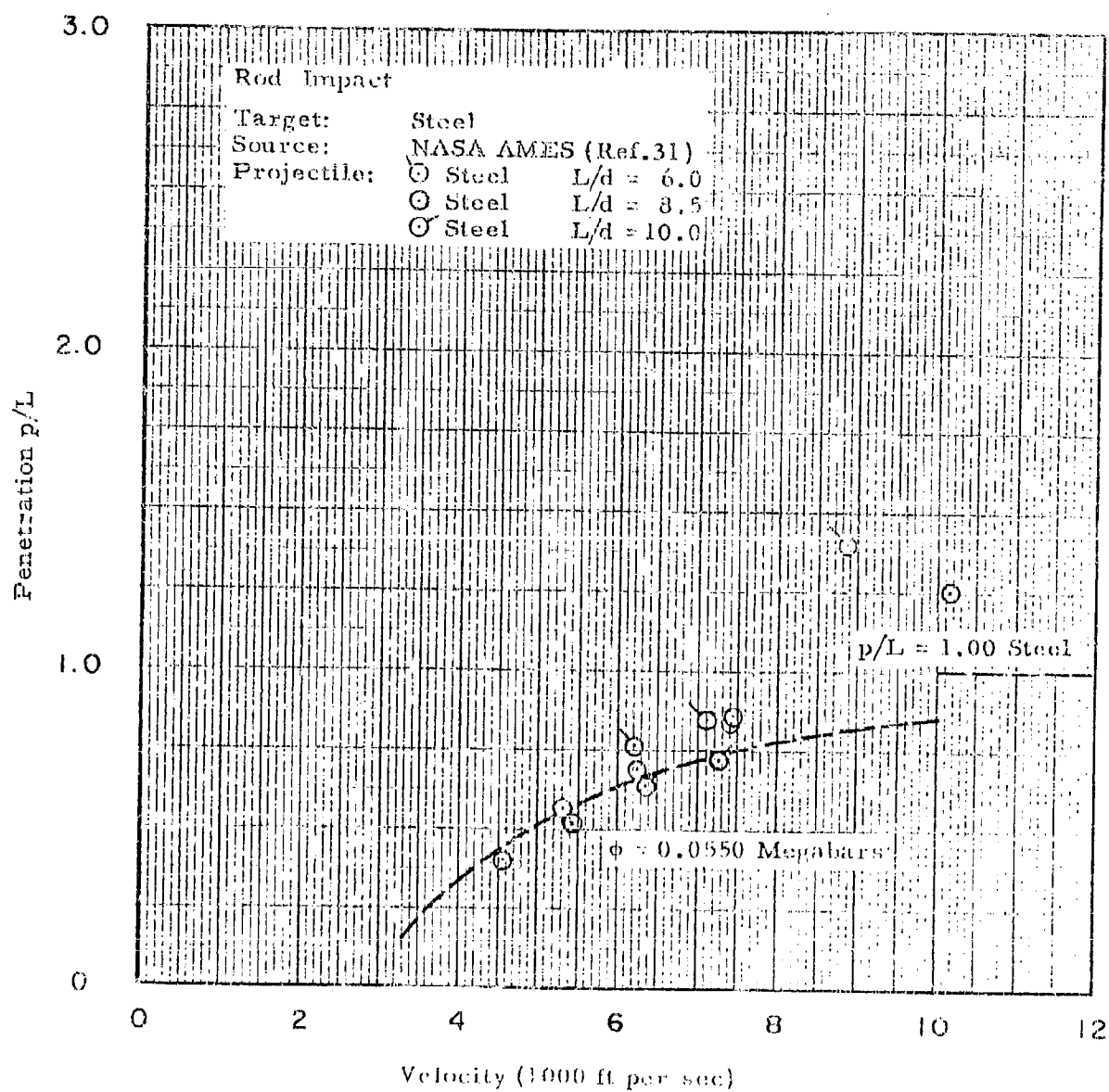


Fig. 6.16 The Penetration of Steel Targets by Steel Rods

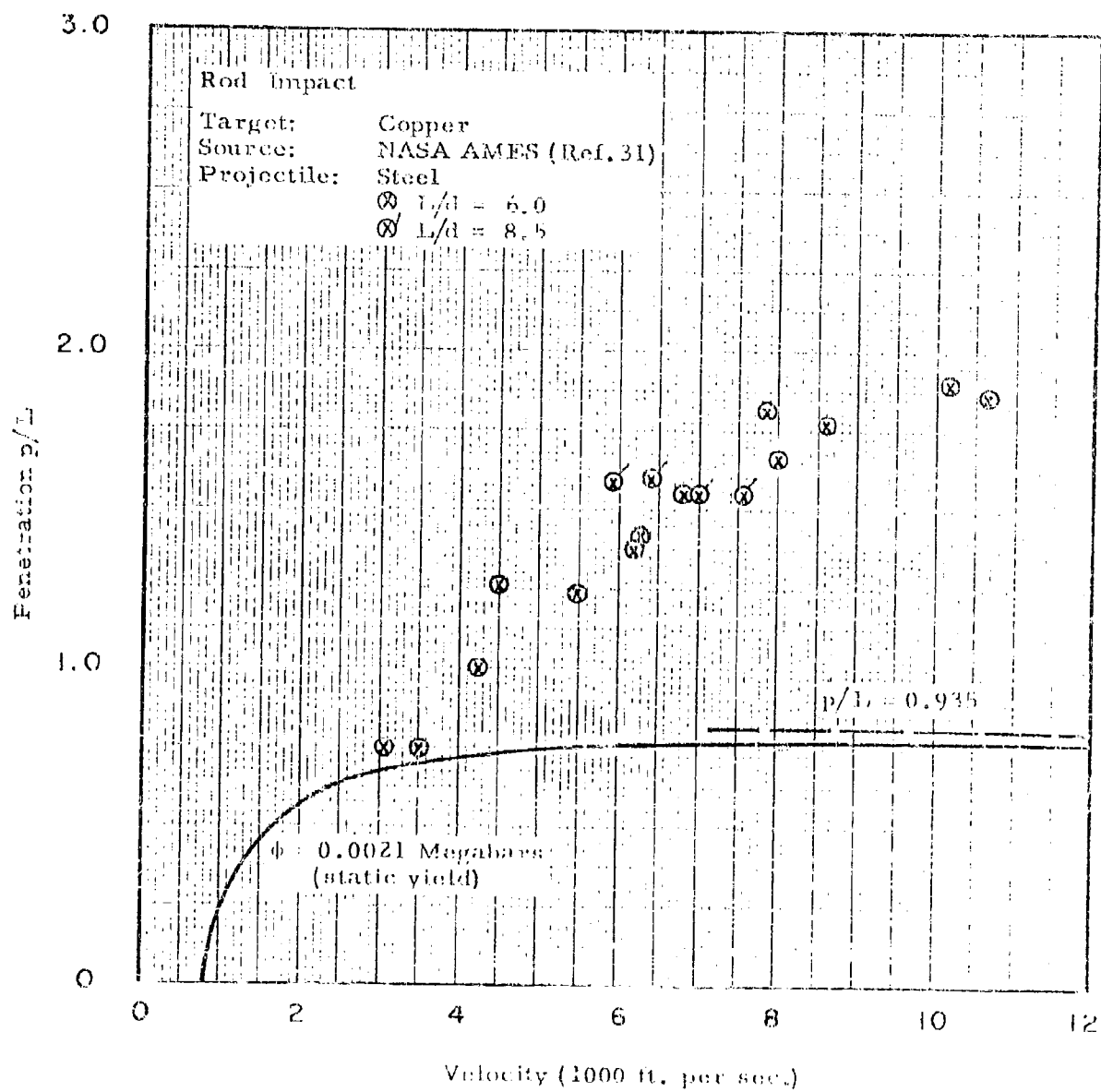


Fig. 6.17 The Penetration of Copper Targets by Steel Rods.

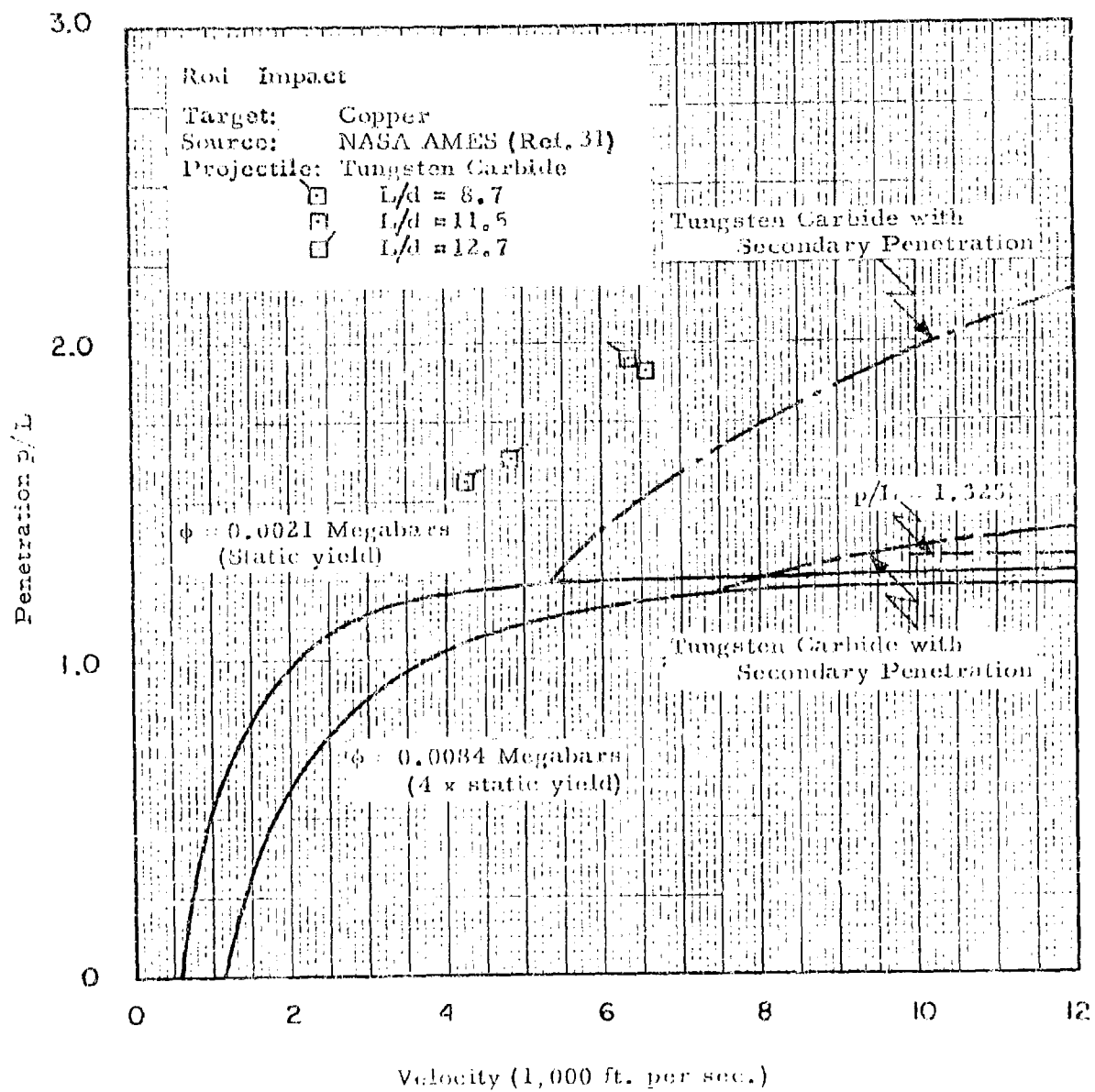


Fig. 6.18 The Penetration of Copper Targets by Tungsten Carbide Rods

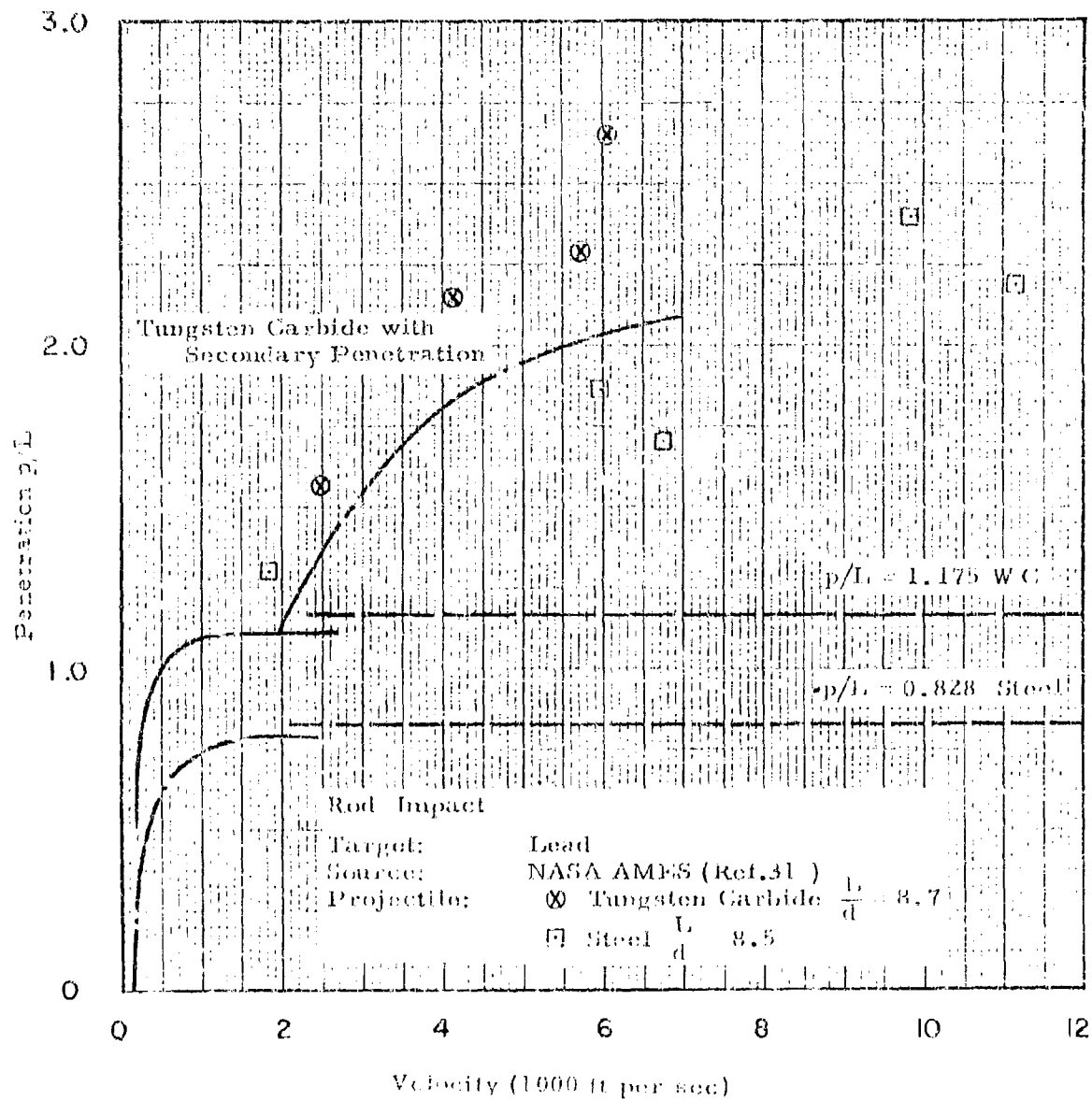


Fig. 6.19 The Penetration of Lead Targets by Tungsten Carbide and Steel Rods

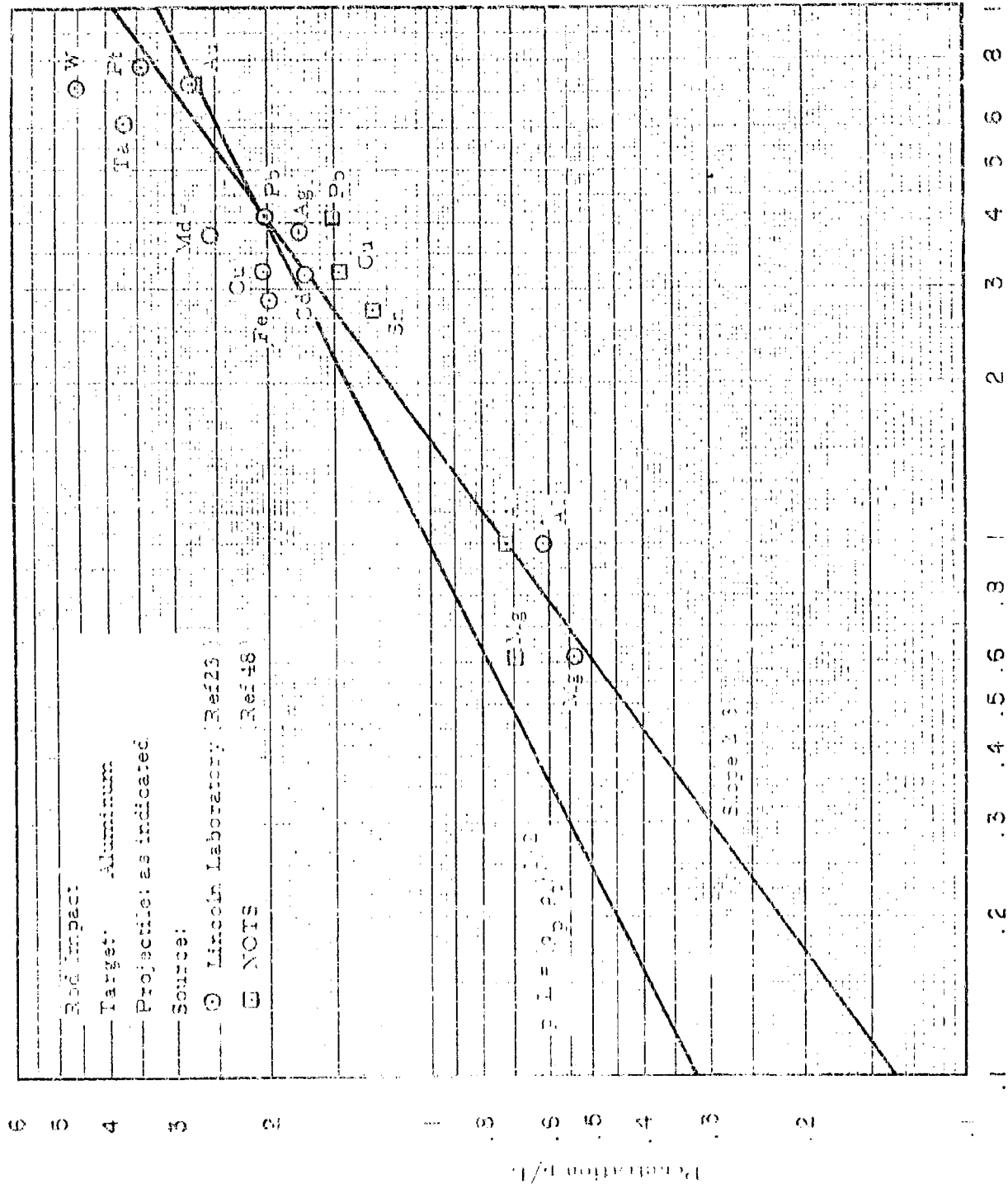
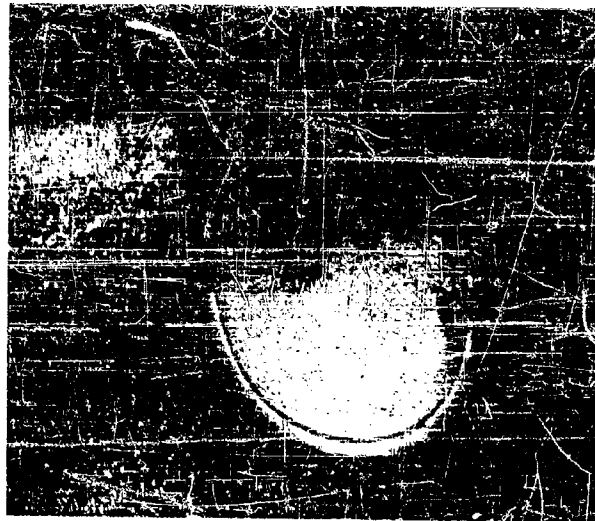


Fig. 2.20 Penetration of Rods of Different Materials into Aluminum Targets at 8300 ft. per sec.



Released for Publication by
NATIONAL AERONAUTICS AND SPACE ADMINISTRATION
LANGLEY RESEARCH CENTER, LANGLEY FIELD, VIRGINIA

Fig. 6.21 Crater formed by a Slender Unyawed Ductile Rod at Low Velocity



Released for Publication by
Lincoln Laboratory
Massachusetts Institute of Technology
Lexington, Massachusetts

Fig. 6.22 Crater formed by a Slender Rod Yawed at 10° to Direction of Motion

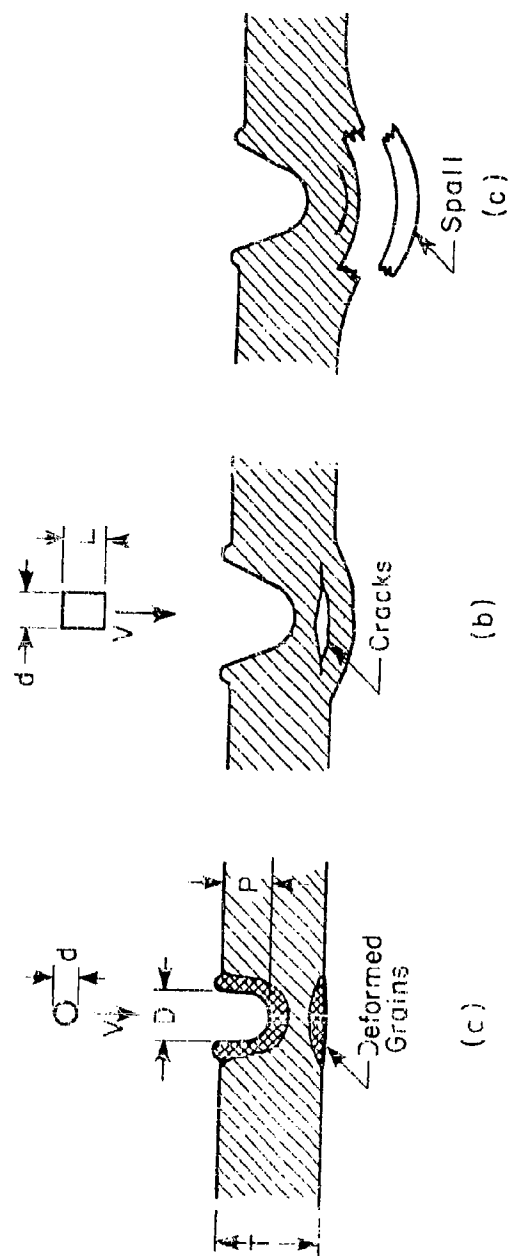


Fig. 6.23 Rear Surface Damage in Relatively Thick Targets

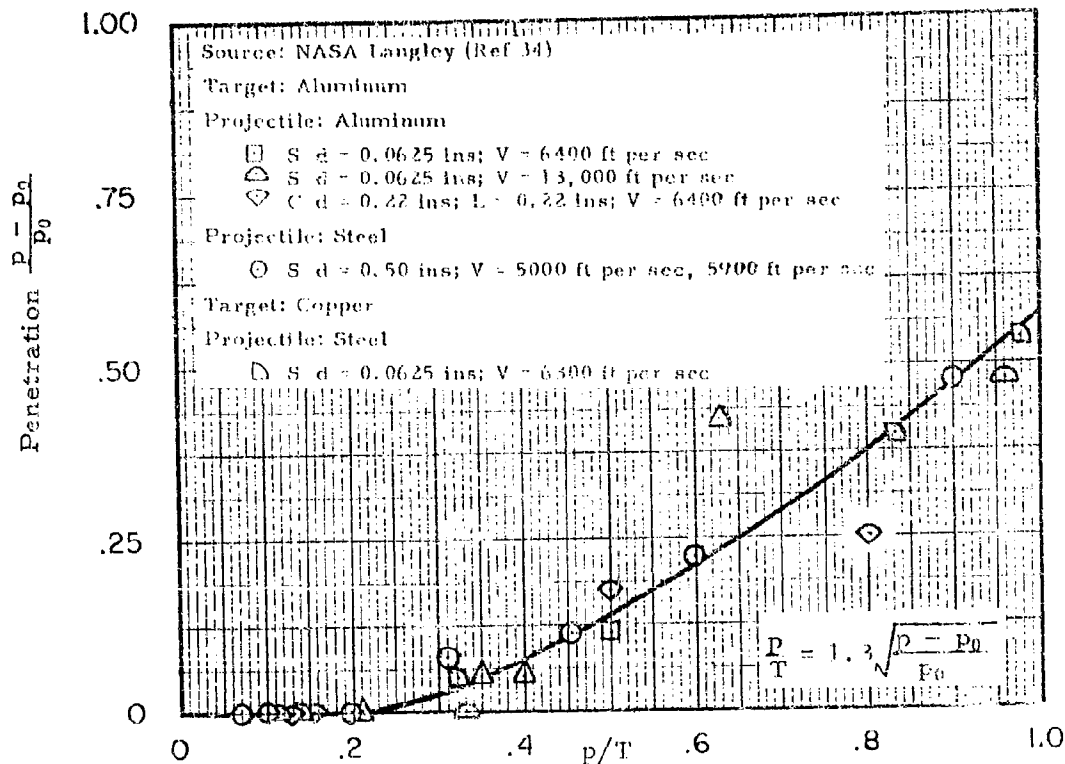


Fig. 6.24a Penetration in Finite Thickness Target in Terms of Penetration in a Quasi-Infinite Target

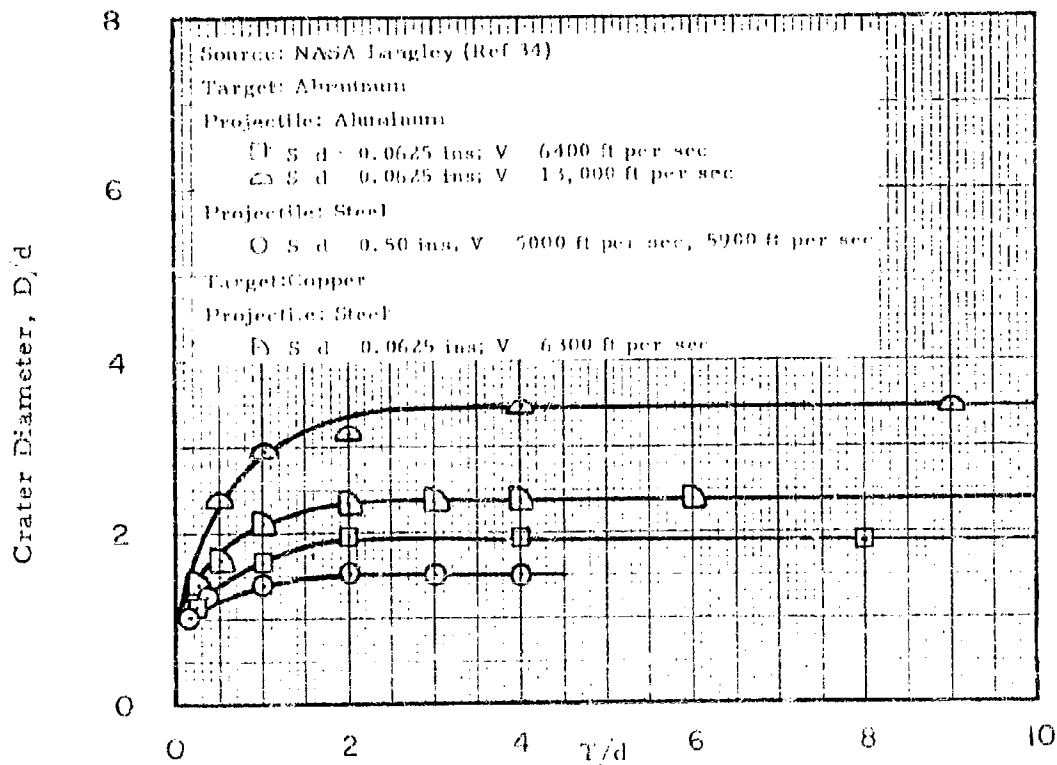
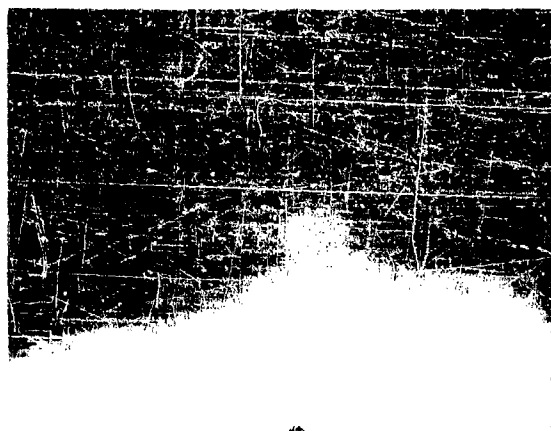


Fig. 6.24b Diameter of Crater in Finite Thickness Target in Terms of Projectile Diameter



$V = 3,100 \text{ ft/sec}$

Low Velocity Region



$V = 7,300 \text{ ft/sec}$

Transition Region



$V = 7,300 \text{ ft/sec}$

Transition Region

PHOTOGRAPH BY COLLEGE OF
NAVY AND AIR FORCE RESEARCH
LANGLEY RESEARCH CENTER, LANGLEY FIELD, VIRGINIA

Fig. 6.25 Photographs of Projectile Penetrating a Thin Target. The target is at the Left, and Projectile Motion is from Right to Left. (0.22 inch Aluminum Sphere Impacting 1/8 inch Aluminum Target)



$t = 6.5 \mu\text{sec}$



$t = 13.1 \mu\text{sec}$



$t = 16.3 \mu\text{sec}$

Reproduced by permission of
NATIONAL AERONAUTICS AND SPACE ADMINISTRATION
LANGLEY RESEARCH CENTER, HAMPTON FIELD, VIRGINIA

Fig. 6.26 Framing Camera Sequence of Penetration of a Thin Target by a High Velocity Projectile, Showing Resultant Spray (0.22 inch Aluminum Sphere Impacting 1/8 inch Aluminum)

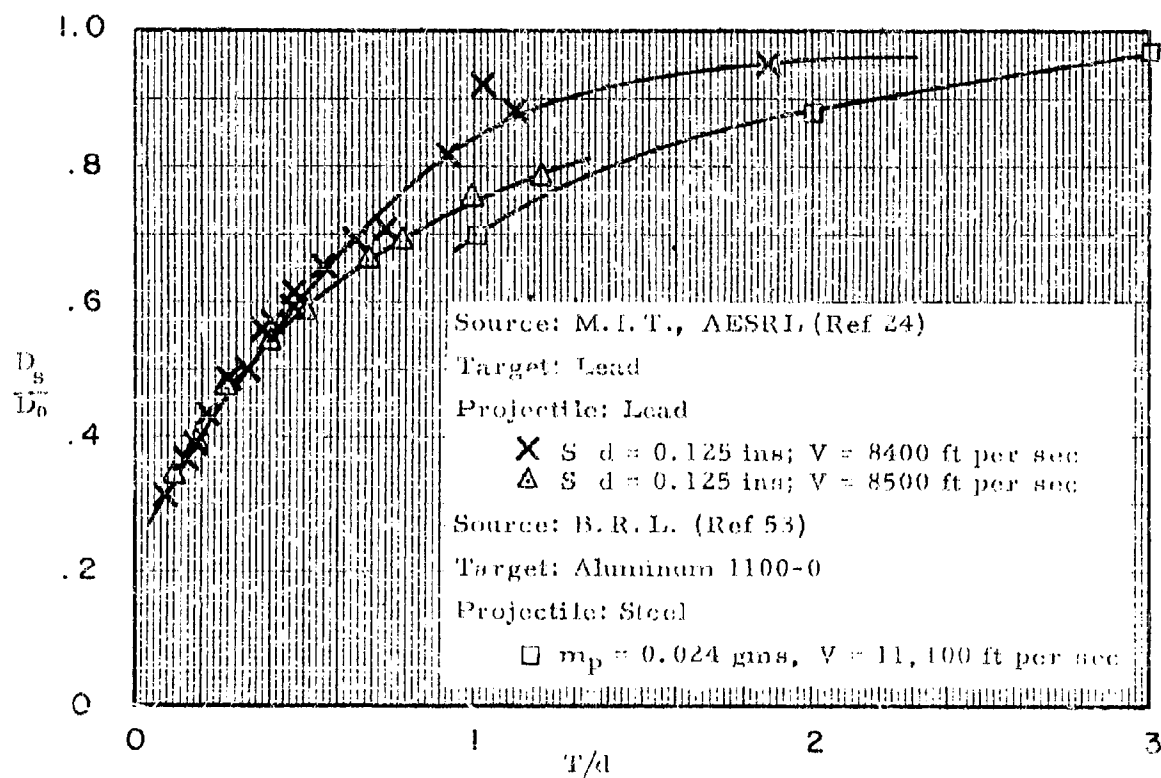


Fig. 6.27 Hole Diameter in a Thin Shield in Terms of Crater Diameter in an Unshielded Target as a Function of Shield Thickness

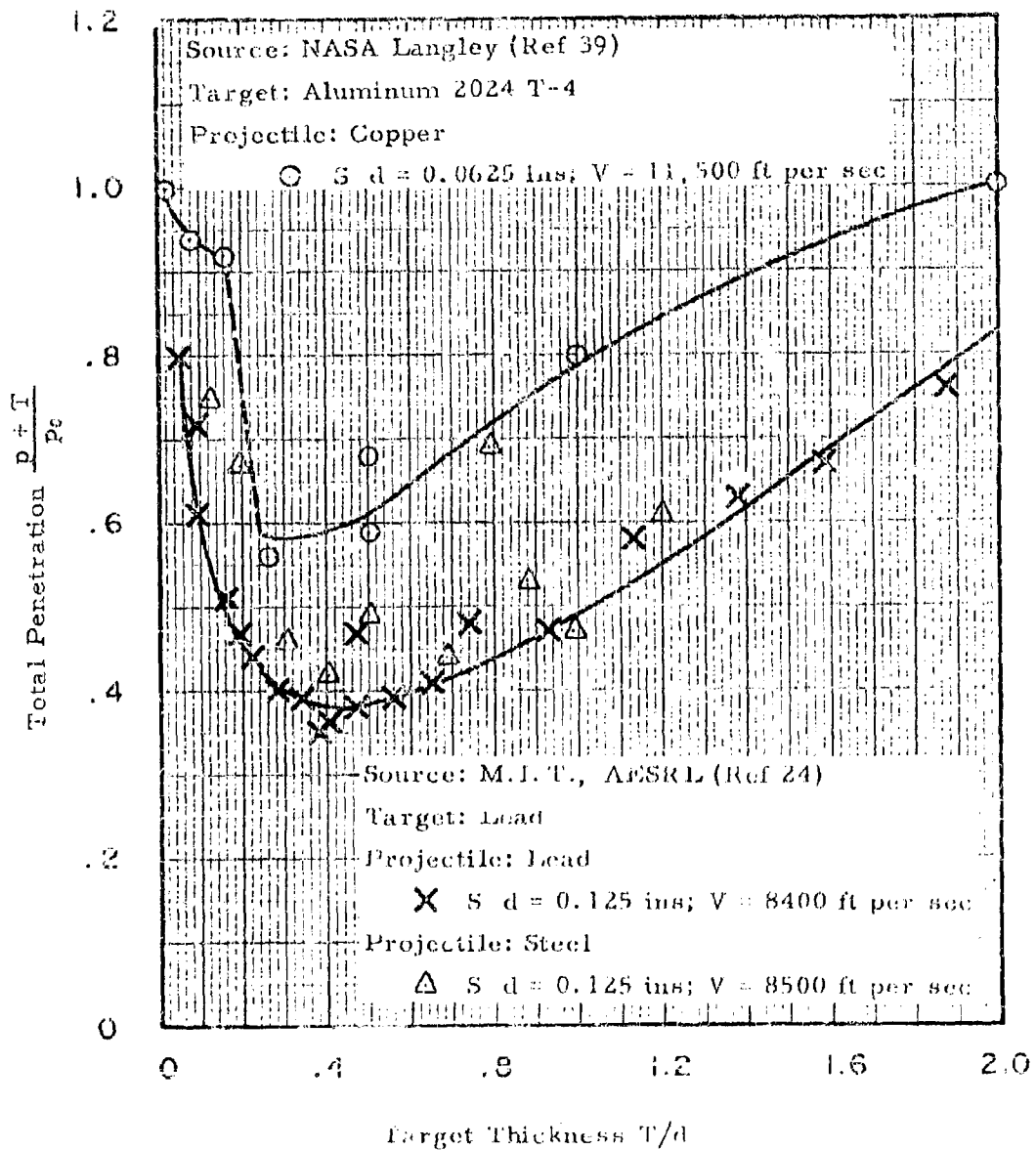


Fig. 6.28 Total Penetration of a Shielded Target in Terms of Penetration in an Unshielded Target as a Function of Shield Thickness

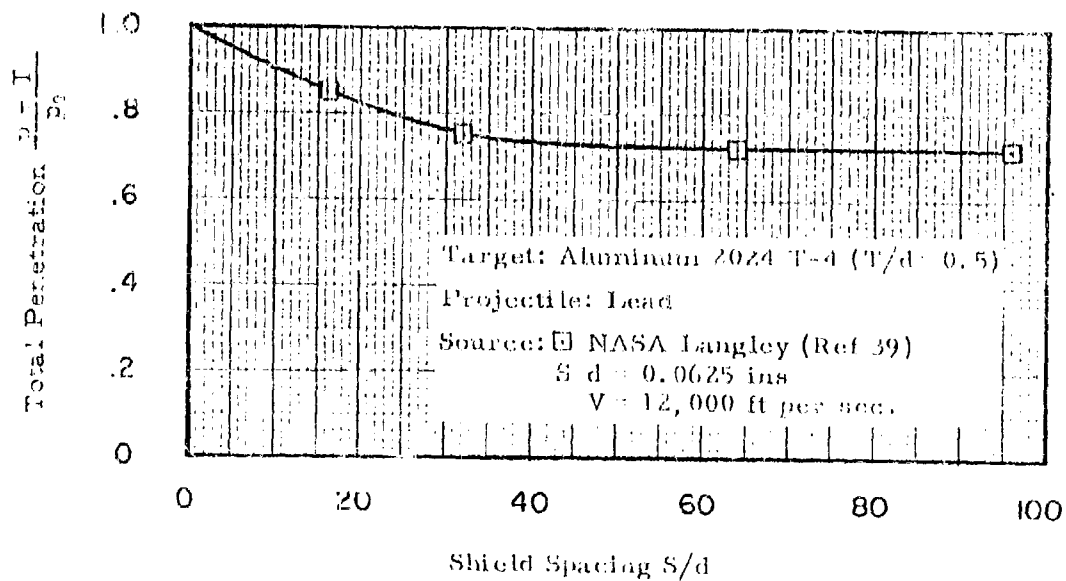
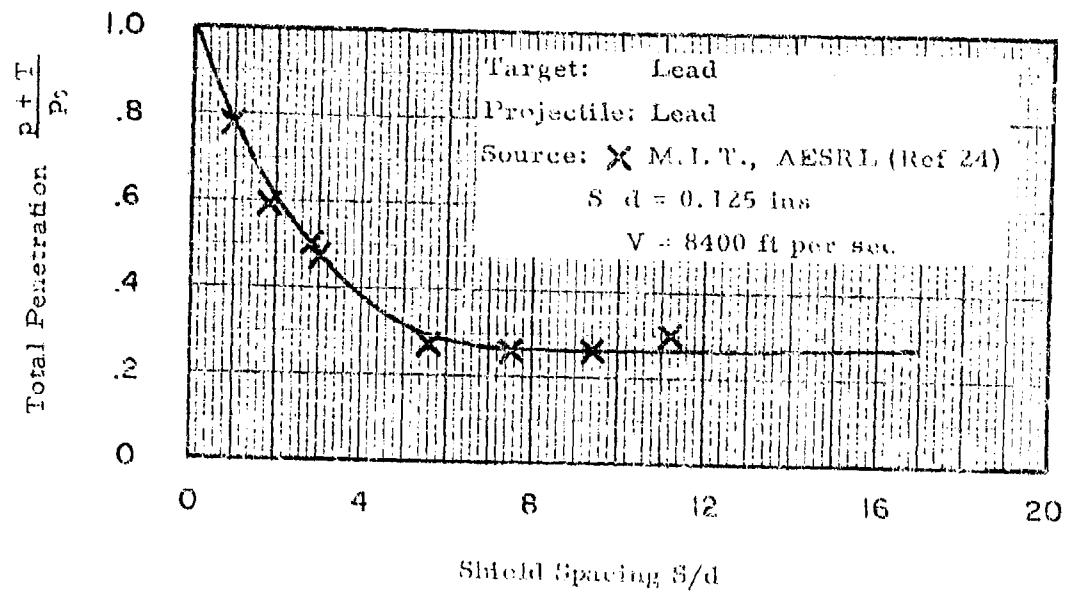


Fig. 6.29 Total Penetration of a Shielded Target in Terms of Penetration in an Unshielded Target as a Function of Shield Spacing

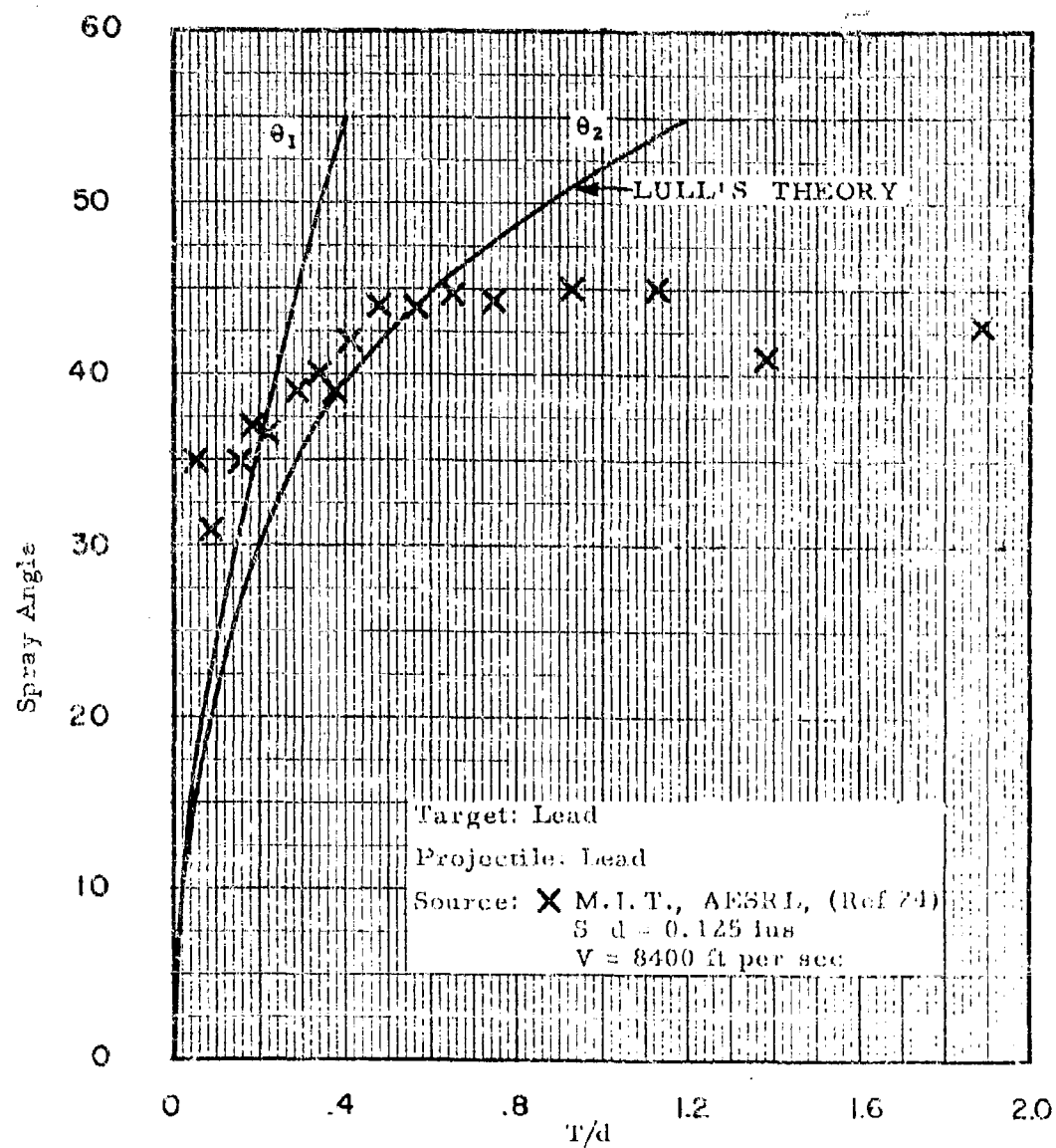


Fig. 6.30 Spray Half Angle ($\theta = \text{Arc tan } \frac{Dc}{2S}$) as a Function of Shield Thickness (Ref. 102)

This Document
Reproduced From
Best Available Copy

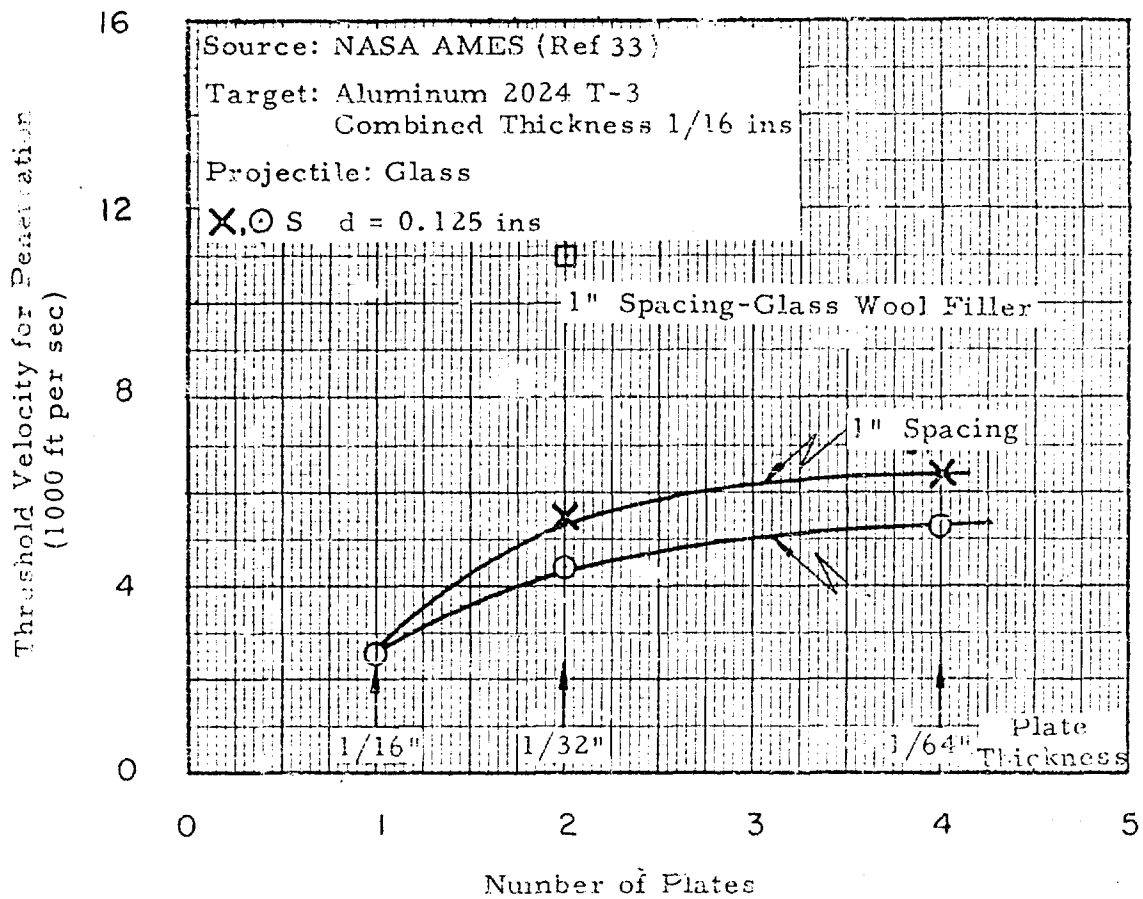


Fig. 6.31 Threshold Velocity to just Penetrate all Plates as a Function of Number of Plates

This Document
Reproduced From
Best Available Copy

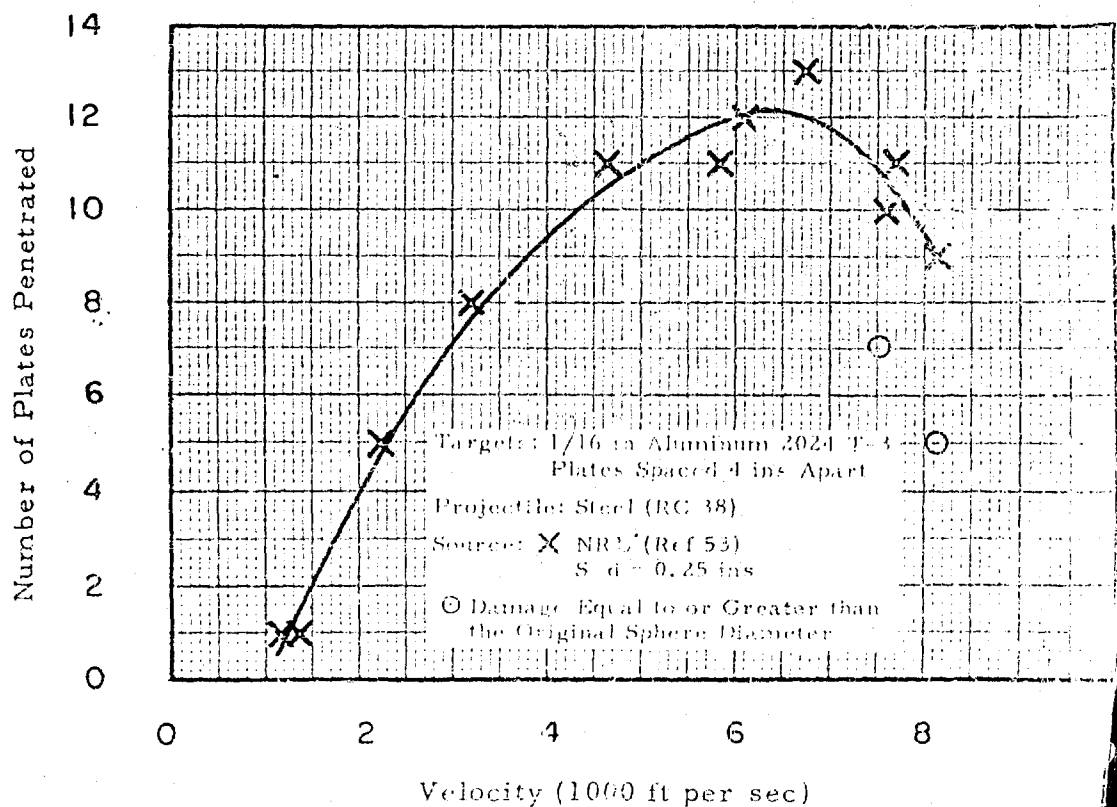
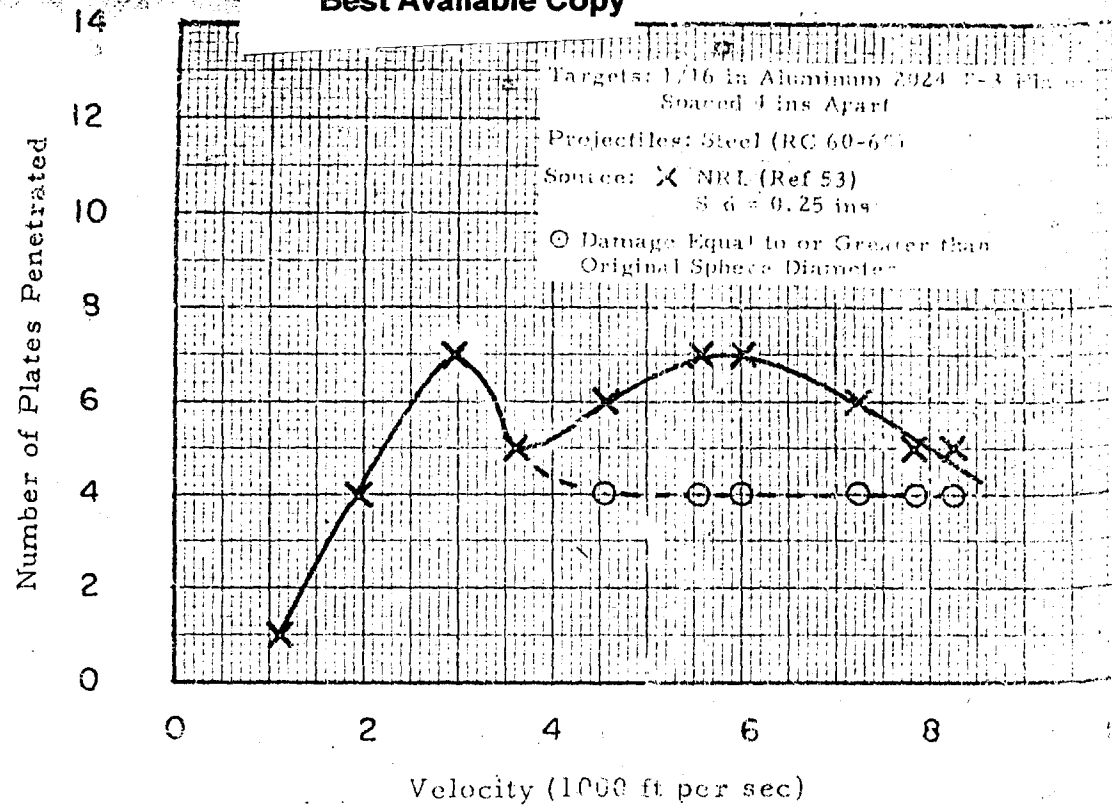


Fig. 6.32 Number of Plates Penetrated as a Function of Velocity